

Numerical simulations of gas transport in argillaceous rocks: A molecular dynamics and pore-scale simulation study

Inaugural dissertation
of the Faculty of Science,
University of Bern

presented by

Jerry Peprah Owusu

from Ghana

Supervisor of the doctoral thesis:

Prof. Dr. Sergey V. Churakov
Institute of Geological Sciences, University of Bern

Co-advisor of the doctoral thesis:

Dr. Nikolaos I. Prasianakis
Laboratory for Waste Management, Paul Scherrer Institut



^b
UNIVERSITÄT
BERN

Numerical simulations of gas transport in argillaceous rocks: A molecular dynamics and pore-scale simulation study

Inaugural dissertation
of the Faculty of Science,
University of Bern

presented by

Jerry Peprah Owusu

from Ghana

Supervisor of the doctoral thesis

Prof. Dr. Sergey V. Churakov
Institute of Geological Sciences, University of Bern

Co-advisor of the doctoral thesis

Dr. Nikolaos I. Prasianakis
Laboratory for Waste Management, Paul Scherrer Institut

Accepted by the Faculty of Science.

Bern, 14.04.2023

The Dean

Prof. Dr. Marco Herwegh

“So then it is not of him that willeth, nor of him that runneth but of God that showeth mercy”

Romans 9:16

Acknowledgements

I would like to begin by expressing my heartfelt gratitude to the Almighty God for His grace, guidance, and blessings throughout my Ph.D. journey.

I would like to extend my sincere appreciation to my main supervisor, Prof Dr. Sergey V. Churakov, for his invaluable support, mentorship, and encouragement that helped me navigate through the challenges of my research. I am also grateful to my co-advisor, Dr. Nikolaos I. Prasianakis, for his insightful feedback and constructive criticism that helped me improve the quality of my work.

I would like to express my gratitude to Dr. Konstantinos Karalis for his assistance in my simulations, coding, and setups. I am also thankful to all the staff of the Paul Scherrer Institut, Laboratory of Waste Management, transport mechanism group, for their assistance and cooperation during my research. In addition, I would like to thank Dr. Athanasios Mokos for his incredible contribution to the random walk and lattice Boltzmann modeling. Special thanks also go to Prof. Dr. Ian C Bourg for the provision of clay structures for large-scale molecular dynamics simulations.

I would like to extend my appreciation to my father in the faith, Prophet O.O Manuel, and my brother Prophet Samuel Opoku, for their unwavering prayers and support throughout my journey. Their constant encouragement helped me stay focused and motivated during difficult times.

I sincerely acknowledge the immense support and love from my parents and all my siblings throughout my academic journey. Your unwavering belief in me, constant encouragement, and motivation kept me going during good and difficult times. I am grateful for your sacrifices, understanding, and patience, as I pursued my dreams.

Finally, I would like to express my heartfelt gratitude to my girlfriend Rachel Vera Agyei for her unwavering love, understanding, and support. Her constant encouragement and motivation helped me maintain a healthy work-life balance and made my journey a pleasant one.

Thank you all for your contributions to my success.

Abstract

This dissertation investigates the gas transport and clay behavior within the context of deep geological disposal of nuclear waste. The repository for spent fuel and high-level waste can generate substantial amounts of gas through processes such as anaerobic corrosion of carbon steel, radiolysis of water, and radioactive decay in the waste. Likewise, gas production can occur in low and intermediate-level waste repositories due to chemical degradation of organic waste materials and corrosion of metals. If these gases cannot sufficiently escape from the vicinity of the repository, a localized build-up of gas pressure could compromise the integrity of the barriers and the safety design of the repository. Therefore, a thorough understanding of gas transport mechanisms and processes is crucial for assessing the repository's performance. Diffusion is the primary mechanism governing solute and fluid transport in these clays due to their low permeability. While experiments can provide valuable transport parameters for designing the barrier materials, they may not fully capture the long-term evolution of transport processes and specific subsurface conditions. Consequently, numerical and computer simulations become indispensable for determining the transport mechanisms and exploring the behavior of the system beyond the limits of experimental detection. These simulations offer the opportunity to explain experimental results, probe scales, and processes that are below the detection limit of experiments, and enhance our understanding of the transport mechanisms involved.

Gas diffusion simulation in fully saturated Na-montmorillonite (Na-MMT) was performed and the effects of pore size, gas species, and temperature were investigated. Classical molecular dynamics simulations were utilized to study the diffusion coefficients of various gases (CO_2 , H_2 , CH_4 , He, Ar). The findings indicate that the diffusion coefficients are influenced by the pore size, with H_2 and He demonstrating higher mobility compared to Ar, CO_2 , and CH_4 . The behavior of gases is affected by the confinement and the structuring of water molecules near the clay surface, as evidenced by density profiles and radial distribution functions. The obtained diffusion coefficients for different gases and slit pore sizes were parameterized using a single empirical relationship, enabling their application in macroscopic simulations of gas transport. Considering the long-term desaturation and resaturation process, the study extends to simulate gas diffusion in partially saturated Na-MMT and investigates the partitioning of gas molecules between the gas-rich and water-rich phases. Classical molecular dynamics simulations were employed to explore the impact of gas-filled pore widths, temperature, gas mean free path, gas

size, and gas molecular weights on diffusion coefficients and partitioning coefficients. The results demonstrate that the diffusion coefficient in the gas phase increases with larger gas-filled pore widths and eventually converges asymptotically towards the diffusion coefficient in the bulk state. Partitioning coefficients were found to be strongly dependent on temperature and gas molecular weights. Furthermore, non-equilibrium molecular dynamics simulations were conducted to investigate the mobility of gases in a pressure-driven flow within a partially saturated Na-MMT mesopore. The results reveal the presence of slip boundary conditions at the microscale, which challenges the assumptions made in continuum models. To predict the diffusion coefficient and dynamic viscosity of the gas, a Bosanquet-type equation was developed as a function of the average pore width, gas mean free path, geometric factor, and thickness of the adsorbed water film.

Na-montmorillonite, being a swelling clay, undergoes changes in its swelling behavior when exposed to different chemical species like gas due to variations in chemical potential. These alterations can subsequently impact the hydraulic properties and transport mechanism of the clay. Consequently, we investigated the influence of gas presence on the swelling pressure of Na-MMT. To achieve this, classical molecular dynamics simulations were employed as a methodology to examine the effect of gas on swelling pressure. The findings indicate that gas molecules cause an increase in the swelling pressure of Na-montmorillonite, with an approximate rise of 3 MPa. The specific behavior observed is influenced by factors such as the dry density and the characteristics of the gas species. Additionally, the analysis includes a comprehensive exploration of structural transformations occurring within the clay interlayer, providing insights into the discrepancies observed between experimental and simulated curves, particularly at high levels of compaction.

The thesis delves into pore-scale modeling to determine diffusion coefficients of water in compacted porous smectite clay structures. This exploration is motivated by the limitations inherent in conventional approaches used to obtain transport parameters, which tend to oversimplify the intricate porous nature of clay media by treating them as a continuum. This oversimplification neglects the behaviors occurring at smaller scales. To overcome this limitation, the thesis employs various techniques such as random walk simulations, lattice Boltzmann modeling, and large-scale molecular dynamics simulations to investigate transport mechanisms. These advanced modeling techniques take into account local diffusivities within the representative elementary volume, allowing for a more accurate understanding of transport phenomena. By considering local diffusivities, particularly near chemically reactive clay surfaces, this approach sheds light on the significance of accurately comprehending transport phenomena in porous materials. By overcoming the limitations of conventional approaches, the thesis provides valuable insights into the diffusion coefficients of water within compacted porous smectite clay structures.

This thesis offers a comprehensive exploration of gas transport and clay behavior, focusing on their relevance to deep geological disposal of nuclear waste and energy storage. By establishing connections between simulations conducted under fully saturated and partially saturated conditions, examining the influence of gases on swelling pressure, and incorporating pore-scale

modeling, this research provides valuable insights into diffusion, swelling, and pore-scale processes. These findings contribute to the development of effective barrier materials and enhance our understanding of waste management strategies in complex geological environments. The knowledge gained from this study has practical implications for improving the safety and efficiency of deep geological disposal systems and advancing energy storage technologies.

Contents

List of Figures	xv
List of Tables	xxi
1 Chapter 1: Introduction	1
1.1 Background and significance	2
1.2 Properties of clay minerals	3
1.3 Gas transport in clays	5
1.4 Numerical modeling and simulations of gas transport in porous clays	10
1.4.1 Molecular dynamics simulation	12
1.4.2 Random walk simulations	13
1.4.3 Lattice Boltzmann modeling	15
1.5 Aim of the thesis	19
1.6 Motivation and outline	20
1.7 References	22
2 Chapter 2: Mobility of Dissolved Gases in Smectites under Saturated Conditions	31
2.1 Introduction	33
2.2 Models and Methods	37
2.2.1 Simulation setup	37
2.2.2 Simulation details	38
2.2.3 Model assumptions and uncertainties	41
2.3 Results and discussion	42
2.3.1 Diffusion in bulk liquid water	42
2.3.2 Pore size effect on the diffusion of gases	44
2.3.3 Pore size and water-gas mixture effect on diffusion of water	49
2.3.4 Activation energy of diffusion	52
2.3.5 Structure of gas and aqueous fluids in clay interlayer	53
2.4 Conclusions	55
2.5 Appendix	57
2.6 References	67
3 Chapter 3: Diffusion and Gas Flow Dynamics in Partially Saturated Smectites	77

3.1	Introduction	80
3.2	Methods	83
3.2.1	System setup	83
3.2.2	Simulation details	83
3.3	Results and Discussion	87
3.3.1	Self-diffusion of gas molecules	87
3.3.2	Gas partitioning	88
3.3.3	Effect of saturation on the diffusion of gases	90
3.3.4	Flow dynamics	94
3.3.5	Viscosity of water in two-phase flow	99
3.4	Conclusions	100
3.5	Appendix	102
3.6	References	112
4	Chapter 4: Swelling Pressure of Na-Montmorillonite in the Presence of Gas from Molecular Dynamics Study	121
4.1	Introduction	123
4.2	Methods	125
4.2.1	Simulation method	125
4.2.2	System setup and simulation details	126
4.3	Results and discussion	128
4.3.1	Swelling pressure of Na-montmorillonite in pure water	128
4.3.2	Swelling pressure of Na-montmorillonite in the presence of dissolved gases	130
4.4	Conclusions	133
4.5	Appendix	135
4.6	References	142
5	Chapter 5: From Molecular Insights to Macroscopic Behavior: Up-scaling Diffusion in Smectites via Heterogeneous Pore-Scale Modeling	147
5.1	Introduction	149
5.2	Methods	152
5.2.1	Molecular dynamics simulation	152
5.2.2	Pore structure setup for the pore-scale simulations	154
5.2.3	Random walk simulation	156
5.2.4	Lattice Boltzmann modeling	158
5.3	Results and discussion	160
5.3.1	Validation of pore-scale simulation methodology	160
5.3.2	Diffusion of water in highly compacted smectite clay	163
5.3.3	Dependence of diffusion on porosity	163
5.4	Conclusions	164
5.5	References	166
6	Chapter 6: Conclusions and Outlook	171

6.1	Conclusions	172
6.2	Outlook	175
6.3	References	177

List of Figures

1.1	"Classification and analysis of gas transport processes in Opalinus Clay: a) phenomenological description based on the microstructural model concept; b) basic transport mechanisms; c) geomechanical regime; and d) effect of gas transport on the barrier function of the host rock." Reproduced with permission [72]. . . .	6
1.2	Illustration of the motion of random walkers and the number of random walkers per box.	14
1.3	"Discrete velocity models (a) D2Q7 (b) D2Q9 (c) D3Q15 (d) D3Q19." Reproduced with permission [47]	19
2.1	A snapshot from MD simulation of Na-montmorillonite, at variable interlayer nanopore distances (\AA). Oxygen atoms are red. Hydrogen atoms are white. Silica atoms are yellow. Aluminium atoms are green. Magnesium atoms are black. Sodium atoms are blue. The carbon atom of Methane is pink and the Hydrogen atom of Methane is light green.	38
2.2	D_{PBC} values for bulk water as a function of inverse simulation cell size (for simulations with 512, 1331, 3375, and 6859) at different temperatures. The size-corrected diffusion coefficient D_0 is determined by linear regression (black dashed line) to $1/L = 0$	42
2.3	Comparison of the density of the SPC/E water model from this study (green markers) and the experimental water density (red line) [83]. The right-hand axis indicates our simulated (black markers) and the experimental (blue line) shear viscosities [47]. Red and yellow circles represent shear viscosities predicted by other MD studies [39, 60].	43
2.4	Self-diffusion coefficients of gas solutes in bulk water as a function of the solute hydrodynamic radius from MD predictions from our results and other results obtained from experiments and previously reported MD predictions [28, 44]. . .	45
2.5	Diffusion coefficient of gases in saturated Na-MMT as a function of pore size fitted with eq 2.10 at temperatures (a) 300 K (b) 350 K and (c) 375 K.	47
2.6	A fit showing the relative diffusion coefficient of gases (D/D_0) in clay nanopores as a function of pore size. The marker dots represent averaged D/D_0 for temperatures of 300, 350, and 375 K. The lines represent the fit of D/D_0 with eq 2.11. . .	49

2.7	Apparent diffusion coefficients obtained from experiments of gases in three different Boom clays with varying pore size distribution and porosity, as well as apparent diffusion coefficients calculated with eq 2.13 fitted as a function of the hydrodynamic radius	50
2.8	Relative diffusion coefficient (D/D_0) of water in a water-gas mixture in clay nanopores as a function of water content/pore size. The marker dots represent D/D_0 for temperatures 300, 350, and 375 K, respectively. The lines represent the fit of D/D_0 with eq 2.11.	51
2.9	Density profiles of gases, water, and Na^+ ions at a pore size of (a) 1.0 and (b) 2.1 nm. The values of O_w and H_w are scaled down to 5% for better visualization . .	54
2.10	Fluid density profile at pore size 1.0nm	59
2.11	Fluid density profile at pore size 1.3 nm	59
2.12	Fluid density profile at pore size 1.5 nm	60
2.13	Fluid density profile at pore size 1.8 nm	60
2.14	Fluid density profile at pore size 2.1 nm	60
2.15	Fluid density profile at pore size 2.4 nm	61
2.16	Fluid density profile at pore size 2.6 nm	61
2.17	Radial distribution functions of gas - oxygen (water) at all pore sizes at temperature 300 K. Hydrogen of CH_4 atom is colour magenta and oxygen of CO_2 atom is colour cyan. The peak magnitude decreases with increasing pore size.	64
2.18	Radial distribution functions of gas - oxygen (basal clay) at all pore sizes at temperature 300 K. Hydrogen of CH_4 atom is colour magenta and oxygen of CO_2 atom is colour cyan. The peak magnitude decreases with increasing pore size. . .	65
2.19	Radial distribution functions of gas - hydrogen (water) at all pore sizes at temperature 300 K. Hydrogen of CH_4 atom is colour magenta and oxygen of CO_2 atom is colour cyan. The peak magnitude decreases with increasing pore size. . .	66
3.1	A snapshot from the MD simulation of a 6 nm Na-montmorillonite slit pore for two different degrees of saturation (gas-filled pore width of 1.8 and 5.3 nm; left and right respectively). Oxygen atoms are red. Hydrogen atoms forming H_2O molecules and OH groups are white. Silica atoms are pink. Aluminium atoms are grey. Magnesium atoms are green. Sodium atoms are blue. Gas molecules, represented by argon in this particular case are yellow. The graphs next to the snapshots show the density distribution of water and gases in the slit pore. The black curve is the density distribution of the gas molecules (magnified by a factor of 10 for the sake of visualization) and the blue is that of the water. The cyan area on the density plot shows the solid-liquid interface, the pink area shows the domains occupied by the bulk-liquid-like phase, the green area shows the central domain occupied by the gas phase and the blue area indicates the gas-water interface regions.	84

3.2	Predicted self-diffusion coefficients for gas molecules as a function of equilibrium gas density at 12 MPa from MD simulations. The graph includes experimental values [16, 36, 81, 109] as well as predictions based on empirical relations. The fitting line shows diffusion coefficients predicted using the Chapman-Enskog theory, described by Chapman and Cowling [15].	89
3.3	Density distribution of water on the external surface of the clay (half pore width). (insert) The cyan-colored area on the density plot shows the solid interface characterized by strong structuring of fluid. This domain is used for the analysis of gas partitioning to the solid-liquid interface. The pink-colored area shows the domain occupied by the bulk-liquid-like phase.	89
3.4	Diffusion coefficient (D ($10^{-6} m^2/s$)) of gas molecules in the bulk gas phase in Na-MMT at 12 MPa as a function of gas-filled pore width (a) 300 K (b) 330 K. . .	91
3.5	Average diffusion coefficient of gas molecules normalized to the diffusion coefficient in a pure bulk system as a function of the Knudsen number and fitted with eqn 3.13. The curve shift observed in this study is attributed to the specific physicochemical conditions considered, which differ from the simplified conditions assumed in the original Bosanquet approximation.	92
3.6	Steady-state velocity profile of water flow in Na-MMT. The force is acting parallel to the surface on each fluid atom in the x-direction. This diagram also shows the mass density profile of water. The black markers represent the velocity values from the MD simulation, the red line is the parabolic fit of the Poiseuille flow extrapolated here to the velocity at zero, and the blue line represents the mass density profile of the water.	95
3.7	Velocity and density profiles of CO ₂ gas in steady state at a pore width of 3.3 nm. The red line fits the velocity profile of water, the black line fits the velocity profile of CO ₂ gas, the blue is the density profile of water and the orange is the density profile of CO ₂ gas. (a) DGPD (b) CGWPD.	97
3.8	Dynamic viscosity of gas molecules in Na-MMT as a function of the Knudsen number(a) DGPD (b) CGWPD.	98
3.9	Dynamic viscosity of water films confined in Na-MMT clay slit pore as a function of the number of adsorbed water layers.	100
3.10	Diffusion coefficient of gas molecules in the gas-water interface in Na-MMT at 12 MPa as a function of gas-filled pore width (a) 300 K (b) 330 K.	104
3.11	Density profile of Ar at 300 K	105
3.12	Density profile of Ar at 330 K	105
3.13	Density profile of He at 300 K	106
3.14	Density profile of He at 330 K	106
3.15	Density profile of H ₂ at 300 K	106
3.16	Density profile of H ₂ at 330 K	107
3.17	Density profile of CH ₄ at 300 K	107
3.18	Density profile of CH ₄ at 330 K	107
3.19	Density profile of CO ₂ at 300 K	108

3.20	Density profile of CO ₂ at 330 K	108
3.21	Velocity profile of Ar at 300K	109
3.22	Velocity profile of He at 300K	109
3.23	Velocity profile of H ₂ at 300K	110
3.24	Velocity profile of CH ₄ at 300K	110
3.25	Velocity profile of CO ₄ at 300K	111
4.1	Illustration of the set-up of the spring model.	126
4.2	Simulation box representing smectite clay mineral (Na-montmorillonite) submerged in water (a) pure water and (b) 0.5 mol/L gas solution (gas molecules are represented in light blue) viewed in the x-direction. The y- and z- directions of the simulation box are approximately 10 nm.	127
4.3	Swelling pressure of Na-montmorillonite in pure water as a function of clay dry density from molecular dynamics simulations [3, 46] and experimental study [22, 23]. The solid black circles represent the simulation of pure water at high density.	129
4.4	The structure of clay from a macroscopic perspective, highlighting poorly aligned platelets at the boundaries between grains. The left image displays an atomistic view, while the right shows a pore-scale view. Reproduced with permission [17, 49].	130
4.5	Swelling pressure of Na-montmorillonite in dissolved gas solution as a function of clay dry density from molecular dynamics simulations. The gray area shows the error margin for simulations with pure water. This consists of 720 individual simulations of different d-spacing, force constant, and gas species combinations.	131
4.6	Mole fraction of gas in the interlayer as a function of equilibrium interlayer spacing.	132
4.7	Comparison of swelling pressure of Na-montmorillonite for dry densities: 0.9 - 1.5 g/cm ³ . Lines are shown to guide the eye. The values below the density values in the legend indicate the interlayer pore size.	133
4.8	Density profiles of water and for CO ₂ molecules in the interlayer ranging from d-spacing of 1.6 to 3.3 nm [34]	136
4.9	Density profiles of water and for CH ₄ molecules in the interlayer ranging from d-spacing of 1.6 to 3.3 nm [34]	137
4.10	Density profiles of water and for Ar molecules in the interlayer ranging from d-spacing of 1.6 to 3.3 nm [34]	138
4.11	Density profiles of water and for H ₂ molecules in the interlayer ranging from d-spacing of 1.6 to 3.3 nm [34]	139
4.12	Density profiles of water and for He molecules in the interlayer ranging from d-spacing of 1.6 to 3.3 nm [34]	140
4.13	Radial distribution function of gas molecules and oxygen of water molecule for all d-spacings and force constants	141

5.1	Snapshot of compacted smectite clay structure solvated with water. The system shows stacking features and correlations representative of the clay matrix. In the visualization, water molecules are depicted in cyan, while the clay platelets are represented by different colors: oxygen in red, silicon in light brown, aluminium in grey, magnesium in green, hydrogen in white, and sodium in blue. Reproduced with permission [56].	153
5.2	Density distribution of water in a 4.7 nm smectite slit pore. The shaded regions represent the different structuring of water within the pore. Green, blue, pink, and cyan shades are used to denote surface 1, surface 2, surface 3, and bulk respectively. These regions are of sizes 0.35, 0.35, 0.40, and 2.5 nm respectively. .	155
5.3	A snapshot of the random walk system configuration illustrating the distribution of diffusion coefficients within the pore space. The corresponding equivalent MD system configuration is on the right. The three systems can be defined as follows: (a) A1: This system is populated with a constant diffusion coefficient throughout the entire pore space. (b) A2: In this system, diffusion coefficients vary locally within the pore space based on proximity to the clay surface. (c) A3: Similar to A2, this system incorporates local diffusion coefficients dependent on proximity to the clay surface. Additionally, it considers pore spaces within 1-3 water layers. The color bar is described in Table 5.1.	156
5.4	A snapshot showing the distribution of diffusion coefficients within the pore space for various pore structures. The pore structures (a) to (e) correspond to different configurations: (a) $\rho_{dry} = 0.33 \text{ g/cm}^3$, $\theta = 0.89$; (b) $\rho_{dry} = 0.67 \text{ g/cm}^3$, $\theta = 0.78$; (c) $\rho_{dry} = 1.00 \text{ g/cm}^3$, $\theta = 0.67$; (d) $\rho_{dry} = 1.32 \text{ g/cm}^3$, $\theta = 0.56$; (e) $\rho_{dry} = 1.67 \text{ g/cm}^3$, $\theta = 0.45$	157
5.5	Comparison of the mean square displacement obtained in large-scale MD and RW simulations from approach (a) A1 (b) A2 (c) A3	161
5.6	Configuration of the 2D clay structure for lattice Boltzmann modeling. Clay particles and pore space are represented by red and blue regions, respectively.	162
5.7	Snapshot of the lattice Boltzmann system configuration showcasing the spatial distribution of diffusion coefficients (nm^2/ps) within the pore space based on proximity to the clay surface.	162
5.8	Relative effective diffusion coefficients of water as a function of clay porosity. Red and blue markers represent values obtained from this study for diffusion parallel and perpendicular to clay layering respectively. Black and green markers represent experimental data obtained for Na-montmorillonite [4] and Na-bentonite [28] respectively.	164

List of Tables

1.1	Summary of weighting coefficients and sound speeds	18
1.2	D3Q19 discrete velocities	18
2.1	MD simulation predictions of the self-diffusion coefficients D ($10^{-9} \text{ m}^2/\text{s}$) and activation energy of diffusion (kJmol^{-1}) values for dissolved gas in bulk water	44
2.2	$D_{0,f}$ and k_c fitting parameters from the fit of the MD simulation using eq 2.8	46
2.3	Coordination numbers of water and clay oxygen around gases at pore size 2.1 nm	55
2.4	Lennard-Jones 6-12 potential parameters used in the MD simulation. The Oxygen atoms are assigned partial charges based on the atoms they are bonded to. Ob: bridging oxygen, Oh: hydroxyl oxygen, Ohs: hydroxyl oxygen with substitution, Obos: bridging oxygen with octahedral substitution, Ho: hydroxyl hydrogen, Hs: hydroxyl oxygen with substitution.	57
2.5	MD simulation predictions of the diffusion coefficients D ($10^{-9} \text{ m}^2/\text{s}$) for dissolved gas solutes in Na-MMT at different pore Sizes and temperatures	58
2.6	Coordination Numbers of Gas-Fluid and Gas-Clay Computed from Radial Pair Correlation functions	63
3.1	Predicted self-diffusion coefficients of gas molecules D ($10^{-6} \text{ m}^2/\text{s}$) at 12 MPa	87
3.2	Partitioning coefficients K (10^{-7}) and Gibbs free energy of transfer G (kJ mol^{-1}) of gas molecules at the solid-liquid interface and at the bulk-like water region	90
3.3	Mean free path of gas molecules (nm) from MD simulations (λ_{MD}) with $\sigma_{col} = \sigma_{gas}$ and kinetic theory (λ_{KT})	91
3.4	Average dynamic viscosity (centipoise) slip length (\AA) values for gas dynamics	96
3.5	MD simulation predictions of the relative diffusion coefficients (D/D_0) of gas in the gas phase in partially saturated Na-MMT	103
5.1	Distribution of Local diffusion coefficients	155
5.2	Effective diffusion coefficients derived from 2D LB and RW simulations	162
5.3	Effective diffusion coefficients derived from large-scale MD and RW simulations for clay sample with density 1.67 g/cm^3	163

Chapter 1: Introduction

1.1 Background and significance

Radioactive waste is generated as a by-product of nuclear energy production, as well as the result of industrial, research, and medical applications. The primary concern associated with radioactive waste is the potential threat it poses to humans and the environment if not adequately disposed of. International experts agree that a deep geological repository represents the safest option for long-term storage. This strategy has been adopted by Switzerland and written into its legislation [26].

The prolonged hazard posed by radioactive waste underlines the necessity for a long-term storage solution. Given its potential to contaminate the environment and jeopardize the well-being of future generations, appropriate disposal is imperative [24, 26, 49, 50]. Consequently, effective radioactive waste management constitutes a pressing concern for modern societies and the nuclear industry.

In Switzerland, the safe disposal of radioactive waste has been a priority for several decades [48]. In 1972, the country's parliament passed the Nuclear Energy Act, which set the framework for the safe use of nuclear energy [15, 102]. In 2006, the Swiss Federal Council approved the Sectoral Plan for Deep Geological Repositories, which outlines the criteria and procedures for selecting sites for deep geological repositories [25].

The selection of a site for a deep geological repository is a complex process that involves extensive geological and technical investigations. The criteria for selecting a site include factors such as the geology of the area, the stability of the rock formations, the hydrology of the area, and the distance from potential human settlements. Once a site is selected, and after obtaining the construction license, a deep geological repository can be constructed, which mainly involves excavating tunnels and chambers in the deep underground. In 2022, Nagra proposed Nördlich Lägern as the candidate location for the building of the repository.

The Swiss deep geological repository concept relies on a combination of natural and engineered barriers to ensure the safe storage of radioactive waste over hundreds of thousands of years [26, 76, 77]. In a high-level waste (HLW) repository, the spent nuclear fuel and high-level waste from the preprocessing is first encapsulated in robust containers that are designed to isolate the waste with an expected durability of at least 10'000 years. The containers are then foreseen to be placed in deep underground tunnels, where they are surrounded by a layer of compacted clay, which acts as a natural barrier to prevent the migration of radioactive materials. The surrounding host rock formations also provide the next element of defense. Although low-level and intermediate-level waste (LLW/ILW) may have low levels of radioactivity, it is still crucial to manage and dispose of it properly to avoid any potential risks. The disposal approach for LLW/ILW differs slightly from that of high-level waste (HLW). The waste is first encapsulated in a cementitious form and then placed inside a stainless steel container. This container is subsequently embedded in a cementitious backfill and stored within the host rock.

Among several challenges during the design of deep geological repositories, gas generation, and transport has to be considered thoroughly. Gas production can occur in the LLW/ILW

due to a variety of processes such as anaerobic corrosion of carbon steel, radiolysis of water, radioactive decay in the waste, chemical degradation of organic waste materials, and corrosion of metals [82, 93, 108]. Studies have shown that these processes can lead to the generation of complex gas mixtures containing species such as hydrogen (H₂), carbon dioxide (CO₂), and methane (CH₄) [114]. It is essential to prevent the accumulation of these gases in the near-field of the repository as they may compromise the integrity of the barriers and the overall safety of the repository. However, conducting experimental studies to investigate the transport mechanisms of these gases in the repository environment is extremely challenging. Therefore, modeling can be a very valuable complementary tool to simulate and predict the behavior of gases in the repository and can support resolving open questions about the transport mechanisms.

It is imperative to understand and investigate the behavior and characteristics of the gases, including their composition, production rates, and migration mechanisms. Such studies will aid in the accurate prediction and modeling of gas transport and fate in the repository and the design and optimization of appropriate gas relief measures.

1.2 Properties of clay minerals

Clays are natural rocks primarily composed of fine-grained phyllosilicates formed through the chemical weathering and alteration of parent rock material [22]. They have diverse physical and chemical properties, making them significant in several geological processes, such as soil formation, sedimentation, and diagenesis.

Clay minerals have a high surface area-to-volume ratio, giving them a large capacity for adsorbing and exchanging ions and molecules, affecting the mobility and availability of solutes, metals, and contaminants in natural systems [3, 12, 31, 70, 78]. Their swelling and shrinking behavior impact the macroscopic properties of argillaceous rocks such as porosity, hydraulic conductivity, and mechanical properties, depending on factors such as the type of clay mineral, ionic strength and pH of the surrounding solution, and degree of compaction [9, 41].

Clays comprise layers of silicate minerals arranged in a sheet-like structure held together by electrostatic forces, facilitating the exchange of cations between them. This gives clays a high cation exchange capacity (CEC), depending on various factors such as the type of clay mineral, pH and ionic strength of the solution, and the type and concentration of cations present [12, 31, 70].

Moreover, clays' physical and chemical properties are responsible for several crucial processes in natural systems, such as retention, sorption, and self-sealing [3, 78, 85, 99]. They are efficient at retaining water and solutes, affecting the transport of metals and contaminants in soils and groundwater systems, and can adsorb and retain pollutants, making them useful in remediating contaminated soils and waters.

Clays' swelling and self-sealing properties make them essential in applications such as geotechnical engineering, reducing permeability, and improving the stability of soil and rock formations [9, 41, 64, 113, 115]. Overall, clays' unique physical and chemical properties make them

significant materials in a wide range of geological and environmental systems.

In various European countries, gas transport is being evaluated through clayey potential host rocks, including Boom Clay (Belgium and Netherlands), Callovo-Oxfordian claystone (France), Boda claystone (Hungary), and Opalinus Clay (Switzerland), as well as engineered clayey materials, such as granular Wyoming sodium bentonite, FEBEX bentonite, Czech bentonite, and their sand mixtures [2, 52, 56, 100]. Clay formations exhibit unique physicochemical properties that render them a suitable candidate for deep geological disposal of radioactive waste. Decades of research and development have underscored these advantageous properties of clays, including:

- **Extremely low water permeability:** Clays possess low permeability, resulting in almost negligible advective water transport. As a result, the repository is well protected against potential water ingress [9, 113].
- **Diffusion dominated transport:** Owing to restricted water movement, transport in clays is primarily diffusive, meaning that the chemical species migrate primarily based on their concentration gradient, and therefore the transport of radionuclides through this medium is significantly delayed [12, 31, 52, 53, 59, 70].
- **Retention capacity:** Clays exhibit robust retention capacity for many radionuclides and chemical contaminants, resulting in considerable retention of the inventory in the vicinity of the source [3, 78].
- **Buffer effect:** Clays show significant buffering effects regarding chemical perturbations. Therefore, the thickness of the chemically perturbed clay around the disposal facility is minimal [74, 112].
- **Self-sealing capacity:** Clays exhibit a high degree of self-sealing, with fractures and fissures closing relatively quickly in the presence of water, especially relevant for those generated by excavation activities [6, 85, 99].
- **Stability:** The selected clay host rocks have remained unchanged for millions of years, maintaining their favorable properties. During the last few million years, migration of natural chemical species through these clay host rocks has remained primarily diffusive [41, 64, 115].
- **Homogeneity:** Radionuclide and chemical contaminant transport properties in the selected clay host rocks remain uniformly homogeneous almost throughout their entire thickness [68, 79, 105].
- **Lateral continuity:** Clays are typically present within simple geological structures that have significant lateral extent, providing a thick barrier and facilitating large-scale characterization [42, 79, 80].

The specific qualities of clays are particularly important in the context of geological disposal systems. These properties, such as low permeability, diffusive transport, retention capacity,

and self-sealing, can significantly delay the migration of radionuclides and chemical contaminants from the disposal site. This delay, coupled with the buffering effect and stability of clay formations, provides a robust barrier against the release of radionuclides into the environment. Furthermore, the vertical homogeneity and lateral continuity of clay host rocks facilitate the characterization and monitoring of the disposal facility. Therefore, considering the advantages of clay formations, they remain a suitable candidate for deep geological disposal of radioactive waste, and understanding these properties is crucial to ensure the safety of such facilities.

1.3 Gas transport in clays

Under the repository conditions, and considering fully water-saturated conditions, the dissolved gases can be transported by diffusion as well as by advection. Additionally, gases may have the ability to sorb onto mineral phases or materials. However, if the production rate surpasses the solubility limits, a distinct gas phase may form and be transported through host rock and engineered barriers based on their characteristics.

Several variables, including the hydraulic and mechanical properties of the rock matrix, the gas pressure at the source, and the hydromechanical state of the rock, can affect the gas migration through rock formations with low permeability. Based on gas concentrations and pressure gradients, the microstructural framework of the Opalinus Clay can be considered to understand four different mechanisms of gas migration [72]: advection and diffusion of dissolved gases, the visco-capillary flow of gas and water, dilatancy-controlled gas flow, and gas transport in tensile fractures. These phenomenologically informed procedures might be useful in explaining how gas moves through rocks with low permeability. These processes are well described in the study of Marschall et al. [72] as shown in Figure 1.1.

The relevant processes associated with gas transport from a deep geological repository can be summarized as follows:

- **Gas generation processes:** Within a deep geological repository, gas can be produced from a variety of waste products, which can affect how the gas is transported afterward. The gas-generating materials, environmental conditions, and waste packaging are just a few of the variables that affect the quantity, the gas species, and the rate of gas production. Processes including radiolysis, microbiological activity, and chemical reactions can all result in the formation of gas [82, 93, 108, 114]. The amount of gas produced is significantly influenced by environmental factors, including water, oxygen, and certain ions, which accelerate metal corrosion, pH, and temperature [82].
- **Gas consuming reactions:** Certain chemical reactions can result in a decrease in the overall amount of gaseous molecules. Gas sorption is a phenomenon that may take place on engineered barrier materials, as well as their corresponding degradation products, and on specific mineral phases [72]. This process can lead to the removal or reduction of gaseous molecules from a system. It is important to note that the sorption capacity and

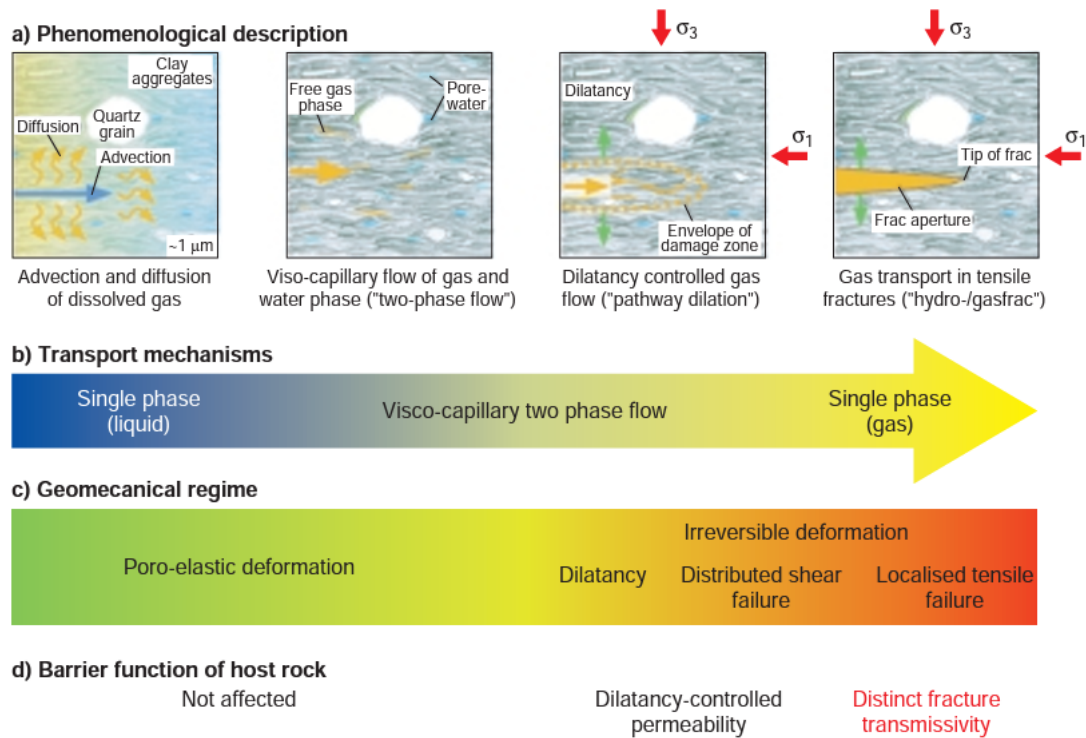


FIGURE 1.1: "Classification and analysis of gas transport processes in Opalinus Clay: a) phenomenological description based on the microstructural model concept; b) basic transport mechanisms; c) geomechanical regime; and d) effect of gas transport on the barrier function of the host rock." Reproduced with permission [72].

mechanisms can vary depending on the type of material or mineral phase involved, as well as the specific gas species and environmental conditions [4].

- **Gas solubility:** The solubility of gaseous species in aqueous systems depends on prevailing temperature and pressure conditions [28]. Low gas quantities can be dissolved in aqueous phase until the solubility limits are reached. Gas exsolution can occur when the pressure and temperature of the groundwater vary, causing the solubility of the gas to decrease, until it exceeds its saturation point [118]. This can result in bubbles of gas (gas phase) forming and accumulating in the pores and fractures of the rock around the waste canister, or even within the canister itself.
- **Advection and diffusion of dissolved gases:** Advective groundwater flow, diffusion of dissolved gas, and solubility of a gas in porewater are the three essential factors that govern the movement of gas dissolved in porewater [72]. Several parameters, including Henry's coefficient, diffusion coefficient, tortuosity, accessible porosity, and hydraulic conductivity, can have an impact on transport behavior. In highly connected porous media, advective transport is likely to be the predominant mechanism for gas transport, whereby gases are transported at the velocity of the groundwater flow. Conversely, in low-permeable media such as clay rocks, gas diffusion becomes the dominant transport mechanism.

- **Visco-capillary flow of gas and water:** Visco-capillary two-phase flow is a complex fluid dynamic phenomenon that occurs when two immiscible fluids (in this case, gas and water) flow through a porous medium, such as clay formations. This type of flow is influenced by both the viscous and capillary forces that exist in the fluid. When the rate of gas generation surpasses the solubility limit of gas in water, a gas phase is formed in the pore space. The mobility of this gas phase is then characterized by the displacement of pore water as a result of an increase in gas pressure in the pore space. Understanding subsurface gas migration in geological formations and in deep geological repositories requires knowledge of this process.
- **Dilatancy-controlled gas flow:** This mechanism manifests at elevated gas pressures, where small pores can expand under the influence of gas pressure. Additionally, pre-existing pores can merge to form flow channels. This process is facilitated in rocks that exhibit a stress state conducive to tensile deformation. When the gas pressure surpasses the minimum principal stress, pores and pre-existing microfractures can undergo dilation without fracturing, enabling gas flow. In dilatancy-controlled flows, visco-capillary forces still govern the gas flow, but the transport properties of the rock depend on the degree of rock deformation.
- **Gas transport in tensile fractures:** As gas pressure increases if the system is unable to dispel the gas by the above-mentioned processes, a macroscopic tensile fracture can be developed, if the sum of the minimum principal stress and the rock's tensile strength is exceeded by the gas pressure [72]. As a result, the fracture propagates almost instantly in what appears to be a single-phase flow process. When the gas pressure inside the fracture drops below the minimal primary stress value, the propagation stops. In low-tensile strength rocks, a macroscopic fracture is formed only when there is a rapid buildup of gas pressure.

The gas transport mechanisms in a deep geological repository are intricate and multifaceted. Gas can be generated through diverse processes within the repository, while chemical reactions can lead to a reduction in the overall concentration of gaseous molecules. The solubility, advection, and diffusion of gas in porewater play essential roles in the movement of dissolved gas. Additionally, the transport of gas in tensile fractures, visco-capillary flow, and dilatancy-controlled gas flow are critical mechanisms that must be considered to understand subsurface gas migration in geological formations and deep geological repositories. Accounting for these processes can aid in predicting and mitigating potential risks associated with gas transport from a deep geological repository.

Gas diffusion in clays

In low-permeability, saturated porous clay media, when the gas generation rate is low, the primary mode of gas transport is through the diffusion of dissolved gas in the porewater of the clay. In the event that the diffusive flux is exceeded by the rate of gas generation, the pore water within the disposal gallery will become oversaturated, resulting in the formation of a

free gas phase. Furthermore, it is anticipated that the host rock will undergo local desaturation during the repository construction phase, and a certain duration of time will be necessary for the repository to regain complete saturation (of the order of about 10^2 in HLW and 10^4 in LLW/ILW [65, 66]). Under such conditions, gas diffusion will transition from that of dry pores to that of partially saturated ones. It is crucial to understand and account for these phenomena as they can have significant implications on the safety and effectiveness of the repository, particularly in regard to gas migration and potential impacts on the surrounding environment.

Gas diffusion is a process in which particles move from regions of high concentration to regions of low concentration, driven by the concentration gradient until equilibrium is established. The kinetic theory of gases can be used to explain this process, which asserts that gases consist of numerous small particles being in constant, stochastic motion [17]. As a result, gas particles regularly collide with each other, exchanging energy and momentum. Such collisions result in a net movement of gas particles from regions of high concentration to those of low concentration, as gas particles dissipate. The rate of gas diffusion is influenced by multiple factors, such as temperature, pressure, and concentration of the gas [43, 54, 60, 69, 109]. The size and shape of molecules, as well as the presence of other gases or particles that can interact with or hinder gas molecule motion, may also impact gas diffusion [92, 94].

Fick's diffusion law is a fundamental equation that is commonly used to describe the behavior of diffusive processes [29]. The first and second laws of Fick's diffusion law provide a mathematical description of the relationship between the diffusion flux and the concentration gradient, as well as the influence of diffusion on the time variation of the concentration.

The first law of Fick's diffusion law relates the diffusion flux to the concentration gradient. In three dimensions, this law can be expressed mathematically as:

$$J_{diff} = - \left(D_x \frac{dC}{dx} + D_y \frac{dC}{dy} + D_z \frac{dC}{dz} \right) \quad (1.1)$$

where J_{diff} is the diffusion flux, D_x , D_y , D_z is the diffusion coefficient in the x,y and z dimensions respectively. C is the concentration in the units of amount of substance per unit volume (mol/m^3). $\frac{dC}{dx}$, $\frac{dC}{dy}$, $\frac{dC}{dz}$ are the concentration gradient in the three dimensions. The negative sign indicates that the diffusion flux is directed from regions of high concentration to regions of low concentration. This law is valid for both homogeneous and heterogeneous systems.

The second law of Fick's diffusion law predicts the influence of diffusion on the time variation of the concentration. In three dimensions, this law can be expressed mathematically as:

$$\frac{\partial C}{\partial t} = D_x \frac{\partial^2 C}{\partial x^2} + D_y \frac{\partial^2 C}{\partial y^2} + D_z \frac{\partial^2 C}{\partial z^2} \quad (1.2)$$

where t is the time in seconds (s).

The diffusion coefficient (D) is a fundamental parameter that establishes the proportionality relationship between the concentration gradient and the material flux. The diffusion coefficient is usually expressed in units of m^2/s or cm^2/s , and it depends on various factors such as temperature, pressure, and the chemical properties of the diffusing species and the medium [43, 54, 60, 69, 109]. The diffusion coefficient is a crucial parameter in the transport of gases in deep geological repositories. The diffusion coefficient is used to predict gas behavior, estimate migration time, and optimize barrier systems to limit gas migration.

Numerous experimental approaches have been devised to understand diffusive phenomena and ascertain transport coefficients of gases in clay materials [8, 40, 52, 53, 73, 90, 101]. Among these methodologies are: the outgassing of clay samples or boreholes, calculating diffusion coefficients using the concentration profile as a natural tracer, and laboratory studies based on the single or through diffusion methodology.

In order to determine the diffusion coefficient, the outgassing method measures the concentration of gas emitted from a clay sample [8, 40, 101]. This technique has been used in studies, such as in situ tests on Opalinus Clay and the degassing of natural gases in a borehole [101]. Based on a He gas concentration profile as a natural tracer derived from outgassing wells or samples of the Opalinus Clay, the method has been utilized to compute the pore diffusion coefficient [8].

In many laboratory investigations, the in-diffusion or through-diffusion method is employed to obtain the gas diffusion coefficients [52, 53, 59, 88]. This method was used to determine the diffusion coefficient after monitoring the concentration of downstream gas after the gas had flowed from an upstream reservoir filled with gas [59]. The through-diffusion method has been used to quantify helium molecular diffusion through water-saturated rocks, however, a number of inaccuracies were observed due to porosity changes and anisotropic effects [88]. A double through-diffusion technique was developed to determine the apparent gas diffusion coefficient for dissolved He and Ar in Boom Clay, Opalinus Clay, and Callovo Oxfordian Clay, in order to get more accurate results [52]. A double-through diffusion test is an efficient approach for determining gas diffusion coefficients since it facilitates the simultaneous measurement of two gases in a single experiment.

The study of gas phase diffusion in unsaturated porous materials has been extensively investigated through field and experimental methods [5, 58, 106]. However, investigations on gas diffusion in partially saturated porous clay systems have been limited, primarily due to the challenge of maintaining a predetermined saturation level of moisture within the sample. The temperature-dependent CO_2 diffusivity and permeability characteristics of two exemplary dry clay materials have been investigated by Wesenauer et al. [106]. The results were modeled with the mean transport-pore model and Darcy's law. The diffusivity of the clay material was affected by the variation in the pretreatment temperature. It was also shown that temperature dependence is only marginally affected by surface diffusion. At temperatures higher than 400°C , the phenomena of CO_2 surface diffusion appears to be a property of natural clays.

It should be noted that in diffusion experiments, two different transport parameters can be obtained, as described by Jacobs et al. [51]: the apparent diffusion coefficient and the capacity factor. These two parameters can be used to derive the effective diffusion coefficient and pore diffusion coefficient. The definitions of these parameters are as follows:

- **Pore diffusion coefficient (D_p):** This refers specifically to the rate of diffusion through the pores of a porous medium. It is affected by factors such as the size and shape of the pores, the concentration of the molecules, and the interactions between the molecules and the pore walls.
- **Effective diffusion coefficient (D_{eff}):** This refers to the overall rate of diffusion through a porous medium, taking into account all the pathways available to the molecules or particles. It is affected by factors such as the porosity of the medium, the size and shape of the pores, and the interactions between the molecules and the medium.
- **Apparent diffusion coefficient (D_{app}):** This is the observed diffusion coefficient when measuring the movement of molecules or particles through a porous medium. It is affected by both the effective diffusion coefficient and the pore diffusion coefficient. The apparent diffusion coefficient takes into consideration the retention of the diffusing species by chemo-physical interactions with the solid phase, e.g. gas sorption processes. It can be calculated experimentally by measuring the rate of diffusion of a molecule or particle through the medium and comparing it to the rate of diffusion in a free solution.
- **Capacity factor (C_F):** The capacity factor provides a measure of the retention capacity of a porous medium with respect to a diffusive fluid. It reflects the ability of the medium to retain the solute.

The mathematical relationships between the transport parameters are given by:

$$G = \frac{D_0}{D_p} = \frac{D_0}{RD_{app}} = \frac{\eta D_0}{D_{eff}} \quad (1.3)$$

where D_0 is the diffusion coefficient of solute in the gas phase or in water, D_p is the pore diffusion coefficient, D_{app} is the apparent diffusion coefficient, D_{eff} is the effective coefficient, R is the retardation factor, η is the accessible porosity. The capacity factor, $C_F = \eta R$, and G is the geometric factor. The geometric factor is a dimensionless measure that characterizes the impact of porous structure geometry on mass transport rates, particularly for diffusion in porous media. It considers the effects of tortuous pathways and pore size variations (constrictivity) on solute transport.

1.4 Numerical modeling and simulations of gas transport in porous clays

Numerical modeling of gas transport in porous clays involves using mathematical equations and computer simulations to study how gases move through clay formations. The modeling

process typically involves developing mathematical models that describe the transport of gases through the porous clay matrix, taking into account factors such as the permeability of the clay, the properties of the gas, and the geometry of the porous media. These models can be solved using numerical methods, such as finite element or finite difference methods, which can accurately simulate the complex behavior of gases in porous media. Numerical modeling can also be used to investigate the impact of various factors on gas transport, such as changes in temperature, pressure, and fluid saturation. This information can be used to develop better strategies for managing gas migration in subsurface environments.

Numerical modeling of gas transport in nuclear repositories is essential because it provides a more comprehensive understanding of the complex processes occurring in these systems. While experimental results are crucial and provide valuable data, numerical modeling allows the simulation of a wider range of conditions, scenarios, and timescales that might not be possible to investigate experimentally. Additionally, numerical models can help us identify the critical parameters that influence the gas transport processes, which is challenging to achieve solely through experiments. Furthermore, numerical modeling can help to interpret and understand experimental results by providing a framework to test hypotheses and validate observations. By combining both experimental results and numerical modeling, we can improve our confidence in predicting the behavior of gas transport in nuclear repositories, which is crucial for ensuring the safe and reliable management of nuclear waste.

The finite element or finite volume discretization approach on a continuum scale is often used for numerical modeling of reactive transport processes at the repository scale. In order to achieve this, the computational domain is partitioned into small voxels (elements or volumes) that are many orders of magnitude larger than the pore diameter. Transport characteristics are homogenized and smoothed out within these voxels, and macroscopic parameters including porosity, tortuosity, diffusivity, and permeability are used to describe the pore space. This method, however, neglects the small-scale geometrical properties and heterogeneities of porous materials, which may cause numerical results to be dependent on spatial grid discretization.

To overcome this limitation, three approaches can be used. Firstly, well-defined laboratory experiments can be conducted to provide the missing information. Secondly, pore-level solvers can be coupled with macroscopic ones in a multiscale simulator to account for pore geometry and connectivity. Thirdly, appropriate correlations can be extracted from pore-level simulations to provide the necessary microscopic feedback.

Pore-level simulations require an explicit representation of pore geometry and connectivity. Representative structures can be generated computationally or obtained via X-ray/ion-beam microtomography techniques. The diffusivity of molecular species in nano-pores can be obtained through molecular dynamics simulations. These effective pore scale diffusion coefficients can be used by pore-level methods, such as random walk, Brownian dynamics, and Lattice Boltzmann, to account for pore space connectivity and mineralogical heterogeneities. This approach can obtain sample-specific effective transport parameters for macroscopic simulations.

1.4.1 Molecular dynamics simulation

Molecular dynamics (MD) simulations are computational tools that allow for the study of the equilibrium and non-equilibrium behavior of molecules over time. These simulations rely on the integration of Newton's equations of motion to simulate the motion of atoms and molecules within a system. The equation of motion takes into account the mass of the molecule, potential energy, force on the molecule, position of the reference particle, and distance between the reference molecule and neighboring molecules. Newton's equation is given by:

$$M_k \frac{d^2 R_k}{dt^2} = - \frac{\partial V(R^n)}{\partial R_k} = f_k(R^n) \quad (1.4)$$

where M_k is the mass of the molecule, V is the potential energy, f_k is the force on the molecule, R_k is the position of the reference particle and R^n is the distance between the reference molecule and the neighboring molecules.

To conduct MD simulations, force potentials are required to describe intermolecular interactions within the system. These force potentials, also known as force fields, typically consist of mathematical functions that describe the potential energy between atoms or molecules as a function of their positions and orientations. Different types of force potentials used in MD simulations include empirical, semi-empirical, and ab initio potentials. Empirical force fields are commonly used due to their computational efficiency and ability to accurately capture the behavior of various substances at a wide range of conditions.

The total potential energy (U) in an MD simulation can be described as the sum of Van der Waals energy (v^{LJ}), Coulombic energy ($v^{Coulomb}$), and bonded interaction (v^{Bonded}) potential term. The Van der Waals energy is represented by the Lennard-Jones (LJ) energy and distance parameters. The Coulombic energy is dependent on the charges of the atoms and their distance apart, with the Lorentz-Berthelot combination rules used to predict interatomic interactions between unequal atomic species. The total potential energy is mathematically written as:

$$U = v^{LJ} + v^{Coulomb} + v^{Bonded} \quad (1.5)$$

with

$$v^{LJ}(r_{ij}) = 4\epsilon_{ij} \left[\left(\frac{\sigma_{ij}}{r_{ij}} \right)^{12} - \left(\frac{\sigma_{ij}}{r_{ij}} \right)^6 \right] \quad (1.6)$$

$$v^{Coulomb}(r_{i,j}) = \frac{Q_i Q_j}{4\pi\epsilon_0 r_{ij}} \quad (1.7)$$

$$v^{Bonded} = \frac{1}{2} \sum_{bonds} k_{i,j} (r_{i,j} - r_{eq})^2 \quad (1.8)$$

where atoms i and j are r_{ij} apart, ϵ_{ij} and σ_{ij} are the Lennard-Jones (LJ) energy and distance parameters, respectively. Q_i is the charge of atom i , Q_j is the charge of atom j and ϵ_0 is the vacuum permittivity. $k_{i,j}$ is the harmonic force constant and r_{eq} is the equilibrium bond distance.

Molecular dynamics simulation code

Numerous molecular dynamics codes have been developed for molecular dynamics simulations. Specifically, for the present study, two such codes were implemented:

- **LAMMPS:** The LAMMPS package [84] was employed to conduct the simulations. LAMMPS is an open-source classical molecular dynamics code with a focus on materials modeling. The acronym LAMMPS stands for Large-scale Atomic/Molecular Massively Parallel Simulator. This software is suitable for simulating particles at various scales, including atomic, meso, or continuum levels, and can serve as a parallel particle simulator.
- **GROMACS:** GROMACS [7] (GRONingen MACHine for Chemical Simulations) is a widely used open-source software package for molecular dynamics simulations of biomolecules, such as proteins, lipids, and nucleic acids. It is designed to perform a range of simulation types, including energy minimization, equilibration, and production runs, with support for a variety of force fields and algorithms. GROMACS is particularly well-suited for high-performance computing environments, with scalable parallelization and optimization for different hardware architectures. The software is freely available under the GNU Lesser General Public License (LGPL) and is actively maintained by a large community of developers and users.

Molecular dynamics simulations have been widely used to study fluid, solute, and gas interactions, as well as transport mechanisms [13, 14, 33, 38, 44, 55, 57, 98, 120]. These simulations involve modeling the behavior of individual atoms and molecules over time to understand how they interact with each other and their surroundings. In fluid systems, molecular dynamics simulations have been used to study phenomena such as viscosity, diffusion, and flow behavior [13, 14, 57, 98, 120]. In solute systems, simulations can help predict solubility, partitioning, and adsorption behavior [16, 33, 55, 91]. In gas systems, simulations have been used to study gas dynamics, coordination, and mobility. Overall, molecular dynamics simulations provide a powerful tool for investigating complex interactions and transport phenomena in fluid, solute, and gas systems.

1.4.2 Random walk simulations

Random walk (RW) simulations are a valuable tool for effectively studying the diffusion of chemical species within clays. These simulations provide insights into the intricate network of pores and channels, enabling a better understanding of the complex behavior of particles in a porous clay medium at the pore scale. By tracking the random movements of molecules within the clay's porous structure, random walk simulations capture the heterogeneous nature of pore-scale diffusion. To enhance the accuracy and applicability of these simulations, they

can be combined with other modeling techniques. For example, coupling random walk simulations with computational fluid dynamics (CFD) techniques allows for a more comprehensive analysis of coupled diffusion and advection processes [23, 30, 75]. By integrating CFD, it becomes possible to simulate the flow of fluid within the porous medium, providing a deeper understanding of the transport behavior of substances. One of the significant advantages of random walk simulations is their ability to account for the complex and tortuous diffusion paths within the porous clay medium. With its wide range of pore sizes, shapes, and connectivity, the clay medium poses challenges for accurately predicting diffusion behavior. Random walk simulations overcome this challenge by incorporating probability distributions that reflect the likelihood of particles traversing different types of pores [21, 39, 62, 63]. This capability is instrumental in assessing the effective diffusion properties of substances within the porous medium.

In a random walk method, particles known as random walkers move stochastically with random displacements and directions defined by a probability distribution function. If these random walkers encounter impermeable boundaries, specific reflection conditions are implemented. By applying appropriate statistical treatment, the random walk model can reproduce Fick's equation, which describes diffusion. Figure 1.2 illustrates a 2-dimensional system where a domain ($S_{i,j}$) within the material is examined, with 'i' and 'j' representing the dimensions in the x and y directions, respectively.

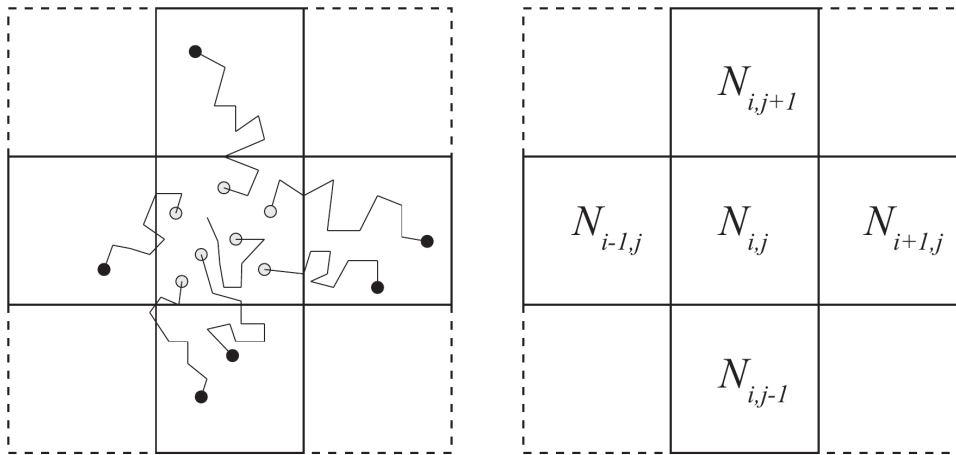


FIGURE 1.2: Illustration of the motion of random walkers and the number of random walkers per box.

By considering the number of particles entering and leaving the domain, we can establish a mass balance equation. Assuming the probability of particle movement or exiting the domain as $p = R^p \Delta t$, we can express the mass balance equation after a time step of Δt as follows:

$$N_{i,j}(t + \Delta t) = N_{i,j}(t) + R^p \Delta t (-2N_{i,j}(t) - 2N_{i,j}(t) + N_{i-1,j}(t) + N_{i+1,j}(t) + N_{i,j-1}(t) + N_{i,j+1}(t)) \quad (1.9)$$

To simplify and further analyze this equation, we can rearrange the terms and introduce Δx^2 and Δy^2 , representing the step distances in the x and y directions within the system, respectively:

$$\frac{N_i(t + \Delta t) - N_i(t)}{\Delta t} = (R^p \Delta x^2) \frac{(N_{i+1,j}(t) - 2N_{i,j}(t) + N_{i-1,j}(t))}{\Delta x^2} + (R^p \Delta y^2) \frac{(N_{i,j+1}(t) - 2N_{i,j}(t) + N_{i,j-1}(t))}{\Delta y^2} \quad (1.10)$$

This equation represents the discrete form of a partial differential equation with respect to $N_{x,y}(t)$, which denotes the number of particles at position x, y at time t. Therefore, we can express it as:

$$\frac{\partial N}{\partial t} = (R^p \Delta x^2) \frac{\partial^2 N}{\partial x^2} + (R^p \Delta y^2) \frac{\partial^2 N}{\partial y^2} \quad (1.11)$$

Alternatively, if we describe the system in terms of the number of particles per box, represented as $C_{i,j}(t) = N/V_b$ (where V_b is the volume per box), we can derive the diffusion equation as follows:

$$\frac{\partial C}{\partial t} = D_{xx} \frac{\partial^2 C}{\partial x^2} + D_{yy} \frac{\partial^2 C}{\partial y^2} \quad (1.12)$$

Here, D_{xx} and D_{yy} denote the effective diffusion coefficients in the x and y directions, respectively. When D_{xx} equals D_{yy} , the diffusion coefficient can be expressed as:

$$\frac{\partial C}{\partial t} = D_e \left(\frac{\partial^2 C}{\partial x^2} + \frac{\partial^2 C}{\partial y^2} \right) \quad (1.13)$$

where D_e is the effective diffusion coefficient.

1.4.3 Lattice Boltzmann modeling

Lattice Boltzmann Modeling (LBM) is a computational fluid dynamics method used to simulate single and multiphase fluids at the pore scale. It is a relatively new approach compared to traditional computational fluid dynamics (CFD) methods such as finite difference and finite element methods. This technique has proven to be effective in replicating the behavior of real fluids in various applications. The Lattice Boltzmann Modeling approach offers a diverse range of dynamic phenomena that can be simulated with relative ease, such as unsteady flows, phase separation, evaporation, condensation, cavitation, solute and heat transport, buoyancy, and surface interactions [11, 19, 20, 27, 36, 45, 67, 83, 87, 89, 95, 97, 103, 110, 116, 119]. Furthermore, persistent metastable states can be effectively achieved using this method [96].

The LBM method is based on the Boltzmann equation, which describes the behavior of a gas as a function of its velocity distribution function. The conceptual framework of the model is based

on a particle perspective, in which collisions, streaming, and interactions between particles, as well as between particles and surfaces, are considered the fundamental components. The Boltzmann equation is solved on a lattice, hence the name Lattice Boltzmann Modeling.

Model concept

Boltzmann proposed that a gas can be viewed as a collection of particles that interact with each other according to classical mechanics. However, due to the vast number of particles involved, a statistical treatment is necessary. In the lattice Boltzmann framework, the gas molecules kinetics is simplified to two basic operations: **streaming of fictitious particles through space** and **colliding at specific grid locations on the lattice**. The Boltzmann distribution function describes the probability distribution of particle velocities in a gas at thermodynamic equilibrium, and it is derived based on the assumption that the gas particles undergo random collisions with each other at their maximum entropy state. In a gas, the particles are in constant motion and undergo collisions with each other. These collisions result in the exchange of energy between the particles, which causes the particle velocities to be distributed according to the Boltzmann distribution. At thermodynamic equilibrium, the probability of finding a particle with a given velocity is described by the Boltzmann distribution function (1.14).

$$f(v) = \left[\frac{m}{2\pi k_b T} \right]^{3/2} 4\pi v^2 \exp\left(-\frac{mv^2}{2k_b T}\right) \quad (1.14)$$

where $f(v)$ is the Maxwell-Boltzmann equilibrium distribution function for velocity (v). The mass of the particle is denoted as m , T denotes the temperature and k_b is the Boltzmann constant.

Lattice Boltzmann models take Boltzmann's initial conceptual view of gas kinetics and simplify it even further, allowing for the simulation of fluid behavior using even fewer parameters. Instead of considering an infinite number of possible particle positions and momenta, the lattice model reduces them to just a few discrete positions and momenta. This is achieved by discretizing time and space into a regular Cartesian grid, where particles at a given time step exist within the nodes of the lattice. In the 2D model case, the number of possible momentum variations is also significantly reduced, to just 8 directions, 3 magnitudes. The model is referred to as D2Q9, given its two-dimensional nature and the inclusion of nine discrete velocities [86]. By reducing the complexity of the fluid dynamics problem, Lattice Boltzmann models are able to simulate fluid behavior with high accuracy while requiring less computational resources than traditional methods which aim at solving the Boltzmann Equation. In a typical dimensionalization, the LBM models utilize the lattice unit (lu) as the fundamental measure of length, and time steps (ts) are employed as the unit of time. This approach provides a standard framework for LBM simulations, facilitating comparison and reproducibility of results across different studies.

The typical Lattice Boltzmann Method (LBM) implementation simplifies the Boltzmann collision integral by a relaxation to equilibrium, namely the BGK approximation of the Boltzmann equation [46]:

$$\frac{\partial f}{\partial t} + \zeta \cdot \nabla f + F \cdot \nabla_{\zeta} f = -\frac{f - f^{eq}}{\tau} \quad (1.15)$$

where the single-particle distribution function in the phase space (x, ζ, t) is represented by $f(x, \zeta, t)$, while the corresponding Maxwell-Boltzmann distribution function is denoted as $f^{eq}(x, \zeta)$. Here, x refers to the position vector, ζ represents the microscopic velocity, $F(x, t)$ is a body force, and τ is the relaxation time.

The lattice BGK method (i.e. the fully discretized Boltzmann equation with the BGK collision operator [10]) employs a discrete distribution function, f_i , to represent the velocity distribution of fictitious particles of the fluid. This distribution function satisfies the Lattice Boltzmann equation as follows [46]:

$$f_i(x + e_i \Delta t, t + \Delta t) = f_i(x, t) - \frac{1}{\tau} (f_i(x, t) - f_i^{eq}(x, t)) + S_i(x, t) \quad (1.16)$$

where $f_i(x, t)$ denotes the velocity distribution function related to the discrete velocity direction i , f_i^{eq} is the equilibrium distribution function (Maxwell-Boltzmann distribution function), τ is the relaxation time and $S_i(x, t)$ is the source term added to the standard Lattice Boltzmann equation.

Equation 1.16 can be decomposed into two distinct parts that are performed in succession:

- The first part is collision (or relaxation)

$$f_i^*(x, t) = f_i(x, t) - \frac{\Delta t}{\tau} (f_i(x, t) - f_i^{eq}(x, t)) \quad (1.17)$$

where f_i^* represents the distribution function after the collision and f_i .

- The second part is streaming (or propagation)

$$f_i(x + c_i \Delta t, t + \Delta t) = f_i^*(x, t) \quad (1.18)$$

The equilibrium distribution function $f_i^{eq}(x, t)$ can be calculated as [71]:

$$f_i^{eq}(x, t) = \omega_i \rho \left[1 + \frac{e_i \cdot u}{c_s^2} + \frac{(e_i \cdot u)^2}{2c_s^4} - \frac{(u)^2}{2c_s^2} \right] \quad (1.19)$$

with

$$\rho = \sum_i f_i \quad (1.20)$$

and

$$u = \frac{1}{\rho} \sum_i f_i e_i \quad (1.21)$$

In Equation (1.16) and (1.19), the e_i denote the discrete velocities, and ω_i represent their respective weights listed in Table 1.1. The macroscopic density and macroscopic velocity vector are denoted by ρ and u respectively. Discrete velocity models are typically denoted as $DnQm$, where n refers to the number of dimensions in space, and m indicates the total number of velocities.

TABLE 1.1: Summary of weighting coefficients and sound speeds

Model	w_i	c_s^2
D2Q7	1/2 (i=0), 1/12 (i=1, ..., 6)	$c^2/4$
D2Q9	4/9 (i=0), 1/9 (i=1, 2, 3, 4), 1/36 (i=5, 6, 7, 8)	$c^2/3$
D3Q15	2/9 (i=0), 1/9 (i=1, ..., 6), 1/72 (i=7, ..., 14)	$c^2/3$
D3Q19	1/3 (i=0), 1/18 (i=1, ..., 6), 1/36 (i=7, ..., 18)	$c^2/3$

Figure 1.3 illustrates the widely used 2D and 3D discrete velocity models, namely D2Q7, D2Q9, D3Q15, and D3Q19. Specifically for the D3Q19 model [107], the discrete velocities are given in Table 5.10. In the Table 5.10, the discrete velocities are multiplied by the parameter c , which is the lattice speed and is defined as $c = \Delta x / \Delta t$

TABLE 1.2: D3Q19 discrete velocities

e_0	e_1	e_2	e_3	e_4	e_5	e_6	e_7	e_8	e_9	e_{10}	e_{11}	e_{12}	e_{13}	e_{14}	e_{15}	e_{16}	e_{17}	e_{18}
0	1	-1	0	0	0	0	1	-1	1	-1	1	-1	1	-1	0	0	0	0
0	0	0	1	-1	0	0	1	1	-1	-1	0	0	0	0	1	-1	1	-1
0	0	0	0	0	1	-1	0	0	0	0	1	1	-1	-1	1	1	-1	-1

In conclusion, Lattice Boltzmann modeling is a computational technique that has been widely used to simulate fluid transport in porous media, including porous clay materials [1, 18, 32, 34, 35, 37, 81, 104, 111, 117]. In the context of shale gas extraction, the Lattice Boltzmann method has been applied to study the transport of fluids in the nanopores of shale rocks, which is crucial for the productivity of gas wells [104, 117]. The technique has also been used to investigate the geochemical reactions that occur in clay materials during CO₂ sequestration, which can provide important insights into the long-term stability of geological CO₂ storage sites [35]. Furthermore, Lattice Boltzmann modeling has been employed in geotechnical engineering to investigate the flow of fluids through compacted clay liners [61], which are commonly used as barriers to prevent contamination of groundwater. In addition to these applications, Lattice Boltzmann modeling with coupled chemical reaction can also be used to simulate fluid transport in clay-based porous media for geochemical applications such as the diffusion, adsorption, and desorption of contaminants in soils and sediments [1, 18, 37, 81, 111]. By accurately simulating fluid transport in porous clay materials, the Lattice Boltzmann method can help to understand the mechanisms of transport and facilitate the development of efficient and sustainable solutions for various practical problems in geoenvironmental science.

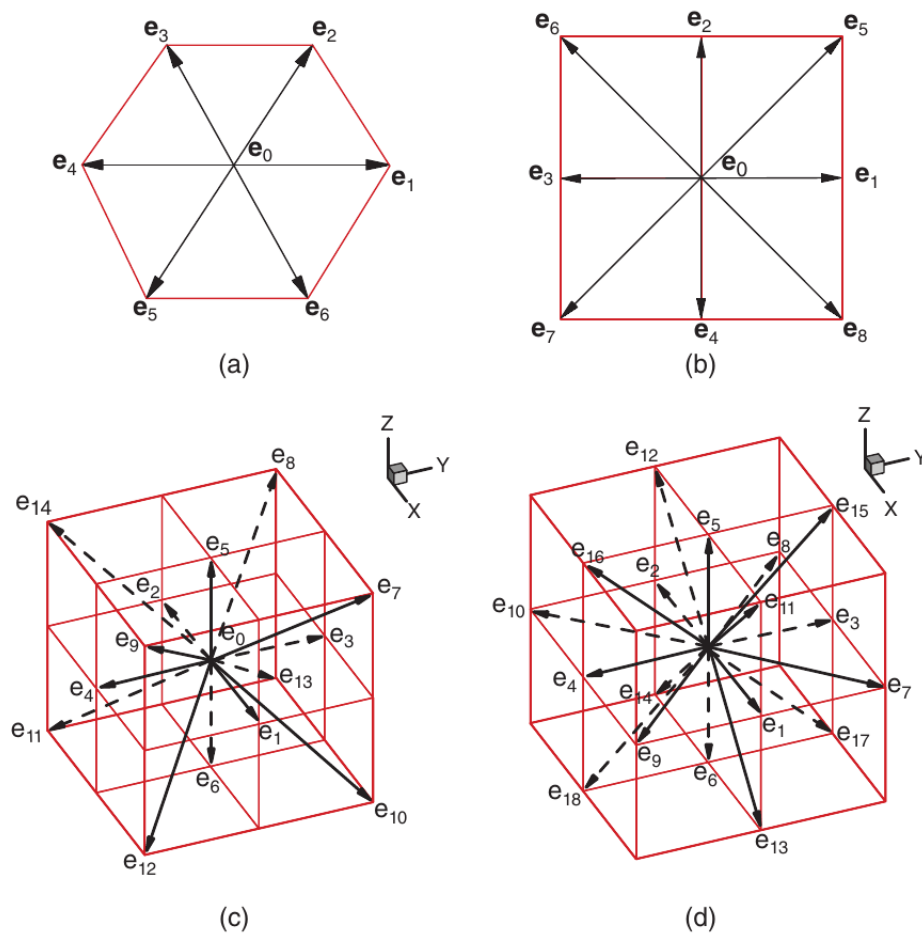


FIGURE 1.3: "Discrete velocity models (a) D2Q7 (b) D2Q9 (c) D3Q15 (d) D3Q19."
Reproduced with permission [47]

1.5 Aim of the thesis

The aim of this thesis is to investigate the behavior of gas diffusion in nuclear waste repositories, focusing on the interaction between gas molecules and the surrounding clay materials. This will be achieved by using molecular dynamics (MD) simulations to gain a molecular-level understanding of the diffusion process and then upscaling to pore scale simulations to predict the macroscopic behavior of gas diffusion in porous clay materials.

To achieve the aim of this thesis, the following objectives have been set:

- Investigate the effects of various factors such as pore size, gas types, temperature, and surface interactions on the mobility of dissolved gases in smectites under saturated conditions.
- Examine the dynamics of gas diffusion and flow in partially saturated smectites to understand the changes in gas diffusion as the clay material undergoes decreasing levels of saturation.

- Study the impact of gas molecules on the mechanical properties of Na-montmorillonite by analyzing its swelling pressure in the presence of gas.
- Upscale gas diffusion in porous clay materials from molecular dynamics to pore scale using the random walk and lattice Boltzmann method to predict the macroscopic behavior of gas diffusion in nuclear waste repositories.
- Estimation of effective sample scale diffusivities in saturated and partially saturated pore geometries for relevant gases and thermodynamic conditions.

The ultimate goal of this thesis is to develop a comprehensive understanding of gas diffusion in nuclear waste repositories and provide insights into the design and construction of safe and effective nuclear waste disposal systems. By achieving the specific objectives outlined above, this thesis aims to contribute to the scientific knowledge of gas diffusion in clay materials and provide a foundation for future research in this field. Additionally, this thesis aims to develop a computational model that can be used to simulate gas diffusion in real-world scenarios, helping to inform future nuclear waste repository design and safety assessments.

1.6 Motivation and outline

In a geological system, a hierarchy of scales exists, comprising the molecular scale, pore-scale, and large geological/continuum scale, with each scale corresponding to different pore sizes. The Geological Scale is of interest in achieving the ultimate goal of gas transport in a deep geological repository. Molecular Dynamics can be used to study diffusion at the molecular scale, while Pore Scale Modelling can be employed to investigate fluid transport through diffusion and advection. Continuum numerical modeling can simulate large geological scales, where the complex porous media is represented by a continuum and averaged over all the properties of the media within a certain volume.

In material studies, a certain Representative Elementary Volume (REV) is usually selected. The REV is the smallest volume that can yield a measurement representative of the whole. At smaller sampled volumes, there are fluctuations in material properties, while at larger volumes, properties become constant. In continuum modeling, domains are typically discretized into smaller volumes, and the smallest volume represents the REV. Thus, continuum models are unable to capture complex behavior below the REV, as the properties within the REV are averaged.

Therefore, to obtain a more realistic understanding and prediction of gas transport in a deep geological repository, a comprehensive approach spanning across multiple scales (from the molecular to the continuum scale) is necessary. However, transitioning from the microscale to the continuum scale has been a great challenge over the years.

The main focus of this thesis is to gain a better understanding of diffusion in porous clay media. To achieve this, two kinds of simulations were performed: molecular dynamics and pore-scale simulations. The molecular dynamics simulations investigate diffusion within small pores, while the pore scale simulation examines the effect of porosity, connectivity, and arrangement

of particles on microscopic diffusion. The microscopic transport parameters obtained from the pore scale simulation can be used in other models at the continuum scale. To obtain a more comprehensive understanding of diffusion in porous clay media, an upscaling method is applied in pore-scale simulations which incorporate behaviors occurring below the REV. This approach considers both the pore-scale properties and complexities, as well as the local clay interaction properties (i.e., the local diffusive coefficients obtained from molecular dynamics simulations). The successful validation of this approach for water diffusivity was achieved through a comparison of the 3D simulations of water transport in complex porous geometry obtained by molecular dynamic simulations (including full interatomic interactions) with the upscaling approach, using random walk simulation of non-interacting particles and lattice-based representation of pore geometry [21].

It should be noted that during the construction phase of the repository, it is expected that the host rock will undergo local de-saturation, necessitating a temporary re-saturation period estimated to range between $10^3 - 10^4$ years before achieving full saturation. Therefore, different degrees of saturation are expected to occur in the pores. According to Kelvin's equation, big pores are expected to desaturate first, followed by small pores as relative humidity reduces. Our model is expected to capture the flow of gases at different saturation states. To better understand diffusive transport, we aim to answer the following questions: (a) What is the preferential diffusion pathway of gas in porous clay media, interlayer or micropore, and how does the diffusion coefficient vary with pore size and geometry? (b) In the context of gas transport in porous clay media, what is the spatial distribution and partitioning of gas phases, and how do they relate to the complex pore geometry and interlayer/micropore structures?

This thesis presents a comprehensive investigation of the transport properties of gas in smectite clay. In Chapter 2, equilibrium molecular dynamics simulation was applied to understand the diffusion mechanism of dissolved gases in a smectite clay nanopore. The influence of pore size, gas species, and temperature on the molecular scale diffusive transport was further explored. In Chapter 3, equilibrium molecular dynamics was applied to understand the diffusion of gases in a partially saturated smectite clay nanopore and how gas partitions between the gas-rich phase and the water phase in the nanopore. Furthermore, non-equilibrium molecular dynamics was applied to investigate the dynamics of viscous gas flow in the nanopore. It has been shown by studies that the dissolution of solutes in saturated porous clay materials can change the swelling behavior of the clay materials, which, in turn, can change the porosity and thereby change the transport properties. Therefore, in Chapter 4, an equilibrium molecular dynamics methodology was implemented to study the influence of dissolved gases on the swelling pressure of smectite clay. Finally, in Chapter 5, an upscaling approach was performed where local diffusion coefficients were implemented in a random walk and lattice Boltzmann simulations to understand pore scale diffusivity.

1.7 References

- [1] Akai, T., Blunt, M. J., and Bijeljic, B. (2020). Pore-scale numerical simulation of low salinity water flooding using the lattice boltzmann method. *Journal of colloid and interface science*, 566:444–453.
- [2] Arkai, P., Balogh, K., Demény, A., Fórizs, I., Nagy, G., and Máthé, Z. (2000). Composition, diagenetic and post-diagenetic alterations of a possible radioactive waste repository site: the boda albitic claystone formation, southern hungary. *Acta Geologica Hungarica*, 43(4):351–378.
- [3] Avisar, D., Primor, O., Gozlan, I., and Mamane, H. (2010). Sorption of sulfonamides and tetracyclines to montmorillonite clay. *Water, Air, & Soil Pollution*, 209:439–450.
- [4] Aylmore, L. (1974). Gas sorption in clay mineral systems. *Clays and Clay Minerals*, 22:175–183.
- [5] Bardelli, F., Mondelli, C., Didier, M., Vitillo, J. G., Cavicchia, D. R., Robinet, J.-C., Leone, L., and Charlet, L. (2014). Hydrogen uptake and diffusion in callovo-oxfordian clay rock for nuclear waste disposal technology. *Applied Geochemistry*, 49:168–177.
- [6] Bastiaens, W., Bernier, F., and Li, X. L. (2007). Selfrac: Experiments and conclusions on fracturing, self-healing and self-sealing processes in clays. *Physics and Chemistry of the Earth, Parts A/B/C*, 32(8-14):600–615.
- [7] Bekker, H., Berendsen, H., Dijkstra, E., Achterop, S., Vondrumen, R., Vanderspoel, D., Sibbers, A., Keegstra, H., and Renardus, M. (1993). Gromacs-a parallel computer for molecular-dynamics simulations. In *4th international conference on computational physics (PC 92)*, pages 252–256. World Scientific Publishing.
- [8] Bensenouci, F., Michelot, J., Matray, J., Savoye, S., Lavielle, B., Thomas, B., and Dick, P. (2011). A profile of helium-4 concentration in pore-water for assessing the transport phenomena through an argillaceous formation (tournemire, france). *Physics and Chemistry of the Earth, Parts A/B/C*, 36(17-18):1521–1530.
- [9] Benson, C. H. and Trast, J. M. (1995). Hydraulic conductivity of thirteen compacted clays. *Clays and clay minerals*, 43:669–681.
- [10] Bhatnagar, P. L., Gross, E. P., and Krook, M. (1954). A model for collision processes in gases. i. small amplitude processes in charged and neutral one-component systems. *Physical review*, 94(3):511.
- [11] Boek, E. S. and Venturoli, M. (2010). Lattice-boltzmann studies of fluid flow in porous media with realistic rock geometries. *Computers & Mathematics with Applications*, 59(7):2305–2314.
- [12] Borden, D. and Giese, R. (2001). Baseline studies of the clay minerals society source clays: cation exchange capacity measurements by the ammonia-electrode method. *Clays and Clay Minerals*, 49(5):444–445.

- [13] Botan, A., Marry, V., Rotenberg, B., Turq, P., and Noetinger, B. (2013). How electrostatics influences hydrodynamic boundary conditions: Poiseuille and electro-osmotic flows in clay nanopores. *The Journal of Physical Chemistry C*, 117(2):978–985.
- [14] Botan, A., Rotenberg, B., Marry, V., Turq, P., and Noetinger, B. (2011). Hydrodynamics in clay nanopores. *The Journal of Physical Chemistry C*, 115(32):16109–16115.
- [15] Buehlmann, W. (1991). Political and legal aspects of the nuclear power phaseout in Switzerland.
- [16] Campos, M. D., Akkutlu, I. Y., and Sigal, R. F. (2009). A molecular dynamics study on natural gas solubility enhancement in water confined to small pores. In *SPE annual technical conference and exhibition*. OnePetro.
- [17] Chapman, S. and Cowling, T. G. (1990). *The mathematical theory of non-uniform gases: an account of the kinetic theory of viscosity, thermal conduction and diffusion in gases*. Cambridge university press.
- [18] Chen, C., Hu, D., Westacott, D., and Loveless, D. (2013). Nanometer-scale characterization of microscopic pores in shale kerogen by image analysis and pore-scale modeling. *Geochemistry, Geophysics, Geosystems*, 14(10):4066–4075.
- [19] Chen, S., Tölke, J., and Krafczyk, M. (2009). Simulation of buoyancy-driven flows in a vertical cylinder using a simple lattice boltzmann model. *Physical Review E*, 79(1):016704.
- [20] Chen, X.-P., Zhong, C.-W., and Yuan, X.-L. (2011). Lattice boltzmann simulation of cavitating bubble growth with large density ratio. *Computers & Mathematics with Applications*, 61(12):3577–3584.
- [21] Churakov, S. V. and Gimmi, T. (2011). Up-scaling of molecular diffusion coefficients in clays: A two-step approach. *The Journal of Physical Chemistry C*, 115(14):6703–6714.
- [22] Corominas, J., Martínez-Bofill, J., and Soler, A. (2015). A textural classification of argillaceous rocks and their durability. *Landslides*, 12:669–687.
- [23] Dehbi, A. (2011). Prediction of extrathoracic aerosol deposition using random walk and less approaches. *Aerosol Science and Technology*, 45(5):555–569.
- [24] EC (2004). Geological Disposal of Radioactive Wastes Produced by Nuclear Power. From Concept to Implementation. *Report of the European Commission, EUR 21224*. European Commission, Luxembourg, page 43pp.
- [25] ENSI (2008). Sectoral plan for deep geological repositories. <https://www.ensi.ch/en/waste-disposal/deep-geological-repository/sectoral-plan-for-deep-geological-repositories-egt/> [Accessed: 2023-04-08].
- [26] ENSI (2009). Guideline for Swiss Nuclear Installations. Specific design principles for deep geological repositories and requirements for the safety case. *ENSI Report ENSI-G03/e*, Swiss Federal Nuclear Safety Inspectorate (ENSI), Brugg, Switzerland.

- [27] Ezzatneshan, E. (2017). Study of surface wettability effect on cavitation inception by implementation of the lattice boltzmann method. *Physics of Fluids*, 29(11):113304.
- [28] Fernandez-Prini, R., Crovetto, R., Japas, M. L., and Laria, D. (1985). Thermodynamics of dissolution of simple gases in water. *Accounts of Chemical Research*, 18(7):207–212.
- [29] Fick, A. (1855). Poggendorff's flannel. *Physik*, 94(59):297.
- [30] Forsyth, P., Gillespie, D. R., McGilvray, M., and Galoul, V. (2016). Validation and assessment of the continuous random walk model for particle deposition in gas turbine engines. In *Turbo Expo: Power for Land, Sea, and Air*, volume 49682, page V001T01A026. American Society of Mechanical Engineers.
- [31] Foster, M. D. (1951). The importance of exchangeable magnesium and cation-exchange capacity in the study of montmorillonitic clays. *American Mineralogist: Journal of Earth and Planetary Materials*, 36(9-10):717–730.
- [32] Froning, D., Brinkmann, J., Reimer, U., Schmidt, V., Lehnert, W., and Stolten, D. (2013). 3d analysis, modeling and simulation of transport processes in compressed fibrous microstructures, using the lattice boltzmann method. *Electrochimica Acta*, 110:325–334.
- [33] Gadikota, G., Dazas, B., Rother, G., Cheshire, M. C., and Bourg, I. C. (2017). Hydrophobic solvation of gases (co₂, ch₄, h₂, noble gases) in clay interlayer nanopores. *The Journal of Physical Chemistry C*, 121(47):26539–26550.
- [34] Gao, J., Xing, H., Tian, Z., and Muhlhaus, H. (2014). Lattice boltzmann modeling and evaluation of fluid flow in heterogeneous porous media involving multiple matrix constituents. *Computers & Geosciences*, 62:198–207.
- [35] Gao, J., Xing, H., Tian, Z., Pearce, J. K., Sedek, M., Golding, S. D., and Rudolph, V. (2017). Reactive transport in porous media for co₂ sequestration: Pore scale modeling using the lattice boltzmann method. *Computers & Geosciences*, 98:9–20.
- [36] Genty, A. and Pot, V. (2013). Numerical simulation of 3d liquid–gas distribution in porous media by a two-phase trt lattice boltzmann method. *Transport in porous media*, 96:271–294.
- [37] Ghanbarian, B., Daigle, H., Hunt, A. G., Ewing, R. P., and Sahimi, M. (2015). Gas and solute diffusion in partially saturated porous media: Percolation theory and effective medium approximation compared with lattice boltzmann simulations. *Journal of Geophysical Research: Solid Earth*, 120(1):182–190.
- [38] Gimmi, T. and Churakov, S. V. (2019a). Water retention and diffusion in unsaturated clays: Connecting atomistic and pore scale simulations. *Applied Clay Science*, 175:169–183.
- [39] Gimmi, T. and Churakov, S. V. (2019b). Water retention and diffusion in unsaturated clays: Connecting atomistic and pore scale simulations. *Applied Clay Science*, 175:169–183.
- [40] Gomez-Hernandez, J. (2000). Fm-c experiment: Part a) effective diffusivity and accessible porosity derived from in-situ he-4 tests. part b) prediction of he-3 concentration in a cross-hole experiment.

- [41] Grambow, B. (2016). Geological disposal of radioactive waste in clay. *Elements*, 12(4):239–245.
- [42] Haldorsen, H. H. and Lake, L. W. (1984). A new approach to shale management in field-scale models. *Society of Petroleum Engineers Journal*, 24(04):447–457.
- [43] Han, P. and Bartels, D. M. (1996). Temperature dependence of oxygen diffusion in h₂o and d₂o. *The Journal of physical chemistry*, 100(13):5597–5602.
- [44] He, S., Jiang, Y., Conrad, J. C., and Qin, G. (2015). Molecular simulation of natural gas transport and storage in shale rocks with heterogeneous nano-pore structures. *Journal of Petroleum Science and Engineering*, 133:401–409.
- [45] He, X. and Luo, L.-S. (1997). Lattice boltzmann model for the incompressible navier–stokes equation. *Journal of statistical Physics*, 88:927–944.
- [46] He, X., Zou, Q., Luo, L.-S., and Dembo, M. (1997). Analytic solutions of simple flows and analysis of nonslip boundary conditions for the lattice boltzmann bgk model. *Journal of Statistical Physics*, 87:115–136.
- [47] Huang, H., Sukop, M., and Lu, X. (2015). Multiphase lattice boltzmann methods: Theory and application.
- [48] Hummel, W. and Schneider, J. W. (2005). Safety of nuclear waste repositories. *Chimia*, 59(12):909–909.
- [49] IAEA (2009). Classification of Radioactive Waste. *IAEA Safety Standards Series. No. GSG-1. IAEA, Vienna, Austria.*
- [50] IAEA (2011). Geological disposal facilities for radioactive waste. *IAEA Safety Standards Series. No. SSG-14. IAEA, Vienna, Austria.*
- [51] Jacops, E., Aertsens, M., Maes, N., Bruggeman, C., Krooss, B., Amann-Hildenbrand, A., Swennen, R., and Littke, R. (2017a). Interplay of molecular size and pore network geometry on the diffusion of dissolved gases and h₂o in boom clay. *Applied Geochemistry*, 76:182–195.
- [52] Jacops, E., Maes, N., Bruggeman, C., and Grade, A. (2017b). Measuring diffusion coefficients of dissolved he and ar in three potential clay host formations: Boom clay, callovo-oxfordian clay and opalinus clay. *Geological Society, London, Special Publications*, 443(1):349–360.
- [53] Jacops, E., Volckaert, G., Maes, N., Weetjens, E., and Govaerts, J. (2013). Determination of gas diffusion coefficients in saturated porous media: He and ch₄ diffusion in boom clay. *Applied Clay Science*, 83:217–223.
- [54] Jaynes, D. and Rogowski, A. (1983). Applicability of fick’s law to gas diffusion. *Soil Science Society of America Journal*, 47(3):425–430.

- [55] Jiang, W. and Lin, M. (2018). Molecular dynamics investigation of conversion methods for excess adsorption amount of shale gas. *Journal of Natural Gas Science and Engineering*, 49:241–249.
- [56] Karnland, O., Nilsson, U., Weber, H., and Wersin, P. (2008). Sealing ability of wyoming bentonite pellets foreseen as buffer material–laboratory results. *Physics and Chemistry of the Earth, Parts A/B/C*, 33:S472–S475.
- [57] Kosakowski, G., Churakov, S. V., and Thoenen, T. (2008). Diffusion of na and cs in montmorillonite. *Clays and Clay Minerals*, 56(2):190–206.
- [58] Kristensen, A. H., Thorbjørn, A., Jensen, M. P., Pedersen, M., and Moldrup, P. (2010). Gas-phase diffusivity and tortuosity of structured soils. *Journal of contaminant hydrology*, 115(1-4):26–33.
- [59] Krooss, B. and Schaefer, R. (1987). Experimental measurements of the diffusion parameters of light hydrocarbons in water-saturated sedimentary rocks—i. a new experimental procedure. *Organic Geochemistry*, 11(3):193–199.
- [60] Krynicki, K., Green, C. D., and Sawyer, D. W. (1978). Pressure and temperature dependence of self-diffusion in water. *Faraday Discussions of the Chemical Society*, 66:199–208.
- [61] Kutay, M. E., Aydilek, A. H., and Masad, E. (2006). Laboratory validation of lattice boltzmann method for modeling pore-scale flow in granular materials. *Computers and Geotechnics*, 33(8):381–395.
- [62] LaBolle, E. M., Fogg, G. E., and Tompson, A. F. (1996). Random-walk simulation of transport in heterogeneous porous media: Local mass-conservation problem and implementation methods. *Water Resources Research*, 32(3):583–593.
- [63] LaBolle, E. M., Quastel, J., and Fogg, G. E. (1998). Diffusion theory for transport in porous media: Transition-probability densities of diffusion processes corresponding to advection-dispersion equations. *Water Resources Research*, 34(7):1685–1693.
- [64] Lee, S. and Tank, R. (1985). Role of clays in the disposal of nuclear waste: a review. *Applied clay science*, 1(1-2):145–162.
- [65] Leupin, O., Marschall, P., Johnson, L., Cloet, V., Schneider, J., Smith, P., Savage, D., and Senger, R. (2016a). High-level waste repository-induced effects. NAGRA Technical Report NTB–14-13, National Cooperative for the Disposal of Radioactive Waste (NAGRA).
- [66] Leupin, O., Marschall, P., Johnson, L., Cloet, V., Schneider, J., Smith, P., Savage, D., and Senger, R. (2016b). Low- and intermediate-level waste repository-induced effects. NAGRA Technical Report NTB–14-14, National Cooperative for the Disposal of Radioactive Waste (NAGRA).
- [67] Li, Q., Luo, K., Kang, Q., and Chen, Q. (2014). Contact angles in the pseudopotential lattice boltzmann modeling of wetting. *Physical Review E*, 90(5):053301.

- [68] Liu, H.-H. (2014). Non-darcian flow in low-permeability media: key issues related to geological disposal of high-level nuclear waste in shale formations. *Hydrogeology Journal*, 22(7):1525.
- [69] Longworth, L. (1954). Temperature dependence of diffusion in aqueous solutions. *The Journal of Physical Chemistry*, 58(9):770–773.
- [70] Lorenz, P., Meier, L., and Kahr, G. (1999). Determination of the cation exchange capacity (cec) of clay minerals using the complexes of copper (ii) ion with triethylenetetramine and tetraethylenepentamine. *Clays and clay minerals*, 47(3):386–388.
- [71] Luo, L.-S. (1998). Unified theory of lattice boltzmann models for nonideal gases. *Physical review letters*, 81(8):1618.
- [72] Marschall, P., Horseman, S., and Gimmi, T. (2005). Characterisation of gas transport properties of the opalinus clay, a potential host rock formation for radioactive waste disposal. *Oil & gas science and technology*, 60(1):121–139.
- [73] Mazurek, M., Alt-Epping, P., Bath, A., Gimmi, T., Waber, H. N., Buschaert, S., De Cannière, P., De Craen, M., Gautschi, A., Savoye, S., et al. (2011). Natural tracer profiles across argillaceous formations. *Applied Geochemistry*, 26(7):1035–1064.
- [74] McGregor, F., Heath, A., Shea, A., and Lawrence, M. (2014). The moisture buffering capacity of unfired clay masonry. *Building and Environment*, 82:599–607.
- [75] Mofakham, A. A. and Ahmadi, G. (2020). On random walk models for simulation of particle-laden turbulent flows. *International Journal of Multiphase Flow*, 122:103157.
- [76] NEA (2007). Regulating the Long-term Safety of Geological Disposal: Towards a Common Understanding of the Main Objectives and Bases of Safety Criteria. *OECD Nuclear Energy Agency, Publication 6182, Paris (2007)*.
- [77] NEA (2014). The safety case for deep geological disposal of radioactive waste: 2013 state of the art. *Symposium Proceedings 7–9 October 2013, Paris, France. Radioactive Waste Management Report NEA/RWM/R(2013)9, OECD/NEA, Paris, France*.
- [78] Ng, E.-P. and Mintova, S. (2008). Nanoporous materials with enhanced hydrophilicity and high water sorption capacity. *Microporous and Mesoporous Materials*, 114(1-3):1–26.
- [79] Norris, S. (2017). Radioactive waste confinement: clays in natural and engineered barriers—introduction.
- [80] Norris, S. (2019). Multiple roles of clays in radioactive waste confinement—introduction.
- [81] O’Brien, G., Bean, C., and McDermott, F. (2002). A comparison of published experimental data with a coupled lattice boltzmann-analytic advection–diffusion method for reactive transport in porous media. *Journal of Hydrology*, 268(1-4):143–157.

- [82] Ortiz, L., Volckaert, G., and Mallants, D. (2002). Gas generation and migration in boom clay, a potential host rock formation for nuclear waste storage. *Engineering geology*, 64(2-3):287–296.
- [83] Peng, Y., Zhou, J., and Burrows, R. (2011). Modelling solute transport in shallow water with the lattice boltzmann method. *Computers & fluids*, 50(1):181–188.
- [84] Plimpton, S. (1995). Fast parallel algorithms for short-range molecular dynamics. *Journal of computational physics*, 117(1):1–19.
- [85] Pusch, R. (2006). Clays and nuclear waste management. *Developments in Clay Science*, 1:703–716.
- [86] Qian, Y.-H., d’Humières, D., and Lallemand, P. (1992). Lattice bkg models for navier-stokes equation. *Europhysics letters*, 17(6):479.
- [87] Qin, F., Del Carro, L., Moqaddam, A. M., Kang, Q., Brunschwiler, T., Derome, D., and Carmeliet, J. (2019). Study of non-isothermal liquid evaporation in synthetic micro-pore structures with hybrid lattice boltzmann model. *Journal of Fluid Mechanics*, 866:33–60.
- [88] Rebour, V., Billiotte, J., Deveughele, M., Jambon, A., and Le Guen, C. (1997). Molecular diffusion in water-saturated rocks: A new experimental method. *Journal of contaminant hydrology*, 28(1-2):71–93.
- [89] Rosén, T., Eller, J., Kang, J., Prasianakis, N. I., Mantzaras, J., and Büchi, F. N. (2012). Saturation dependent effective transport properties of pefc gas diffusion layers. *Journal of The Electrochemical Society*, 159(9):F536.
- [90] Rübel, A. P., Sonntag, C., Lippmann, J., Pearson, F., and Gautschi, A. (2002). Solute transport in formations of very low permeability: Profiles of stable isotope and dissolved noble gas contents of pore water in the opalinus clay, mont terri, switzerland. *Geochimica et Cosmochimica Acta*, 66(8):1311–1321.
- [91] Sarkisov, L. and Monson, P. (2001). Modeling of adsorption and desorption in pores of simple geometry using molecular dynamics. *Langmuir*, 17(24):7600–7604.
- [92] Shimmo, M., Saarnio, K., Aalto, P., Hartonen, K., Hyötyläinen, T., Kulmala, M., and Riekkola, M.-L. (2004). Particle size distribution and gas-particle partition of polycyclic aromatic hydrocarbons in helsinki urban area. *Journal of Atmospheric Chemistry*, 47(3):223.
- [93] Small, J. S., Nykyri, M., Vikman, M., Itävaara, M., and Heikinheimo, L. (2017). The biogeochemistry of gas generation from low-level nuclear waste: Modelling after 18 years study under in situ conditions. *Applied Geochemistry*, 84:360–372.
- [94] Smedes, F., Geertsma, R. W., Zande, T. v. d., and Booij, K. (2009). Polymer- water partition coefficients of hydrophobic compounds for passive sampling: Application of cosolvent models for validation. *Environmental science & technology*, 43(18):7047–7054.
- [95] Spaid, M. A. and Phelan Jr, F. R. (1997). Lattice boltzmann methods for modeling microscale flow in fibrous porous media. *Physics of fluids*, 9(9):2468–2474.

- [96] Sukop, M. (2006). Dt thorne, jr. lattice boltzmann modeling lattice boltzmann modeling.
- [97] Sukop, M. C. and Or, D. (2004). Lattice boltzmann method for modeling liquid-vapor interface configurations in porous media. *Water Resources Research*, 40(1).
- [98] Torgersen, T., Kennedy, B., and van Soest, M. (2004). Diffusive separation of noble gases and noble gas abundance patterns in sedimentary rocks. *Earth and Planetary Science Letters*, 226(3-4):477–489.
- [99] Van Geet, M., Bastiaens, W., and Ortiz, L. (2008). Self-sealing capacity of argillaceous rocks: review of laboratory results obtained from the selfrac project. *Physics and Chemistry of the Earth, Parts A/B/C*, 33:S396–S406.
- [100] Villar, M., García-Siñeriz, J., Bárcena, I., and Lloret, A. (2005). State of the bentonite barrier after five years operation of an in situ test simulating a high level radioactive waste repository. *Engineering Geology*, 80(3-4):175–198.
- [101] Vinsot, A., Appelo, C. A. J., Lundy, M., Wechner, S., Cailteau-Fischbach, C., de Donato, P., Pironon, J., Lettry, Y., Lerouge, C., and De Canniere, P. (2018). Natural gas extraction and artificial gas injection experiments in opalinus clay, mont terri rock laboratory (switzerland). In *Mont Terri Rock Laboratory, 20 Years*, pages 377–392. Springer.
- [102] Vomvoris, S., Claudel, A., Blechschmidt, I., and Muller, H. (2013). The swiss radioactive waste management program-brief history, status, and outlook. *Journal of Nuclear Fuel Cycle and Waste Technology*, 1(1):9–27.
- [103] Walsh, S. D. and Saar, M. O. (2010). Macroscale lattice-boltzmann methods for low peclet number solute and heat transport in heterogeneous porous media. *Water Resources Research*, 46(7).
- [104] Wang, J., Chen, L., Kang, Q., and Rahman, S. S. (2016). The lattice boltzmann method for isothermal micro-gaseous flow and its application in shale gas flow: A review. *International Journal of Heat and Mass Transfer*, 95:94–108.
- [105] Wemaere, I., Marivoet, J., and Labat, S. (2008). Hydraulic conductivity variability of the boom clay in north-east belgium based on four core drilled boreholes. *Physics and Chemistry of the Earth, Parts A/B/C*, 33:S24–S36.
- [106] Wesenauer, F., Jordan, C., Azam, M., Harasek, M., and Winter, F. (2021). Considerations on temperature dependent effective diffusion and permeability of natural clays. *Materials*, 14(17):4942.
- [107] Wolf-Gladrow, D. A. (2004). *Lattice-gas cellular automata and lattice Boltzmann models: an introduction*. Springer.
- [108] Xu, T., Senger, R., and Finsterle, S. (2008). Corrosion-induced gas generation in a nuclear waste repository: Reactive geochemistry and multiphase flow effects. *Applied Geochemistry*, 23(12):3423–3433.

- [109] Yi, M., Wang, L., Cheng, Y., Wang, C., and Hu, B. (2022). Calculation of gas concentration-dependent diffusion coefficient in coal particles: Influencing mechanism of gas pressure and desorption time on diffusion behavior. *Fuel*, 320:123973.
- [110] Yin, H., Felicelli, S., and Wang, L. (2011). Simulation of a dendritic microstructure with the lattice boltzmann and cellular automaton methods. *Acta Materialia*, 59(8):3124–3136.
- [111] Yin, Y., Qu, Z., and Zhang, J. (2019). Multiple diffusion mechanisms of shale gas in nanoporous organic matter predicted by the local diffusivity lattice boltzmann model. *International Journal of Heat and Mass Transfer*, 143:118571.
- [112] Yong, R. N., Warkentin, B. P., Phadungchewit, Y., and Galvez, R. (1990). Buffer capacity and lead retention in some clay materials. *Water, Air, and Soil Pollution*, 53:53–67.
- [113] Yu, L., Rogiers, B., Gedeon, M., Marivoet, J., De Craen, M., and Mallants, D. (2013). A critical review of laboratory and in-situ hydraulic conductivity measurements for the boom clay in belgium. *Applied Clay Science*, 75:1–12.
- [114] Yu, L. and Weetjens, E. (2009). Summary of gas generation and migration. *Current State-of-the-Art. SCK-CEN ER-106. SCK+ CEN, Mol, Belgium*.
- [115] Zhang, C.-L. (2018). Thermo-hydro-mechanical behavior of clay rock for deep geological disposal of high-level radioactive waste. *Journal of Rock Mechanics and Geotechnical Engineering*, 10(5):992–1008.
- [116] Zhang, J. (2011). Lattice boltzmann method for microfluidics: models and applications. *Microfluidics and Nanofluidics*, 10:1–28.
- [117] Zhang, X., Xiao, L., Shan, X., and Guo, L. (2014). Lattice boltzmann simulation of shale gas transport in organic nano-pores. *Scientific reports*, 4(1):4843.
- [118] Zhou, W. and Arthur, R. (2017). Near-field processes, evolution, and performance assessment in geological repository systems. In *Geological Repository Systems for Safe Disposal of Spent Nuclear Fuels and Radioactive Waste*, pages 297–318. Elsevier.
- [119] Zhou, Y., Zhang, R., Staroselsky, I., and Chen, H. (2004). Numerical simulation of laminar and turbulent buoyancy-driven flows using a lattice boltzmann based algorithm. *International journal of heat and mass transfer*, 47(22):4869–4879.
- [120] Zhu, H.-L., Wang, S.-F., Yin, G.-J., Chen, Q., Xu, F.-L., Peng, W., Tan, Y.-H., and Zhang, K. (2018). Study of the numerical simulation of tight sandstone gas molecular diffusion based on digital core technology. *Petroleum Science*, 15(1):68–76.

Chapter 2: Mobility of Dissolved Gases in Smectites under Saturated Conditions

(published in *Journal of Physical Chemistry C*, 126, 40, 17441–17455 (2022); available at: <https://doi.org/10.1021/acs.jpcc.2c05678>)

Mobility of Dissolved Gases in Smectites under Saturated Conditions: Effects of Pore Size, Gas Types, Temperature, and Surface Interaction †

Jerry P. Owusu,^{*,‡,¶} Konstantinos Karalis,[¶] Nikolaos I. Prasianakis,[‡] and Sergey V. Churakov^{*,‡}

[‡]*Laboratory for Waste Management, Paul Scherrer Institute, 5232 Villigen-PSI, Switzerland*

[¶]*University of Bern, Institute of Geological Sciences, 3012 Bern, Switzerland*

Abstract

In a nuclear waste repository, the corrosion of metals and the degradation of organic material in the waste matrix can generate significant amounts of gases. These gases should be able to migrate through the multi-barrier system to prevent a potential pressure build-up that could lead to a loss of barrier integrity. Smectite mineral particles form a tortuous pore network consisting of larger inter-particle pores and narrow interlayer pores between the platelets of the smectite minerals. These pores are normally saturated with water, so one of the most important mechanisms for the transport of gases is diffusion. The diffusion of gases through the interparticle porosity depends on the distribution of gas molecules in the water-rich phase, their self-diffusion coefficients, and the tortuosity of the pore space. Classical molecular dynamics simulations were applied to study the mobility of gases (CO_2 , H_2 , CH_4 , He, Ar) in Na-montmorillonite (Na-MMT) under saturated conditions. The simulations were used to estimate the gas diffusion coefficient (D) in saturated Na-MMT as a function of nanopore size and temperature. The temperature dependence of the diffusion coefficient was expressed by the Arrhenius equation for activation energy (E_a). The predicted D -values of gases were found to be sensitive to pore size, as the D -values gradually increase with increasing pore size and asymptotically converge to the gas diffusion coefficient in bulk water. This behavior is also observed in the self-diffusion coefficients of water in Na-MMT. In general, H_2 and He exhibit higher D values compared to Ar, CO_2 , and CH_4 . The predicted E_a values indicate that the confinement affects the activation energy. This effect is due to the structuring of the water molecules near the clay surface, which is more pronounced in the first two layers of water near the surface and decreases thereafter. Atomic density profiles and radial distribution functions obtained from the simulations show that the interaction of the gas with the liquid and the clay surface influences mobility. The obtained diffusion coefficient for different gases and slit pore size were parameterized with a single empirical relationship, which can be applied to macroscopic simulations of gas transport.

2.1 Introduction

Deep geological disposal of nuclear waste is considered worldwide to be the most reliable and sustainable long-term solution, which makes it possible to ensure the long-term safety of people and the natural environment from possible radiotoxic effects [24, 41]. The most advanced repository concepts are based on the 'multi-barrier system', where a combination of natural

and engineered barriers with specific functions are used together to ensure integral repository safety [25, 66].

Significant amounts of gas may be generated in the repository for spent fuel and high-level waste due to anaerobic corrosion of carbon steel, radiolysis of water, and radioactive decay in the waste [71, 85, 106]. Similarly, chemical degradation of organic waste materials in low and intermediate-level waste repositories and corrosion of metals can also produce large amounts of gas mainly H_2 , CO_2 and CH_4 [108]. If these gases cannot escape from the near field of the repository at a sufficient rate, a local gas pressure build-up may compromise the integrity of the barriers and the safety design of the repository [34]. Therefore, understanding the gas transport mechanisms and processes is critical to assessing the performance of the repository.

The increasing demand for energy over the years has led to the demand for gas storage in geological reservoirs. For example, geological storage of CO_2 gas has been considered as a sustainable option for sequestration of anthropogenic CO_2 emissions [13, 38, 56]. Over the years, H_2 storage in underground aquifers has been considered a viable solution for renewable energy storage [76, 81, 92]. These trapped gases have the potential to migrate into and through the water-saturated pore space of the sealing geological medium (caprock), a phenomenon called caprock leakage [4, 53, 88]. Therefore, understanding gas transport through such systems is crucial for quantifying the efficiency of the geological sealing medium.

Several European countries considered claystone formations (argillaceous; Boom Clay, Callovo-Oxfordian Claystone, Opalinus Clay, Claystone Formation of Boda) as potential host rocks for geological disposal. Furthermore, clayey materials are foreseen to be used for engineered barriers in most repository concepts currently under development. Claystones are low-permeability materials consisting of a stack of smectite and illite particles forming a polycrystalline aggregate mixed with secondary phases (e.g. carbonate cement, sulphates, etc.) and accessory minerals [19]. These minerals form a complex pore network consisting of larger inter-particle pores and narrow nanopores between platelets of smectite minerals. Due to the small size of the pores, the hydraulic conductivity of argillaceous rocks is very low, and radionuclide transport is limited to the diffusive mechanism.

Gas transport through low-permeability rock formations is governed by the hydraulic and mechanical properties of the rock matrix, as well as the gas pressure at the source and the hydromechanical state of the rock [58]. Phenomenological considerations guided by the microstructural conceptualization of the Opalinus Clay suggest that gas migration can be driven by four (4) different mechanisms depending on the gas concentrations and pressure gradients: Dissolved gas advection and diffusion, the visco-capillary flow of gas and water flow, dilatancy-controlled gas flow, gas transport in tensile fractures [58]. Other gas transport mechanisms that have been studied over the years are capillary invasion, conduit opening, and volume flow [15, 53].

During the repository construction phase, the host rock is expected to be locally de-saturated and a temporary re-saturation period of the order of $10^3 - 10^4$ years will be required until the host rock becomes fully re-saturated with water. During the re-saturation phase, the water

content in the host rock (degree of saturation), especially in clayey rock, is one of the critical parameters controlling the transport of gas and solutes. The temperature gradient can contribute to the gas fluxes due to a phenomenon called thermodiffusion or Sorret effect [18, 62, 77].

It is evident that an assessment of the gas transport mechanism in clay materials under saturated, partially saturated, and de-saturated conditions is necessary. It can be anticipated that the larger pores become unsaturated first either due to thermally induced storage effects or due to gas production. Interlayer nanopores, on the other hand, remain water-filled even at very low water potentials [16, 29]. Large gas-saturated pores are therefore unconnected and gas transport under such conditions is dominated by molecular diffusion and thus depends on the distribution of gas molecules in the water-rich phase, their self-diffusion coefficients, and the tortuosity of the pore space. This makes the diffusive mobility of gases in the host rock to be one of the most important parameters controlling gas discharge in disposal systems with engineered barriers.

Diffusion in argillaceous rocks

Three main approaches are followed to obtain a mechanistic understanding of the diffusive transport of gases in argillaceous rocks. While some have explored this topic experimentally, others follow theoretical and numerical simulations for understanding gas transport. Many experimental methods described in the literature for determining the gas diffusion coefficients in saturated porous media are often very complex or limited to specific gases [43].

Over the years, three different approaches have been used to experimentally determine gas diffusion coefficients: Outgassing clay samples or boreholes, calculating the diffusion coefficient based on the concentration profile as a natural tracer and performing laboratory experiments based on the single diffusion or through diffusion technique.

The outgassing method involves measuring the concentration of gas released from a clay sample stored in a vacuum vessel or introduced into a borehole [5, 30, 98]. The diffusion coefficient is then derived from these measurements. Gomez-Hernandez [30] performed diffusion of He gas in an in situ in and out-diffusion experiment on Opalinus Clay in the Mont Terri underground laboratory. However, there were some uncertainties associated with the porosity used, which was assumed to be influenced by the EDZ of the well. Vinsot et al. [98] studied the degassing of natural gases (CO₂, light alkanes, He, N₂) dissolved in pore water into a borehole using two experiments conducted in 2004 and 2009 at the Mont Terri URL. The evolution of the gas content in the injection interval was followed over many years and provided data for calculating diffusion from the natural concentration of the gases [98]. Bensenouci et al. [5] also applied this technique to calculate the pore diffusion coefficient based on a He gas concentration profile as a natural tracer obtained from outgassing wells or samples of the Opalinus Clay.

Measurements of diffusion coefficients for naturally occurring gases based on their concentration profile are subject to large uncertainties [5, 59, 78]. In addition, the method has the disadvantage that it is only applicable to naturally occurring gases in the clay, which limits the

study to Ar, He, CH₄ [43]. Uncertainties arise from the difficulty of handling the samples to perform laboratory experiments in the initial state, where the samples may outgas or absorb gas from the atmosphere [43]. According to Mazurek et al. [59], outgassing of noble gases from rock core samples requires more sophisticated equipment, as sampling, gas generation, and analysis are very demanding, and the gases are also prone to leakage at different stages.

The in-diffusion or through-diffusion technique is a widely used method for determining the diffusion coefficients of gases in laboratory experiments. [42, 43, 51, 75]. Kroos and Schaefer [51] applied a through-diffusion apparatus by allowing gas to flow from an upstream gas-filled reservoir and then observing the composition of the gas downstream (the reservoir was initially free of a diffusant) and calculating the diffusion coefficient using the time-lag approach. Rebour et al. [75] also performed a similar experiment, but the upstream reservoir was filled with gas dissolved in water. Numerous errors occurred in both experiments, including the reduction of sample size to compensate for gas and atmospheric pressure, the change in porosity, and the influence of anisotropic effects. [51, 75]. Therefore, a more accurate apparent gas diffusion coefficient for dissolved He and CH₄ in Boom Clay was experimentally determined by developing a double diffusion method [43]. This method was later extended by the double-through diffusion method to measure the apparent diffusion coefficients of He and Ar in Boom Clay, Opalinus Clay and Callovo-Oxfordian Clay [42]. Unlike the classical through-diffusion test, the double through diffusion test consists of 2 dissolved gases (one in each reservoir on each side of the sample) that can diffuse simultaneously but in opposite directions. [42, 43]. The advantage of this method is its versatility, which allows the measurement of two gases in a single experiment.

Over the years, there have been a number of numerical studies of gas transport in rocks. [1, 2, 28, 29, 36, 45, 93, 110, 112]. However, most of these studies have focused on macroscopic models (particularly the transport of oil and gas in shale rocks). Bourg and Sposito [11] have done extensive work on the diffusion of noble gases in ambient liquid water using molecular dynamics simulations, as data on the diffusion coefficients of minor noble gas isotopes were essentially unavailable.

Molecular dynamics simulations have been widely used to study solute, fluid, and clay surface interactions [3, 10, 11, 16, 17, 20, 31, 90]. To date, however, few MD simulations have been used specifically to study the behavior of dissolved gases in hydrated clay systems. While a significant portion of these studies has focused on gas dynamics and coordination, only a few studies have specifically investigated the mobility and effect of different gas types in hydrated clay systems [7, 21, 73]. Gadikota et al. [28] investigated the adsorption of different gas types in clay interlayer nanopores. Using their simulation, they also measured the diffusion coefficient for gases in a 6 Å wide interlayer nanopore. However, the influence of nanopore size, gas type (size, shape, structure) and temperature on the mobility of gases in water-saturated clays is not well known.

Recently, the ability of molecular dynamics to predict the elemental and isotopic kinetic fractionation of noble gases due to molecular diffusion in geological fluids has been used to improve the understanding of the transport mechanisms of gases in aqueous phases [37, 103]. In the studies of Hoang et al. [37], they found that the elemental fractionation of noble gases can be quantitatively estimated by the square root relation for the main noble gas, not only in water, as previously shown in the literature using experiments and molecular simulations, but also in oil and in gas. In the study by Wanner et al. [103], molecular dynamics simulations have shown that the mass of the diffusing species is the decisive control factor for diffusion-induced isotopic fractionation and not the molecular volume, as assumed in previous studies.

In this work, classical molecular dynamics simulations have been applied to gain a mechanistic understanding of the mobility of various gases in smectite minerals, particularly Na-montmorillonite, under fully saturated conditions. In particular, the effects of temperature, pore size, gas type, and surface interactions on gas mobility have been investigated. The obtained data on the local pore-specific mobility of gases are necessary to further investigate an upscaling approach to gas mobility in polycrystalline rocks by multiscale numerical simulations.

2.2 Models and Methods

2.2.1 Simulation setup

The simulation setup consists of a model clay structure in which the nanopore between the layers is filled with water (Figure 2.1). The clay studied is sodium montmorillonite with the structural formula $\text{Na}_{0.5}[\text{Al}_{3.5}\text{Mg}_{0.5}]\text{Si}_8\text{O}_{20}(\text{OH})_4$. The system was setup according to a protocol used by Churakov et al. [16]. The clay particle consists of parallel stacks of TOT layers, which can be thought of as di-octahedral sheets (O) occupied by Al and Mg, sandwiched between two tetrahedral sheets (T) occupied by Si [16]. Isomorphous substitutions of Mg^{2+} for Al^{2+} in the octahedral sheets were randomly distributed with the constraint that adjacent substitutions were not allowed. Therefore, for the sake of simplicity of the model, substitutions were considered only in the octahedra sheet. These cation substitutions lead to a permanent structural charge on the TOT layers, which is compensated by Na^+ occupying the macropore between the TOT layers. In total, 24 isomorphous substitutions were present in the system in each configuration to obtain a mean basal surface charge density (about -0.1 Cm^{-2}) typical of montmorillonite [89]. The interlayer nanopore of the clay was then filled with 48 Na^+ counterions to compensate for the negative structural charge of the clay.

Two TOT layers of Na-MMT were aligned in the XY plane of the supercell to obtain a nanopore. The initial dimensions of the simulation supercell were $31.32 \times 36.12 \times 47.46 \text{ \AA}^3$. Several system configurations with interlayer nanopore sizes ranging from 1.0 to 2.6 nm (Figure 2.1) were set up to investigate the effects of nanopore size on gas mobility. The interlayer nanopore of each structure is then solvated with water, resulting in systems with different hydration states. Finally, some of the water molecules are replaced by gas molecules, corresponding to

a molar ratio of 0.01. In this work, 5 types of gases (CO_2 , CH_4 , He, Ar, H_2) were studied by individual simulations.

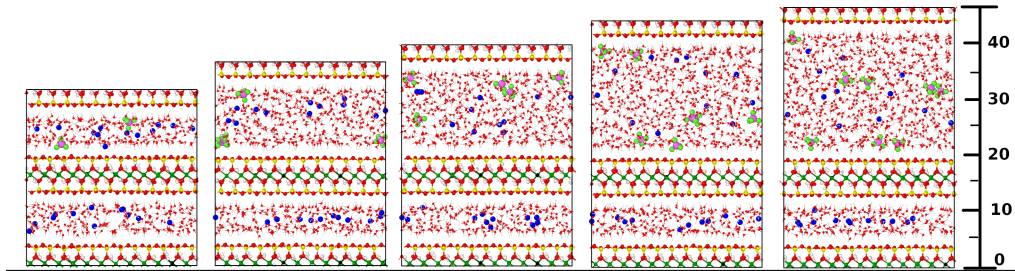


FIGURE 2.1: A snapshot from MD simulation of Na-montmorillonite, at variable interlayer nanopore distances (Å). Oxygen atoms are red. Hydrogen atoms are white. Silica atoms are yellow. Aluminium atoms are green. Magnesium atoms are black. Sodium atoms are blue. The carbon atom of Methane is pink and the Hydrogen atom of Methane is light green.

2.2.2 Simulation details

The interatomic interactions were described with the CLAYFF model [22] for clay atoms, the SPC/E water model [6], and the Smith-Dang model of Na^+ [87]. Gas molecules were described with the EPM2 model of CO_2 [35], the TKM-AA model of CH_4 [94], the noble gas interaction parameters of Bourg and Sposito for Ar and He [11], the spherical H_2 model of Mondal and coworkers [63]. Several models have been proposed for hydrogen [63, 80, 86]. The simple spherical H_2 model used in this study has been shown to predict well the diffusion coefficient of H_2 in water [28]. Ning et al. [68] successfully used a combination of the TKM-AA potential of CH_4 and the TIP4P2005 of water to predict the lattice parameters of hydrates. Gadikota et al. [28] have accurately predicted the diffusion coefficient of Ar, He, CO_2 using the noble gas interaction parameters for Ar and He and the EPM2 model for CO_2 respectively. The chosen interatomic potentials (Table S1) are suitable for accurate prediction of the structure and dynamics of water and gases in bulk water [10, 28, 40, 80, 104] and of water in smectite interlayer nanopores at standard temperature and pressure [12, 39]. The total potential energy can be written as:

$$E_{total} = E_{VDW} + E_{Coul} + E_{bond} \quad (2.1)$$

with

$$E_{VDW} = 4\epsilon_{ij} \left[\left(\frac{\sigma_{ij}}{r_{ij}} \right)^{12} - \left(\frac{\sigma_{ij}}{r_{ij}} \right)^6 \right] \quad (2.2)$$

$$E_{Coul} = \frac{q_i q_j e^2}{4\pi\epsilon_0 r_{ij}} \quad (2.3)$$

where atoms i and j are r_{ij} apart, ϵ_{ij} and σ_{ij} are the Lennard-Jones (LJ) energy and distance parameters, respectively. Interatomic interactions between unequal atomic species were predicted using the Lorentz-Berthelot combination rules. q_i is the charge of atom i , q_j is the charge of atom j , e is the elementary charge of an electron, ϵ_0 is the vacuum permittivity. E_{bond} , the bonded interaction potential term, is used only for the hydroxyl groups of the clay layer, which is considered harmonic.

The simulations were carried out with the LAMMPS package [74]. For each system, energy minimization was performed before the MD runs, followed by equilibration in the NP_zT ensemble (using the Noose-Hoover thermostat and the barostat for pressure coupling) for 1 ns to relax the clay layers in the z-Direction (normal to the surface) and produce a fully saturated system in the nanopore region [61, 69, 70]. The final snapshot of the equilibrated configuration and average cell size for each system was used for the production of 10 ns long trajectories (with a time step of 1 fs) in the NVT ensemble at temperatures of 300, 350, 375 K using the Noose-Hoover thermostat [69, 70]. Sampling accuracy was evaluated by splitting each simulation trajectory into two 5-ns blocks and treating each block as an independent replicate. The water molecules were kept rigid using the SHAKE algorithm [79]. The clay atoms were kept fully flexible, while the CO₂ and CH₄ molecules were kept rigid using the rigid-body algorithm [46]. Short-range interactions were calculated using the Lennard-Jones and the short-range Coulomb potentials with a cutoff of 10 Å. The long-range electrostatic interaction was calculated using the particle-particle particle-mesh solver (PPPM). The simulation results were analyzed to determine the diffusion coefficients, activation energies, radial distribution functions, atomic density distribution, and immersion energies of gases and water in the interlayer nanopore.

The diffusion coefficients D were derived from the slope of a plot of the mean square displacement $\langle l^2 \rangle$ using the Einstein relation:

$$D = \frac{1}{2n} \lim_{t \rightarrow \infty} \frac{d\langle l^2 \rangle}{dt} \quad (n = \text{order of dimension}) \quad (2.4)$$

The asymptotic long time limit in eq 2.4 was approximated by calculating the slope $\langle l^2 \rangle$ versus t for the probe time scale $\tau = 100$ ps, which is consistent with the convergence tests performed by Bourg et al. [12]. The $\langle l^2 \rangle$ was calculated in all three dimensions in the bulk aqueous system ($n=3$). In the clay nanopore, only the x and y components of the trajectory were used ($n=2$), and they describe the two-dimensional diffusion parallel to the interlayer nanopore.

Correction for system size dependence

The estimation of the diffusion coefficient in molecular dynamics simulations with periodic boundary conditions is known to depend on the system size [107]. This dependence was first analyzed for bulk water, followed by simulations of dissolved gases in water, which were necessary to check the force potential parameters value. This artifact can be corrected with the relation of Yeh and Hummer [107]:

$$D = D_{PBC} + \frac{k_B T \zeta}{6\pi\eta L} \quad (2.5)$$

where D_{PBC} is the diffusion coefficient predicted using periodic boundary conditions, D is the corrected diffusion coefficient in the limit $L \rightarrow \infty$, k_B is the Boltzmann constant, $\zeta \approx 2.837$ is the self term for a cubic lattice at 298 K and η is the viscosity of the medium.

Activation energy of diffusion

From the D_0 and D values we can evaluate the temperature dependence of diffusion by predicting the activation energy of diffusion of gases using the Arrhenius equation:

$$D = D_0 e^{-E_a/RT} \quad (2.6)$$

where D is the gas diffusion coefficient (m^2/s); E_a is the activation energy; R is the gas constant ($(8.314 \text{ JK}^{-1}\text{mol}^{-1})$); T is the absolute temperature (K); and D_0 is the pre-exponential factor. Subtracting two diffusion coefficients at two temperatures and writing the equation in logarithm can get rid of the pre-exponential factor and yields a new equation without a pre-exponential term:

$$\ln \frac{D_2}{D_1} = -\frac{E_a}{R} \left(\frac{1}{T_2} - \frac{1}{T_1} \right) \quad (2.7)$$

Similar to the work of Holmboe et al. [39], we have a corrected value for the activation energy of diffusion (E_a) with the relation in eq 2.6 to account for the fact that our force field models underestimate E_a in bulk water by a factor ΔE_a :

$$E_a = E_{a,MD} + \Delta E_a \quad (2.8)$$

where $E_{a,MD}$ is the uncorrected activation energy predicted by the MD simulations. This correction was calculated for water and all gases and the corrections were applied to the activation energy values obtained from the MD simulations in clay.

Stokes-Einstein radius

The Stokes-Einstein radius (also known as the hydrodynamic radius) of a solute is the radius of a hard sphere diffusing at the same rate as the solute. It is closely related to the mobility of the solute and takes into account not only the size but also the effects of the solvent. This parameter was used to establish a relationship between the diffusion coefficients of gases from MD simulations and experiments.

$$D_0 = \frac{k_B T}{6\pi\eta R_s} \quad (2.9)$$

where D_0 is the diffusion coefficient in bulk water, k_B is the Boltzmann constant, η is the viscosity of water, R_s is the hydrodynamic radius and T is temperature.

2.2.3 Model assumptions and uncertainties

As a compromise between computational efficiency and statistical uncertainty, the concentration of all gases in the simulations was set to a dilution of 1%. This concentration is higher than the typical gas solubility measured in bulk water at ambient conditions [105]. However, the recent studies of Benazzouz et al. [4], indicate that the solubility of methane and ethane increases under confinement and becomes comparable with the concentration used in this study. The molar ratio of 1% has been widely used in previous molecular dynamics simulations and provides a good agreement with the experimental data [28, 44]. In fact, gas concentration in the simulations is low enough that the direct interaction and collision between gas molecules is negligible. Furthermore, no accumulation of gases was observed when analyzing the trajectories, which means that the particles are well dispersed in the water phase and no gas phase nuclei are formed. This simulation setup thus provides a good estimate of the diffusivity of gas molecules in natural systems.

The use of periodic boundary conditions is known to influence the obtained diffusion coefficients in bulk simulation [39, 84]. Simmonin et al. [84] investigated the finite-size effects of a Lennard-Jones fluid under confinement and derived a hydrodynamic correction due to finite-size effects in the systems with periodic boundaries. Holmboe et al. [39], on the other hand, investigated the effects of finite size on the diffusion of water and Na ions in Na-montmorillonite and found that finite size has no effect on the diffusion of water and Na ions in Na-montmorillonite, unlike the bulk system. Accordingly, the finite-size corrections were applied only to the diffusion coefficients in bulk and not to the diffusion coefficients in Na-montmorillonite.

For simplicity, only octahedral substitutions were considered in this study. It should be noted however that in natural montmorillonite, Al can also substitute for Si in the tetrahedral sheet, albeit the substitutions predominate in the octahedral sheets. Gas molecules are neutral and thus have weaker interaction with structural substitution compared to the strongly polar solvent molecules and ions. The influence of surface charge on gas diffusion can appear only indirectly due to the interaction of the ions with the mineral surface. Liu et al. [54] studied the influence of layer charge distribution on the thermodynamic and microscopic properties of Cs-smectites. It was found that the layer charge distribution has a significant influence on the mobility of interlayer species and the preference for ion-binding sites. In contrast, Ngouana et al. [67] studied the effects of differently distributed Al/Si and Mg/Al substitutions in the tetrahedral and octahedral Cs-montmorillonite clay layers on aqueous species mobility, swelling behavior, and interlayer structure. They found that only minor differences were observed between the Cs-montmorillonite models studied, except for a higher charge density of the clay layers and/or interlayer cations. We expect that the effect for Na montmorillonite used in this study is less pronounced since Na forms outer sphere complexes and this have lower integration with the surface compared to Cs forming inner sphere complexes and thus tightly bind to

the substitution sites [16, 50], We argue therefore that the influence of the layer charge distribution on the mobility of uncharged gas species in our system is small.

2.3 Results and discussion

2.3.1 Diffusion in bulk liquid water

In order to verify our model parameters and thus accurately determine the influence of clay particles on the diffusion coefficient and activation energy of water and gases, we first examined the ability of our MD simulations to reproduce the values of the self-diffusion coefficient (D_0) and activation energy (E_a) values of bulk water and dissolved gas molecules. Figure 2.2 shows the D_{PBC} of bulk water as a function of inverse simulation cell size (L^{-1}) for systems with 512, 1331, 3375, 6859 water molecules.

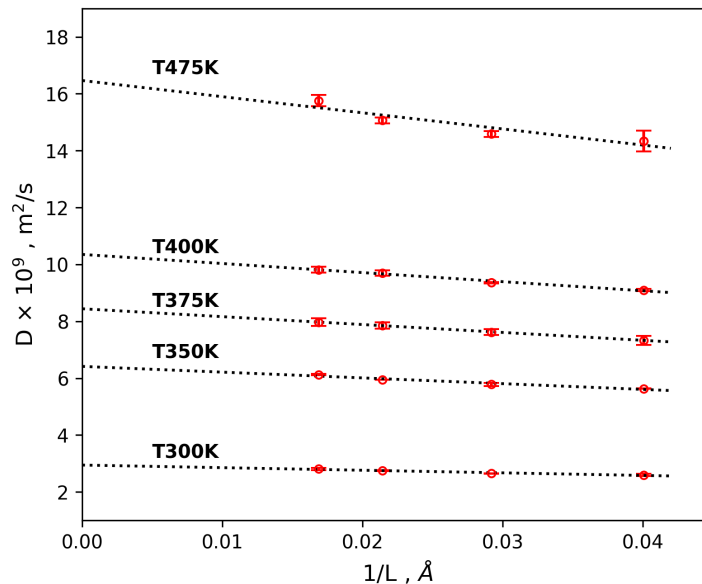


FIGURE 2.2: D_{PBC} values for bulk water as a function of inverse simulation cell size (for simulations with 512, 1331, 3375, and 6859) at different temperatures. The size-corrected diffusion coefficient D_0 is determined by linear regression (black dashed line) to $1/L = 0$.

The dashed line illustrates the linear regression of the plotted data for each temperature. A size-corrected D_0 value was obtained by extrapolating the D_{PBC} against L^{-1} values by linear regression to $1/L = 0$. Holmboe et al. [39] applied a similar method to MD simulations of water and compared the size dependence of the D_0 values from the extrapolated fit with that obtained from the Green-Kubo method. They performed separate simulations from the fitted data and obtained an SPC/E viscosity (η) for each temperature by applying the Green-Kubo relations to the autocorrelation function of the stress tensor elements. It was concluded that eq 2.5 accurately predicts the size dependence of D_0 at 298 K, but slightly overestimates the temperature dependence of this size dependence.

In this simulation, a corrected D_0 value of $2.92 \pm 0.03 \times 10^{-9} \text{ m}^2/\text{s}$ was obtained for water at ambient conditions. This value overestimates the D_0 value from experiments [95]. (2.65×10^{-9}

m^2/s) by about 21%. This is consistent with the studies of Tsimpanogiannis et al. [95], who performed a critical review of the classical molecular studies of bulk water. In their studies, they calculated the deviation of the relative self-diffusion coefficient from the experimental value at ambient conditions for different force fields. They calculated that the deviation of the SPC/E water model is about 30% from the experimental values.

It was also found that the resulting D_0 values from the SPC/E water model from this work underestimate the E_a values of the bulk water by $\Delta E_a = 4.9 \text{ kJ mol}^{-1}$ (about 30% deviation), as shown in Table 2.1. This is probably because most interatomic potentials used in MD simulations have been parameterized to describe the system of interest at a particular temperature, and sometimes perform poorly when applied at very different temperatures because of the temperature dependence of viscosity. To determine if this effect is solely due to the SPC/E model underestimating the temperature dependence of viscosity (η), the calculated η values from the MD simulation were compared to the experimental values. The results show a less significant deviation of the simulated η values from those of the experiment (at least at temperature $> 350 \text{ K}$), as shown in Figure 2.3. Therefore, viscosity alone cannot fully account for the deviation between experimentally measured and predicted E_a values.

Studies by Yeh and Hummer [107], Holmboe et al. [39], and Medina et al. [60] show that the viscosity of the SPC/E water model is insensitive to the size of the simulation cell. However, the difference in E_a could be due to the fact that the water density of SPC/E from MD simulations was not equated with the experimentally measured bulk density of water. The density of the SPC/E water was then compared to the experimental density and it can be seen from Figure 2.3 that the SPC/E water model in our simulations underestimates the density of the water by 0.82 - 5.8% (with increasing temperature). The observed underestimation of the density could explain the corresponding underestimation of the activation energy for diffusion.

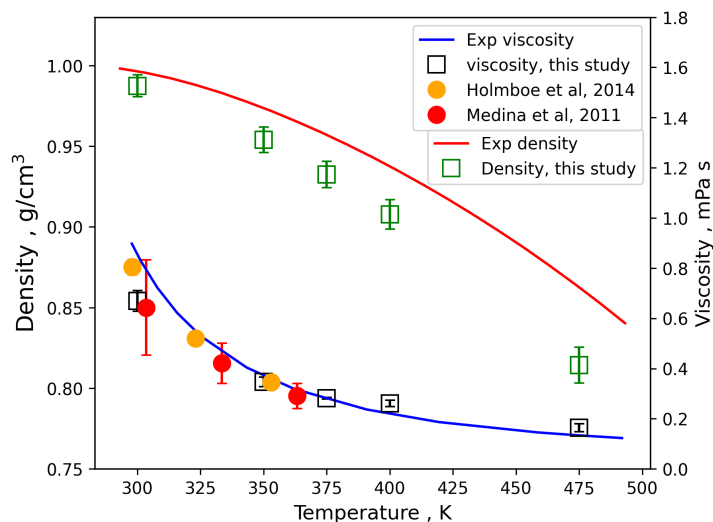


FIGURE 2.3: Comparison of the density of the SPC/E water model from this study (green markers) and the experimental water density (red line) [83]. The right-hand axis indicates our simulated (black markers) and the experimental (blue line) shear viscosities [47]. Red and yellow circles represent shear viscosities predicted by other MD studies [39, 60].

TABLE 2.1: MD simulation predictions of the self-diffusion coefficients D ($10^{-9} \text{ m}^2/\text{s}$) and activation energy of diffusion ($kJmol^{-1}$) values for dissolved gas in bulk water

	He	H ₂	CO ₂	Ar	CH ₄	H ₂ O
T [K]						
300	8.52 ± 0.53	6.35 ± 0.26	2.64 ± 0.06	2.86 ± 0.10	2.61 ± 0.08	2.95 ± 0.01
350	16.11 ± 0.7	11.05 ± 0.78	5.11 ± 0.11	6.32 ± 0.31	5.59 ± 0.15	6.41 ± 0.05
375	20.79 ± 1.28	13.61 ± 0.44	6.57 ± 0.21	8.95 ± 0.34	6.96 ± 0.23	8.44 ± 0.11
$E_{a,MD}$	11.13 ± 0.00	9.54 ± 0.00	11.41 ± 0.00	14.16 ± 0.00	12.44 ± 0.04	11.58 ± 0.12
$E_{a,EXP}$	11.70 ^a	16.06 ^a	19.51 ^a	19.81 ^a	18.36 ^a	16.50 ^b

^a Boudreau (1997) [9]. and Jähne et al. (1987). [44]. ^b Ioannis et al. (2019) [95].

The predicted diffusion coefficients and activation energy of diffusion of gases in bulk water are shown in Figure 2.4 and Table 2.1. The results are in general agreement with the experimental data [9, 44]. An average deviation of about 26% is observed and could be related to the inability of the SPC/E-gas model to accurately predict the experimental value of the diffusion coefficient. For example, Moulton et al. [64] have done extensive work on the diffusivity of CO₂ gas by combining different CO₂ and H₂O force field models. In their work, they have a D_0 value of $2.7 \pm 0.5 \cdot 10^{-9} \text{ m}^2/\text{s}$ for CO₂ in the SPC/E-EPM2 model at 1 bar and 298.15 K. This is in agreement with the experimental value of the diffusion coefficient. This agrees with the value predicted in this work ($2.80 \pm 0.30 \cdot 10^{-9} \text{ m}^2/\text{s}$ at 1 bar and 300 K). They concluded from their work that the combination of the TIP4P/2005 H₂O model with the EPM2 CO₂ model (approximately 2% deviation) accurately predicts the experimental diffusion coefficient of CO₂ in bulk water. In this study, the rigid SPC/E water model for H₂O was chosen because it is able to reproduce the D-value of bulk water, the vapor-liquid equilibrium, and the swelling behavior of clays [12, 26, 27, 32, 57].

As expected, the D_0 values increase with increasing temperature (Table 2.1). The directly proportional relationship between the diffusion coefficient and temperature is a well-known concept from a theoretical and experimental understanding of diffusion [33, 52, 55]. Furthermore, the D_0 values were fitted to the Stokes-Einstein relation (eq 2.9). Figure 2.4 shows that D_0 generally decreases as the size (hydrodynamic radius) of the gas molecule increases, and it asymptotically reaches zero. It can also be seen that MD deviates slightly from the experiment, which represents the overestimation of the MD simulation compared to the experiment. Similar to water, the E_a values for gases are also underestimated with an average deviation of about 30%. A correction value is calculated according to eq 2.8 which is added to the E_a values from the MD simulations gases in clay.

2.3.2 Pore size effect on the diffusion of gases

To investigate the dependence of the mobility of gases in Na-MMT interlayer nanopores on pore size and temperature, a series of simulations were performed for 5 gases (He, H₂, CO₂, Ar, CH₄) at 7 different nanopore sizes (with an average increase in base distance of about 0.265

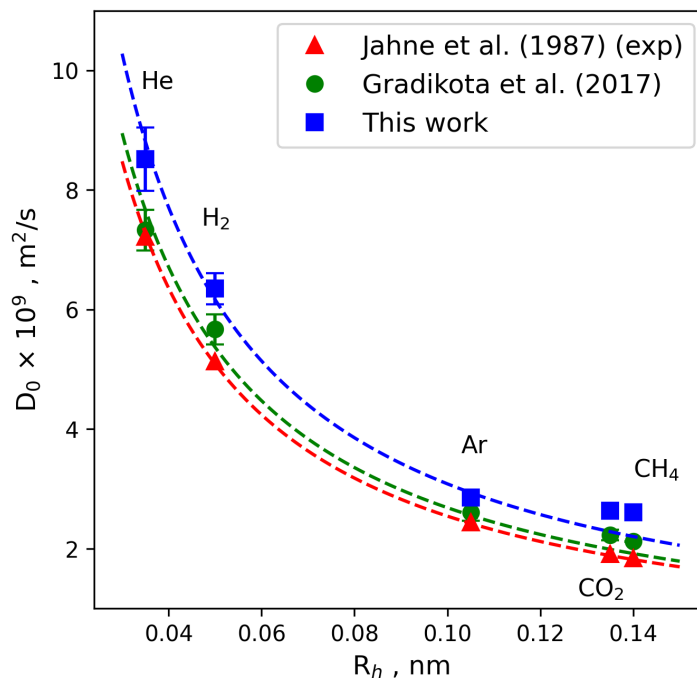


FIGURE 2.4: Self-diffusion coefficients of gas solutes in bulk water as a function of the solute hydrodynamic radius from MD predictions from our results and other results obtained from experiments and previously reported MD predictions [28, 44].

nm). Simulations were performed at temperatures 300, 350, and 375 K. Table S2 in the Supporting Information shows all simulation results representing the diffusion coefficient of gases as a function of nanopore size and temperature. In the results, an increase in the D value of gases with increasing temperature is observed in the clay nanopore. This is similar to the behavior observed in the bulk simulations, experimental and theoretical studies. However, for different pore sizes, the D value of the gases increases at different rates. For example, when the temperature increases from 300 to 350 K, the D value for He gas increases from 2.59×10^{-9} to $5.18 \times 10^{-9} m^2/s$ for a pore size of 1.0 nm, an increase of about 2 times, while it is only about 1.5 times higher for a pore size of 2.6 nm.

It is also observed that the self-diffusion coefficient of He at a pore size of 1.0 nm, for example, is $2.59 \pm 0.14 \times 10^{-9} m^2/s$ at 300 K. However, when the pore size is increased to 2.6 nm at the same temperature, an approximately 3-fold increase in diffusivity is observed with a resultant value of $7.46 \pm 0.67 \times 10^{-9} m^2/s$ at 300 K. A similar increase is observed in all other gas simulations with an average factor of about 2.5 times. It can be concluded that the diffusion coefficient of gases confined in Na-MMT increases with increasing pore size and shows different rates at different temperature-pore size pairs. This relationship is also supported by other previous studies [48, 100, 109]. For example, Wang et al. [100] reported in their MD simulation that the self-diffusion of CH₄ in Ca-MMT increases with increasing interlayer pore size in the range of 1.8 - 50 nm. Experimental diffusion methods used by Yuan et al. [109] on a shale rock also show that gas diffusion is higher in micrometer-sized pores than in nanometer-sized pores. Furthermore, Kim et al. [48] concluded in their experimental studies that the Knudsen diffusion

TABLE 2.2: $D_{0,f}$ and k_c fitting parameters from the fit of the MD simulation using eq 2.8

	He	H ₂	CO ₂	Ar	CH ₄	
T [K]						
$D_{0,f}$	300	9.85	7.02	2.58	2.91	2.22
	350	15.86	12.58	5.05	64.44	4.57
	375	18.82	15.14	6.25	6.81	8.80
k_c	300	0.67	0.69	0.74	0.71	0.71
	350	0.68	0.73	0.76	0.71	0.71
	375	0.67	0.71	0.75	0.70	0.70

coefficient of gas increases with increasing pore radius. Wang et al. [101, 102] sufficiently characterized the pressure-driven flow behavior of hydrocarbons and carbon dioxide in shale nanopores by the slip-corrected Poiseuille equation and derived that the slip length depends exponentially on the pore size.

A power curve given by eq 2.10 was fitted to the MD simulation results to model the behavior of the diffusion coefficient of gas as a function of pore size:

$$D = D_{0,f} - \frac{k_c}{h} D_{0,f} \quad (2.10)$$

where h is the pore width (expressed as pore diameter in nm) of the clay, $D_{0,f}$ is the diffusion coefficient in bulk water from the fit, and k_c is a fitting parameter relating to the clay surface. $D_{f,0}$ and k_c values from the fit are listed in Table 2.2.

Figure 2.5 shows the results for the diffusion of gases in Na-MMT at temperatures of 300, 350, and 375 K, fitted with eq 2.10. The $D_{0,f}$ values obtained from the fitting agree with the D_0 values measured in the bulk MD simulations. k_c values range from 0.67 - 0.76 nm with an average of 0.71 nm. A similar trend in diffusion behavior with respect to pore size is observed for all gases, with the D value increasing with increasing pore size. It is also observed that for the same pore size, the size of the gas affects the diffusion coefficient in a similar way as observed in the bulk simulations. For example, it can be observed that He gas with the smallest size is the fastest (black curve in Figure 2.5) and CH₄ gas with the largest size is the slowest (blue curve in Figure 2.5).

Gadikota et al. [28] studied the hydrophobic solvation of gases (CO₂, CH₄, H₂, noble gases) in interlayer clay nanopores. In their simulation, the predicted diffusion coefficient of the studied gases at ambient conditions is about 1.5 times larger than the values obtained in this work for a 2W hydrated layer system. This difference can be attributed to the charge of the clay layer used in their studies and also to the fact that their clay layer was simulated as a rigid body. In this work, the clay layer was simulated as a fully flexible body. Nevertheless, the D value for CH₄ from the MD simulation of Hu et al. (2021) (0.43×10^{-9} m²/s) is close to the value determined in this work (0.49×10^{-9} m²/s) for a 2W hydrated layer system. In the study by Myshakin et al. [65], they give simulation values for the diffusion of CO₂ in hydrated Na-MMT. They

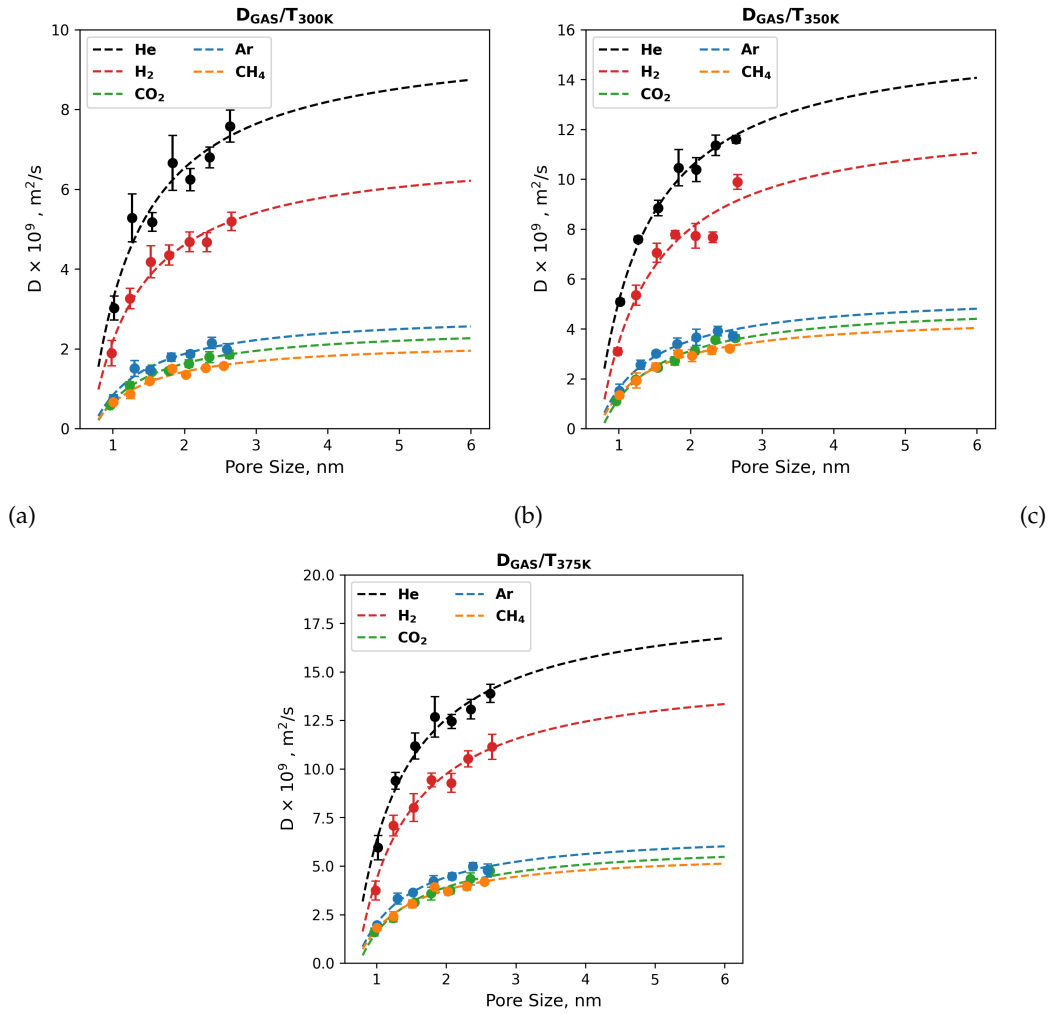


FIGURE 2.5: Diffusion coefficient of gases in saturated Na-MMT as a function of pore size fitted with eq 2.10 at temperatures (a) 300 K (b) 350 K and (c) 375 K.

obtained a D value of $0.82 \pm 0.05 \cdot 10^{-9} \text{ m}^2/\text{s}$, which agrees with the value obtained in this work ($0.60 \pm 0.10 \cdot 10^{-9} \text{ m}^2/\text{s}$) for a 2W hydrated layer at 300 K and 1 bar. The slightly lower value can be attributed to the different concentrations of CO_2 in the hydrated nanopore in the two studies (molar ratio of 0.2 in their work and 0.01 in this study). From their work, they deduced that the diffusion coefficient for CO_2 increases with increasing concentration due to the associated expansion of the interlayer nanopore.

To investigate the influence of the clay layer on the diffusion of the interlayer species, the diffusion coefficients of the gas in the clay layer nanopore were normalized by the diffusion coefficient of the gas in the bulk water (D_0) predicted by our MD simulation. The normalized values could then be fitted to the function in eq 2.11 by a simple rearrangement of eq 2.10.

$$\frac{D}{D_0} = 1 - \frac{k_c}{h} \quad (2.11)$$

The curve in Figure 2.6 represents an average value for all temperatures and follows the conclusion of Wang et al. [102], that the ratio at different temperatures almost converges to a single

curve as a function of pore spacing, indicating an empirical correlation. Due to the limited transport space, diffusion of entrapped species through the clay layers is hindered. Therefore, the diffusion coefficients of gases are slower under confinement than in bulk. As the size of the nanopores increases, the D of the gases shows a monotonically increasing trend and asymptotically approaches the value of the bulk. However, this behavior is different for all gases, so that H_2 approaches the bulk value faster than, for example, CH_4 . This shows that the effect of confinement is different for different gases. One could argue that this difference could be due to the nature of the interactions between the gas, liquid, and clay layer. This will be further investigated in the next sections.

From the fit, we could derive a more robust equation relating the diffusion coefficient to the pore size for all types of gases by inculcating macroscopic variables. To achieve this, eq 2.11 was further expanded by applying Bourg et al. [12] formulation which connects molecular scale diffusion to continuum scale (eq 2.12). With this formulation, we are able to calculate the apparent diffusion coefficient of gases in clay medium for variable pore sizes as described by eq 2.13.

$$D_a = \frac{q_{nano}}{G} D_0 \quad (2.12)$$

$$D_a = \frac{D_0}{G} \left(1 - \frac{k_c}{h_{av}} \right) \quad (2.13)$$

where D_a is the apparent diffusion coefficient of the gas, D_0 is the diffusion coefficient of the gas in bulk water, q_{nano} is the relative diffusion coefficient (D/D_0) from MD simulation, G is the geometric factor and h_{av} is average pore width.

In most diffusion experiments, a single effective or pore diffusion coefficient is given, which is an average sum over all pore sizes. These simple formulations, such as eq 2.11 and eq 2.13, are useful for testing theories and explaining experimental results by providing a microscopic view. In addition, they provide a basis for easy incorporation into an up-scaling framework, such as Lattice Boltzmann, which can be advantageous in linking nanoscale simulations with macroscale measurements.

Comparison of MD simulation with experimental investigations

In general, direct experimental measurement of gas diffusion coefficients in clay nanopores is not possible [28]. Therefore, a direct one-to-one mapping of simulation to experimental data is not easily achieved. The reason is that the experimental measurements are performed at a macro scale, where all the complex geometry of the clay matrix such as heterogeneity, pore network, pore distribution, and tortuosity is taken into account. Therefore, observing the relative trends in the experimental and theoretical data is more appropriate for validating the simulation. Nevertheless, it is possible to compare the simulation results for the bulk fluid. A cross-comparison of simulations and experimental data as a function of macroscopic parameters such as temperature and porosity could also be performed.

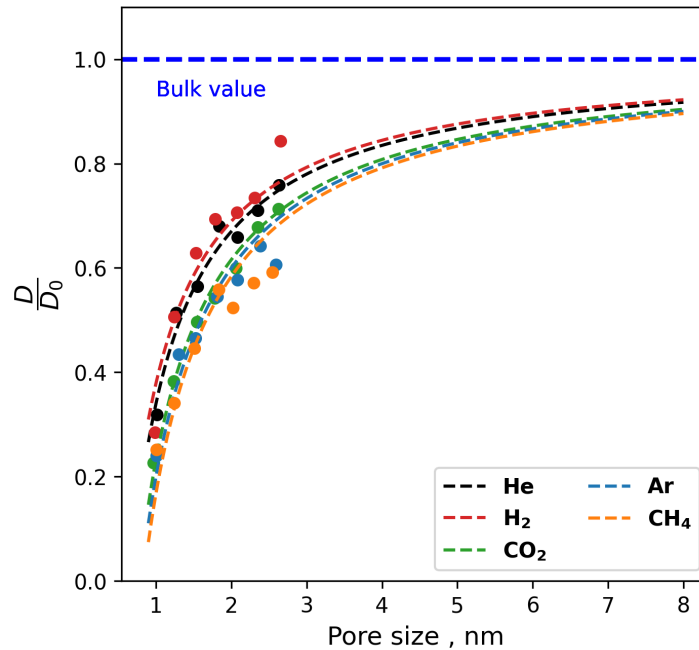


FIGURE 2.6: A fit showing the relative diffusion coefficient of gases (D/D_0) in clay nanopores as a function of pore size. The marker dots represent averaged D/D_0 for temperatures of 300, 350, and 375 K. The lines represent the fit of D/D_0 with eq 2.11.

In order to compare our simulations with the experimental results, eq 2.13 was used to calculate the apparent diffusion coefficients (D_a). The D_a obtained from the formulation is then compared to the D_a measured directly from the double-through diffusion experiment of Jacops et al. [42]. They calculated geometric factors for gases in Boom clays. They also reduced the pore size distribution to a single pore size (R_{pore}) calculated by fitting their data to a single pore size hydraulic conductivity model obtained from hydraulic conductivity experiments. Using the geometric factors and pore sizes from their experiments as input parameters for eq 2.13 we can reproduce the apparent diffusion coefficients measured directly from the experiments.

Figure 2.7 shows a plot of the apparent diffusion coefficients obtained from experiments with gases in three different types of Boom clay having varying porosity and pore size distribution. It also shows a plot of apparent diffusion coefficients calculated using eq 2.13 and fitted as a function of hydrodynamic radius. It can be seen from the plots that the values obtained from experiments agree with those obtained from eq 2.13 [42]. Although Jacops et al. [42] had some challenges in their measurements, the plots show that with accurate values for the geometric factor and dominant pore size, it is possible to reproduce the experimental results of the apparent diffusion coefficient for clays with eq 2.13.

2.3.3 Pore size and water-gas mixture effect on diffusion of water

To investigate the degree of influence of the clay layer on the self-diffusion of water in the water-gas mixture, the diffusion coefficients of water in the clay layer nanopore were normalized by the diffusion coefficient of water (D_0) in the bulk water predicted by our MD simulation

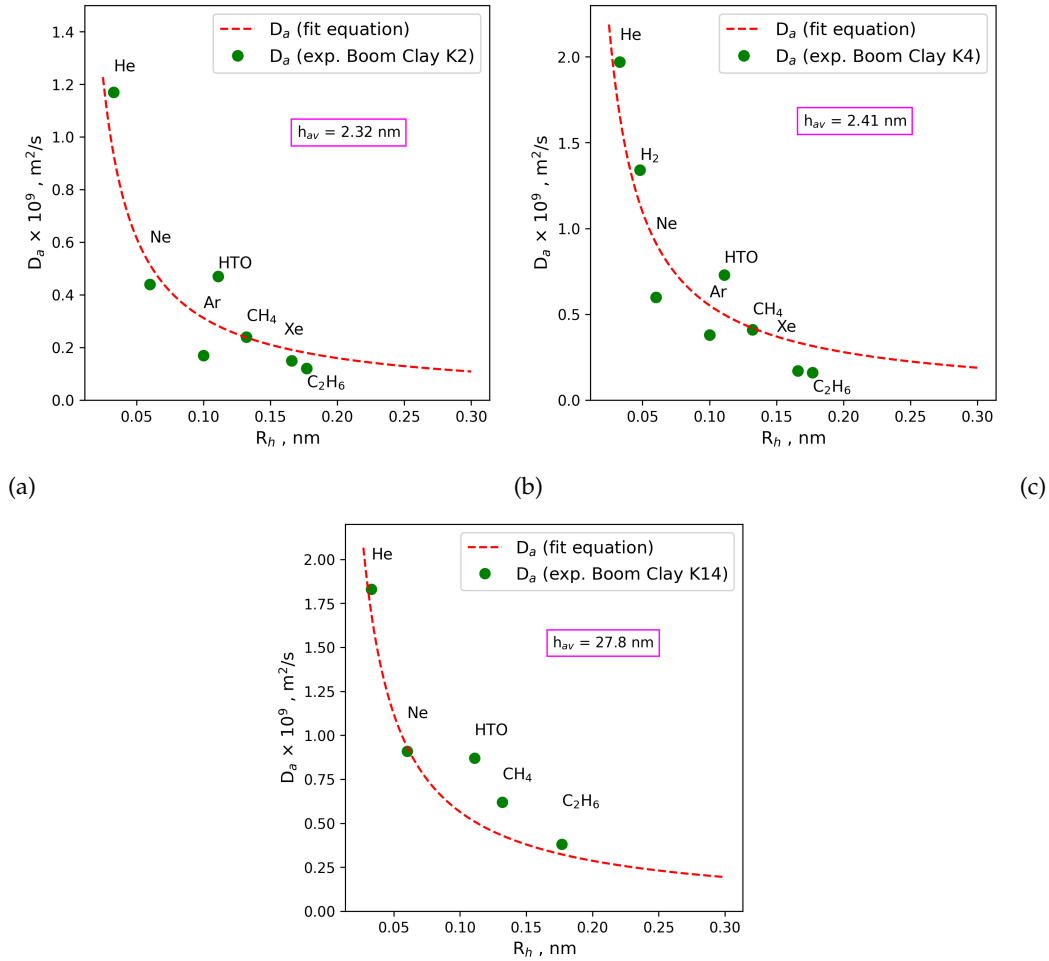


FIGURE 2.7: Apparent diffusion coefficients obtained from experiments of gases in three different Boom clays with varying pore size distribution and porosity, as well as apparent diffusion coefficients calculated with eq 2.13 fitted as a function of the hydrodynamic radius

procedure.

Figure 2.8 shows a plot of the D/D_0 values of water in Na-MMT nanopores as a function of pore size, calculated for each hydration state of the water-gas mixture and averaged over all temperatures (fitted with eq 2.11). It can be observed that confinement has a significant effect on the diffusion of water in the Na-MMT nanopores, with an increase in pore size leading to a corresponding increase in D values. This behavior is similar to that observed in previous studies for water and ion diffusion from MD simulations [8, 39, 67, 95, 99]. Holmboe et al. [39] investigated the diffusion of water through MD simulations in Na-MMT nanopores and found that confinement significantly affects the diffusion of bulk water by a reduction factor of about 20-90% at different pore sizes. In the studies of Botan et al. [8], the D value of diffusion of SPC/E water in Na-MMT pores is reduced by about 70% compared to the bulk value due to the higher density and surface effects near the clay walls. Other types of clays have also been studied for their confining effect on water dynamics: Zhou et al. [111] showed that the self-diffusion coefficient of water in montmorillonite is faster than that of water in an Mg-rich clay. Nguwana et al. [67] studied the structure and dynamics of hydrated Cs-montmorillonite

and found that the mobility of Cs ions and H₂O diffusion coefficients increased with increasing water content and distance from the clay surface. They observed the typical structuring of water molecules due to their increased concentration at the surface of the clay layer with increasing water content, indicating a hydrophilic nature of water at the clay surface. Wang et al. [99] applied molecular dynamics simulations to study the properties of interfacial water on surfaces of brucite, gibbsite, hydrotalcite, etc. They found that the differences in structural charge on the octahedral layer, the cation occupancies and distributions, and the orientations of the OH groups affect the surface water structure. From the atomic density profiles, they were able to determine that the structural properties of the water at the surface of talc and muscovite are different. The water exhibits a hydrophobic property at the talc surface and hydrophilic properties at the muscovite surface [99]. The smectite interactions in this study show high hydrophilicity. This could be observed from the high-density water structure at the surface of the Na-montmorillonite (see Figure 2.9). This is consistent with a comprehensive study by Szczerba et al. [91]. They applied molecular dynamics simulations to quantify the hydrophobicity and hydrophilicity of charged smectite-siloxane surfaces. They found that the hydrophobicity and hydrophilicity of smectite surfaces depend on the consideration of counterions in the integral part of the surface. They concluded that a smectite surface without counterions is hydrophobic or moderately hydrophilic. However, when counterions are included, the surface is strongly hydrophilic [91].

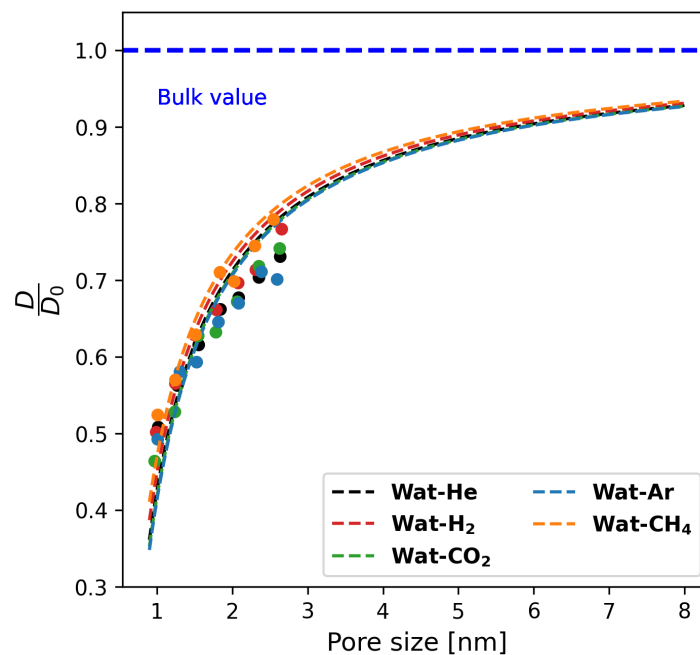


FIGURE 2.8: Relative diffusion coefficient (D/D_0) of water in a water-gas mixture in clay nanopores as a function of water content/pore size. The marker dots represent D/D_0 for temperatures 300, 350, and 375 K, respectively. The lines represent the fit of D/D_0 with eq 2.11.

In the work of Tsimpanogiannis et al. [95], they evaluated the self-diffusion of confined water for a variety of confinement systems representing materials that differ in chemical nature, shape, size, and surface charge distribution. These features significantly affect the structural

and transport properties of the confined fluid near the interface. They observed differences in the confinement effects of carbon compounds, minerals, biomolecules, and other confining media. From this, they concluded that the type of confining material plays an important role in affecting water diffusion [95]. At mineral surfaces, in particular, the presence of water leads to interactions between the water and the surface. Thus, water with hydrophilic mineral surfaces can form hydrogen bonds at the interface, which can divide the water in the pore into so-called water layers and thus cause a reduction in diffusion [72].

Our results show that confinement affects the self-diffusion coefficient of water by 30-90% compared to the bulk value. Interestingly, we found that the diffusion of water in the nanopore is slightly affected by the type of gas present in the mixture. It could be argued that these differences could be due to the nature of the interactions between the gas, water, and clay layer. This will be further explored in later sections.

2.3.4 Activation energy of diffusion

To determine the temperature dependence of gases and water in Na-MMT, Arrhenius plots of diffusion coefficients were constructed and fitted with a least squares regression line. In this way, the activation energy (E_a) of the diffusion of water (in the water-gas mixture) and of gases could be determined. Corrected E_a values of 8.8, 15.7, 19.0, 16.6, 18.3, and 18.54 were obtained for He, H₂, CO₂, Ar, CH₄, and water respectively.

In general, our results show that the E_a values for water are influenced slightly by the confinement. This effect is due to the structuring of the water molecules near the clay surface, which is more pronounced in the first two layers of water near the surface and decreases thereafter. The average activation energy for water in the Na-MMT is about 18.54 ± 0.31 kJ/mol. This agrees with values obtained by experiments for pure water in clay [82, 96]. Van Loon et al. [96] investigated the activation energy of water in Opalinus clay by diffusion and neutron spectroscopy experiments and obtained a value of 22 kJ/mol. Sanchez et al. [82] performed macroscopic and microscopic diffusion experiments on different types of clay materials. In particular, for Na-MMT they obtained values of 20.78 and 11.57 kJ/mol for macro and micro experiments, respectively [82].

On average, the E_a values of water in the confined state are about 11% higher than in the bulk, which is consistent with experimental observations [82, 96]. This increase in E_a values is due to the fact that the interaction of water molecules with their neighbors in bulk water is largely based on hydrogen bonds. Therefore, when the environment of a water molecule changes, e.g. water in a Na-MMT, the interactions of the molecule with the clay surface can greatly increase the E_a value from the bulk.

Similarly, for water, confinement has a slight influence on the E_a values of gases. As far as we know, the activation energy of dissolved gases in saturated clay nanopores has not yet been studied. From our results, the monoatomic gases (He, Ar) in the Na-MMT confinement have E_a values deviating about 20% below that of the bulk water, while the polyatomic gases in the Na-MMT confinement have E_a values deviating about 3% below that of the bulk water. One

could argue that He and Ar are spherically symmetric, non-polar gases, so we do not expect strong interactions with the clay surface. However, the water itself in the water-gas mixture interacts with the clay surface, changing the dynamics of the water so that the monoatomic gases can move more freely from one water cage to another than is the case in the bulk. In the case of polyatomic gases, a much stronger interaction with the clay surface and with the water is possible, therefore gases are not able to move freely as compared to monoatomic gases. Nevertheless, the E_a for gases in clay can be taken as that of the E_a obtained in bulk water.

2.3.5 Structure of gas and aqueous fluids in clay interlayer

To further investigate the structure of the intercalated gas-water mixture, atomic density profiles, and radial pair correlation calculations were performed. Atomic density profiles for pore sizes 1.0 and 2.1 nm are presented in this section. The rest of the profiles are shown in Figure S1 in the Supporting Information.

Atomic density profiles

The average density profile of the gases in the interlayer region along the vertical axis is shown in Figure 2.9. Regions 1 and 2 show the regions of inner- and outer- spheres defined by Vasconcelos et al. [97] at a distance from the siloxane surface. The water molecules in Region 1 on both surfaces form hydrogen bonds with oxygen atoms on both surfaces and are therefore strongly oriented. The shoulder peaks of Hw (hydrogen of water) at about 15.0 and 9.8 Å (pore size 1.0 and 2.1 nm respectively) on the z-axis indicate the orientation of the Hw molecules on the siloxane surface. The presence of the surface strongly influences the distribution of the water molecules up to a distance of about 5 Å from the clay surface. From this point on, the water molecules are distributed rather randomly, as is to be expected in the bulk and as can be seen from the almost flat central area of the profile in Figure 2.9b. This is not the same for pore size at 1.0 nm as molecules tend to be distributed only at the surface of the clay. Although the negatively charged clay surface attracts the Na^+ ions, as can be seen from the two peaks near the surface, Na^+ tends to form outer-sphere complexes due to its hydrophilic nature and the orientation of the water molecules.

In all seven cases where the pore size varies between 1.0 and 2.6 nm, gases have two distinct peaks near the two clay surfaces, indicating that gases have a fairly strong affinity for the clay surface. He and H_2 have a broader peak whose tails extend closer to the siloxane surface than the other gases (see Figure 2.9). This is probably due to the small size of the gas molecules. It appears that He and H_2 have a large mobility parallel to the clay surface. Ar, CO_2 , and CH_4 , on the other hand, have peaks in the density overlapping with high-density water regions due to their large size.

Radial distribution functions

The RDF values are summarised in Table 2.3 and the curves are shown in full in the Supporting Information (Figure S2-S4). It can be observed that the peak distances vary with molecular

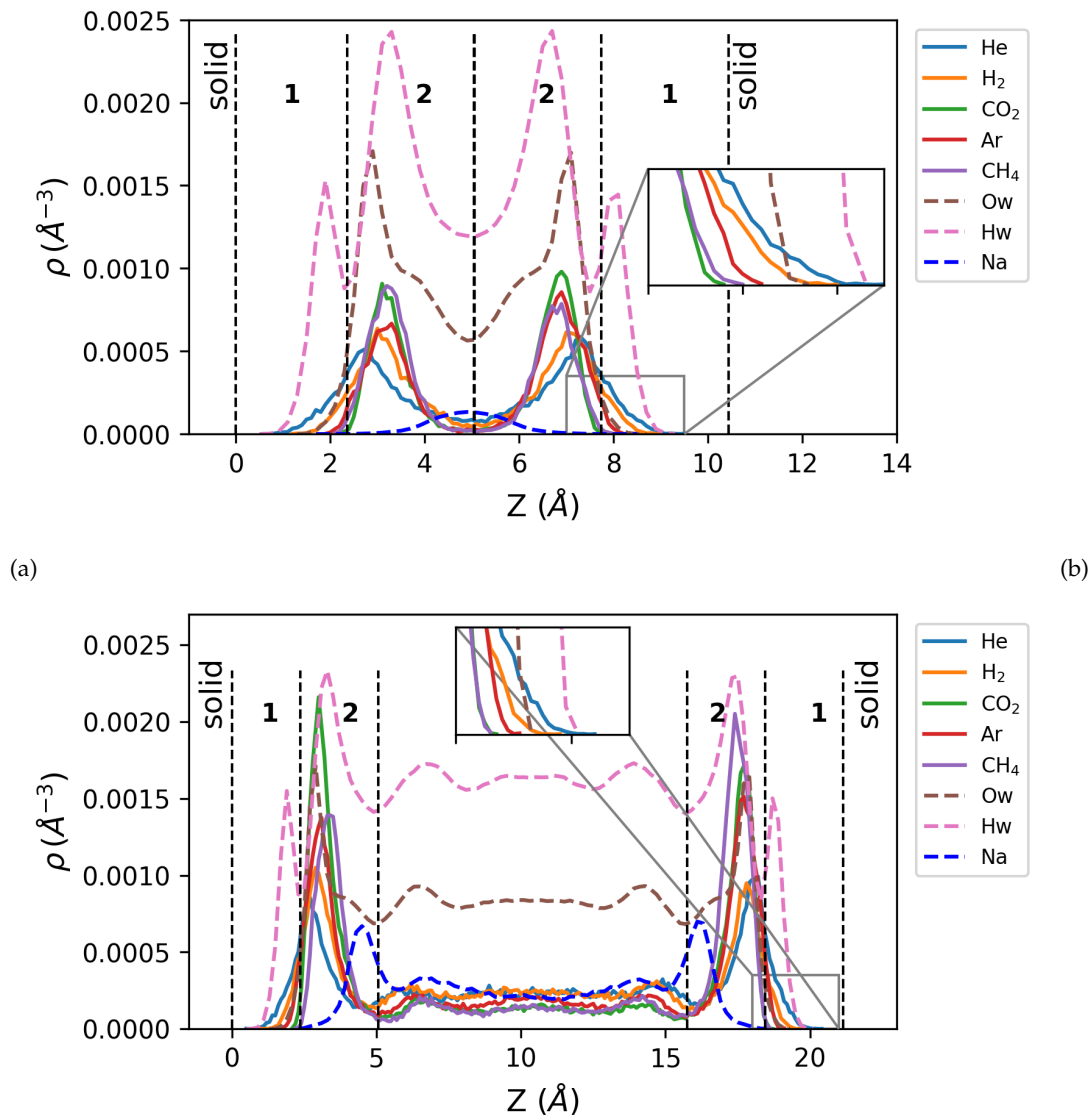


FIGURE 2.9: Density profiles of gases, water, and Na⁺ ions at a pore size of (a) 1.0 and (b) 2.1 nm. The values of Ow and Hw are scaled down to 5% for better visualization

size (see Table S3). To fully understand the interaction strength of the gas-liquid and gas-surface structure, we calculated the average coordination number of oxygen atoms around a gas particle.

Table 2.3 shows the coordination numbers of Ow and Ob around gases at a pore size of 2.1 nm. The total number of oxygen atoms surrounding the gases was calculated as N_{tO} , which is the sum of the coordination numbers of the oxygen of the water and the oxygen of the siloxane surface. The values are in agreement with the results reported in previous studies [14, 23, 28, 49]. As for the gas-oxygen (water) coordination number, our results are in agreement with the values obtained by neutron diffraction (CH₄, 19 ± 2 [23]; Ar, 16 ± 2 [14]). The results show that the least coordinated gas has the highest mobility and vice versa. It can be concluded that as the interaction with the water and the clay surface increases, the mobility of the gases decreases.

TABLE 2.3: Coordination numbers of water and clay oxygen around gases at pore size 2.1 nm

	$Nt_O^a(O_w, O_b)$	r_{max}^b	r_{min}^c
He	13.8 (11.8, 2.0)	3.00	4.42
H ₂	16.8 (14.3, 2.5)	3.23	4.65
Ar	17.3 (14.3, 3.0)	3.52	4.80
CO ₂	19.7 (15.0, 4.7)	3.82	5.10
CH ₄	20.2 (15.3, 3.7)	3.67	4.96

^a Nt_O is the total coordination number of oxygen around gases.

^b r_{max} is the maximum peak distance of first coordination shell.

^c r_{min} is the minimum peak distance of first coordination shell.

2.4 Conclusions

The pore scale diffusivity of gases and its dependency on pore size is of fundamental interest for gas transport modeling. These properties are not readily accessible experimentally. MD simulations provide an effective tool to study these physicochemical properties of confined systems. In this study, the influence of pore size, temperature, and gas type on MD simulation predictions for the diffusion of He, Ar, H₂, CO₂, CH₄ and water in Na-montmorillonite nanopores was determined. The simulations provide information for diffusion coefficient (D) and activation energy (E_a) values of gases and water in saturated Na-montmorillonite nanopores which allow revealing generic relationships with respect to fundamental molecular parameters of molecules. The D and E_a values from these studies are largely in agreement with experimental data. The predictions from this study show that gas diffusion is influenced by the mineralogy of the confinement, the size of the clay nanopore, and the hydrodynamic radius of the gas. An equation linking these parameters was derived, which will be a very useful tool for macro-scale numerical modeling and laboratory experiments.

$$D_a = \frac{D_0}{G} \left(1 - \frac{k_c}{h_{av}} \right) \quad (2.14)$$

where D_a is the apparent diffusion coefficient of the gas, D_0 is the diffusion coefficient of the gas in the bulk water, q_{nano} is the relative diffusion coefficient (D/D_0) from the MD simulation, G is the geometric factor and h_{av} is the average pore width.

In the absence of experimental data for the diffusion of gases in clay nanopores, a comparison of the simulation results with macroscopic apparent diffusion coefficients from experiments was performed. For this purpose, macroscopic parameters of clay from experiments were substituted into our equation and the curve and experimental data were fitted as a function of the hydrodynamic radius of the gases. The curve is in reasonable agreement with the apparent diffusion coefficients obtained from experiments. Since the equation depends on the geometric

factor and average pore size from the pore size distributions, a good determination of these parameters can increase the accuracy of desired results.

It was found that the interactions of gases with water and the clay surface strongly influence mobility. He, with a lower interaction strength, has the highest mobility compared to CH₄, which has a stronger interaction strength and thus the lowest mobility. The results also show that the presence of gases changes the mobility of water even in the clay nanopore depending on the type of the water-gas mixture. The results also show that the clay nanopore affects the activation energy of diffusion of gases. It was observed that symmetrically nonpolar monatomic gases in the clay nanopore have a lower value for the activation energy than the bulk value, while the opposite behavior is observed for the polyatomic gases CO₂ with quadrupole moments and CH₄ with octupole moments. The activation energy of water in the water-gas mixture is slightly higher than that of the bulk in the clay. However, the value of 18 kJ/mol from the simulations agrees with the experimental values.

Supporting Information

The Supporting Information (Appendix) of this manuscript contains the values of the force potential model used in this simulation. We have also included a table with the results of the diffusion coefficients for all gases at all temperatures and all pore sizes. The coordination numbers and radial distribution function graphs for gases with different pore sizes are also included in the Supporting Information. Finally, density distribution diagrams for gases and water were presented.

Acknowledgements

The research reported in this paper was supported by EURAD GAS FUTURE and DONUT Work Packages, Laboratory for Waste Management at the Paul Scherrer Institute, NAGRA, and the University of Bern Geological Institute. Molecular dynamics simulations were carried out using resources from the Paul Scherrer Institute (MERLIN 6), the University of Bern (UBELIX), and the Swiss National Super Computing Centre (Piz Daint). The authors acknowledge the co-funding from Horizon 2020 EURAD project Grant ID 847593.

2.5 Appendix

Force potential parameters

TABLE 2.4: Lennard-Jones 6-12 potential parameters used in the MD simulation. The Oxygen atoms are assigned partial charges based on the atoms they are bonded to. Ob: bridging oxygen, Oh: hydroxyl oxygen, Ohs: hydroxyl oxygen with substitution, Obos: bridging oxygen with octahedral substitution, Ho: hydroxyl hydrogen, Hs: hydroxyl oxygen with substitution.

Particles	ϵ (kcal/mol)	σ (Å)	charge	Ref
Parameters for the clay				
Si	1.800e-6	3.302	2.10000	[21]
Al	1.300e-6	4.271	1.57500	[21]
Mg	9.000e-7	5.264	1.35998	[21]
Ob	1.554e-1	3.166	-1.05000	[21]
Oh	1.554e-1	3.166	-9.50000	[21]
Ohs	1.554e-1	3.166	-1.08083	[21]
Obos	1.554e-1	3.166	-1.18083	[21]
Ho	-	-	0.42500	[21]
Hs	-	-	0.42500	[21]
Parameters for Na and Water				
Na	1.301e-1	2.350	1.00000	[87]
Ow	1.554e-1	3.166	-0.8476	[6]
Hw	-	-	0.4238	[6]
Parameters for Gases				
He	1.544e-2	2.78044	-	[11]
H ₂	1.902e-2	3.14000	-	[63]
Ar	2.757e-1	3.36340	-	[11]
CO ₂ -C	5.590e-2	2.7570	0.65120	[35]
CO ₂ -O	1.5998e-1	3.0330	-0.32560	[35]
CH ₄ -C	3.2624e-1	3.6400	-0.56000	[94]
CH ₄ -H	-	-	0.1400	[94]

Diffusion coefficients of gases in Na-MMT

TABLE 2.5: MD simulation predictions of the diffusion coefficients D ($10^{-9} \text{ m}^2/\text{s}$) for dissolved gas solutes in Na-MMT at different pore sizes and temperatures

	pore size (h) [nm]	1.0	1.3	1.5	1.8	2.1	2.4	2.6
	T [K]							
He	300	3.02 ± 0.30	5.28 ± 0.60	5.18 ± 0.23	6.66 ± 0.69	6.24 ± 0.28	6.8 ± 0.26	7.58 ± 0.40
	350	5.09 ± 0.11	7.59 ± 0.12	8.85 ± 0.31	10.46 ± 0.73	10.38 ± 0.48	11.36 ± 0.41	11.60 ± 0.15
	375	5.95 ± 0.63	9.39 ± 0.43	11.18 ± 0.67	12.68 ± 1.04	12.45 ± 0.36	13.08 ± 0.50	13.89 ± 0.47
H ₂	300	1.89 ± 0.32	3.26 ± 0.26	4.18 ± 0.40	4.35 ± 0.25	4.68 ± 0.25	4.67 ± 0.24	5.19 ± 0.23
	350	3.10 ± 0.14	5.35 ± 0.40	7.05 ± 0.38	7.78 ± 0.16	7.73 ± 0.50	7.67 ± 0.21	9.89 ± 0.30
	375	3.74 ± 0.49	7.09 ± 0.53	8.01 ± 0.72	9.43 ± 0.35	9.28 ± 0.49	10.52 ± 0.41	11.14 ± 0.65
CO ₂	300	0.58 ± 0.06	1.09 ± 0.09	1.42 ± 0.17	1.45 ± 0.06	1.63 ± 0.09	1.79 ± 0.14	1.86 ± 0.10
	350	1.11 ± 0.06	1.96 ± 0.09	2.44 ± 0.11	2.72 ± 0.17	3.12 ± 0.15	3.56 ± 0.10	3.64 ± 0.12
	375	1.60 ± 0.20	2.31 ± 0.19	3.12 ± 0.08	3.58 ± 0.33	3.74 ± 0.17	4.34 ± 0.31	4.75 ± 0.27
Ar	300	0.75 ± 0.10	1.51 ± 0.20	1.47 ± 0.10	1.79 ± 0.10	1.87 ± 0.10	2.15 ± 0.14	1.99 ± 0.14
	350	1.51 ± 0.27	2.56 ± 0.19	3.01 ± 0.12	3.39 ± 0.25	3.66 ± 0.32	3.91 ± 0.19	3.72 ± 0.16
	375	1.96 ± 0.12	3.32 ± 0.28	3.64 ± 0.13	4.23 ± 0.27	4.47 ± 0.17	4.98 ± 0.20	4.77 ± 0.34
CH ₄	300	0.66 ± 0.05	0.87 ± 0.12	1.19 ± 0.07	1.50 ± 0.08	1.35 ± 0.03	1.52 ± 0.05	1.57 ± 0.04
	350	1.34 ± 0.14	1.93 ± 0.30	2.48 ± 0.15	3.01 ± 0.13	2.92 ± 0.24	3.15 ± 0.16	3.21 ± 0.12
	375	1.82 ± 0.14	2.40 ± 0.26	3.05 ± 0.20	3.92 ± 0.34	3.70 ± 0.18	3.96 ± 0.20	4.18 ± 0.14

Density profiles of gases, water, and Na ions at 300 K

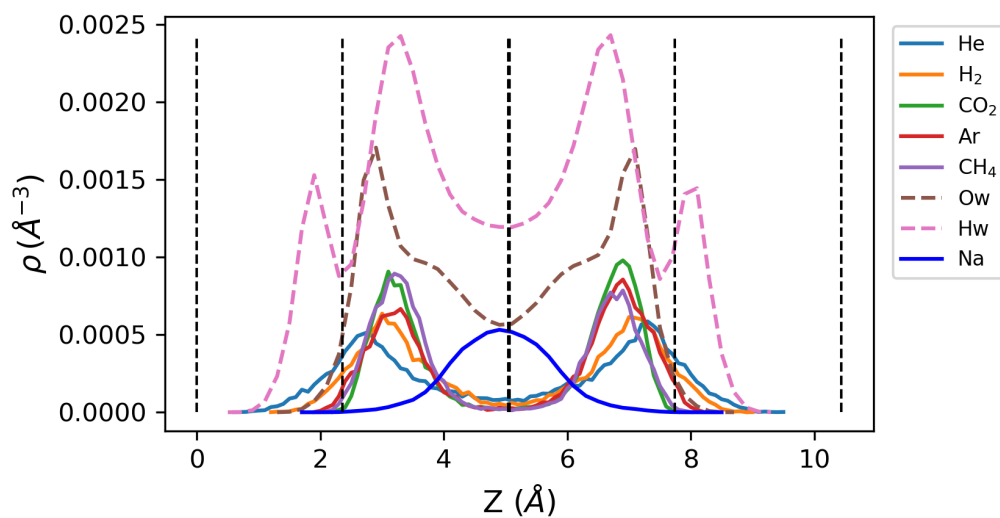


FIGURE 2.10: Fluid density profile at pore size 1.0nm

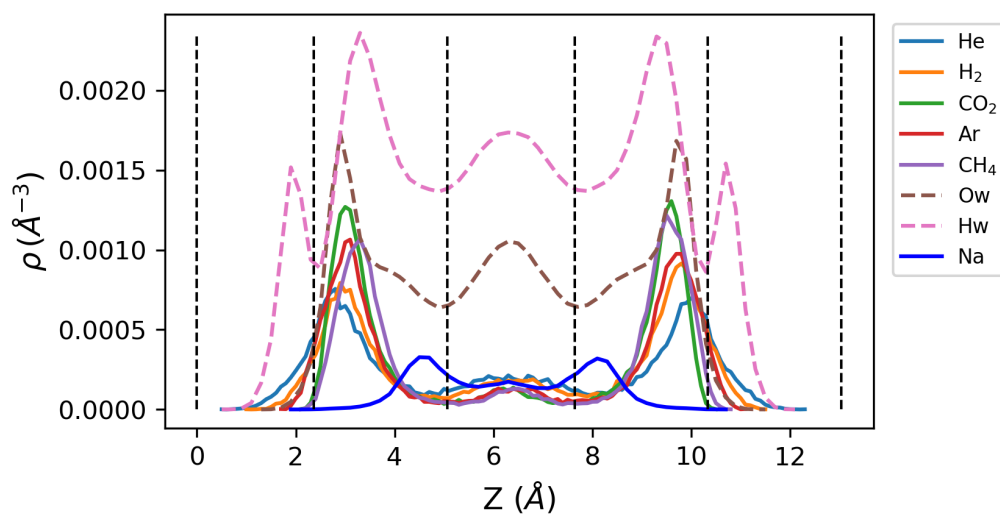


FIGURE 2.11: Fluid density profile at pore size 1.3 nm

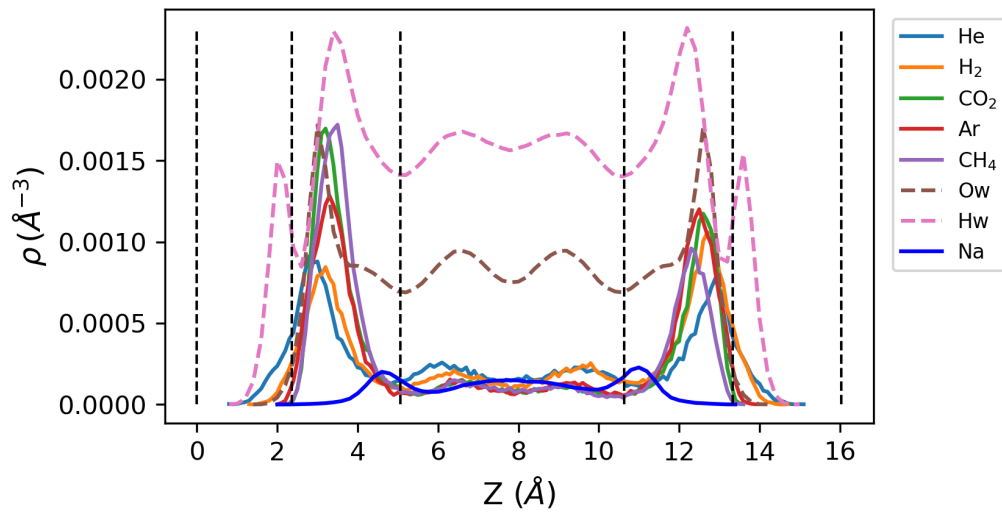


FIGURE 2.12: Fluid density profile at pore size 1.5 nm

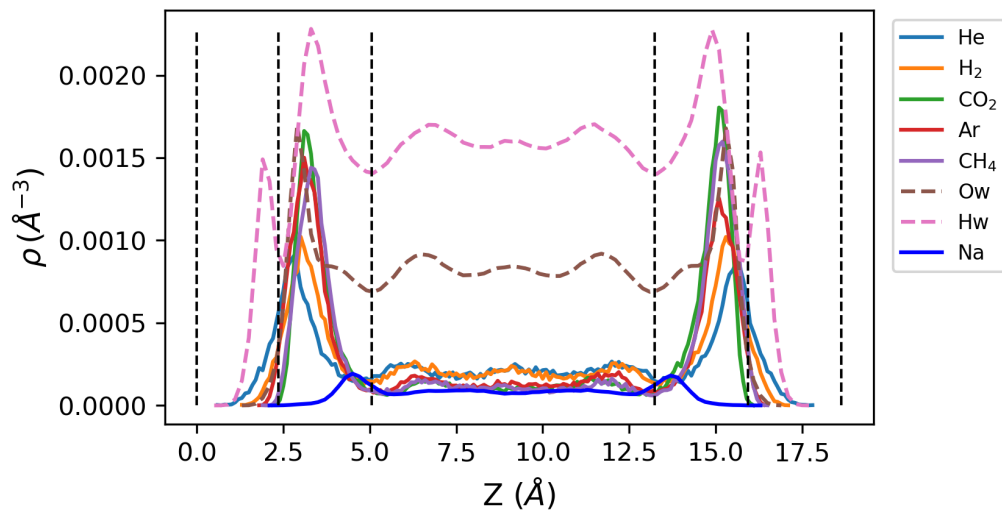


FIGURE 2.13: Fluid density profile at pore size 1.8 nm

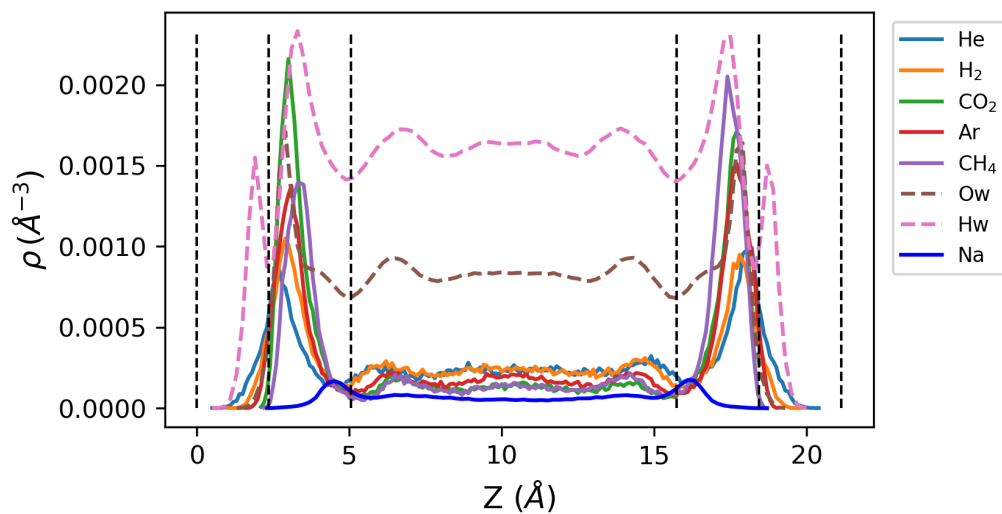


FIGURE 2.14: Fluid density profile at pore size 2.1 nm

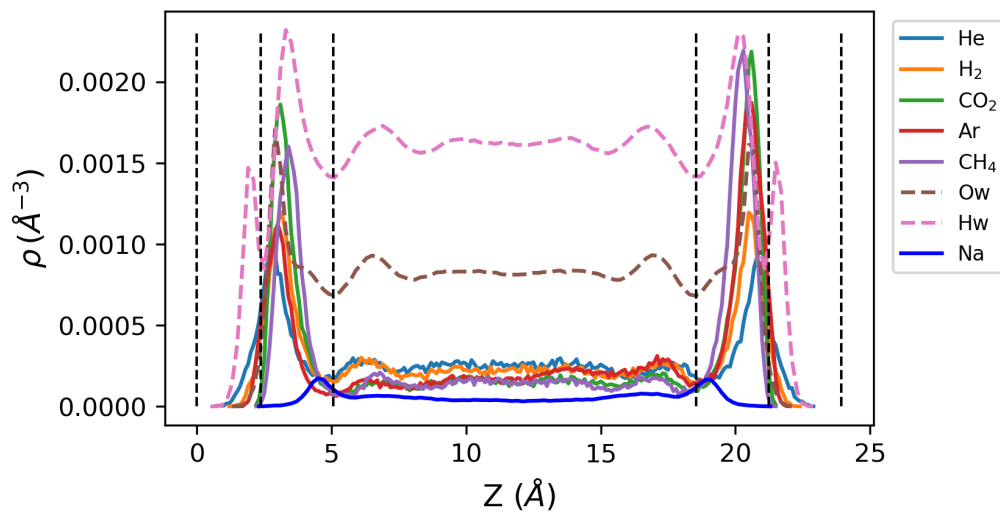


FIGURE 2.15: Fluid density profile at pore size 2.4 nm

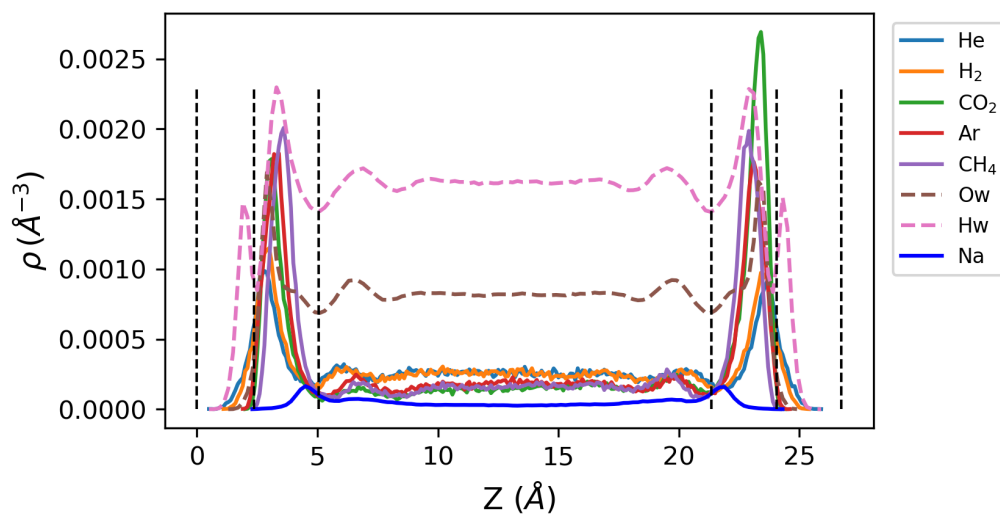


FIGURE 2.16: Fluid density profile at pore size 2.6 nm

Radial distribution functions

Radial distribution functions (RDF) are used to characterize the structure of gas-fluid and gas-surface interactions. It gives the probability, averaged over time, of finding a particle at a radial distance from a given reference particle. The RDF enables the determination of relative affinities for the gases in the aqueous phase and clay system. The RDF at 300 K curves are shown in Figure S8, Figure S9, and Figure S10.

From Figures S8, S9, and S10, it is observed that the peak distances are in relation to the size of the gas molecules, thus the smaller the gas the closer to the oxygen atoms in the clay-water phase. To fully understand the interaction strength of the gas-liquid and gas-surface structure, we calculated the average number of atoms in a coordinated atomic shell at a given distance (r_{min}) around the reference particle. This is given by the area under the peak and is obtained by integrating the RDF function from immediately before to immediately after the peak.

Table S3 shows the coordination numbers of Ow, Hw, and Ob in the environment of gases at all pore sizes. The values are consistent with results reported in previous studies [14, 23, 28, 49]. With regard to the gas-Oxygen (water) coordination number, our results are consistent with the values obtained by neutron diffraction results (CH₄, 19 ± 2 ; [23] Ar, 16 ± 2 [14]). The results show that coordination numbers in the first hydration shell increase to that seen in bulk water, as pore size increases. The results also show that He is the least coordinated, followed by H₂ and Ar. The carbon atoms of CO₂ and CH₄ are the most coordinated with close coordination numbers of 19.7 and 20.2 respectively. This trend is consistent with the diffusion coefficient values obtained in this work, where the mobility of He, H₂, Ar, CO₂ to CH₄ decreases. It follows that with increasing interaction with the water and the clay surface, the mobility of the gases decreases.

TABLE 2.6: Coordination Numbers of Gas-Fluid and Gas-Clay Computed from Radial Pair Correlation functions

pore size [nm]	1.0	1.3	1.5	1.8	2.1	2.4	2.6	average
He								
n_{He-Ow}	10.1	10.2	11.7	11.2	11.8	13.0	13.3	11.0
n_{He-Hw}	25.6	26.3	27.9	29.1	30.6	31.4	31.9	27.8
n_{He-Ob}	3.4	3.2	2.4	2.1	2.0	1.6	1.41	1.2
H ₂								
n_{H_2-Ow}	12.3	12.0	13.3	13.0	14.3	13.8	14.6	13.2
n_{H_2-Hw}	32.4	30.5	34.0	35.9	36.9	35.5	37.4	33.7
n_{H_2-Ob}	4.4	3.6	3.4	3.1	2.5	2.5	1.9	1.6
CO ₂								
$n_{C(CO_2)-Ow}$	14.6	13.8	14.2	14.7	15.0	15.4	15.3	14.3
$n_{C(CO_2)-Hw}$	35.5	34.7	35.9	37.4	38.3	39.3	39.0	36.2
$n_{C(CO_2)-Ob}$	6.5	5.5	4.8	4.6	4.7	3.9	3.8	4.1
$n_{O(CO_2)-Ow}$	13.5	13.6	14.0	14.5	14.8	15.2	15.1	14.1
$n_{O(CO_2)-Hw}$	35.3	32.0	33.1	34.4	32.6	33.5	33.2	32.7
$n_{O(CO_2)-Ob}$	4.4	3.7	3.2	3.0	2.8	2.7	2.5	1.4
Ar								
n_{Ar-Ow}	13.3	12.5	14.1	14.7	14.3	14.5	15.7	14.0
n_{Ar-Hw}	32.6	31.6	33.5	35.0	36.5	36.9	37.4	34.8
n_{Ar-Ob}	4.5	4.1	4.3	3.4	3.0	2.7	2.8	1.8
CH ₄								
$n_{C(CH_4)-Ow}$	13.4	14.0	14.2	14.6	15.3	15.5	15.9	15.3
$n_{C(CH_4)-Hw}$	34.6	35.1	36.0	37.0	38.8	39.5	40.4	37.0
$n_{C(CH_4)-Ob}$	4.9	4.7	4.2	3.8	3.7	3.4	3.2	1.9
$n_{H(CH_4)-Ow}$	18.6	16.4	15.4	18.4	17.9	18.2	17.3	17.1
$n_{H(CH_4)-Hw}$	46.8	40.7	36.2	39.9	39.0	39.7	40.7	38.2
$n_{H(CH_4)-Ob}$	7.8	10.7	8.9	8.9	8.5	8.0	6.8	3.9

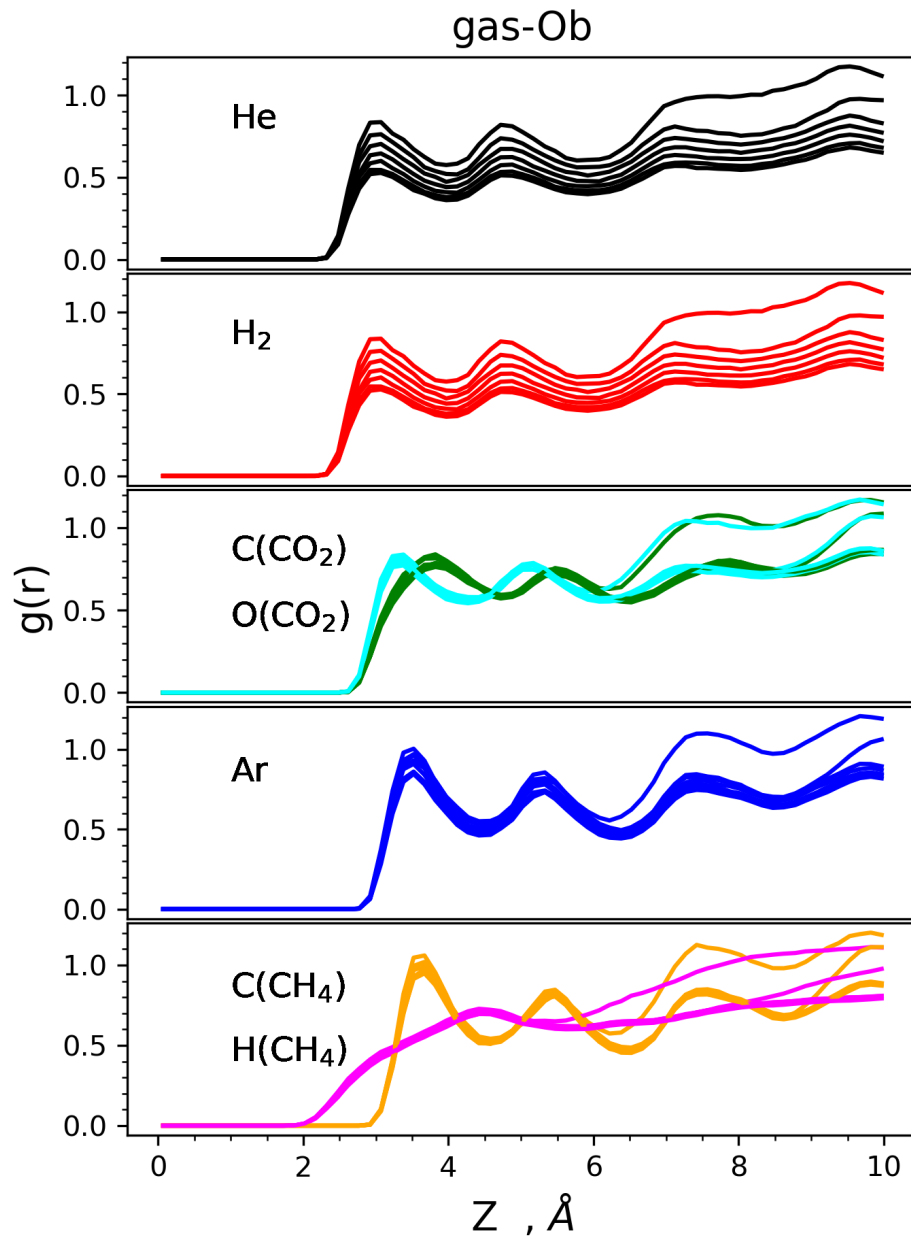


FIGURE 2.17: Radial distribution functions of gas - oxygen (water) at all pore sizes at temperature 300 K. Hydrogen of CH₄ atom is colour magenta and oxygen of CO₂ atom is colour cyan. The peak magnitude decreases with increasing pore size.

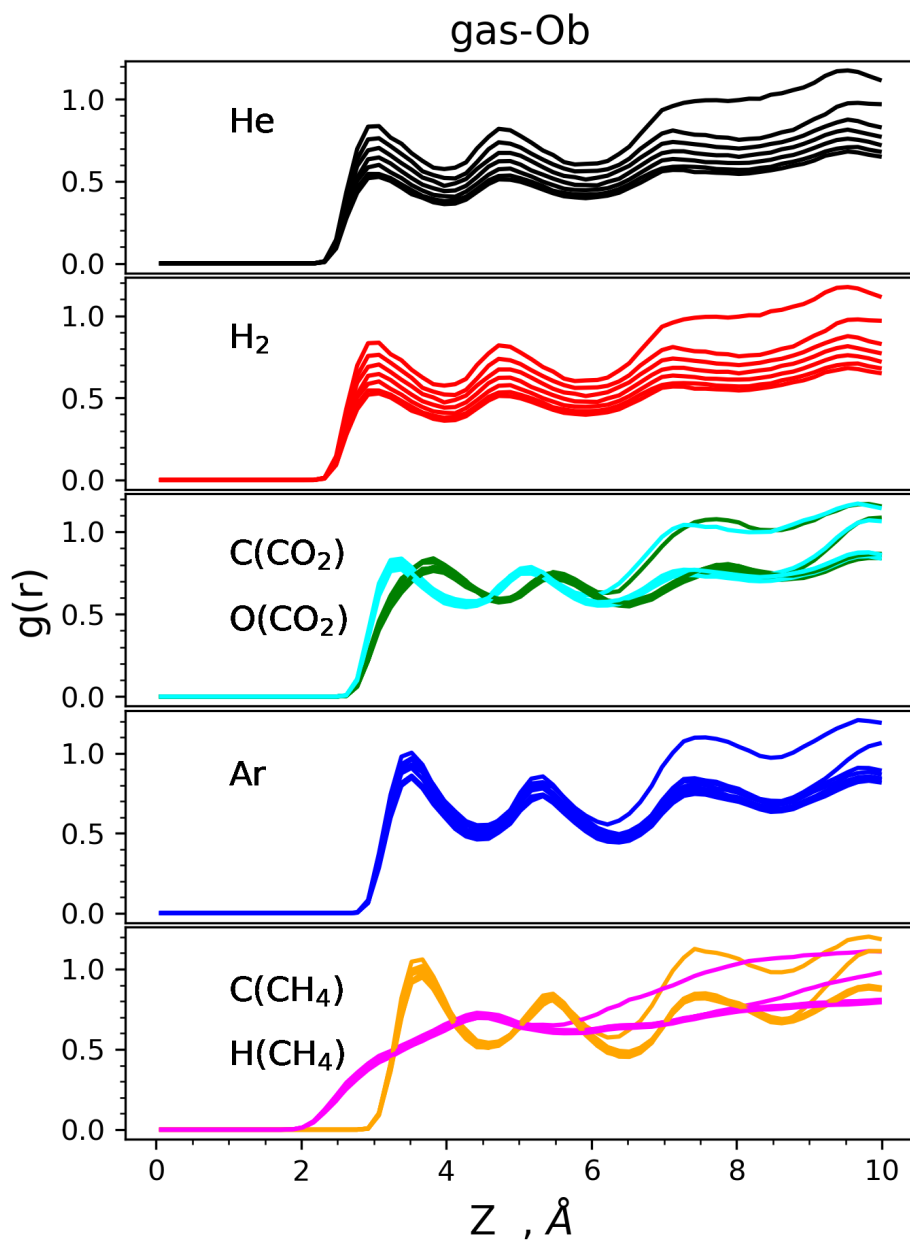


FIGURE 2.18: Radial distribution functions of gas - oxygen (basal clay) at all pore sizes at temperature 300 K. Hydrogen of CH₄ atom is colour magenta and oxygen of CO₂ atom is colour cyan. The peak magnitude decreases with increasing pore size.

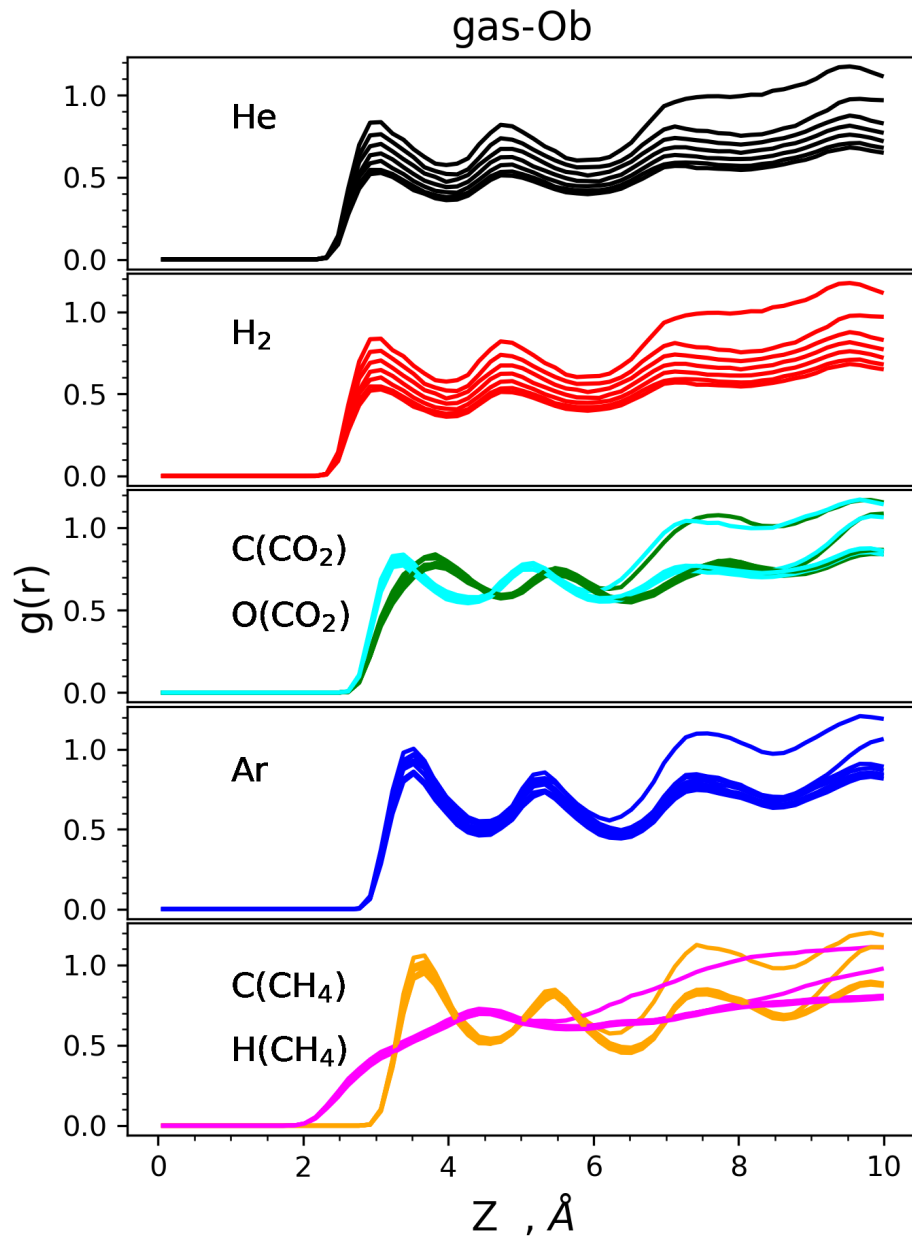


FIGURE 2.19: Radial distribution functions of gas - hydrogen (water) at all pore sizes at temperature 300 K. Hydrogen of CH_4 atom is colour magenta and oxygen of CO_2 atom is colour cyan. The peak magnitude decreases with increasing pore size.

2.6 References

- [1] Afagwu, C., Alafnan, S., Mahmoud, M. A., and Patil, S. (2021). Permeability model for shale and ultra-tight gas formations: Critical insights into the impact of dynamic adsorption. *Energy Reports*, 7:3302–3316.
- [2] Ali, I. and Malik, N. A. (2018). A realistic transport model with pressure-dependent parameters for gas flow in tight porous media with application to determining shale rock properties. *Transport in Porous Media*, 124(3):723–742.
- [3] Aljama, H. and Wilcox, J. (2017). Microscopic diffusion of co₂ in clay nanopores. *Chemical Physics Letters*, 677:162–166.
- [4] Benazzouz, B. K., Ho, K. H., Nguyen, P. T., Hoang, H., and Galliero, G. (2022). Diffusive transport of gases in saturated nanopores: Caprock leakage from a molecular simulation perspective. *Journal of Natural Gas Science and Engineering*, 98:104383.
- [5] Bensenouci, F., Michelot, J., Matray, J., Savoye, S., Lavielle, B., Thomas, B., and Dick, P. (2011). A profile of helium-4 concentration in pore-water for assessing the transport phenomena through an argillaceous formation (tournemire, france). *Physics and Chemistry of the Earth, Parts A/B/C*, 36(17-18):1521–1530.
- [6] Berendsen, H., Grigera, J., and Straatsma, T. (1987). The missing term in effective pair potentials. *Journal of Physical Chemistry*, 91(24):6269–6271.
- [7] Botan, A., Rotenberg, B., Marry, V., Turq, P., and Noetinger, B. (2010). Carbon dioxide in montmorillonite clay hydrates: thermodynamics, structure, and transport from molecular simulation. *The Journal of Physical Chemistry C*, 114(35):14962–14969.
- [8] Botan, A., Rotenberg, B., Marry, V., Turq, P., and Noetinger, B. (2011). Hydrodynamics in clay nanopores. *The Journal of Physical Chemistry C*, 115(32):16109–16115.
- [9] Boudreau, B. P. (1997). *Diagenetic models and their implementation*, volume 505. Springer Berlin.
- [10] Bourg, I. C., Richter, F. M., Christensen, J. N., and Sposito, G. (2010). Isotopic mass dependence of metal cation diffusion coefficients in liquid water. *Geochimica et Cosmochimica Acta*, 74(8):2249–2256.
- [11] Bourg, I. C. and Sposito, G. (2008). Isotopic fractionation of noble gases by diffusion in liquid water: Molecular dynamics simulations and hydrologic applications. *Geochimica et Cosmochimica Acta*, 72(9):2237–2247.
- [12] Bourg, I. C. and Sposito, G. (2010). Connecting the molecular scale to the continuum scale for diffusion processes in smectite-rich porous media. *Environmental science & technology*, 44(6):2085–2091.

- [13] Bradshaw, J., Bachu, S., Bonijoly, D., Burruss, R., Holloway, S., Christensen, N. P., and Mathiassen, O. M. (2007). Co₂ storage capacity estimation: issues and development of standards. *International journal of greenhouse gas control*, 1(1):62–68.
- [14] Broadbent, R. and Neilson, G. (1994). The interatomic structure of argon in water. *The Journal of chemical physics*, 100(10):7543–7547.
- [15] Choi, J.-H., Seol, Y., Boswell, R., and Juanes, R. (2011). X-ray computed-tomography imaging of gas migration in water-saturated sediments: From capillary invasion to conduit opening. *Geophysical Research Letters*, 38(17).
- [16] Churakov, S. V. (2013). Mobility of Na and Cs on montmorillonite surface under partially saturated conditions. *Environmental science & technology*, 47(17):9816–9823.
- [17] Churakov, S. V. and Kosakowski, G. (2010). An ab initio molecular dynamics study of hydronium complexation in Na-montmorillonite. *Philosophical magazine*, 90(17-18):2459–2474.
- [18] Colombani, J., Bert, J., and Dupuy-Philon, J. (1999). Thermal diffusion in (LiCl, Rb₂O). *The Journal of chemical physics*, 110(17):8622–8627.
- [19] Corominas, J., Martínez-Bofill, J., and Soler, A. (2015). A textural classification of argillaceous rocks and their durability. *Landslides*, 12:669–687.
- [20] Cygan, R. T., Greathouse, J. A., Heinz, H., and Kalinichev, A. G. (2009). Molecular models and simulations of layered materials. *Journal of Materials Chemistry*, 19(17):2470–2481.
- [21] Cygan, R. T., Guggenheim, S., and Koster van Groos, A. F. (2004a). Molecular models for the intercalation of methane hydrate complexes in montmorillonite clay. *The Journal of Physical Chemistry B*, 108(39):15141–15149.
- [22] Cygan, R. T., Liang, J.-J., and Kalinichev, A. G. (2004b). Molecular models of hydroxide, oxyhydroxide, and clay phases and the development of a general force field. *The Journal of Physical Chemistry B*, 108(4):1255–1266.
- [23] DE JONG, B. P., Wilson, J., Neilson, G., and Buckingham, A. (1997). Hydrophobic hydration of methane. *Molecular physics*, 91(1):99–104.
- [24] EC (2004). Geological Disposal of Radioactive Wastes Produced by Nuclear Power. From Concept to Implementation. *Report of the European Commission, EUR 21224. European Commission, Luxembourg*, page 43pp.
- [25] ENSI (2009). Guideline for Swiss Nuclear Installations. Specific design principles for deep geological repositories and requirements for the safety case. *ENSI Report ENSI-G03/e, Swiss Federal Nuclear Safety Inspectorate (ENSI), Brugg, Switzerland*.
- [26] Errington, J. R. and Panagiotopoulos, A. Z. (1998). A fixed point charge model for water optimized to the vapor-liquid coexistence properties. *The Journal of Physical Chemistry B*, 102(38):7470–7475.

- [27] Ferrage, E., Sakharov, B. A., Michot, L. J., Delville, A., Bauer, A., Lanson, B., Grangeon, S., Frapper, G., Jiménez-Ruiz, M., and Cuello, G. J. (2011). Hydration properties and interlayer organization of water and ions in synthetic na-smectite with tetrahedral layer charge. part 2. toward a precise coupling between molecular simulations and diffraction data. *The Journal of Physical Chemistry C*, 115(5):1867–1881.
- [28] Gadikota, G., Dazas, B., Rother, G., Cheshire, M. C., and Bourg, I. C. (2017). Hydrophobic solvation of gases (co₂, ch₄, h₂, noble gases) in clay interlayer nanopores. *The Journal of Physical Chemistry C*, 121(47):26539–26550.
- [29] Gimmi, T. and Churakov, S. V. (2019). Water retention and diffusion in unsaturated clays: Connecting atomistic and pore scale simulations. *Applied Clay Science*, 175:169–183.
- [30] Gomez-Hernandez, J. (2000). Fm-c experiment: Part a) effective diffusivity and accessible porosity derived from in-situ he-4 tests. part b) prediction of he-3 concentration in a cross-hole experiment.
- [31] Greenwell, H. C., Jones, W., Coveney, P. V., and Stackhouse, S. (2006). On the application of computer simulation techniques to anionic and cationic clays: A materials chemistry perspective. *Journal of Materials Chemistry*, 16(8):708–723.
- [32] Guillot, B. (2002). A reappraisal of what we have learnt during three decades of computer simulations on water. *Journal of molecular liquids*, 101(1-3):219–260.
- [33] Han, P. and Bartels, D. M. (1996). Temperature dependence of oxygen diffusion in h₂o and d₂o. *The Journal of physical chemistry*, 100(13):5597–5602.
- [34] Harrington, J., Milodowski, A., Graham, C., Rushton, J., and Cuss, R. (2012). Evidence for gas-induced pathways in clay using a nanoparticle injection technique. *Mineralogical Magazine*, 76(8):3327–3336.
- [35] Harris, J. G. and Yung, K. H. (1995). Carbon dioxide’s liquid-vapor coexistence curve and critical properties as predicted by a simple molecular model. *The Journal of Physical Chemistry*, 99(31):12021–12024.
- [36] He, S., Jiang, Y., Conrad, J. C., and Qin, G. (2015). Molecular simulation of natural gas transport and storage in shale rocks with heterogeneous nano-pore structures. *Journal of Petroleum Science and Engineering*, 133:401–409.
- [37] Hoang, H., Ho, K. H., Battani, A., Pujol, M., and Galliero, G. (2021). On elemental and isotopic fractionation of noble gases in geological fluids by molecular diffusion. *Geochimica et Cosmochimica Acta*, 315:172–184.
- [38] Holloway, S. (2005). Underground sequestration of carbon dioxide—a viable greenhouse gas mitigation option. *Energy*, 30(11-12):2318–2333.
- [39] Holmboe, M. and Bourg, I. C. (2014). Molecular dynamics simulations of water and sodium diffusion in smectite interlayer nanopores as a function of pore size and temperature. *The Journal of Physical Chemistry C*, 118(2):1001–1013.

- [40] Hura, G., Russo, D., Glaeser, R. M., Head-Gordon, T., Krack, M., and Parrinello, M. (2003). Water structure as a function of temperature from x-ray scattering experiments and ab initio molecular dynamics. *Physical Chemistry Chemical Physics*, 5(10):1981–1991.
- [41] IAEA (2009). Classification of Radioactive Waste. *IAEA Safety Standards Series. No. GSG-1.IAEA, Vienna, Austria.*
- [42] Jacobs, E., Maes, N., Bruggeman, C., and Grade, A. (2017). Measuring diffusion coefficients of dissolved he and ar in three potential clay host formations: Boom clay, callovo-oxfordian clay and opalinus clay. *Geological Society, London, Special Publications*, 443(1):349–360.
- [43] Jacobs, E., Volckaert, G., Maes, N., Weetjens, E., and Govaerts, J. (2013). Determination of gas diffusion coefficients in saturated porous media: He and ch₄ diffusion in boom clay. *Applied Clay Science*, 83:217–223.
- [44] Jähne, B., Heinz, G., and Dietrich, W. (1987). Measurement of the diffusion coefficients of sparingly soluble gases in water. *Journal of Geophysical Research: Oceans*, 92(C10):10767–10776.
- [45] Jiang, W. and Lin, M. (2018). Molecular dynamics investigation of conversion methods for excess adsorption amount of shale gas. *Journal of Natural Gas Science and Engineering*, 49:241–249.
- [46] Kamberaj, H., Low, R., and Neal, M. (2005). Time reversible and symplectic integrators for molecular dynamics simulations of rigid molecules. *The Journal of chemical physics*, 122(22):224114.
- [47] Kestin, J., Imaishi, N., Nott, S., Nieuwoudt, J., and Sengers, J. (1985). Viscosity of light and heavy water and their mixtures. *Physica A: Statistical Mechanics and its Applications*, 134(1):38–58.
- [48] Kim, C., Jang, H., and Lee, J. (2015). Experimental investigation on the characteristics of gas diffusion in shale gas reservoir using porosity and permeability of nanopore scale. *Journal of Petroleum Science and Engineering*, 133:226–237.
- [49] Koh, C. A., Wisbey, R. P., Wu, X., Westacott, R. E., and Soper, A. K. (2000). Water ordering around methane during hydrate formation. *The Journal of Chemical Physics*, 113(15):6390–6397.
- [50] Kosakowski, G., Churakov, S. V., and Thoenen, T. (2008). Diffusion of na and cs in montmorillonite. *Clays and Clay Minerals*, 56(2):190–206.
- [51] Krooss, B. and Schaefer, R. (1987). Experimental measurements of the diffusion parameters of light hydrocarbons in water-saturated sedimentary rocks—i. a new experimental procedure. *Organic Geochemistry*, 11(3):193–199.
- [52] Krynicki, K., Green, C. D., and Sawyer, D. W. (1978). Pressure and temperature dependence of self-diffusion in water. *Faraday Discussions of the Chemical Society*, 66:199–208.

- [53] Li, Z., Dong, M., Li, S., and Huang, S. (2006). Co₂ sequestration in depleted oil and gas reservoirs—caprock characterization and storage capacity. *Energy Conversion and Management*, 47(11-12):1372–1382.
- [54] Liu, X., Lu, X., Wang, R., and Zhou, H. (2008). Effects of layer-charge distribution on the thermodynamic and microscopic properties of cs-smectite. *Geochimica et Cosmochimica Acta*, 72(7):1837–1847.
- [55] Longworth, L. (1954). Temperature dependence of diffusion in aqueous solutions. *The Journal of Physical Chemistry*, 58(9):770–773.
- [56] Luboń, K. and Tarkowski, R. (2021). Influence of capillary threshold pressure and injection well location on the dynamic co₂ and h₂ storage capacity for the deep geological structure. *International Journal of Hydrogen Energy*, 46(58):30048–30060.
- [57] Marry, V., Dubois, E., Malikova, N., Durand-Vidal, S., Longeville, S., and Brey, J. (2011). Water dynamics in hectorite clays: Influence of temperature studied by coupling neutron spin echo and molecular dynamics. *Environmental Science & Technology*, 45(7):2850–2855.
- [58] Marschall, P., Horseman, S., and Gimmi, T. (2005). Characterisation of gas transport properties of the opalinus clay, a potential host rock formation for radioactive waste disposal. *Oil & gas science and technology*, 60(1):121–139.
- [59] Mazurek, M., Alt-Epping, P., Bath, A., Gimmi, T., Waber, H. N., Buschaert, S., De Canière, P., De Craen, M., Gautschi, A., Savoye, S., et al. (2011). Natural tracer profiles across argillaceous formations. *Applied Geochemistry*, 26(7):1035–1064.
- [60] Medina, J., Prosimi, R., Villarreal, P., Delgado-Barrio, G., Winter, G., González, B., Alemán, J., and Collado, C. (2011). Molecular dynamics simulations of rigid and flexible water models: Temperature dependence of viscosity. *Chemical Physics*, 388(1-3):9–18.
- [61] Melchionna, S., Ciccotti, G., and Lee Holian, B. (1993). Hoover npt dynamics for systems varying in shape and size. *Molecular Physics*, 78(3):533–544.
- [62] Mialdun, A. and Shevtsova, V. (2008). Development of optical digital interferometry technique for measurement of thermodiffusion coefficients. *International Journal of Heat and Mass Transfer*, 51(11-12):3164–3178.
- [63] Mondal, S., Ghosh, S., and Chattaraj, P. (2013). A molecular dynamics study on si hydrogen hydrate. *Journal of molecular modeling*, 19(7):2785–2790.
- [64] Moulton, O. A., Tsimpanogiannis, I. N., Panagiotopoulos, A. Z., and Economou, I. G. (2014). Atomistic molecular dynamics simulations of co₂ diffusivity in h₂o for a wide range of temperatures and pressures. *The Journal of Physical Chemistry B*, 118(20):5532–5541.
- [65] Myshakin, E. M., Saidi, W. A., Romanov, V. N., Cygan, R. T., and Jordan, K. D. (2013). Molecular dynamics simulations of carbon dioxide intercalation in hydrated nantmorillonite. *The Journal of Physical Chemistry C*, 117(21):11028–11039.

- [66] NEA (2014). The safety case for deep geological disposal of radioactive waste: 2013 state of the art. *Symposium Proceedings 7–9 October 2013, Paris, France. Radioactive Waste Management Report NEA/RWM/R(2013)9, OECD/NEA, Paris, France.*
- [67] Ngouana W, B. F. and Kalinichev, A. G. (2014). Structural arrangements of isomorphic substitutions in smectites: Molecular simulation of the swelling properties, interlayer structure, and dynamics of hydrated cs–montmorillonite revisited with new clay models. *The Journal of Physical Chemistry C*, 118(24):12758–12773.
- [68] Ning, F. L., Glavatskiy, K., Ji, Z., Kjelstrup, S., and H. Vlugt, T. J. (2015). Compressibility, thermal expansion coefficient and heat capacity of ch₄ and co₂ hydrate mixtures using molecular dynamics simulations. *Phys. Chem. Chem. Phys.*, 17:2869–2883.
- [69] Nosé, S. (1984a). A molecular dynamics method for simulations in the canonical ensemble. *Molecular physics*, 52(2):255–268.
- [70] Nosé, S. (1984b). A unified formulation of the constant temperature molecular dynamics methods. *The Journal of chemical physics*, 81(1):511–519.
- [71] Ortiz, L., Volckaert, G., and Mallants, D. (2002). Gas generation and migration in boom clay, a potential host rock formation for nuclear waste storage. *Engineering geology*, 64(2-3):287–296.
- [72] Ou, X., Li, J., and Lin, Z. (2014). Dynamic behavior of interfacial water on mg (oh) 2 (001) surface: a molecular dynamics simulation work. *The Journal of Physical Chemistry C*, 118(51):29887–29895.
- [73] Park, S.-H. and Sposito, G. (2003). Do montmorillonite surfaces promote methane hydrate formation? monte carlo and molecular dynamics simulations. *The Journal of Physical Chemistry B*, 107(10):2281–2290.
- [74] Plimpton, S. (1995). Fast parallel algorithms for short-range molecular dynamics. *Journal of computational physics*, 117(1):1–19.
- [75] Rebour, V., Billiotte, J., Deveughele, M., Jambon, A., and Le Guen, C. (1997). Molecular diffusion in water-saturated rocks: A new experimental method. *Journal of contaminant hydrology*, 28(1-2):71–93.
- [76] Reitenbach, V., Ganzer, L., Albrecht, D., and Hagemann, B. (2015). Influence of added hydrogen on underground gas storage: a review of key issues. *Environmental Earth Sciences*, 73(11):6927–6937.
- [77] Rosanne, R., Paszkuta, M., Tevissen, E., and Adler, P. (2003). Thermodiffusion in compact clays. *Journal of Colloid and Interface Science*, 267(1):194–203.
- [78] Rübel, A. P., Sonntag, C., Lippmann, J., Pearson, F., and Gautschi, A. (2002). Solute transport in formations of very low permeability: Profiles of stable isotope and dissolved noble gas contents of pore water in the opalinus clay, mont terri, switzerland. *Geochimica et Cosmochimica Acta*, 66(8):1311–1321.

- [79] Ryckaert, J.-P., Ciccotti, G., and Berendsen, H. J. (1977). Numerical integration of the cartesian equations of motion of a system with constraints: molecular dynamics of n-alkanes. *Journal of computational physics*, 23(3):327–341.
- [80] Sabo, D., Rempe, S., Greathouse, J., and Martin, M. (2006). Molecular studies of the structural properties of hydrogen gas in bulk water. *Molecular Simulation*, 32(3-4):269–278.
- [81] Samsatli, S. and Samsatli, N. J. (2019). The role of renewable hydrogen and inter-seasonal storage in decarbonising heat—comprehensive optimisation of future renewable energy value chains. *Applied Energy*, 233:854–893.
- [82] Sánchez, F. G., Gimmi, T., Jurányi, F., Loon, L. V., and Diamond, L. W. (2009). Linking the diffusion of water in compacted clays at two different time scales: Tracer through-diffusion and quasielastic neutron scattering. *Environmental science & technology*, 43(10):3487–3493.
- [83] Sengers, J. and Watson, J. T. R. (1986). Improved international formulations for the viscosity and thermal conductivity of water substance. *Journal of physical and chemical reference data*, 15(4):1291–1314.
- [84] Simonnin, P., Noetinger, B., Nieto-Draghi, C., Marry, V., and Rotenberg, B. (2017). Diffusion under confinement: Hydrodynamic finite-size effects in simulation. *Journal of Chemical Theory and Computation*, 13(6):2881–2889.
- [85] Small, J. S., Nykyri, M., Vikman, M., Itävaara, M., and Heikinheimo, L. (2017). The biogeochemistry of gas generation from low-level nuclear waste: Modelling after 18 years study under in situ conditions. *Applied Geochemistry*, 84:360–372.
- [86] Smirnov, G. S. and Stegailov, V. V. (2013). Toward determination of the new hydrogen hydrate clathrate structures. *The Journal of Physical Chemistry Letters*, 4(21):3560–3564.
- [87] Smith, D. E. and Dang, L. X. (1994). Computer simulations of nacl association in polarizable water. *The Journal of Chemical Physics*, 100(5):3757–3766.
- [88] Song, J. and Zhang, D. (2013). Comprehensive review of caprock-sealing mechanisms for geologic carbon sequestration. *Environmental science & technology*, 47(1):9–22.
- [89] Sposito, G. et al. (1984). *The surface chemistry of soils*. Oxford university press.
- [90] Sposito, G., Skipper, N. T., Sutton, R., Park, S.-h., Soper, A. K., and Greathouse, J. A. (1999). Surface geochemistry of the clay minerals. *Proceedings of the National Academy of Sciences*, 96(7):3358–3364.
- [91] Szczerba, M., Kalinichev, A. G., and Kowalik, M. (2020). Intrinsic hydrophobicity of smectite basal surfaces quantitatively probed by molecular dynamics simulations. *Applied Clay Science*, 188:105497.
- [92] Tarkowski, R. (2019). Underground hydrogen storage: Characteristics and prospects. *Renewable and Sustainable Energy Reviews*, 105:86–94.

- [93] Torgersen, T., Kennedy, B., and van Soest, M. (2004). Diffusive separation of noble gases and noble gas abundance patterns in sedimentary rocks. *Earth and Planetary Science Letters*, 226(3-4):477–489.
- [94] Tse, J. S., Klein, M. L., and McDonald, I. R. (1984). Computer simulation studies of the structure i clathrate hydrates of methane, tetrafluoromethane, cyclopropane, and ethylene oxide. *The Journal of chemical physics*, 81(12):6146–6153.
- [95] Tsimpanogiannis, I. N., Moulton, O. A., Franco, L. F., Spera, M. B. d. M., Erdős, M., and Economou, I. G. (2019). Self-diffusion coefficient of bulk and confined water: a critical review of classical molecular simulation studies. *Molecular Simulation*, 45(4-5):425–453.
- [96] Van Loon, L., Mueller, W., Gimmi, T., and Iijima, K. (2002). Activation energy of the self-diffusion of water in compacted clay systems: a case study with opalinus clay.
- [97] Vasconcelos, I. F., Bunker, B. A., and Cygan, R. T. (2007). Molecular dynamics modeling of ion adsorption to the basal surfaces of kaolinite. *The Journal of Physical Chemistry C*, 111(18):6753–6762.
- [98] Vinsot, A., Appelo, C. A. J., Lundy, M., Wechner, S., Cailteau-Fischbach, C., de Donato, P., Pironon, J., Lettry, Y., Lerouge, C., and De Canniere, P. (2018). Natural gas extraction and artificial gas injection experiments in opalinus clay, mont terri rock laboratory (switzerland). In *Mont Terri Rock Laboratory, 20 Years*, pages 377–392. Springer.
- [99] Wang, J., Kalinichev, A. G., and Kirkpatrick, R. J. (2006). Effects of substrate structure and composition on the structure, dynamics, and energetics of water at mineral surfaces: A molecular dynamics modeling study. *Geochimica et cosmochimica acta*, 70(3):562–582.
- [100] Wang, S., Feng, Q., Zha, M., Javadpour, F., and Hu, Q. (2018). Supercritical methane diffusion in shale nanopores: effects of pressure, mineral types, and moisture content. *Energy & fuels*, 32(1):169–180.
- [101] Wang, S., Javadpour, F., and Feng, Q. (2016a). Fast mass transport of oil and supercritical carbon dioxide through organic nanopores in shale. *Fuel*, 181:741–758.
- [102] Wang, S., Javadpour, F., and Feng, Q. (2016b). Molecular dynamics simulations of oil transport through inorganic nanopores in shale. *Fuel*, 171:74–86.
- [103] Wanner, P. and Hunkeler, D. (2019). Molecular dynamic simulations of carbon and chlorine isotopologue fractionation of chlorohydrocarbons during diffusion in liquid water. *Environmental Science & Technology Letters*, 6(11):681–685.
- [104] Wasserman, E., Wood, B., and Brodhol, J. (1995). The static dielectric constant of water at pressures up to 20 kbar and temperatures to 1273 k: experiment, simulations, and empirical equations. *Geochimica et cosmochimica acta*, 59(1):1–6.
- [105] Wilhelm, E., Battino, R., and Wilcock, R. J. (1977). Low-pressure solubility of gases in liquid water. *Chemical reviews*, 77(2):219–262.

- [106] Xu, T., Senger, R., and Finsterle, S. (2008). Corrosion-induced gas generation in a nuclear waste repository: Reactive geochemistry and multiphase flow effects. *Applied Geochemistry*, 23(12):3423–3433.
- [107] Yeh, I.-C. and Hummer, G. (2004). System-size dependence of diffusion coefficients and viscosities from molecular dynamics simulations with periodic boundary conditions. *The Journal of Physical Chemistry B*, 108(40):15873–15879.
- [108] Yu, L. and Weetjens, E. (2009). Summary of gas generation and migration. *Current State-of-the-Art. SCK-CEN ER-106. SCK+CEN, Mol, Belgium*.
- [109] Yuan, W., Pan, Z., Li, X., Yang, Y., Zhao, C., Connell, L. D., Li, S., and He, J. (2014). Experimental study and modelling of methane adsorption and diffusion in shale. *Fuel*, 117:509–519.
- [110] Zhang, M., Chakraborty, N., Karpyn, Z. T., Emami-Meybodi, H., and Ayala, L. F. (2021). Experimental and numerical study of gas diffusion and sorption kinetics in ultratight rocks. *Fuel*, 286:119300.
- [111] Zhou, J., Lu, X., and Boek, E. S. (2016). Confined water in tunnel nanopores of sepiolite: Insights from molecular simulations. *American Mineralogist*, 101(3):713–718.
- [112] Zhu, H.-L., Wang, S.-F., Yin, G.-J., Chen, Q., Xu, F.-L., Peng, W., Tan, Y.-H., and Zhang, K. (2018). Study of the numerical simulation of tight sandstone gas molecular diffusion based on digital core technology. *Petroleum Science*, 15(1):68–76.

Chapter 3: Diffusion and Gas Flow Dynamics in Partially Saturated Smectites

(published in *Journal of Physical Chemistry C*, 127, 29, 14425–14438 (2023); available at: <https://doi.org/10.1021/acs.jpcc.3c02264>)

Diffusion and Gas Flow Dynamics in Partially Saturated Smectites [†]

Jerry P. Owusu,^{*,‡,¶} Konstantinos Karalis,[¶] Nikolaos I. Prasianakis,[‡] and Sergey
V. Churakov^{*,‡}

[‡]*Laboratory for Waste Management, Paul Scherrer Institute, 5232 Villigen-PSI,
Switzerland*

[¶]*University of Bern, Institute of Geological Sciences, 3012 Bern, Switzerland*

Abstract

Clays and clay rocks are considered good natural and engineered barriers for deep geological disposal of nuclear waste worldwide. Metal corrosion and organic waste degradation in underground repositories generate significant amounts of gas that should be able to migrate through the multi-barrier system to avoid potential pressure build-up, which could be compromising the integrity of the barriers and host rocks. The gas is expected to accumulate in larger pores and eventually form an interconnected network. Under such conditions, the migration of gas molecules takes place both in pore water films and in gas-filled macropores. Therefore mass fluxes depend on the distribution of gas molecules between the water-rich and gas-rich phases, and their mobility in both compartments. Classical molecular dynamics simulations (MD) were employed to investigate the mobility of He, H₂, CO₂, Ar, and CH₄ in a Na-montmorillonite mesopore as a function of the degree of saturation, as well as evaluate the hydrodynamic behavior of the pore fluid in partially saturated clays. The diffusivity of the gas molecules was determined by observing the asymptotic behavior of the mean square displacement in the gas-rich phase and at the gas-water interface. The partition coefficient and Gibbs free energy were analyzed to investigate the transfer of gas molecules between the gas-rich and water-rich phases by observing the molecular trajectories as they cross the vapor-liquid interface. The results revealed that the diffusion coefficient in the gas phase increased with increasing gas-filled pore width and converged asymptotically towards the diffusion coefficient in the bulk state. It could be shown, that the diffusion coefficient of gas molecules dissolved in the water films remained constant as long as the interacting water surface was in the bulk liquid-like phase. This behavior changes in very thin water films. It was observed that the partitioning coefficient of gas molecules at the solid-liquid interface is nearly the same as that in the bulk-liquid-like phase. Partitioning is observed to be strongly dependent on the temperature and gas molecular weights. In the second part of the study, non-equilibrium molecular dynamics (NEMD) simulations were performed to investigate the mobility of gases in pressure driven Decoupled Gas Phase Dynamics (DGPD) and Coupled Gas and Water Phase Dynamics (CGWPD) in a partially saturated Na-montmorillonite slit mesopore. The dynamic viscosity of the gas phase was calculated from the NEMD simulations and indicated that the viscosity of the gas phase was almost the same in both methods (DGPD and CGWPD). The average slip length for gas molecules at the gas-water interface was also calculated, revealing that the slip-free boundary condition assumed in continuum models was generally invalid for microfluidics and that a slip boundary condition exists at the microscale for certain surface interactions.

Finally, a Bosanquet-type equation was developed to predict the diffusion coefficient and dynamic viscosity of gas as a function of the average pore width, gas mean-free path, geometric factor, and thickness of the adsorbed water film.

3.1 Introduction

In several countries, clay rocks are considered potential host rocks for the geological disposal of radioactive waste. Clay materials are also considered as backfill material and as buffer material due to their low permeability and the adsorption capacity of their charged surfaces [34, 47, 60, 64, 66, 83]. Gases generated in the repository due to corrosion and biodegradation processes should be able to migrate through the multi-barrier system so as not to compromise the integrity of the barrier [24, 78, 82]. Therefore, understanding the mechanism of gas transport from such a system is necessary to ensure the safety of the repository.

Advective transport in low permeability clay rock is negligible under the natural hydraulic conditions in fully saturated rocks [9, 34, 75]. Therefore, molecular diffusion is expected to be the predominant gas transport mechanism through the multi-barrier system. The low-permeability clay materials are expected to undergo a de-saturation and a re-saturation phase caused by repository ventilation, thermally induced effects of the repository, or gas production [5, 33]. Unconnected pores thus facilitate the diffusion mechanism at different degrees of saturation. [20, 32].

Several studies addressed the diffusion of water and tracers in clays in laboratory experiments [4, 12, 35, 49, 58, 61, 71, 106]. Very challenging gas transport experiments have also been conducted in the laboratory and in the field [8, 10, 42, 43, 52, 80, 84, 100]. Gas diffusion experiments were supported and proved by numerical and molecular multiscale simulations to gain a deeper understanding of the diffusion mechanism under variable conditions [21, 22, 31, 39, 45, 48, 63, 95, 98, 112]. Most of these studies were investigated under the two limiting conditions; (a) fully saturated and (b) fully dry clay conditions. In a typical repository, gas transport would take place under saturated and partially saturated conditions. It is therefore necessary to understand the mechanism of gas migration in clays under partially saturated conditions. Furthermore, the viscosity of gas in a macropore is expected to depend on the degree of saturation and the properties of the gas molecules. Gas diffusivity under saturated conditions was addressed in our earlier study [74]. Here, the earlier simulation approach is extended to partially saturated conditions.

Due to the hydrophilic nature of smectite clays in particular, a water film is adsorbed on the outer surface of the clay particles during the desaturation of the mesopores. The thickness of the water film depends on the water potential, which is related to the relative humidity of the vapor phase [32]. Studies have shown that this water film, also called electrical double layer (EDL), is the main transport pathway for ions [20, 56].

In an unsaturated clay medium, the diffusion of gas in a pore can undergo two main diffusion regimes; (a) diffusion in the gas-rich phase and (b) diffusion in the liquid-rich phase. Diffusion

of He, CH₄, Ar, CO₂, N₂ was measured in saturated clays using field experiments and laboratory studies. [10, 42, 43, 80, 100]. It was shown that the diffusion of gases in saturated systems depends on the size of the gas molecules and the geometric factor [42, 43]. Gadikota et al. [31] performed molecular dynamics simulations of the diffusion and distribution of noble gases in the interlayer of saturated Na-montmorillonite. The results confirmed the experimental observations that diffusion in clays is slower than in bulk water and that the diffusion and partition coefficients of gases depend on the type and size of the diffusion gas molecule. The partitioning of gases is crucial for understanding the retardation and retention of gases during transport, and its influence on the rate and extent of gas movement [13].

In general, the rate of diffusion is significantly higher in the gas phase compared to the liquid phase. To illustrate this, let's consider the self-diffusion coefficient of helium (He) at standard conditions, which is $7.1 \times 10^{-5} \text{ m}^2/\text{s}$, whereas the diffusion coefficient in water is $7.2 \times 10^{-9} \text{ m}^2/\text{s}$ [27, 44]. Moreover, when it comes to diffusion in clays, partially saturated clays are expected to exhibit higher diffusion rates than fully saturated ones. A study by Mohammed et al. [70] demonstrated that the diffusion coefficients of CO₂ and CH₄ confined in partially saturated calcite pores were respectively one and two orders of magnitude higher compared to the diffusion rates in saturated calcite pores. A number of studies have been carried out to investigate gas diffusion at partially saturated conditions, ranging from very loose soil material to highly compacted clay material [7, 17, 51, 69, 87, 107]. Recently, Wesenauer et al. [107] experimentally investigated the gas phase diffusion and permeability of O₂, CO₂, and N₂ at different pretreatment temperatures (298.15 - 1173.15 K) in a dry porous clay sample, in a diffusion chamber. They derived the diffusive transport properties using a pore-scale transport model. Based on the observation of a strong increase in gas diffusivity of CO₂ compared to O₂, they suggested that solid-gas interfacial diffusion should be considered to fully understand the diffusion mechanism. The pore-scale transport model was extended to account for interfacial diffusion.

Macroscopic diffusion phenomena are usually described by Fick's diffusion law [29]. The first Fick's law relates the diffusion flux to the concentration gradient, and the second law predicts the influence of diffusion on the time variation of the concentration. The first and second of Fick's laws in 1-dimension can be written mathematically as follows:

$$J = -D \frac{dC}{dx} \quad (3.1)$$

$$\frac{\partial C}{\partial t} = D \frac{\partial^2 C}{\partial x^2} \quad (3.2)$$

where J is the diffusion flux in $\text{mol}/\text{m}^2/\text{s}$, D is the diffusion coefficient in m^2/s , x is the position in the dimension of length (m), C is the concentration in the dimension of amount of substance per unit volume (mol/m^3) and t is the time (s).

Fick's law is a widely used fundamental law for the diffusion of gases where the concentration, pressure, and temperature gradients lead to a net mass flux. Fick's equations are used in most macroscopic numerical simulations and diffusion models [2, 25, 28, 41, 99, 104, 105]. However,

Fick's law has some limitations that make it inapplicable in certain systems [96]. In addition, Fick's law is inadequate when dealing with stagnant gases or very slowly diffusing gases, for example, Ar and N₂ [96]. According to Thorstenson et al. [96] an accurate understanding of gas transport in fine-grained porous media must include the possible contribution of Knudsen diffusion, molecular and non-equimolar components of diffusive flux, and viscous (pressure-driven) flux.

Over the years, molecular dynamics simulations have been used to study the transport of fluids in clays [3, 20, 30, 31, 94, 102, 103, 111]. It is a powerful tool to understand the diffusion mechanism of gas molecules in nanopores as well as the interactions between the fluid of interest and its environment and how these affect the diffusion behavior. These insights are not easily obtained through experimental studies and macroscopic numerical modeling. Apostolopoulou et al. [3] used molecular dynamics simulations to investigate the transport properties of methane in dry, nano-confined slit pores as a function of pore width. The methane fluid structure and diffusion coefficient within 5 nm wide pores were quantified in different pore regions and the results were scaled up using a kinetic Monte Carlo model to predict diffusion in mesopores [3]. Similarly, Sui et al. [94] used Grand Canonical Monte Carlo and molecular dynamics methods to study the adsorption and diffusion of shale gas in a dry and wet Na-montmorillonite nanopore at different temperatures and pore sizes. It was found that short-range dispersive interactions affect CH₄ sorption on clay walls and that CH₄ diffusion increases with increasing pore size [94]. In addition, it was found that pre-loading the pore area with water reduces the sorption of CH₄ in clay, as CH₄ is hydrophobic and therefore does not mix with water molecules [94]. Wang et al. [102] used molecular dynamics simulations to investigate the diffusion behavior of supercritical methane in shale nanopores as a function of pore size, pore pressure, and moisture content [102]. One of their findings was that moisture slows down methane diffusion, but this behavior is more pronounced in organic materials than in inorganic materials; which is due to the clustering and adsorption membrane effect of water in organic and inorganic pores, respectively [102]. The diffusion coefficient of each gas within a mixture can be significantly influenced by the varying compositions of the gases [46]. Through the use of molecular dynamics simulation, Kadoura et al. [46] investigated the structural and transport characteristics of CO₂, CH₄, and their mixture at a temperature of 298.15K. The study revealed that the self-diffusion coefficients of CH₄ experience a notable decrease when exposed to high loadings of CO₂, primarily due to steric hindrance effects.

Although much progress has been achieved in understanding the diffusion behavior of gas in a clay medium, there are still a number of unresolved issues. The first concerns the diffusion mechanism of different gas molecules, the influence of system composition, and interactions with the confinement. So far, most studies have focused on the diffusion of CH₄. The second challenge is that most studies have focused on either dry clays or fully saturated clays. Studies on partially saturated clays have mostly been conducted at the macroscopic scale, so the diffusion of gases at the molecular scale in partial saturation has not been fully understood. The third challenge is that unlike anions, where adsorbed water films become the transport pathway for diffusion in partially saturated systems [20], gas transport occurs simultaneously

in three domains: (1) diffusion in the gas phase, (2) diffusion in the adsorbed water phase and (3) gas diffusion in the transition zone at the gas-water interface.

To address these questions, molecular dynamics is applied here to study the diffusion of molecular gas (He, H₂, CO₂, Ar, CH₄) through partially saturated smectite clay. The influencing factors, e.g. gas type, temperature, and degree of saturation, are analyzed. The partition coefficient, which indicates the retention and retardation capacity of the gas transport, is also analyzed. The simulation is performed under natural conditions at a pressure of 12 MPa, which is typical of the confining pressure expected in the geological repository. Finally, non-equilibrium molecular dynamics is used to study the gas dynamics and hydrodynamics of gas and water molecules confined in partially saturated smectite. In particular, the dynamic viscosity and the behavior of the gas-water interface as a function of the degree of saturation is studied. The aim is to gain a comprehensive mechanistic understanding of the diffusion of gases in partially saturated smectite clays, as well as to demonstrate the ability of MD to complement experiments and macroscopic numerical modeling. The obtained results propose a mathematical model required for further investigation in an upscaling approach for the diffusion of gases in clay rocks through multiscale numerical modeling.

3.2 Methods

3.2.1 System setup

Molecular dynamics simulations (MD) were carried out to study the diffusion of different gas molecules in a clay slit pore as a function of temperature and degree of saturation (water to gas ratio in the system). Further analysis was applied to estimate fluid viscosity and the gas-liquid partition coefficients. The simulation setup is very similar to the one used by Churakov [20]. Briefly, the setup consists of a stack of two layers of Na-montmorillonite (tetrahedra-octahedra-tetrahedra sheets) arranged parallel to each other in the XY plane with a nanopore of 0.6 nm between them. An external mesopore of about 6 nm was introduced in which the gas-filled pore width as well as the composition of the gas phase could be varied. A snapshot of the simulation cell is shown in Figure 3.1. The solid phase composition is $2 \times 4 \text{ Na}_{0.5}[\text{Al}_{3.5}\text{Mg}_{0.5}]\text{Si}_8\text{O}_{20}(\text{OH})_4$. Isomorphous substitutions of Mg ions for Al ions in the octahedral sheet were randomly distributed to avoid Al-Al pairs in adjacent octahedra. These substitutions create a permanent structural charge on the clay layer, which is compensated by Na ions. A total of 24 isomorphous substitutions were included. To ensure an even distribution of charges in the system, 12 Na ions were placed in the center of the interlayer pore, while 6 Na ions were placed near either side of the mesopore.

3.2.2 Simulation details

Equilibrium molecular dynamics

Molecular dynamics simulations were performed using the open-source package LAMMPS [76]. The interatomic interaction potentials for clay atoms, water, and gas molecules are the

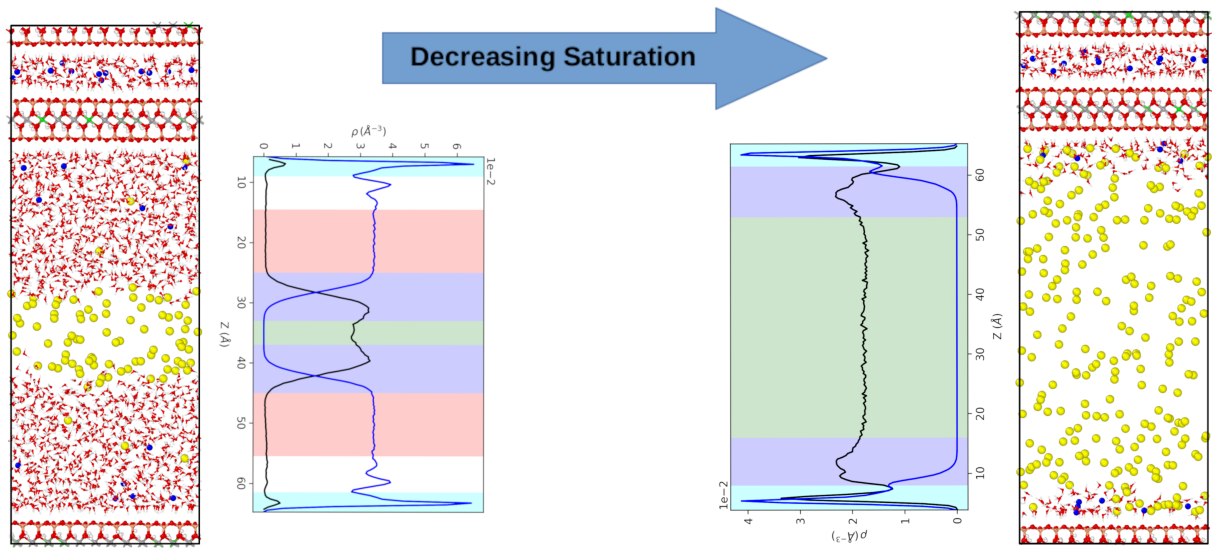


FIGURE 3.1: A snapshot from the MD simulation of a 6 nm Na-montmorillonite slit pore for two different degrees of saturation (gas-filled pore width of 1.8 and 5.3 nm; left and right respectively). Oxygen atoms are red. Hydrogen atoms forming H_2O molecules and OH groups are white. Silica atoms are pink. Aluminium atoms are grey. Magnesium atoms are green. Sodium atoms are blue. Gas molecules, represented by argon in this particular case are yellow. The graphs next to the snapshots show the density distribution of water and gases in the slit pore. The black curve is the density distribution of the gas molecules (magnified by a factor of 10 for the sake of visualization) and the blue is that of the water. The cyan area on the density plot shows the solid-liquid interface, the pink area shows the domains occupied by the bulk-liquid-like phase, the green area shows the central domain occupied by the gas phase and the blue area indicates the gas-water interface regions.

same as those used in our previous work, which also explains the model uncertainties [74].

The setup and the equilibration of the system take full account of the gas molecules partitioning between gas-rich and water-rich phases (solubility) by implementing an iterative equilibration process under imposed PVT constraints. For the sake of data comparison, all the simulations are conducted in the same d-spacing of 6 nm distance between the TOT layers. The gas-rich phase is confined between the two water-rich films wetting the TOT layers. To achieve the desired density (pressure) and enable gas molecules to dissolve (partition) from the gas phase into the water phase, we use an iterative NPT equilibration process. Initially water saturated system was equilibrated in the NPT ensemble at a temperature of 300 K and a pressure of 12 MPa. The final size of the simulation cell after equilibration was $31.17 \times 35.88 \times 83.72 \text{ \AA}^3$. Then a fraction of water molecules in the middle of the slit pore was removed from the center of the slit pore and replaced with gas phase according to a density estimate for the target P-T conditions (Figure 3.1). Subsequently, the system was iteratively equilibrated in the NPT ensemble under an external pressure of 12 MPa. This ensemble allows the system to relax and account for the interactions between the gas and the surrounding components. Additionally, it ensures the equilibrium partitioning of gas and water molecules between the water and gas-rich phases. Since the behavior of a gas under high pressure may deviate from the ideal gas

relation, the NPT ensemble is essential for achieving a more realistic representation. To ensure that the system maintained a structure equivalent to the saturated system (with an average pressure of 12 MPa and dimensions of $31.17 \times 35.88 \times 83.72$ Å), the system size and average pressure after equilibration were examined. If these parameters did not match the desired values, the number of gas molecules was adjusted accordingly, and the NPT simulation was repeated. This iterative process was carried out until the target mesopore size of approximately 6 nm and the equilibrium molar density of the gas phase were consistently maintained. The simulations were performed at two temperatures (300 and 330 K) for 8 saturation states and 5 gas species.

For each system, a 10 ns production run with a time step of 1 fs was performed in the NVT ensemble at temperatures of 300, and 330 K after equilibration. The temperature of 330 is close to in situ conditions in an underground repository. The Nosé-Hoover thermostat was applied to keep the temperature constant [72, 73]. The fully flexible force field was applied to the atoms of the clay particles, while the water molecules were kept rigid using the SHAKE algorithm [86]. Short-range interactions were calculated using the Lennard-Jones potentials with a cutoff of 12 Å. Long-range electrostatic interactions were calculated using the particle-particle particle-mesh method (PPPM) with a cutoff value of 12 Å. The final 8-ns trajectories were split into two blocks to obtain two independent replicates for further uncertainty analysis.

Diffusion coefficient

Due to the coexistence of two-phase fluid and its strong interaction with the surface of clay minerals, structurally distinct areas were identified in the simulated mesopore (Figure 3.1). These include 1) the mineral fluid interface with strong density fluctuations, 2) a bulk liquid-like water film, 3) a transition zone between water-rich and gas-rich regions, and 4) a low-density gas-rich phase. To accurately calculate the diffusion coefficient in the mesopore for gas molecules, the mesopore was divided into three regions: liquid phase, gas-rich phase, and water-gas interface. In this study, we focused only on diffusion in the gas phase and the water-gas interface. Diffusion in the liquid phase was investigated in our previous study on the mobility of gas molecules in saturated smectites [74]. To obtain the diffusion coefficient in different regions, we adopted the MD-calculated survival probability and the mean square displacement method of Liu et al. [59]. In this study, only the x and y components of the diffusion tensor, describing the two-dimensional diffusion parallel to the gas-water interface were analyzed. Assuming a layer parallel to the basal surface of the clay particle with intervals in the z-dimension defined as {a,b}, the diffusion coefficient of particles located in the region of the interval {a,b} in one dimension is given as follows:

$$D_{xx}(\{a, b\}) = \lim_{t \rightarrow \infty} \frac{\langle \Delta x(\tau)^2 \rangle_{\{a,b\}}}{2\tau P(\tau)} \quad (3.3)$$

and

$$\langle \Delta x(\tau)^2 \rangle_{\{a,b\}} = \frac{1}{T} \sum_{t=1}^T \frac{1}{N(t)} \sum_{i \in S(t,t+\tau)} (x_i(t+\tau) - x_i(t))^2 \quad (3.4)$$

and

$$P(\tau) = \frac{1}{T} \sum_{t=1}^T \frac{N(t, t + \tau)}{N(t)} \quad (3.5)$$

where $\langle \Delta x(\tau)^2 \rangle_{\{a,b\}}$ is the mean square displacement of the atoms in the region {a,b}, $P(\tau)$ is the survival probability, T is the total number of time steps, over which is averaged, $N(t)$ denotes the number of particles in the region at time t , $N(t, t + \tau)$ is the set of all particles remaining in the region {a,b} during the time interval between t and $t + \tau$.

Partition Coefficient and Gibbs free energy of molecule transfer

The equilibrium partitioning of water and gas molecules between co-existing water-rich and gas-rich phases could be determined by molecular dynamics simulations. At equilibrium, the partition coefficient K of the gas molecules in the liquid phase is calculated from the ratio of the number densities of gas molecules in the liquid phase ($\rho_{gas\ in\ water-phase}$) and gas phase ($\rho_{gas\ in\ gas-phase}$), normalized to the number density of water molecules ($\rho_{water\ in\ water-phase}$) and ($\rho_{water\ in\ gas-phase}$) in each phase respectively:

$$K = \left(\frac{\langle \rho_{gas\ in\ water-phase} \rangle}{\langle \rho_{gas\ in\ gas-phase} \rangle} \frac{\langle \rho_{water\ in\ gas-phase} \rangle}{\langle \rho_{water\ in\ water-phase} \rangle} \right)_{eq} \quad (3.6)$$

From the partition coefficient K , the Gibbs free energy difference associated with the transfer of a gas molecule from the gas phase to the liquid phase [65, 108] can be calculated directly as:

$$\Delta G_{gas \rightarrow water} = -RT \ln K \quad (3.7)$$

where R and T are the molar gas constant ($8.3145\ \text{J mol}^{-1}\ \text{K}^{-1}$) and the absolute temperature, respectively.

Non-Equilibrium molecular dynamics

To evaluate the effects of viscous stresses in the system and their correlation with diffusion, partial saturation, and gas type, non-equilibrium molecular dynamics was used to study the hydrodynamic properties of the confined fluid. In equilibrium molecular dynamics, the macroscopic impulse of the simulation cell and its angular moment is set and maintained at zero. In non-equilibrium molecular dynamics, a constant external force is applied to the particles in a specific direction. This corresponds to the introduction of a uniform pressure gradient along the given direction in the system, resulting in a flow of particles. In this study, two simulation approaches were used to analyze the dynamics of gas: (a) a constant force acting only on the gas molecules in the gas phase (Decoupled Gas Phase Dynamics), and (b) a constant force acting on all fluid particles (Coupled Gas and Water Phase Dynamics). To drive the flow, a constant external force of 5.0×10^{-3} kcal/mol in the x -direction, parallel to the surface, was applied to each fluid atom. This force is low enough to maintain the linear response conditions between applied stress and fluid velocity. A temperature of 300 K was set with the Nosé-Hoover thermostat and this thermostat was coupled only to the degrees of freedom of the fluid in the

y-direction, which is along the surface and perpendicular to the fluid flow. The clay particles were kept rigid throughout the simulation. The velocities of the fluid were recorded every 1 ps for 6 ns in bins along the z-direction (pore width) with a bin width of 0.1 Å, after a 2 ns equilibration.

At a steady state, the velocity distribution of a pressure-driven flow (F_x) in a pore channel can be described by the Poiseuille flow. The Poiseuille flow leads to a parabolic velocity profile that can be described by the Stokes equation for the velocity component in the x direction as a function of the distance from the middle of the slit pore (h):

$$v_{x(h)} = \frac{\rho F_x L_h^2}{2\mu} \left[\frac{1}{4} - \left(h - \frac{1}{2} \right)^2 \right] \quad (3.8)$$

The dynamic viscosity of the fluid, assuming constant viscosity and density in the pore can be computed from the velocity profile as:

$$\mu = - \frac{\rho F_x}{\left(\frac{d^2 v_{x(h)}}{dh^2} \right)} \quad (3.9)$$

where $v_{x(h)}$ is velocity along the slit pore width (h), F_x is the applied external force, ρ is the number density, μ is the dynamic viscosity and L_h is the total slit pore length.

3.3 Results and Discussion

3.3.1 Self-diffusion of gas molecules

The self-diffusion coefficients of gas molecules were first studied by simulating a system of 1000 gas molecules at temperatures of 300 K and 330 K and a pressure of 12 MPa for each type of gas. The system was equilibrated in the NVE ensemble for 200 ps. A further equilibration of 1 ns was performed in the NPT ensemble. This was followed by a production run of 5 ns in the NVT ensemble to calculate the self-diffusion coefficients. Table 3.1 shows the values of the self-diffusion coefficients of gas molecules from the MD predictions.

TABLE 3.1: Predicted self-diffusion coefficients of gas molecules D ($10^{-6} m^2/s$) at 12 MPa

	H ₂	He	CH ₄	Ar	CO ₂
T [K]					
300	1.470	1.257	0.164	0.134	0.040
330	1.511	1.486	0.217	0.161	0.069

To verify and validate the model parameters and the values of the self-diffusion coefficients, the results of the MD simulations were compared with experimental data [16, 36, 81, 109] and also evaluated using an empirical procedure [55, 89, 93]. Both data sets agree very well with the empirical relationships. Calculations from the kinetic theory of gases have been used in

the past to estimate the diffusion coefficient, viscosity, and thermal conductivity of dilute gases using their intermolecular forces [40]. This approach was extended by Slattery et al. [89] by developing a relation from dimensional analysis considerations and experimental diffusivities using Enskog's kinetic theory for dense gases. Their formulation can predict the self-diffusion coefficients of dense non-polar gases. Based on the work of Slattery and Bird. [89], Stiel et al. [93] developed a comprehensive relation for calculating the self-diffusion coefficient of polar, non-polar, and binary gas mixtures for dense gases.

In this study, the density of gas molecules at equilibrium was used to predict the self-diffusion coefficients using the empirical formulation of Stiel et al. [93] (Eq 3.10 and Eq 3.11) and Slattery et al. [89] (Eq 3.12). Equation 3.10 and Eq 3.11 apply to Ar, H₂, CO₂, and CH₄ gas, while Eq 3.12 applies to He gas:

$$(\rho D)\zeta = 0.464 \times 10^{-5} [1.391 T_R - 0.381]^{2/3} \text{ for } T_R < 1.5 \quad (3.10)$$

and

$$(\rho D)\zeta = 0.488 \times 10^{-5} T_R^{0.777} \text{ for } T_R \geq 1.5 \quad (3.11)$$

and

$$(pD) \frac{M^{1/2}}{P_c^{2/3} T_c^{5/6}} = 3.882 \times 10^{-4} T_R^{1.823} \quad (3.12)$$

where ρ is the gas density, D is the diffusion coefficient, $\zeta = T_c^{1/6} / M^{1/2} P_c^{2/3}$, p is system pressure, T_c is critical temperature of gas, P_c is critical pressure of gas, M is the molecular weight and T_r is the reduced temperature (T/T_c).

Figure 3.2 shows a plot of the self-diffusion coefficients of gas molecules as a function of gas density from MD predictions. The graph also shows the values calculated from the empirical procedure and experiments. From Figure 3.2 it can be seen that the self-diffusion coefficient of gas molecules is inversely proportional to the gas density. The fitting line in Figure 3.2 represents a fitting of the diffusion coefficients at low densities using the Chapman-Enskog theory described by Chapman and Cowling [15].

3.3.2 Gas partitioning

The distribution of the gas molecules in the water-rich phase was determined from the density profiles (Figure S2-S11) of the gas in the water-rich phase. The partition coefficient (K) and the free energy difference (ΔG) associated with the transfer of the gas molecules into the water-rich phase are obtained from eq 3.6 and eq 3.7 respectively. Figure 3.3 illustrates the density distribution of water on the external surface of the clay as a function of gas-filled pore width. At a smaller gas-filled pore width, the density profile shows three highly structured layers of water at distances of 0.3, 0.6, and 0.9 nm from the surface of the clay. This behavior is typical of what can be expected under fully saturated conditions [20, 74]. Further away from the surface > 1.0 nm, the density distribution is constant and the water shows a bulk-like behavior.

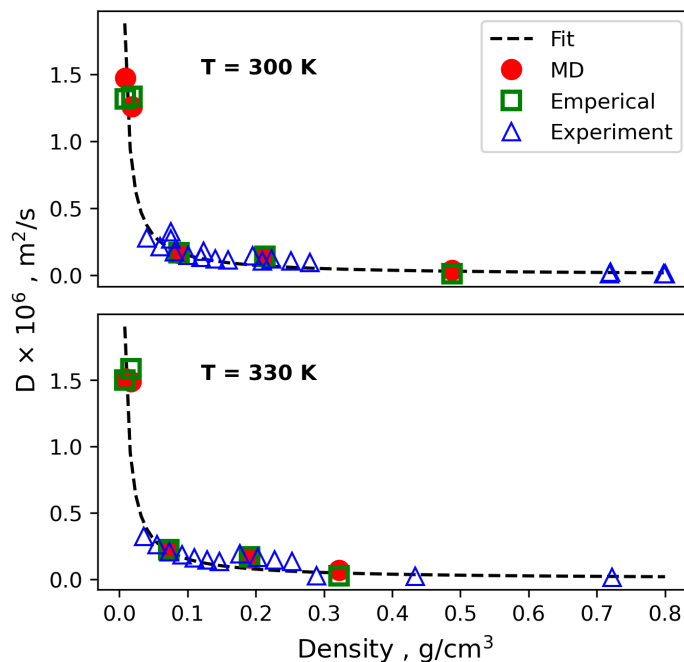


FIGURE 3.2: Predicted self-diffusion coefficients for gas molecules as a function of equilibrium gas density at 12 MPa from MD simulations. The graph includes experimental values [16, 36, 81, 109] as well as predictions based on empirical relations. The fitting line shows diffusion coefficients predicted using the Chapman-Enskog theory, described by Chapman and Cowling [15].

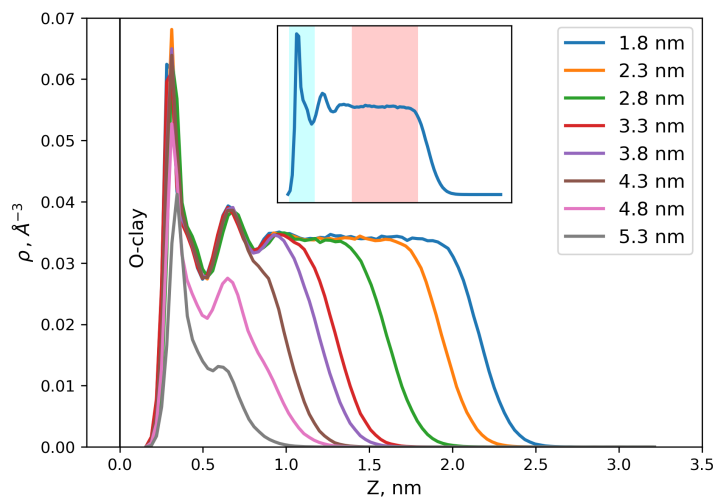


FIGURE 3.3: Density distribution of water on the external surface of the clay (half pore width). (insert) The cyan-colored area on the density plot shows the solid interface characterized by strong structuring of fluid. This domain is used for the analysis of gas partitioning to the solid-liquid interface. The pink-colored area shows the domain occupied by the bulk-liquid-like phase.

Taking into account the structuring of the liquid near the clay surface, the partition coefficients and Gibbs free energy of gas transfer were determined for two regions: (a) the partitioning of gas molecules to the solid-liquid interface and (b) the partitioning to the bulk-like water-rich region. These regions are indicated in Figure 3.3 by the colors cyan and pink respectively (insert).

The values of gas molecules at the solid-liquid interface (K_I , ΔG_I) and in the bulk-like water region (K_B , ΔG_B) are given in Table 3.2. For a wide range of saturation, the K and ΔG values are essentially constant within the statistical uncertainties of the simulation. Therefore, the results in Table 3.2 represent averaged values over several simulations with different gas-filled pore widths. It is important to note that, in the context of partitioning in the bulk-like water region, our averaging calculations were limited to a range of gas-filled pore widths between 1.8 and 3.3 nm. This restriction was implemented as the region in question is no longer present beyond a gas-filled pore width of 3.3 nm. Similarly, for partitioning at the solid-liquid interface, our results were limited to a range of gas-filled pore widths between 1.8 and 4.3 nm. This was done in accordance with our trajectory analysis, which indicated that for gas-filled pore widths exceeding 4.3 nm (in the case of thin water films), the water molecules tend to cluster around the Na ions, resulting in discontinuous coverage of the clay surface by the water film. As a consequence, gas-filled domains make direct contact with the clay surface.

The results indicate that K_B and K_I increase as the temperature is raised. Moreover, the particle density of the gas molecules was found to impact gas partitioning. CO_2 and Ar, which have molecular masses of 44 and 39.95 g/mol, respectively, exhibit significantly higher partitioning coefficients than He, H_2 , and CH_4 . Interestingly, despite He having a smaller molecular mass than CH_4 , its small molecular size allows for easier penetration into the interstitial spaces between water molecules, resulting in greater partitioning. Prior research has demonstrated a direct relationship between partition coefficient and molecular weight [88, 90], as well as polarizability [19, 57, 79, 92].

TABLE 3.2: Partitioning coefficients K (10^{-7}) and Gibbs free energy of transfer G (kJ mol^{-1}) of gas molecules at the solid-liquid interface and at the bulk-like water region

	H_2	He	CH_4	Ar	CO_2
T [K]					
300					
K_B	0.97 ± 0.46	2.45 ± 1.30	1.51 ± 0.82	7.90 ± 1.49	138.97 ± 26.29
K_I	1.22 ± 0.58	2.56 ± 1.02	1.34 ± 0.66	7.26 ± 2.80	142.14 ± 21.72
G_B	40.64 ± 1.46	38.29 ± 1.23	39.52 ± 1.24	35.09 ± 0.48	27.94 ± 0.50
G_I	40.07 ± 1.45	38.06 ± 1.00	39.68 ± 0.99	35.53 ± 1.29	27.87 ± 0.41
330					
K_B	10.94 ± 3.95	20.06 ± 4.44	10.05 ± 4.32	53.02 ± 7.21	389.24 ± 58.56
K_I	9.15 ± 3.80	20.12 ± 3.46	9.83 ± 5.24	49.03 ± 7.46	392.30 ± 78.15
G_B	37.84 ± 1.00	36.07 ± 0.64	38.16 ± 1.21	33.35 ± 0.36	27.89 ± 0.41
G_I	38.35 ± 0.97	36.03 ± 0.50	38.44 ± 1.73	33.57 ± 0.39	27.89 ± 0.55

3.3.3 Effect of saturation on the diffusion of gases

The self-diffusion coefficient of gas molecules in the gas phase at temperatures of 300 K and 330 K as a function of the gas-filled pore width, normalized to the diffusion coefficient in the bulk (D_0), is shown in Figure 3.4. It should be noted that gas-filled pore widths below 1.8 nm were excluded from this study because a larger quantity of gas molecules was required to keep the

pore space open for gas-phase diffusion. This behavior is likely due to dispersive interactions between opposing water platelets that result in a net attractive force between closely spaced platelets. As the gas-phase pore size increases, this effect diminishes.

The results show that the diffusion coefficient increase with pore size and asymptotically converges towards the value in the bulk state. It was originally believed that a constant value (D_0) over a wide range of pore widths would be obtained by using the survival probability method to calculate the diffusion coefficient associated exclusively with the gas phase in the bulk and that this would eliminate the effects of confinement. However, the opposite was found. The results showed that He gas specifically, was strongly affected by confinement compared to other gases; possibly due to the Knudsen effect. To investigate this, the mean free path of the gas molecules was calculated based on the collisions in the trajectories of the molecular dynamics simulations, and compared with the calculations of the mean free path performed with kinetic theory, which agreed well. Table 3.3 shows the values for the mean free path from molecular dynamics calculations and from kinetic theory for temperatures of 300 and 330 K.

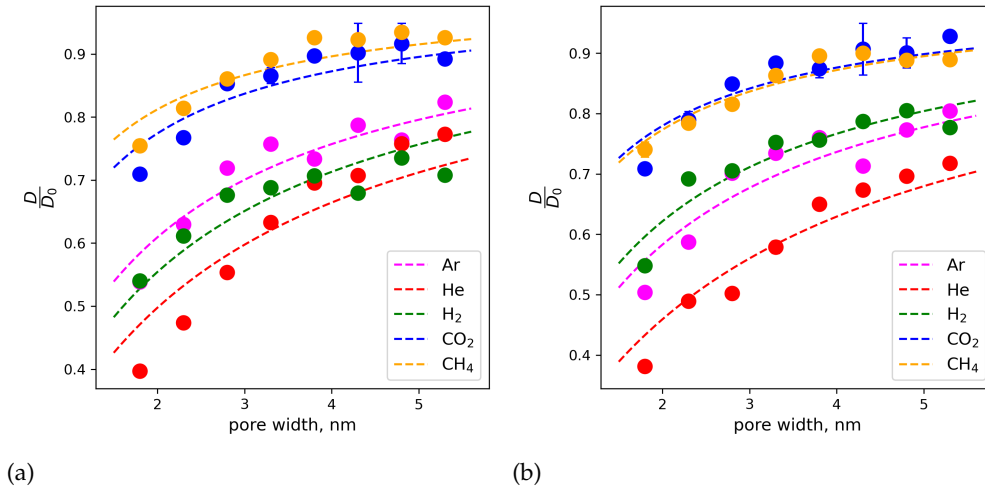


FIGURE 3.4: Diffusion coefficient (D ($10^{-6} m^2/s$)) of gas molecules in the bulk gas phase in Na-MMT at 12 MPa as a function of gas-filled pore width (a) 300 K (b) 330 K.

TABLE 3.3: Mean free path of gas molecules (nm) from MD simulations (λ_{MD}) with $\sigma_{col} = \sigma_{gas}$ and kinetic theory (λ_{KT})

Gas	300 K		330 K	
	λ_{KT}	λ_{MD}	λ_{KT}	λ_{MD}
H ₂	8.45	10.47	9.13	12.02
He	10.40	10.91	11.65	11.89
Ar	6.23	6.01	6.87	6.31
CH ₄	4.98	4.76	6.09	5.93
CO ₂	3.01	3.04	4.59	5.20

σ_{col} is the collision diameter and σ_{gas} is the diameter of the gas molecule which is the Lennard-Jones collision diameter (σ)

In general, it can be observed that the maximum gas-filled pore size is still smaller than the mean free path for most gas molecules. Consequently, the diffusion coefficient is reduced due to collisions with the water interface, which results in gas molecules having a shorter mean free path under confinement. Strong influence is exerted on the He gas because it has the largest mean free path compared to the other gases.

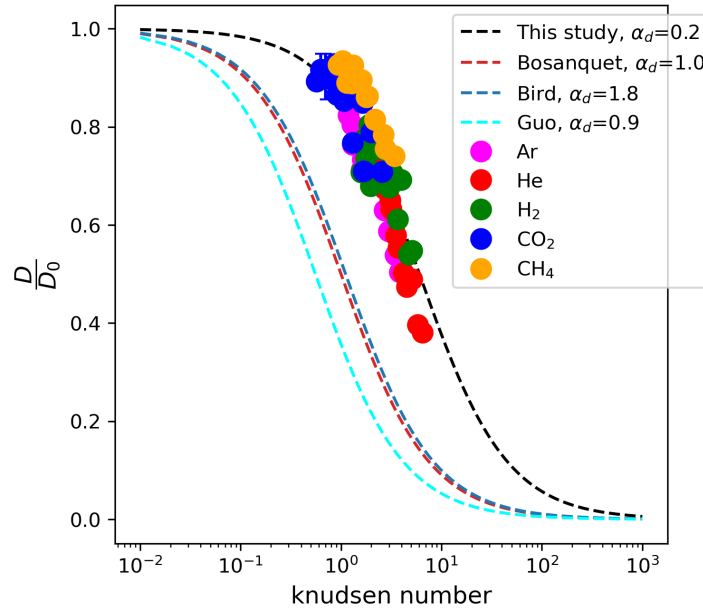


FIGURE 3.5: Average diffusion coefficient of gas molecules normalized to the diffusion coefficient in a pure bulk system as a function of the Knudsen number and fitted with eqn 3.13. The curve shift observed in this study is attributed to the specific physicochemical conditions considered, which differ from the simplified conditions assumed in the original Bosanquet approximation.

The Knudsen number was calculated from the mean free path and the gas-filled pore sizes. A diagram showing the relationship between the diffusion coefficient and the Knudsen number is shown in Figure 3.5. A mathematical equation developed from the graph after the Bosanquet approximation [50, 77] is given as:

$$D = D_0 \left(\frac{1}{1 + \alpha_d \left(\frac{\lambda}{h - 2t_w} \right)} \right) \quad (3.13)$$

and

$$Kn = \left(\frac{\lambda}{h - 2t_w} \right) \quad (3.14)$$

where D_0 represents the bulk diffusion coefficient in the gas phase at 12 MPa, λ denotes the mean free path of the gas at 12 MPa, h is the width of the pore, t_w is the thickness of the adsorbed water film, which varies with the degree of saturation. The parameter α_d is the Bosanquet correction parameter obtained through fitting and has a value of 0.2.

Based on the work of Yin et al. [110], the identification of three gas diffusion regimes can be

made in a porous media, determined by the local Knudsen number. The regimes are characterized by Kn values of ≤ 0.1 , $0.1 < \text{Kn} < 10$, and $\text{Kn} \geq 10$. In the case of molecular diffusion ($\text{Kn} \leq 0.1$), intermolecular collisions are dominant. When Knudsen diffusion occurs ($\text{Kn} \geq 10$), the dominant collisions are between molecules and a solid wall. In the case of transition diffusion ($0.1 < \text{Kn} < 10$), significant intermolecular collisions and collisions between molecules and the solid wall occur. The Knudsen number ranges from 0.6 to 6 in our results, indicating that diffusion is in the transition regime, and not purely molecular.

Several studies have shown that the original Bosanquet formula can approximate gas diffusion well in the transition regime [37, 77, 85, 97]. Guo et al. [37] used the Boltzmann transport equation to study gas diffusion, and found a Bosanquet correction parameter, α_d of 0.9, where the Knudsen number was determined using the method of the largest sphere. The Knudsen diffusivity derived from the kinetic theory of gases yielded an α_d of 1.8, which underestimated the value obtained by Guo et al. [37]. In this study, we obtained an α_d of 0.2, which appears to overestimate the other predictions. It is worth noting that the original Bosanquet approximation was developed from empirical studies and relies on several idealized conditions. The current system exhibits non-ideal gas behavior due to the high pressure. In addition, the gas-wall collisions may not be perfectly elastic since the wall consists of water molecules. Hence, surface phenomena such as adsorption and water vapor mobility at the gas-water interface may not be captured by the original Bosanquet approximation. Chen et al. [18] investigated the validity of the Bosanquet approximation using equilibrium molecular dynamics simulations and concluded that further modifications to the Bosanquet approximation are necessary to account for the intermolecular forces of fluid molecules and the smoothness of the pore walls.

Experimental data regarding gas diffusion coefficients in partially saturated smectite micropores as a function of gas-filled pore width are currently unavailable. However, a previous investigation of gas diffusion in saturated smectite incorporated a geometric factor and utilized an empirically derived function from a molecular dynamics study [74]. This approach produced predictions that closely matched experimental gas diffusion data in Boom clay. Therefore, we propose to adopt a similar methodology in our current study and modify eqn 3.13 accordingly.

$$D = \frac{D_0}{G} \left(\frac{1}{1 + \alpha_d \left(\frac{\lambda}{h_{av} - 2t_w} \right)} \right) \quad (3.15)$$

where G is the geometric factor and h_{av} is the average pore width. The geometric factor refers to an empirical parameter accounting for the reduction of the diffusive transport of species in porous media in comparison with the bulk phase due to the geometric complexity of pore space [23]. The geometric factor takes into account the tortuosity of diffusion paths, pore constrictivity, and the overall complexity of the clay pore structure. In general, the tortuosity and constrictivity can not be measured independently and are thus often lumped in a single parameter referred to as a geometric factor. This equation allows to predict the gas phase diffusivity for general conditions based on the geometric properties of porous media, mean pore size, and

the partial water pressure via the corresponding parameters, G , h_{av} , t_w . A further effect of temperature can be considered following the approach described in our previous study [74].

Gas-water interface diffusion

Accurately determining the diffusion coefficient at the gas-water interface is challenging due to the imprecise definition of the region encompassing the interface. To address this issue, we have defined the interface region as the area bounded by the adsorbed gas layer at the water interface, indicated by a cyan margin in Figure 3.1. Figure S1 in the supporting information display the diffusion coefficient at the gas-water interface. The results indicate that diffusion at the gas-water interface is approximately 10% lower than in the bulk. Notably, we observe from Figure S1 that the diffusion coefficient remains constant when the interaction water surface is in the bulk water phase. However, this behavior changes and increases as a function of adsorbed water film thickness for water film thicknesses below 1.0 nm. This is probably due to the structuring of water molecules close to the clay surface.

3.3.4 Flow dynamics

The study of fluid behavior necessitates a fundamental understanding of dynamic viscosity. As such, non-equilibrium molecular dynamics simulations were conducted in order to address this objective. A constant force acting on each fluid atom in the direction parallel to the clay surface initiated a fluid flow. Subsequently, the steady-state velocity profiles were analyzed to determine the dynamic viscosity of gas in partially saturated Na-MMT. The Navier-Stokes equation (eq 3.8) predicted a parabolic (Poiseuille) velocity profile assuming constant viscosity and density. Using eq 3.9, the dynamic viscosity was then obtained. These findings provide valuable insights into the properties of fluids in confined spaces.

Method validation

To validate the simulation setup, non-equilibrium molecular dynamics simulations were conducted for water flow in fully saturated Na-MMT. The resulting velocity and density profiles are shown in Figure 3.6. The density profile of water at the center of the pore remains constant at 1 g/cm^3 , indicative of bulk water behavior. Close to the surface, notable fluctuations in water density are observed within a 1 nm region, with a maximum density of approximately 2 g/cm^3 . The calculated dynamic viscosity for water in a 6 nm nanopore is 0.634 cP, a value that is in agreement with prior research on the dynamic viscosity of bulk water [11], flow simulations in a 6 nm Na-MMT nanopore [11], and experiments with bulk water [38], which reported values of 0.66 cP, 0.68 cP, and 0.891 cP, respectively. In contrast to the findings of Botan et al. [11], deviations from the parabolic flow profile near the surface were not significant in this study. This may be due to the use of a constant force, which is approximately one magnitude of order higher than that utilized in their study [11]. A higher force leads to greater water mobility, thereby diminishing the impact of water-surface interactions. The sliding velocity at the surface was roughly 75 m/s, indicating higher mobility than the study by Botan et al [11], which reported a velocity of about 4 m/s [11].

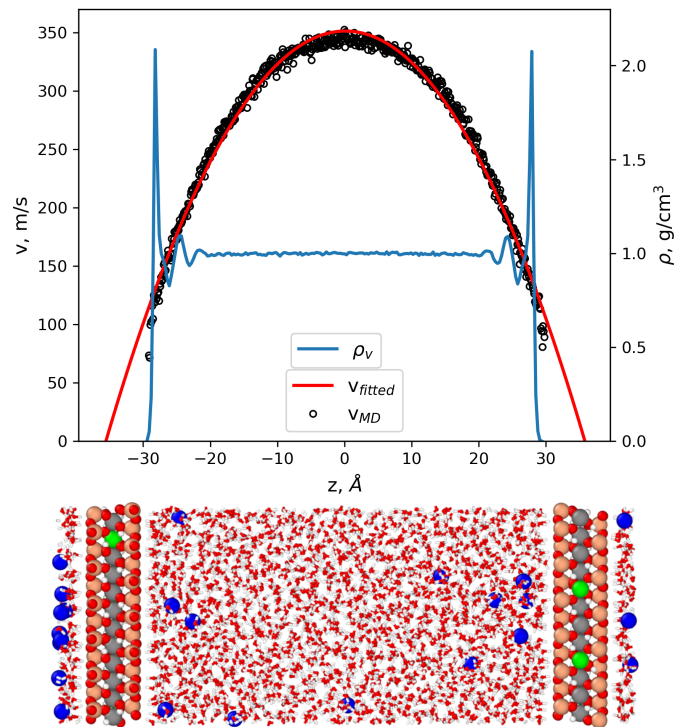


FIGURE 3.6: Steady-state velocity profile of water flow in Na-MMT. The force is acting parallel to the surface on each fluid atom in the x -direction. This diagram also shows the mass density profile of water. The black markers represent the velocity values from the MD simulation, the red line is the parabolic fit of the Poiseuille flow extrapolated here to the velocity at zero, and the blue line represents the mass density profile of the water.

The boundary condition responsible for the parabolic profile at the center of the pore is a crucial parameter that has been extensively studied [91]. The slip boundary condition has conventionally been assumed for continuum-scale fluids. In their review on microfluidics, Squire et al. [91] demonstrated that the no-slip boundary condition is not valid for gas within distances smaller than the mean free path from the wall. They also showed that non-continuum effects play a role in the boundary conditions of fluids confined to a molecular scale. Experimental techniques used to study microfluidic behavior generally indicate that wetting (hydrophilic) surfaces follow the no-slip boundary condition, whereas non-wetting (hydrophobic) surfaces follow a slip boundary condition [91]. To reveal the appropriate boundary conditions best applicable to the system and estimate the slip at the solid-liquid and liquid-gas interface the slip length was calculated for each interface. The slip length is defined as the distance within the surface/wall at which the (extrapolated) fluid velocity would be stationary; this can be expressed as:

$$L_s = \pm \frac{v_x(z_{surf})}{\left(\frac{dv_x}{dz}\right)_{z_{surf}}} \quad (3.16)$$

where L_s is the slip length, v_x is the slip velocity at the liquid-solid or gas-water boundary, z_{surf}

is the location of the slip surface, and $\left(\frac{dv_x}{dz}\right)_{z_{surf}}$ is the derivative of the slip velocity at the slip surface.

The simulation resulted in a slip length value of $5.00 \pm 0.45 \text{ \AA}$ for flow water in Na-MMT. Although there are no experimental determinations of the slip length, our value is in agreement with the value of 6 \AA obtained by Marry et al. [62] when studying electro-osmosis in Na-MMT.

Gas dynamics in slit pore

As an initial approach, the bulk viscosity of gas species was determined through bulk equilibrium molecular dynamics simulations, utilizing the Green-Kubo method at a temperature of 300 K and pressure of 12 MPa. The obtained results, presented in Table 3.4, indicate good agreement with the experimental values obtained at a temperature of 300 K and pressure of 0.1 MPa. It is thereby demonstrated that the dependence of viscosity on pressure is moderate. Nevertheless, the molecular weight presents a strong influence on the viscosity values.

TABLE 3.4: Average dynamic viscosity (centipoise) slip length (\AA) values for gas dynamics

Gas	μ_0	${}^a\mu_{exp}$	μ_{dry}	<i>Div</i> [%]	L_{DGPD}	L_{CGWPD}	L_{dry}
H ₂	0.009	0.009	0.007	-24.4	3.94 ± 1.02	4.29 ± 0.52	41.78
He	0.018	0.020	0.013	-29.2	3.16 ± 0.34	4.24 ± 0.67	54.14
Ar	0.028	0.023	0.021	-1.3	1.24 ± 0.32	1.81 ± 0.35	2.98
CH ₄	0.010	0.011	0.004	-5.0	0.65 ± 0.19	0.94 ± 0.45	8.58
CO ₂	0.033	0.015	0.014	83.3	0.74 ± 0.13	2.06 ± 0.47	0.65

^a μ_{exp} is experimental dynamic viscosity values [14, 53, 54, 67, 101]. μ_0 denotes the viscosity of gas from the bulk gas system using the Green-Kubo method. μ_{dry} is the viscosity of gas in a dry pyrophyllite. L_{DGPD} denotes the slip length for gas in the DGPD. L_{CGWPD} denotes the slip length for gas in a CGWPD. L_{dry} denotes the slip length for gas in the dry pyrophyllite. The symbol *Div* represents the percent difference between the relative viscosities (μ/μ_0) in the dry pore width and in the maximum partially saturated gas-filled pore width.

As previously noted, two distinct methodologies have been developed for investigating the dynamics of gas species, as depicted in Figure 3.7: Decoupled Gas Phase Dynamics (DGPD) and Coupled Gas and Water Phase Dynamics (CGWPD). In the DGPD system (Figure 3.7a), the adsorbed water film experience no external forces but rather undergoes weak traction at the gas-water interface due to the coupling of shear stresses resulting from the flow of gas species.

The dynamic viscosity of the gas species is shown in Figure 3.8 as a function of the Knudsen number for DGPD and CGWPD. The findings demonstrate that the viscosity behavior remains unchanged in both DGPD and CGWPD, indicating that dynamic viscosity is an inherent property of the gas. However, a strong dependence of viscosity on the Knudsen number is observed. This means that the pore size and the mean free path of a gas under confinement are crucial in determining the viscous behavior of the gas. Again, a Bosanquet-type approximation that

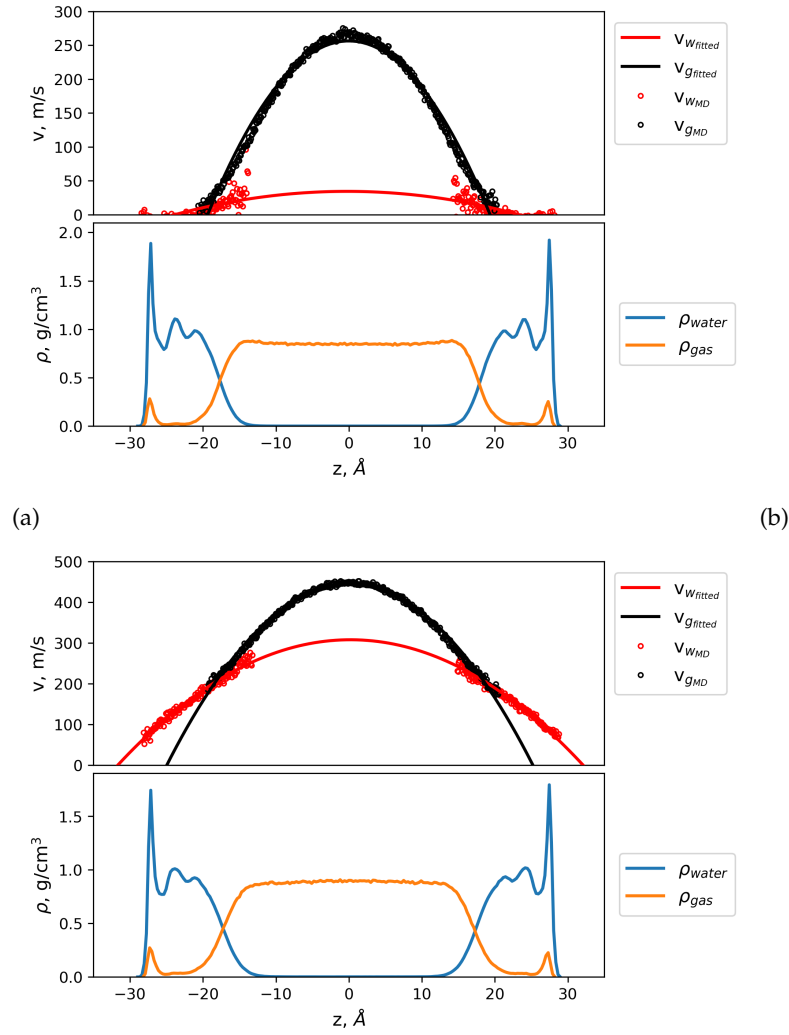


FIGURE 3.7: Velocity and density profiles of CO_2 gas in steady state at a pore width of 3.3 nm. The red line fits the velocity profile of water, the black line fits the velocity profile of CO_2 gas, the blue is the density profile of water and the orange is the density profile of CO_2 gas. (a) DGPD (b) CGWPD.

satisfactorily describes the Knudsen number dependence of the viscosity is given (with an introduction of the geometric factor for macroscopic predictions):

$$\mu = \frac{\mu_0}{G} \left(\frac{1}{1 + \alpha_v \left(\frac{\lambda}{h_{av} - 2t_w} \right)} \right) \quad (3.17)$$

where μ_0 represents the bulk dynamic viscosity of the gas, λ denotes the mean free path of the gas, h_{av} is the average width of the pore, t_w is the thickness of the adsorbed water film, which varies with the degree of saturation, α_d is the Bosanquet correction parameter obtained through fitting and has a value of 0.5.

Based on the Knudsen number, four flow regimes are recognized by a widely used empirical classification of gas flow in rarefied conditions [6]. The Navier-Stokes equation is the best

tool to describe flow when $Kn < 10^{-3}$ because the continuum assumption is valid and is supported by the no-slip boundary condition at the walls. With slip-velocity and temperature-jump boundary conditions, the continuum equations' applicability can be expanded for the regime of $10^{-3} < Kn < 10^{-1}$ (also known as the slip-flow regime) [1, 26]. The transition regime $10^{-1} < Kn < 10^1$, is the most challenging to handle. Intermolecular collisions for $Kn > 10^1$ become negligible, and the kinetic theory is typically used to describe the so-called free-molecular flow regime [68].

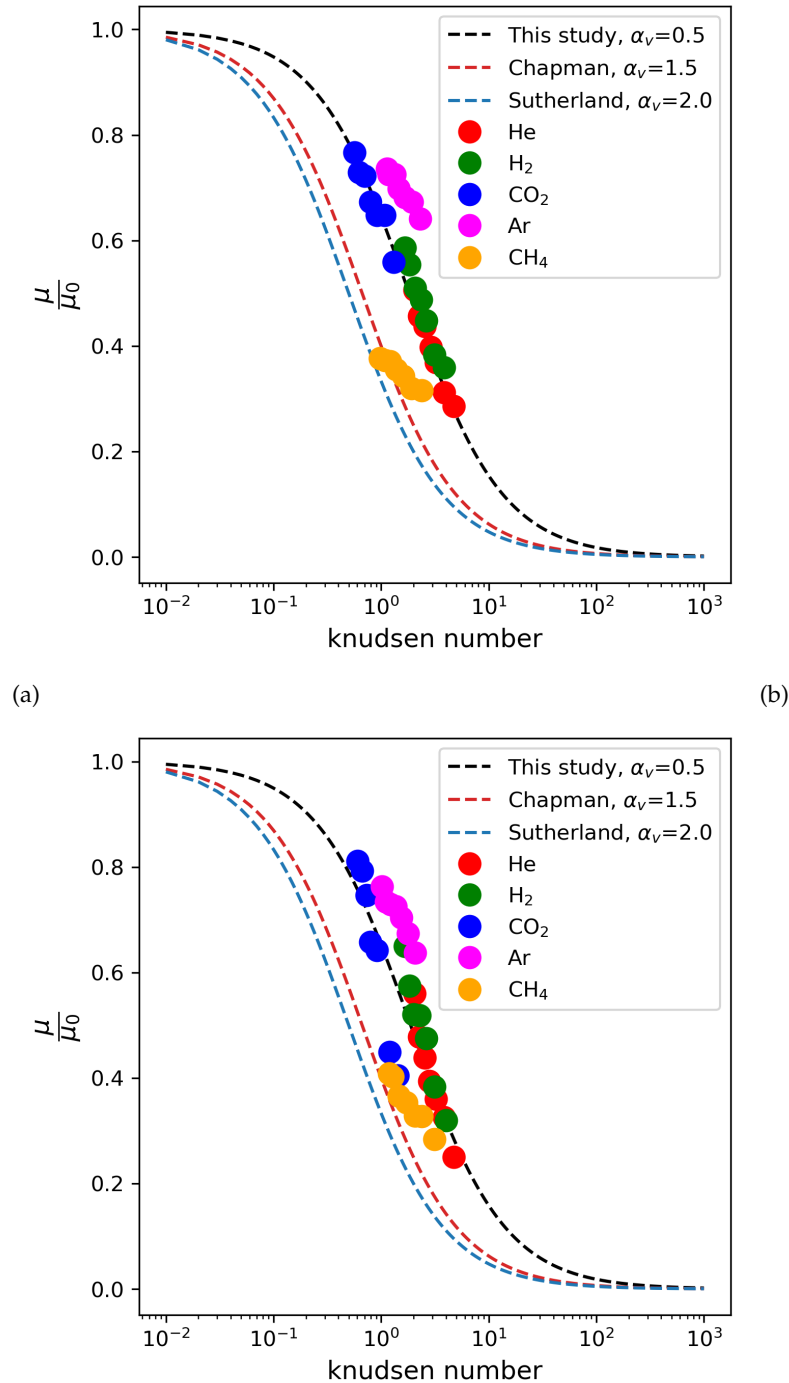


FIGURE 3.8: Dynamic viscosity of gas molecules in Na-MMT as a function of the Knudsen number (a) DGPD (b) CGWPD.

This study investigates the transition regime of the viscous flow of gas species. The rarefaction (correction) parameter α_v for this study is found to be 0.5, which differs from the values reported in previous studies, such as 1.5 and 2.0 [68]. This deviation is attributed to the same underlying factor as that discussed for diffusion. To explore the impact of pore wall type on viscosity, gas flow simulations were conducted in a dry pyrophyllite. The viscosity values and the corresponding percentage deviation of the relative viscosities (μ/μ_0) from the maximum partially saturated gas-filled pore width are presented in Table 3.4. The observed deviation values (*Div*) of the gas species indicate a pronounced influence of the interacting surface on the dynamic viscosity of the confined gas molecules. Specifically, He, H₂, CH₄, and Ar exhibit a higher affinity towards the liquid wall compared to the solid wall, resulting in reduced relative viscosities, upon contact with water molecules. He and H₂ with lower molecular weights show a much stronger affinity. Conversely, CO₂ exhibits the opposite trend, with a very strong affinity for the clay solid wall.

Table 3.4 presents the slip length values (L_{DGPD} , L_{CGWPD} , and L_{dry}) for gas flow in DGPD, CGWPD, and dry pyrophyllite. The results demonstrate that both DGPD and CGWPD exhibit a marginal slip condition at the liquid surface, with CGWPD exhibiting slightly higher slip length values than DGPD. This observation may be attributed to the presence of water molecules moving tangentially to the gas flow at the gas-water interface, resulting in dynamic stresses exerted on the gas surface due to relative motion, which leads to additional traction. The gas flow characteristics of dry pyrophyllite exhibit a more pronounced slip condition compared to those in contact with water, which is an intriguing finding. The slip length is notably larger for helium (He) and hydrogen (H₂), and this trend correlates well with the divergence (*Div*) values. He and H₂ have less affinity for the solid surface, leading to their greater mobility at the interface, resulting in higher slip velocity and subsequently increased slip length. Conversely, CO₂ exhibits a strong affinity for the solid surface, resulting in a considerably lower slip length.

3.3.5 Viscosity of water in two-phase flow

The present study investigates the dynamic viscosity of the water film under partially saturated conditions for CGWPD. Figure 3.9 displays the dynamic viscosity as a function of the number of adsorbed water layers, which indicates the thickness of the adsorbed water film. The findings reveal that the dynamic viscosity of water increases with decreasing thickness of the adsorbed water film. This is consistent with the hypothesis that water molecules near the clay surface have lower mobility, which leads to a higher dynamic viscosity due to interaction with the clay surface. At 3.5 to 1.8 water layers, the dynamic viscosity increases to about 2.0 cP, which is approximately twice the value observed in bulk water. This increase in viscosity is attributed to the fact that, in thin water films, water is more influenced by the clay surface, and mobility is lowered. These findings provide insights into the impact of adsorbed water thickness on water phase mobility near the clay surface and their effect on the dynamic viscosity of water in a CGWPD.

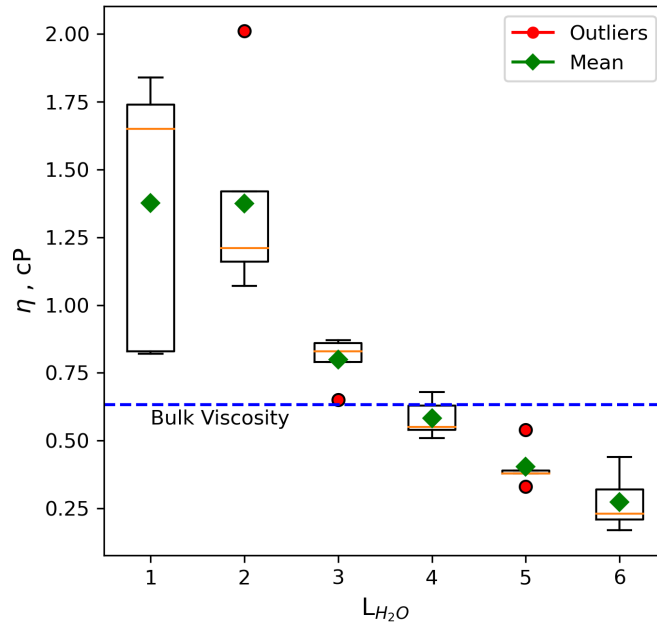


FIGURE 3.9: Dynamic viscosity of water films confined in Na-MMT clay slit pore as a function of the number of adsorbed water layers.

3.4 Conclusions

In this study, a comprehensive understanding of the mobility of gaseous molecules in partially saturated smectite clay (Na-montmorillonite) is provided using molecular dynamics simulations. The porosity of the fluid is subdivided into four distinct domains, including the solid-liquid interface, bulk-like liquid phase, gas-water interface, and bulk-like gas phase, based on density profiles. The diffusion coefficients of five types of gaseous molecules (Ar, He, H₂, CO₂, and CH₄) are separately studied for diffusion in the gas phase and at the gas-water interface. It is found that diffusion in the gas phase increases with gas-filled pore width, asymptotically converging to the diffusion of gas in the bulk state. Furthermore, the diffusion coefficient at the gas-water interface is observed to remain constant as long as it is confined by well-defined bulk-like liquid and gas domains. The system's diffusive behavior is in a transition regime that comprises a mixture of molecular diffusion and Knudsen diffusion, thus rendering Fick's law unsuitable for describing the process. To overcome this challenge, a Bosanquet-type approximation is used to describe the effective diffusion coefficient as a function of the adsorbed water film thickness, gas mean-free path, geometric factor, and average pore width, yielding highly satisfactory results.

Furthermore, an investigation into the partitioning of gases in the water-rich phase was conducted. Based on density profiles for gas molecules in two water-rich regions of interest in the system; (a) solid-liquid interface and (b) bulk-liquid-like phase, the partition coefficient and Gibbs free energy of gas transfer was determined. At the solid-liquid interface, adsorbed water layers are formed due to the interaction between water molecules and the clay surface. Our

findings demonstrate that the partition coefficient is highly dependent on the temperature and molecular weight of the gaseous molecules.

The intrinsic nature of viscosity is confirmed by non-equilibrium molecular dynamics simulations at different degrees of saturation, where the dynamic viscosity of gases in Decoupled Gas Phase Dynamics (DGPD) and Combined Gas and Water Phase Dynamics (CGWPD) is found to be identical. Our modeling further reveals that the no-slip boundary condition often used in continuum models is unsuitable for strongly confined fluids, and that the finite slip boundary condition should be applied instead. Moreover, the dynamic viscosity of water in CGWPD is observed to increase with decreasing thickness of the absorbed water film. Furthermore, our simulations demonstrate that the dynamic viscosity of gases is highly influenced by the interacting wall surface. These parameters are crucial input parameters for the subsequent step in this study, which involves the development of an upscale pore-scale model.

Supporting Information

The Supporting Information (Appendix) of this manuscript contains a plot of the gas diffusion coefficient as a function of gas-filled pore width at the fluid-gas interface. The density distribution diagrams for gases and water are also presented. Finally, the velocity profile of gas flow in the gas-filled pore is also shown.

Acknowledgement

The research reported in this paper was supported by EURAD GAS FUTURE and DONUT Work Packages, Laboratory for Waste Management at the Paul Scherrer Institute, NAGRA, and the University of Bern Geological Institute. Molecular dynamics simulations were carried out using resources from the Paul Scherrer Institute (MERLIN 6), the University of Bern (UBELIX), and the Swiss National Super Computing Centre (Piz Daint). The authors acknowledge the co-funding from Horizon 2020 EURAD project Grant ID 847593.

3.5 Appendix

Gas phase diffusion of gases in Na-MMT

TABLE 3.5: MD simulation predictions of the relative diffusion coefficients (D/D_0) of gas in the gas phase in partially saturated Na-MMT

	h [nm]	1.8	2.3	2.8	3.3	3.8	4.3	4.8	5.3
	T [K]								
He	300	0.40 ± 0.000	0.47 ± 0.004	0.55 ± 0.002	0.63 ± 0.007	0.70 ± 0.008	0.71 ± 0.001	0.76 ± 0.004	0.77 ± 0.005
	330	0.38 ± 0.008	0.49 ± 0.005	0.50 ± 0.003	0.58 ± 0.010	0.65 ± 0.005	0.67 ± 0.003	0.70 ± 0.003	0.72 ± 0.002
H ₂	300	0.54 ± 0.007	0.61 ± 0.000	0.68 ± 0.003	0.69 ± 0.003	0.71 ± 0.003	0.68 ± 0.004	0.74 ± 0.007	0.71 ± 0.002
	330	0.55 ± 0.006	0.69 ± 0.003	0.71 ± 0.000	0.75 ± 0.000	0.76 ± 0.004	0.79 ± 0.005	0.81 ± 0.001	0.78 ± 0.002
CO ₂	300	0.71 ± 0.006	0.77 ± 0.005	0.85 ± 0.002	0.87 ± 0.012	0.90 ± 0.003	0.90 ± 0.046	0.92 ± 0.032	0.89 ± 0.009
	330	0.71 ± 0.003	0.79 ± 0.014	0.85 ± 0.000	0.88 ± 0.001	0.87 ± 0.015	0.91 ± 0.043	0.90 ± 0.025	0.93 ± 0.006
Ar	300	0.54 ± 0.003	0.63 ± 0.005	0.72 ± 0.003	0.76 ± 0.004	0.73 ± 0.002	0.79 ± 0.001	0.76 ± 0.004	0.82 ± 0.006
	330	0.50 ± 0.000	0.59 ± 0.003	0.70 ± 0.007	0.73 ± 0.004	0.76 ± 0.003	0.71 ± 0.000	0.77 ± 0.002	0.80 ± 0.005
CH ₄	300	0.75 ± 0.010	0.81 ± 0.002	0.86 ± 0.006	0.89 ± 0.003	0.93 ± 0.004	0.92 ± 0.005	0.93 ± 0.003	0.93 ± 0.001
	330	0.74 ± 0.013	0.78 ± 0.003	0.82 ± 0.005	0.86 ± 0.004	0.90 ± 0.005	0.90 ± 0.003	0.89 ± 0.003	0.89 ± 0.003

Surface Diffusion

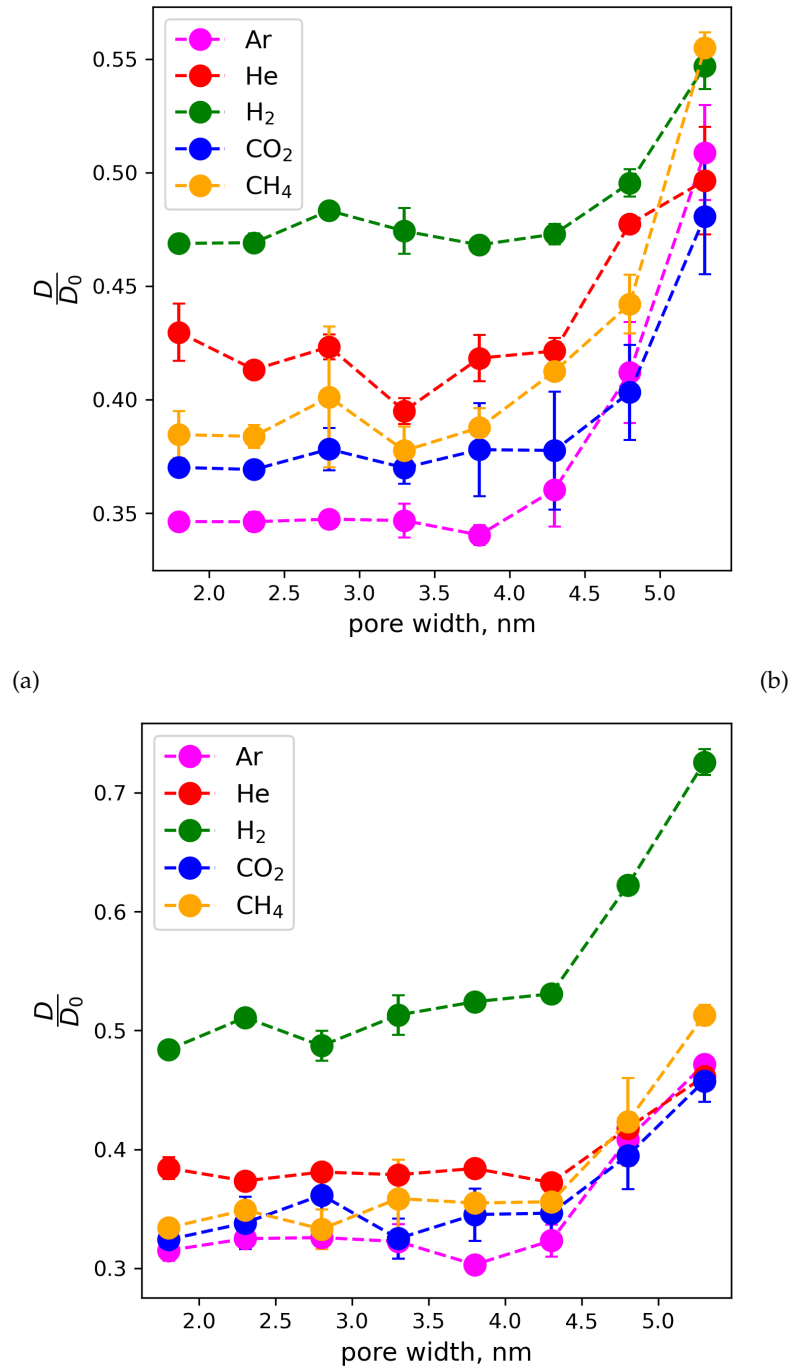


FIGURE 3.10: Diffusion coefficient of gas molecules in the gas-water interface in Na-MMT at 12 MPa as a function of gas-filled pore width (a) 300 K (b) 330 K.

Density profiles of gaseous molecules and water

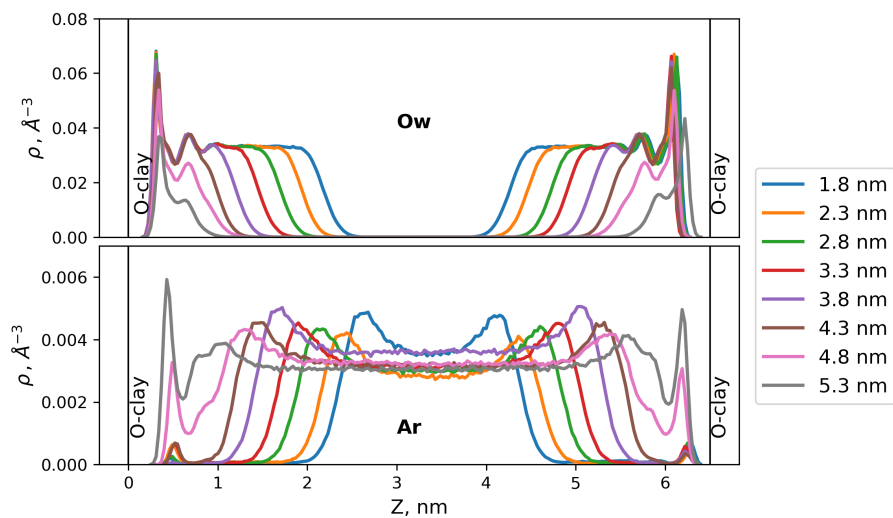


FIGURE 3.11: Density profile of Ar at 300 K

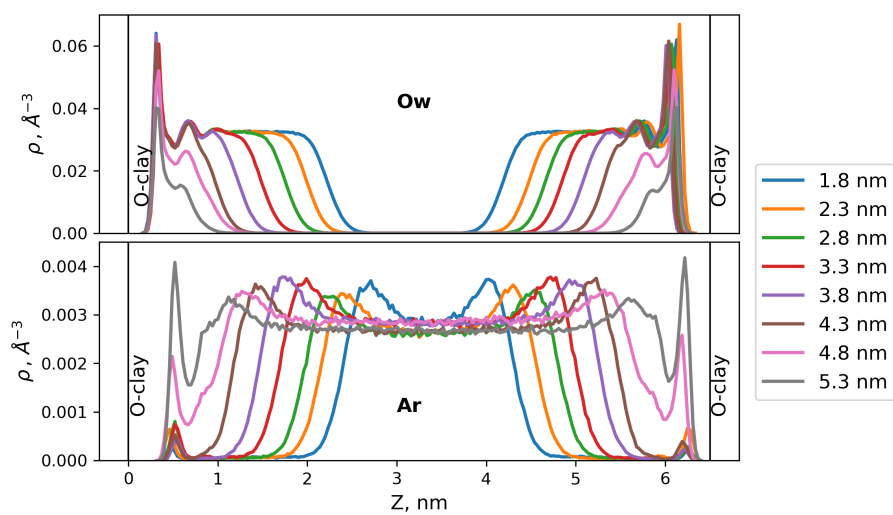


FIGURE 3.12: Density profile of Ar at 330 K

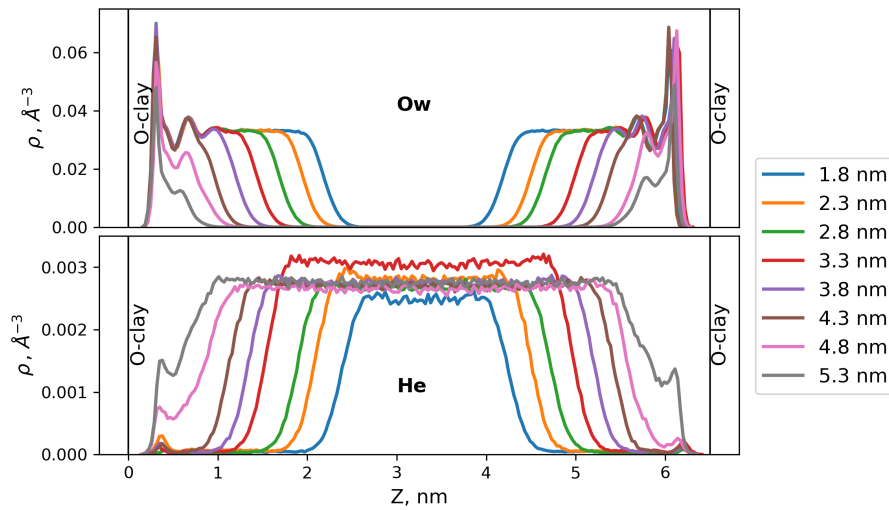


FIGURE 3.13: Density profile of He at 300 K

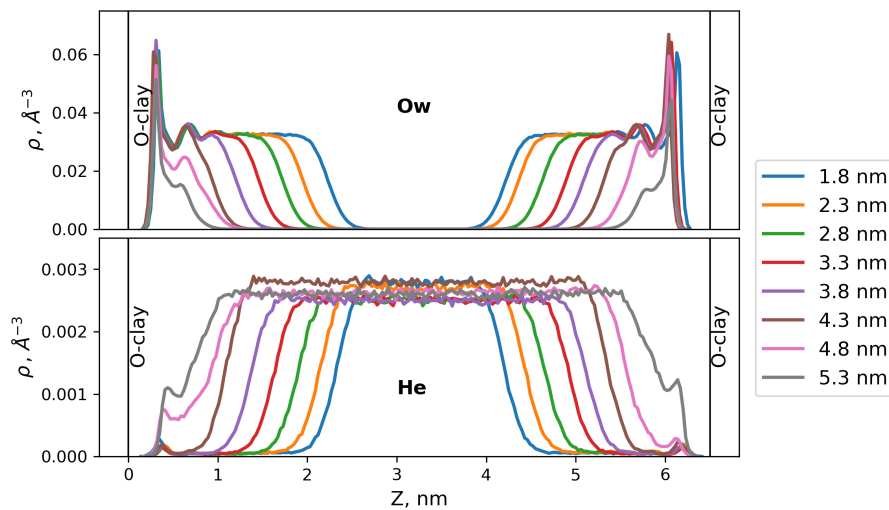
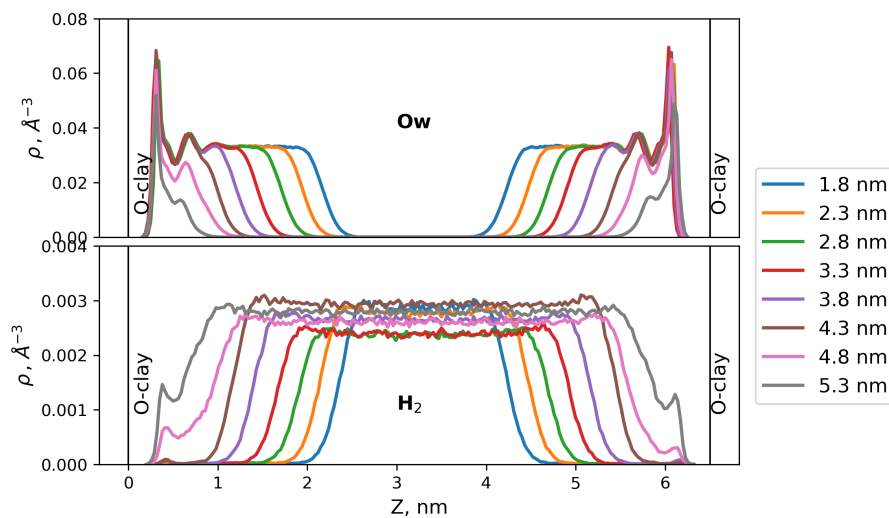
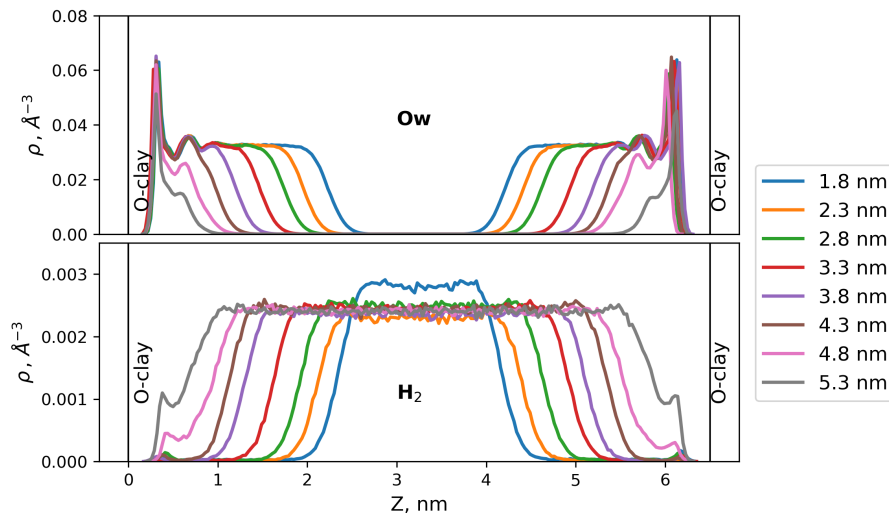
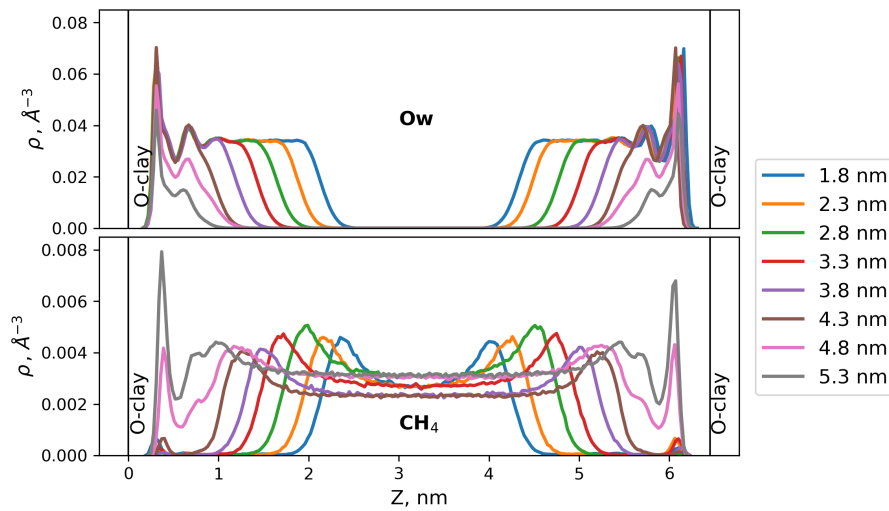
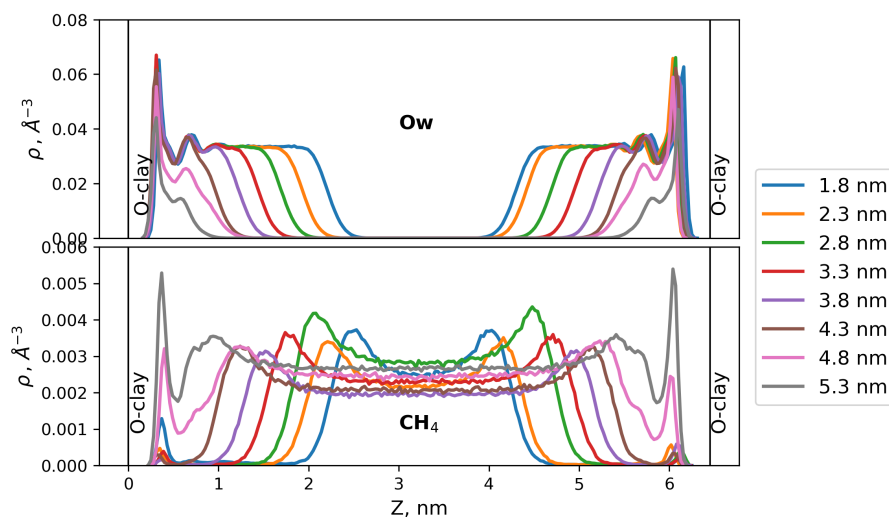
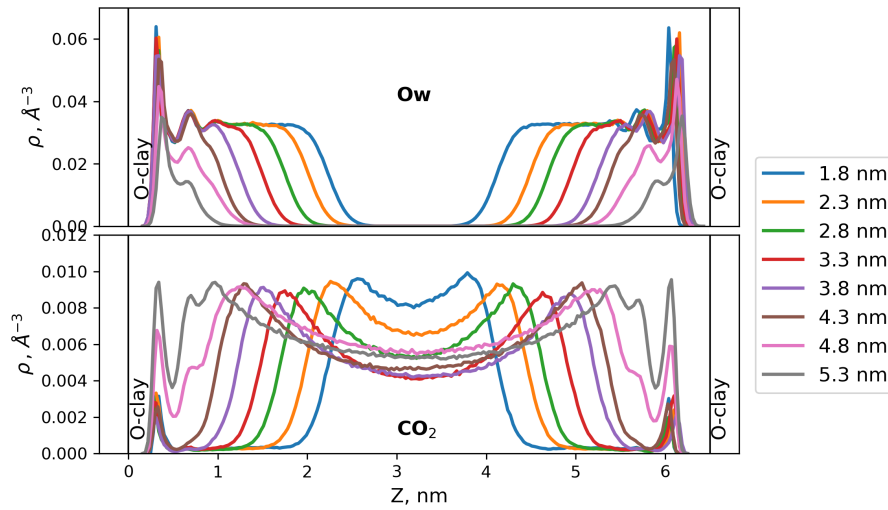
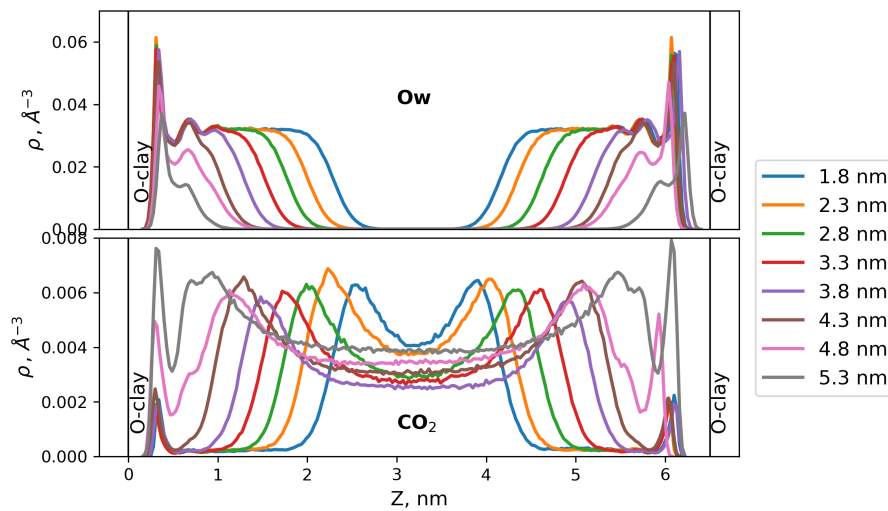


FIGURE 3.14: Density profile of He at 330 K

FIGURE 3.15: Density profile of H_2 at 300 K

FIGURE 3.16: Density profile of H_2 at 330 KFIGURE 3.17: Density profile of CH_4 at 300 KFIGURE 3.18: Density profile of CH_4 at 330 K

FIGURE 3.19: Density profile of CO₂ at 300 KFIGURE 3.20: Density profile of CO₂ at 330 K

Velocity profiles of gas flow in slit pore

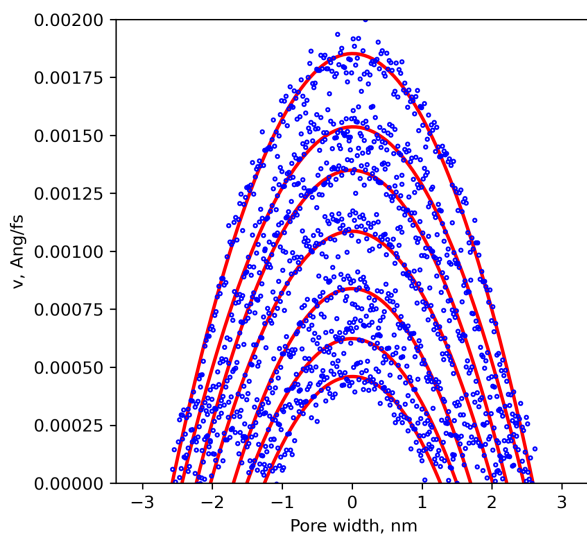


FIGURE 3.21: Velocity profile of Ar at 300K

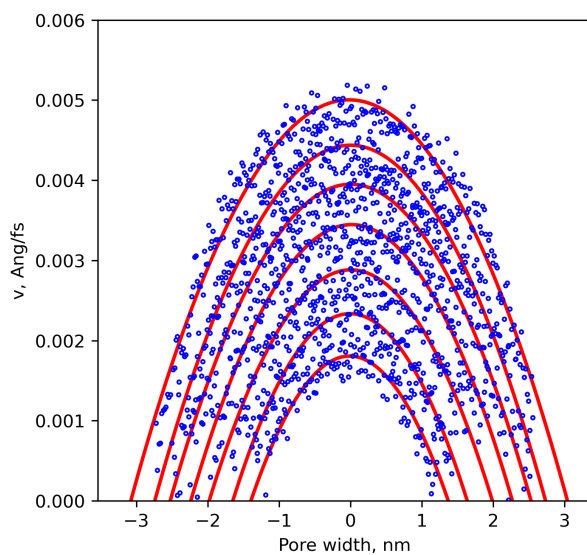
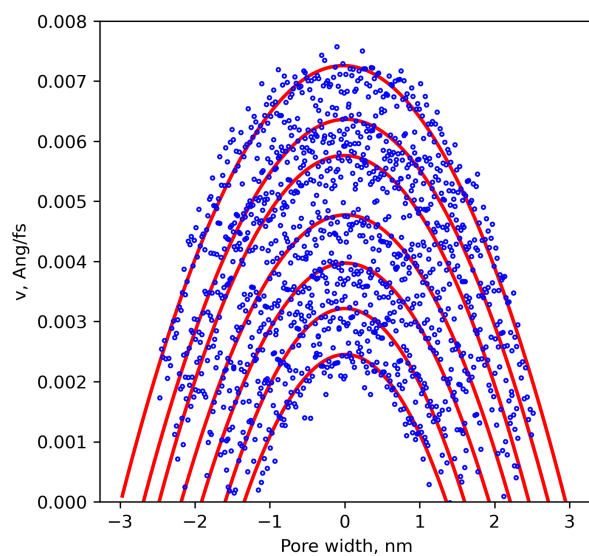
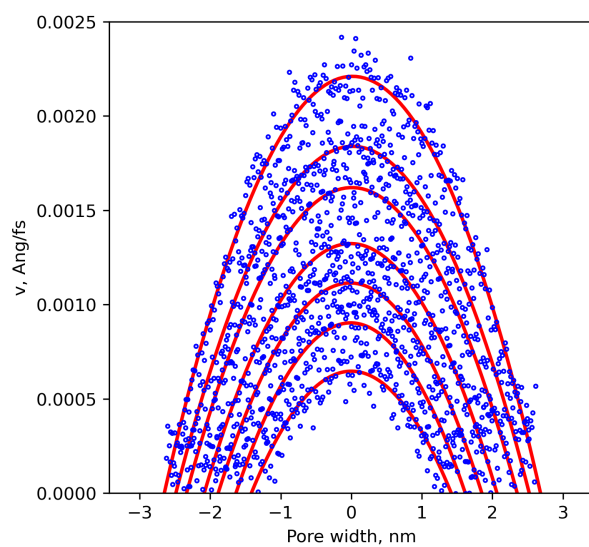
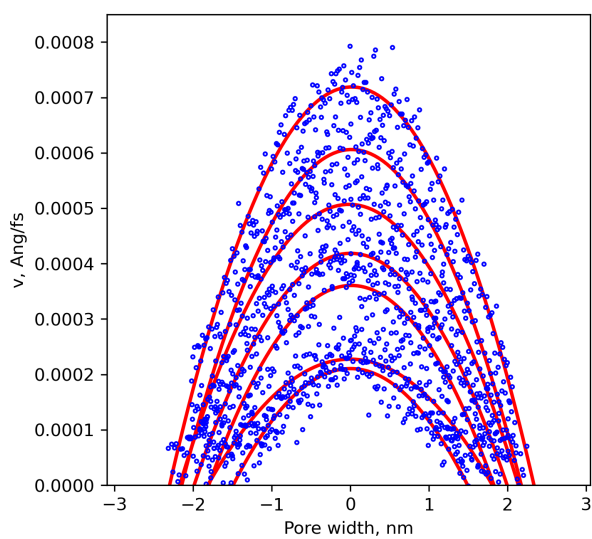


FIGURE 3.22: Velocity profile of He at 300K

FIGURE 3.23: Velocity profile of H₂ at 300KFIGURE 3.24: Velocity profile of CH₄ at 300K

FIGURE 3.25: Velocity profile of CO_4 at 300K

3.6 References

- [1] Agrawal, A. and Prabhu, S. (2008). Deduction of slip coefficient in slip and transition regimes from existing cylindrical couette flow data. *Experimental Thermal and Fluid Science*, 32(4):991–996.
- [2] Altmann, S., Tournassat, C., Goutelard, F., Parneix, J.-C., Gimmi, T., and Maes, N. (2012). Diffusion-driven transport in clayrock formations. *Applied Geochemistry*, 27(2):463–478.
- [3] Apostolopoulou, M., Santos, M. S., Hamza, M., Bui, T., Economou, I. G., Stamatakis, M., and Striolo, A. (2019). Quantifying pore width effects on diffusivity via a novel 3d stochastic approach with input from atomistic molecular dynamics simulations. *Journal of chemical theory and computation*, 15(12):6907–6922.
- [4] Appelo, C., Van Loon, L., and Wersin, P. (2010). Multicomponent diffusion of a suite of tracers (hto, cl, br, i, na, sr, cs) in a single sample of opalinus clay. *Geochimica et Cosmochimica Acta*, 74(4):1201–1219.
- [5] Armand, G., Djizanne, H., Zghondi, J., de La Vaissière, R., Talandier, J., and Conil, N. (2016). Inputs from in situ experiments to the understanding of the unsaturated behaviour of callovo-oxfordian claystone. In *E3S Web of Conferences*, volume 9, page 03004. EDP Sciences.
- [6] Barber, R. W. and Emerson, D. R. (2006). Challenges in modeling gas-phase flow in microchannels: from slip to transition. *Heat Transfer Engineering*, 27(4):3–12.
- [7] Bardelli, F., Mondelli, C., Didier, M., Vitillo, J. G., Cavicchia, D. R., Robinet, J.-C., Leone, L., and Charlet, L. (2014). Hydrogen uptake and diffusion in callovo-oxfordian clay rock for nuclear waste disposal technology. *Applied Geochemistry*, 49:168–177.
- [8] Bensenouci, F., Michelot, J., Matray, J., Savoye, S., Lavielle, B., Thomas, B., and Dick, P. (2011). A profile of helium-4 concentration in pore-water for assessing the transport phenomena through an argillaceous formation (tournemire, france). *Physics and Chemistry of the Earth, Parts A/B/C*, 36(17-18):1521–1530.
- [9] Bensenouci, F., Michelot, J., Matray, J., Savoye, S., Massault, M., and Vinsot, A. (2014). Coupled study of water-stable isotopes and anions in porewater for characterizing aqueous transport through the mesozoic sedimentary series in the eastern paris basin. *Marine and Petroleum Geology*, 53:88–101.
- [10] Bigler, T., Beat, I., Lehmann, B. E., Niklaus Waber, H., Vinsot, A., Latoui, K., Tolstikhin, I., and Gautschi, A. (2005). Helium production and transport in the low permeability callovo-oxfordian at the bure site, france.
- [11] Botan, A., Rotenberg, B., Marry, V., Turq, P., and Noetinger, B. (2011). Hydrodynamics in clay nanopores. *The Journal of Physical Chemistry C*, 115(32):16109–16115.
- [12] Bourg, I. C., Bourg, A. C., and Sposito, G. (2003). Modeling diffusion and adsorption in compacted bentonite: a critical review. *Journal of Contaminant Hydrology*, 61(1-4):293–302.

- [13] Brusseau, M. L., Popovicova, J., and Silva, J. A. (1997). Characterizing gas-water interfacial and bulk-water partitioning for gas-phase transport of organic contaminants in unsaturated porous media. *Environmental science & technology*, 31(6):1645–1649.
- [14] Cencek, W., Przybytek, M., Komasa, J., Mehl, J. B., Jeziorski, B., and Szalewicz, K. (2012). Effects of adiabatic, relativistic, and quantum electrodynamics interactions on the pair potential and thermophysical properties of helium. *The Journal of Chemical Physics*, 136(22):224303.
- [15] Chapman, S. and Cowling, T. G. (1990). *The mathematical theory of non-uniform gases: an account of the kinetic theory of viscosity, thermal conduction and diffusion in gases*. Cambridge University Press: Cambridge, U.K.
- [16] Chen, L., Groß, T., Krienke, H., and Lüdemann, H.-D. (2001). T, p-dependence of the self-diffusion and spin-lattice relaxation in fluid hydrogen and deuterium. *Physical Chemistry Chemical Physics*, 3(11):2025–2030.
- [17] Chen, L. L.-y., Katz, D. L., and Tek, M. R. (1977). Binary gas diffusion of methane-nitrogen through porous solids. *AIChE Journal*, 23(3):336–341.
- [18] Chen, Q. and Zhou, J. (2023). Investigating the validity of the bosanquet equation for predicting the self-diffusivities of fluids inside nanotubes using equilibrium molecular dynamics simulations. *AIP Advances*, 13(2):025338.
- [19] Chenzhong, C. and Zhiliang, L. (1998). Molecular polarizability. 1. relationship to water solubility of alkanes and alcohols. *Journal of chemical information and computer sciences*, 38(1):1–7.
- [20] Churakov, S. V. (2013). Mobility of na and cs on montmorillonite surface under partially saturated conditions. *Environmental science & technology*, 47(17):9816–9823.
- [21] Churakov, S. V. and Dahn, R. (2012). Zinc adsorption on clays inferred from atomistic simulations and exafs spectroscopy. *Environmental science & technology*, 46(11):5713–5719.
- [22] Churakov, S. V. and Gimmi, T. (2011a). Up-scaling of molecular diffusion coefficients in clays: A two-step approach. *The Journal of Physical Chemistry C*, 115(14):6703–6714.
- [23] Churakov, S. V. and Gimmi, T. (2011b). Up-scaling of molecular diffusion coefficients in clays: A two-step approach. *The Journal of Physical Chemistry C*, 115(14):6703–6714.
- [24] Diomidis, N., Cloet, V., Leupin, O., Marschall, P., Poller, A., and Stein, M. (2016). Production, consumption and transport of gases in deep geological repositories according to the swiss disposal concept. NAGRA Technical Report NTB-16-03, National Cooperative for the Disposal of Radioactive Waste (NAGRA).
- [25] Donev, A., Fai, T. G., and Vanden-Eijnden, E. (2014). A reversible mesoscopic model of diffusion in liquids: from giant fluctuations to fick’s law. *Journal of Statistical Mechanics: Theory and Experiment*, 2014(4):P04004.
- [26] Dongari, N., Sambasivam, R., and Durst, F. (2009). Extended navier-stokes equations and treatments of micro-channel gas flows. *Journal of Fluid Science and Technology*, 4(2):454–467.

- [27] Ellis, C. and Holsen, J. (1969). Diffusion coefficients for he-n₂ and n₂-co₂ at elevated temperatures. *Industrial & Engineering Chemistry Fundamentals*, 8(4):787–791.
- [28] Fedoseev, A., Demin, N., Salnikov, M., and Sukhinin, G. (2018). Numerical modelling of heat and moisture transfer in a clay-like porous material. In *Journal of Physics: Conference Series*, volume 1105, page 012048. IOP Publishing.
- [29] Fick, A. (1855). Poggendorff's flannel. *Physik*, 94(59):297.
- [30] Frentrup, H., Avendaño, C., Horsch, M., Salih, A., and Müller, E. A. (2012). Transport diffusivities of fluids in nanopores by non-equilibrium molecular dynamics simulation. *Molecular Simulation*, 38(7):540–553.
- [31] Gadikota, G., Dazas, B., Rother, G., Cheshire, M. C., and Bourg, I. C. (2017). Hydrophobic solvation of gases (co₂, ch₄, h₂, noble gases) in clay interlayer nanopores. *The Journal of Physical Chemistry C*, 121(47):26539–26550.
- [32] Gimmi, T. and Churakov, S. V. (2019). Water retention and diffusion in unsaturated clays: Connecting atomistic and pore scale simulations. *Applied Clay Science*, 175:169–183.
- [33] Gimmi, T., Schneebeil, M., Flühler, H., Wydler, H., and Baer, T. (1997). Field-scale water transport in unsaturated crystalline rock. *Water Resources Research*, 33(4):589–598.
- [34] Gimmi, T., Waber, H., Gautschi, A., and Rübel, A. (2007). Stable water isotopes in pore water of jurassic argillaceous rocks as tracers for solute transport over large spatial and temporal scales. *Water Resources Research*, 43(4).
- [35] Glaus, M. A., Frick, S., Rossé, R., and Van Loon, L. R. (2010). Comparative study of tracer diffusion of hto, ²²na+ and ³⁶cl- in compacted kaolinite, illite and montmorillonite. *Geochimica et Cosmochimica Acta*, 74(7):1999–2010.
- [36] Groß, T., Buchhauser, J., and Lüdemann, H.-D. (1998). Self-diffusion in fluid carbon dioxide at high pressures. *The Journal of chemical physics*, 109(11):4518–4522.
- [37] Guo, Y., He, X., Huang, W., and Wang, M. (2019). Microstructure effects on effective gas diffusion coefficient of nanoporous materials. *Transport in Porous Media*, 126:431–453.
- [38] Haynes, W. M. (2004). *CRC handbook of chemistry and physics*, volume 97. CRC press.
- [39] He, S., Jiang, Y., Conrad, J. C., and Qin, G. (2015). Molecular simulation of natural gas transport and storage in shale rocks with heterogeneous nano-pore structures. *Journal of Petroleum Science and Engineering*, 133:401–409.
- [40] Hirschfelder, J. O., Curtiss, C. F., and Bird, R. B. (1964). Molecular theory of gases and liquids. *Molecular theory of gases and liquids*.
- [41] Hoteit, H. and Firoozabadi, A. (2009). Numerical modeling of diffusion in fractured media for gas-injection and-recycling schemes. *Spe Journal*, 14(02):323–337.

- [42] Jacops, E., Maes, N., Bruggeman, C., and Grade, A. (2017). Measuring diffusion coefficients of dissolved he and ar in three potential clay host formations: Boom clay, callovo-oxfordian clay and opalinus clay. *Geological Society, London, Special Publications*, 443(1):349–360.
- [43] Jacops, E., Volckaert, G., Maes, N., Weetjens, E., and Govaerts, J. (2013). Determination of gas diffusion coefficients in saturated porous media: He and ch₄ diffusion in boom clay. *Applied Clay Science*, 83:217–223.
- [44] Jähne, B., Heinz, G., and Dietrich, W. (1987). Measurement of the diffusion coefficients of sparingly soluble gases in water. *Journal of Geophysical Research: Oceans*, 92(C10):10767–10776.
- [45] Jiang, W. and Lin, M. (2018). Molecular dynamics investigation of conversion methods for excess adsorption amount of shale gas. *Journal of Natural Gas Science and Engineering*, 49:241–249.
- [46] Kadoura, A., Narayanan Nair, A. K., and Sun, S. (2016). Molecular dynamics simulations of carbon dioxide, methane, and their mixture in montmorillonite clay hydrates. *The Journal of Physical Chemistry C*, 120(23):12517–12529.
- [47] Kaufhold, S. and Dohrmann, R. (2016). Distinguishing between more and less suitable bentonites for storage of high-level radioactive waste. *Clay Minerals*, 51(2):289–302.
- [48] Kosakowski, G., Churakov, S. V., and Thoenen, T. (2008). Diffusion of na and cs in montmorillonite. *Clays and Clay Minerals*, 56(2):190–206.
- [49] Kozaki, T., Sato, H., Sato, S., and Ohashi, H. (1999). Diffusion mechanism of cesium ions in compacted montmorillonite. *Engineering Geology*, 54(1-2):223–230.
- [50] Krishna, R. and van Baten, J. M. (2012). Investigating the validity of the bosanquet formula for estimation of diffusivities in mesopores. *Chemical engineering science*, 69(1):684–688.
- [51] Kristensen, A. H., Thorbjørn, A., Jensen, M. P., Pedersen, M., and Moldrup, P. (2010). Gas-phase diffusivity and tortuosity of structured soils. *Journal of contaminant hydrology*, 115(1-4):26–33.
- [52] Krooss, B. and Leythaeuser, D. (1988). Experimental measurements of the diffusion parameters of light hydrocarbons in water-saturated sedimentary rocks—ii. results and geochemical significance. *Organic Geochemistry*, 12(2):91–108.
- [53] Laesecke, A. and Muzny, C. D. (2017a). Ab initio calculated results require new formulations for properties in the limit of zero density: The viscosity of methane (ch₄). *International Journal of Thermophysics*, 38:1–12.
- [54] Laesecke, A. and Muzny, C. D. (2017b). Reference correlation for the viscosity of carbon dioxide. *Journal of physical and chemical reference data*, 46(1):013107.
- [55] Lamb, W., Hoffman, G., and Jonas, J. (1981). Self-diffusion in compressed supercritical water. *The Journal of Chemical Physics*, 74(12):6875–6880.

- [56] Le Crom, S., Tournassat, C., Robinet, J.-C., and Marry, V. (2021). Influence of water saturation level on electrical double layer properties in a clay mineral mesopore: A molecular dynamics study. *The Journal of Physical Chemistry C*, 126(1):647–654.
- [57] Lewis, D. F. (1989). The calculation of molar polarizabilities by the cnd0/2 method: Correlation with the hydrophobic parameter, $\log p$. *Journal of computational chemistry*, 10(2):145–151.
- [58] Lippmann-Pipke, J., Gerasch, R., Schikora, J., and Kulenkampff, J. (2017). Benchmarking pet for geoscientific applications: 3d quantitative diffusion coefficient determination in clay rock. *Computers & Geosciences*, 101:21–27.
- [59] Liu, P., Harder, E., and Berne, B. (2004). On the calculation of diffusion coefficients in confined fluids and interfaces with an application to the liquid- vapor interface of water. *The Journal of Physical Chemistry B*, 108(21):6595–6602.
- [60] Lo, I. M., Mak, R. K., and Lee, S. C. (1997). Modified clays for waste containment and pollutant attenuation. *Journal of Environmental Engineering*, 123(1):25–32.
- [61] Loomer, D. B., Scott, L., Al, T. A., Mayer, K. U., and Bea, S. (2013). Diffusion–reaction studies in low permeability shale using x-ray radiography with cesium. *Applied geochemistry*, 39:49–58.
- [62] Marry, V., Dufrêche, J.-F., Jardat, M., and Turq, P. (2003). Equilibrium and electrokinetic phenomena in charged porous media from microscopic and mesoscopic models: electro-osmosis in montmorillonite. *Molecular Physics*, 101(20):3111–3119.
- [63] Marry, V. and Turq, P. (2003). Microscopic simulations of interlayer structure and dynamics in bihydrated heteroionic montmorillonites. *The Journal of Physical Chemistry B*, 107(8):1832–1839.
- [64] Marschall, P., Horseman, S., and Gimmi, T. (2005). Characterisation of gas transport properties of the opalinus clay, a potential host rock formation for radioactive waste disposal. *Oil & gas science and technology*, 60(1):121–139.
- [65] Martin, M. G. and Siepmann, J. I. (1997). Predicting multicomponent phase equilibria and free energies of transfer for alkanes by molecular simulation. *Journal of the American Chemical Society*, 119(38):8921–8924.
- [66] Marty, B., Dewonck, S., and France-Lanord, C. (2003). Geochemical evidence for efficient aquifer isolation over geological timeframes. *Nature*, 425(6953):55–58.
- [67] May, E. F., Berg, R. F., and Moldover, M. R. (2007). Reference viscosities of h₂, ch₄, ar, and xe at low densities. *International Journal of Thermophysics*, 28(4):1085–1110.
- [68] Michalis, V. K., Kalarakis, A. N., Skouras, E. D., and Burganos, V. N. (2010). Rarefaction effects on gas viscosity in the knudsen transition regime. *Microfluidics and nanofluidics*, 9:847–853.

- [69] Michels, L., Méheust, Y., Altoe, M. A., Dos Santos, É. C., Hemmen, H., Droppa Jr, R., Fossum, J. O., and da Silva, G. J. (2019). Water vapor diffusive transport in a smectite clay: Cationic control of normal versus anomalous diffusion. *Physical Review E*, 99(1):013102.
- [70] Mohammed, S. and Gadikota, G. (2018). The effect of hydration on the structure and transport properties of confined carbon dioxide and methane in calcite nanopores. *Frontiers in Energy Research*, 6:86.
- [71] Nakashima, Y. (2003). Diffusivity measurement of heavy ions in wyoming montmorillonite gels by x-ray computed tomography. *Journal of contaminant hydrology*, 61(1-4):147–156.
- [72] Nosé, S. (1984a). A molecular dynamics method for simulations in the canonical ensemble. *Molecular physics*, 52(2):255–268.
- [73] Nosé, S. (1984b). A unified formulation of the constant temperature molecular dynamics methods. *The Journal of chemical physics*, 81(1):511–519.
- [74] Owusu, J. P., Karalis, K., Prasianakis, N. I., and Churakov, S. V. (2022). Mobility of dissolved gases in smectites under saturated conditions: Effects of pore size, gas types, temperature, and surface interaction. *The Journal of Physical Chemistry C*, 126(40):17441–17455.
- [75] Patriarche, D., Ledoux, E., Michelot, J.-L., Simon-Coinçon, R., and Savoye, S. (2004). Diffusion as the main process for mass transport in very low water content argillites: 2. fluid flow and mass transport modeling. *Water Resources Research*, 40(1).
- [76] Plimpton, S. (1995). Fast parallel algorithms for short-range molecular dynamics. *Journal of computational physics*, 117(1):1–19.
- [77] Pollard, W. and Present, R. D. (1948). On gaseous self-diffusion in long capillary tubes. *Physical Review*, 73(7):762.
- [78] Poller, A., Mayer, G., Darcis, M., and Smith, P. (2016). Modelling of gas generation in deep geological repositories after closure. Technical report, National Cooperative for the Disposal of Radioactive Waste (NAGRA).
- [79] Raevsky, O. A., Perlovich, G. L., Kazachenko, V. P., Strakhova, N. N., and Schaper, K.-J. (2009). Octanol/water partition coefficients of sulfonamides: experimental determination and calculation using physicochemical descriptors. *Journal of Chemical & Engineering Data*, 54(11):3121–3124.
- [80] Rebour, V., Billiotte, J., Deveughele, M., Jambon, A., and Le Guen, C. (1997). Molecular diffusion in water-saturated rocks: A new experimental method. *Journal of contaminant hydrology*, 28(1-2):71–93.
- [81] Robb, W. and Drickamer, H. (1951). Diffusion in co₂ up to 150-atmospheres pressure. *The Journal of Chemical Physics*, 19(12):1504–1508.
- [82] Rodwell, W., Harris, A., Horseman, S., Lalieux, P., Müller, W., Ortiz Amaya, L., and Pruess, K. (1999). Gas migration and two-phase flow through engineered and geological barriers for a deep repository for radioactive waste. *EUR(Luxembourg)*.

- [83] Rowe, R. K. (2005). Long-term performance of contaminant barrier systems. *Geotechnique*, 55(9):631–678.
- [84] Rübél, A. P., Sonntag, C., Lippmann, J., Pearson, F., and Gautschi, A. (2002). Solute transport in formations of very low permeability: Profiles of stable isotope and dissolved noble gas contents of pore water in the opalinus clay, mont terri, switzerland. *Geochimica et Cosmochimica Acta*, 66(8):1311–1321.
- [85] Ruthven, D. M., Kärger, J., and Theodorou, D. N. (2012). *Diffusion in nanoporous materials*. John Wiley & Sons.
- [86] Ryckaert, J.-P., Ciccotti, G., and Berendsen, H. J. (1977). Numerical integration of the cartesian equations of motion of a system with constraints: molecular dynamics of n-alkanes. *Journal of computational physics*, 23(3):327–341.
- [87] Schaefer, C., Arands, R., Van der Sloot, H., and Kosson, D. (1997). Modeling of the gaseous diffusion coefficient through unsaturated soil systems. *Journal of contaminant hydrology*, 29(1):1–21.
- [88] Shimmo, M., Saarnio, K., Aalto, P., Hartonen, K., Hyötyläinen, T., Kulmala, M., and Riekkola, M.-L. (2004). Particle size distribution and gas-particle partition of polycyclic aromatic hydrocarbons in helsinki urban area. *Journal of Atmospheric Chemistry*, 47(3):223.
- [89] Slattery, J. C. and Bird, R. B. (1958). Calculation of the diffusion coefficient of dilute gases and of the self-diffusion coefficient of dense gases. *AIChE Journal*, 4(2):137–142.
- [90] Smedes, F., Geertsma, R. W., Zande, T. v. d., and Booiij, K. (2009). Polymer- water partition coefficients of hydrophobic compounds for passive sampling: Application of cosolvent models for validation. *Environmental science & technology*, 43(18):7047–7054.
- [91] Squires, T. M. and Quake, S. R. (2005). Microfluidics: Fluid physics at the nanoliter scale. *Reviews of modern physics*, 77(3):977.
- [92] Staikova, M., Wania, F., and Donaldson, D. (2004). Molecular polarizability as a single-parameter predictor of vapour pressures and octanol–air partitioning coefficients of non-polar compounds: a priori approach and results. *Atmospheric Environment*, 38(2):213–225.
- [93] Stiel, L. I. and Thodos, G. (1965). The self-diffusivity of dilute and dense gases. *The Canadian Journal of Chemical Engineering*, 43(4):186–190.
- [94] Sui, H., Yao, J., and Zhang, L. (2015). Molecular simulation of shale gas adsorption and diffusion in clay nanopores. *Computation*, 3(4):687–700.
- [95] Sutton, R. and Sposito, G. (2001). Molecular simulation of interlayer structure and dynamics in 12.4 Å cs-smectite hydrates. *Journal of Colloid and Interface Science*, 237(2):174–184.
- [96] Thorstenson, D. and Pollock, D. (1989). Gas transport in unsaturated porous media: The adequacy of fick’s law. *Reviews of Geophysics*, 27(1):61–78.

- [97] Tomadakis, M. M. and Sotirchos, S. V. (1993). Ordinary and transition regime diffusion in random fiber structures. *AIChE Journal*, 39(3):397–412.
- [98] Torgersen, T., Kennedy, B., and van Soest, M. (2004). Diffusive separation of noble gases and noble gas abundance patterns in sedimentary rocks. *Earth and Planetary Science Letters*, 226(3-4):477–489.
- [99] Van Milligen, B. P., Bons, P., Carreras, B. A., and Sanchez, R. (2005). On the applicability of fick’s law to diffusion in inhomogeneous systems. *European journal of physics*, 26(5):913.
- [100] Vinsot, A., Appelo, C. A. J., Lundy, M., Wechner, S., Cailteau-Fischbach, C., Donato, P. d., Pironon, J., Lettry, Y., Lerouge, C., and Cannière, P. D. (2018). Natural gas extraction and artificial gas injection experiments in opalinus clay, mont terri rock laboratory (switzerland). In *Mont Terri Rock Laboratory, 20 Years*, pages 377–392. Springer.
- [101] Vogel, E. (2010). Reference viscosity of argon at low density in the temperature range from 290 k to 680 k. *International Journal of Thermophysics*, 31:447–461.
- [102] Wang, S., Feng, Q., Zha, M., Javadpour, F., and Hu, Q. (2018). Supercritical methane diffusion in shale nanopores: effects of pressure, mineral types, and moisture content. *Energy & fuels*, 32(1):169–180.
- [103] Wang, S., Javadpour, F., and Feng, Q. (2016). Molecular dynamics simulations of oil transport through inorganic nanopores in shale. *Fuel*, 171:74–86.
- [104] Webb, S. W. and Pruess, K. (2003). The use of fick’s law for modeling trace gas diffusion in porous media. *Transport in porous media*, 51(3):327–341.
- [105] Wei, X., Wang, G., Massarotto, P., Golding, S., and Rudolph, V. (2007). Numerical simulation of multicomponent gas diffusion and flow in coals for co2 enhanced coalbed methane recovery. *Chemical engineering science*, 62(16):4193–4203.
- [106] Wersin, P., Van Loon, L., Soler, J., Yllera, A., Eikenberg, J., Gimmi, T., Hernán, P., and Boisson, J.-Y. (2004). Long-term diffusion experiment at mont terri: first results from field and laboratory data. *Applied Clay Science*, 26(1-4):123–135.
- [107] Wesenauer, F., Jordan, C., Azam, M., Harasek, M., and Winter, F. (2021). Considerations on temperature dependent effective diffusion and permeability of natural clays. *Materials*, 14(17):4942.
- [108] Wick, C. D., Siepmann, J. I., and Schure, M. R. (2003). Temperature dependence of transfer properties: Importance of heat capacity effects. *The Journal of Physical Chemistry B*, 107(38):10623–10627.
- [109] Woessner, D., Snowden Jr, B., George, R., and Melrose, J. (1969). Dense gas diffusion coefficients for the methane-propane system. *Industrial & Engineering Chemistry Fundamentals*, 8(4):779–786.

- [110] Yin, Y., Qu, Z., and Zhang, J. (2019). Multiple diffusion mechanisms of shale gas in nanoporous organic matter predicted by the local diffusivity lattice boltzmann model. *International Journal of Heat and Mass Transfer*, 143:118571.
- [111] Zhao, Y., Luo, M., Liu, L., Wu, J., Chen, M., and Zhang, L. (2022). Molecular dynamics simulations of shale gas transport in rough nanopores. *Journal of Petroleum Science and Engineering*, 217:110884.
- [112] Zhu, H.-L., Wang, S.-F., Yin, G.-J., Chen, Q., Xu, F.-L., Peng, W., Tan, Y.-H., and Zhang, K. (2018). Study of the numerical simulation of tight sandstone gas molecular diffusion based on digital core technology. *Petroleum Science*, 15(1):68–76.

Chapter 4: Swelling Pressure of Na-Montmorillonite in the Presence of Gas from Molecular Dynamics Study

(manuscript in preparation)

Swelling Pressure of Na-Montmorillonite in the presence of gas from molecular dynamics study [†]

Jerry P. Owusu,^{*,‡,¶} Konstantinos Karalis,[¶] Nikolaos I. Prasianakis,[‡] and Sergey V. Churakov^{*,‡,¶}

[‡]*Laboratory for Waste Management, Paul Scherrer Institute, 5232 Villigen-PSI, Switzerland*

[¶]*University of Bern, Institute of Geological Sciences, 3012 Bern, Switzerland*

Abstract

The long-term stability of deep geologic repositories relies on the integrity of waste material containment barriers. Bentonite is commonly used as a backfill because of its ability to swell and exhibit self-sealing phenomena. Its properties in the presence of water and ions are well known. However, the swelling behavior of bentonite can be influenced by several factors, including the presence of gases. In particular, the effect of gases on the swelling behavior of bentonite is not known. Various gases such as CO_2 , H_2 , and CH_4 may be present in the repository near-field due to metal corrosion or the degradation of organic wastes. In this study, we used classical molecular dynamics simulations to investigate the effects of the presence of gas on the swelling pressure of Na-montmorillonite clay material. The results show that gas molecules increase the swelling pressure of Na-montmorillonite by about 3 MPa, and the behavior depends on the dry density and the nature of the gas species. This effect can be explained by the increasing partitioning (solubility) of the gas molecules to the interlayer with increasing swelling pressure. A detailed analysis of structural transformations in clay interlayer allows to explain the diverging behavior of the experimentally measured and the simulated curves at a high degree of compaction. These results further improve our understanding of the fundamental mechanisms underlying the swelling behavior of clays used as barrier material in deep geological disposal.

4.1 Introduction

The safe disposal of nuclear waste requires a comprehensive understanding of the interactions among the waste, host rock, and environment. To protect the environment, a multi-barrier system that combines both natural and engineered barriers is employed [11]. Smectite clays possess several desirable properties such as swelling potential, high sorption capacity, crack and pore sealing ability, low permeability, small pore size, and high ion exchange capacity, making them suitable for both natural and engineered barriers [15, 32, 35, 42]. Therefore, smectite clays have been extensively investigated as a potential component in the deep geological disposal of High-Level Radioactive Waste (HLW) to isolate the radioactive waste from the environment [14, 27, 30, 38].

Smectite clay particles consist of octahedral (O) and tetrahedral (T) aluminosilicate sheets arranged in TOT-layers, where an octahedral sheet containing Al is sandwiched between two tetrahedral sheets containing Si [10]. This structure imparts a net negative charge due to the

substitution of Al^{3+} for Si^{4+} in the tetrahedral sheet and metal cations like Mg^{2+} and Fe^{2+} for Al^{3+} in the octahedral sheet. The charge is balanced by cations present in the interlayer space. The clay's ability to absorb and retain large amounts of water leads to swelling upon entry of water into the interlayer space through the hydration of cations [32, 42]. This swelling behavior has significant implications for the hydrochemical and mechanical properties of clay materials, making it a critical parameter to consider in the deep geological disposal of radioactive waste [20, 37].

In the context of nuclear waste management, the utilization of smectite clay as a sealing material in the repository has been proposed. It is expected that smectite clay would exhibit swelling behavior upon contact with subsurface water, thereby effectively sealing the repository by filling the gaps between the waste container and the host rock [3, 24]. In addition, the smectite clay's swelling pressure would exert a confining force that would hold the radioactive waste container in place and protect it from mechanical impacts of the host rock [3]. However, the swelling pressure of the barrier material is a critical parameter in repository design. Insufficient swelling capacity does not provide the necessary sealing of the tunnel and disposal casks, whereas excessive swelling pressure may compromise the integrity of the host rocks. Thus, the safe nuclear waste repository design must take into account, a comprehensive understanding of the swelling mechanisms and the underlying factors governing the swelling capacity of the buffer materials.

There has been extensive research on the swelling behavior of smectite clay, both experimentally and theoretically, over the years [1–3, 6, 15, 16, 18, 21, 26, 28, 31, 32, 40, 41, 46, 47, 51, 52]. These studies have investigated various factors, including the mineralogy of the smectite clay [1, 26, 45, 46], environmental conditions like temperature [3, 28, 52], and groundwater composition [2, 6, 16, 18, 31] that affect the swelling behavior. For instance, Sun et al. [46] conducted a study to investigate the effect of cation species on swelling behavior and found that Ca-montmorillonite and mixed Na/Ca-montmorillonite swell more than Na-montmorillonite due to the greater hydration energy of Ca^{2+} ions. Another study examined the influence of the smectite layer charge and its location on the swelling pressure [45]. The results showed that the pressure was inversely proportional to the magnitude of the smectite layer charge in the range of -0.5 to -1.0 per unit cell. Furthermore, Akinwunmi et al. [3] investigated the thermal effects on the swelling pressure of sodium smectite clay and observed that at temperatures below 200 K, the presence of ice in the clay interlayer and surrounding water hindered swelling. However, at temperatures between 200 K and 250 K, there was a rapid onset of swelling pressure. At higher temperatures between 300 K and 600 K, there was a gradual increase in swelling pressure with increasing temperature [3]. Additionally, Herbert et al. [18] conducted experiments to determine the influence of pore water composition on the swelling capacity of bentonite. They found that the swelling pressure was highest in pure water, intermediate in low ionic strength electrolytes, and lowest in solutions with high salt content. The salinity and pH of the pore space solution in relation to its ionic strength were also shown to influence the swelling capacity of bentonite [18].

The possibility of gas production near a nuclear waste repository has been widely studied [33,

43, 50, 53]. This phenomenon has significant implications for the stability of the containment barrier system [39, 43, 50], which is a crucial factor in repository design. Gases produced in the near field can dissolve in the water present in the pores, leading to changes in the chemical composition of the pore solution. These changes, in turn, can affect the swelling pressure and in situ behavior of the barrier system.

Despite numerous experimental studies on the swelling pressure of smectite clays, a comprehensive computational investigation has yet to be conducted, particularly regarding the effect of gas on the swelling pressure of smectite. Atomistic simulations have proven to be a valuable tool for comprehensively understanding the swelling behavior of clay materials under various conditions. They enable the observation of changes in material behavior resulting from microscopic interactions, which significantly affect the swelling pressure [1–3, 15, 45, 46].

This study aims to investigate the influence of gas composition on the swelling pressure of smectite clays through classical molecular dynamics simulations. Understanding the behavior of smectite clays in the presence of different gases is essential for ensuring their long-term stability and optimal performance. The gases selected for investigation include carbon dioxide (CO₂), methane (CH₄), argon (Ar), hydrogen (H₂), and helium (He). The outcomes of this study will provide valuable insights into the underlying mechanisms that govern the swelling pressure of smectite clays under various gas environments. This, in turn, will advance our knowledge of the behavior of smectite clays and facilitate the development of predictive models for assessing the safety and stability of nuclear waste repositories.

4.2 Methods

4.2.1 Simulation method

The swelling pressure of smectite clay can be quantified by utilizing the spring method, as developed in previous studies [2, 3, 45, 46]. This approach capitalizes on the clay's ability to absorb water, which leads to a change in the d-spacing between the clay layers. In this method, the lower clay layer is fixed in all three dimensions, while the upper clay layer is constrained in the x and y directions but free to move vertically in the z-direction. The upper clay layer is then connected to a set of springs with a known force constant, which restricts its movement in the vertical direction. Upon the introduction of water into the interlayer region between the two clay layers, the upper clay layer moves upwards, compressing the springs and altering the d-spacing. The force exerted by the springs can be determined by measuring the average deformation of the springs from their initial length, which is equivalent to the swelling force of the clay. The configuration of the spring model is depicted in Figure 4.1.

The swelling pressure of the clay system is computed as:

$$P_s = \frac{F_s}{S_A} = \frac{n \times k \times dz}{S_A} \quad (4.1)$$

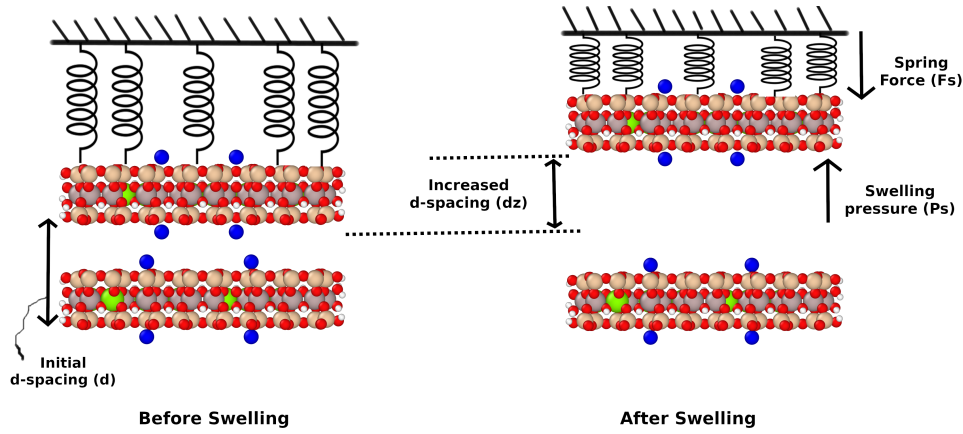


FIGURE 4.1: Illustration of the set-up of the spring model.

where F_s is the spring force, S_A is the clay surface area, n is the total number of springs, k is the force constant of the spring and dz is the average displacement from the initial d-spacing. At any given d-spacing, the dry density of the clay is calculated as:

$$\rho = \frac{m_{clay}}{d\text{-spacing} \times S_A} = \frac{m_{clay}}{V_{clay} + V_{interlayer}} \quad (4.2)$$

where m_{clay} is the mass of the solid clay structure, $d - spacing$ is the basal spacing as shown in Figure 4.1, S_A is the clay surface area, V_{clay} is the volume of the solid clay layers, and $V_{interlayer}$ is the volume of the interlayer space.

4.2.2 System setup and simulation details

The smectite mineral investigated in this study is a montmorillonite with the chemical formula $\text{Na}_{0.5}[\text{Al}_{3.5}\text{Mg}_{0.5}]\text{Si}_8\text{O}_{20}(\text{OH})_4$ per unit cell. In order to repair the ruptured chemical bonds on the (010) edges of the clay particles, OH groups and protons were introduced to the under-coordinated cationic sites and dangling oxygen sites, respectively. The simulation setup considered two parallel clay particles, which are composed of 4×2 unit cells each of montmorillonite. Within the octahedral layer, 24 Al^{3+} ions were replaced by Mg^{2+} ions, resulting in a permanent layer charge of $-1.0 e$ per unit cell. This charge was balanced by 24 Na^+ ions. The clay platelets were positioned at the center of a periodic water box, with varying initial basal spacing (d-spacing). As a result, there were 1-4 water layers within the interlayer and approximately 6000 water molecules in the surrounding area. The simulation cell is shown in Figure 4.2.

The GROMACS simulation package [19] was used to perform molecular dynamics simulations. The interatomic interactions among the clay atoms were described using the CLAYFF force field [12], while the SPC/E model [7] was utilized to represent water molecules. The force field models for the gas molecules were adopted based on previous studies, where the models' uncertainties were also evaluated [34].

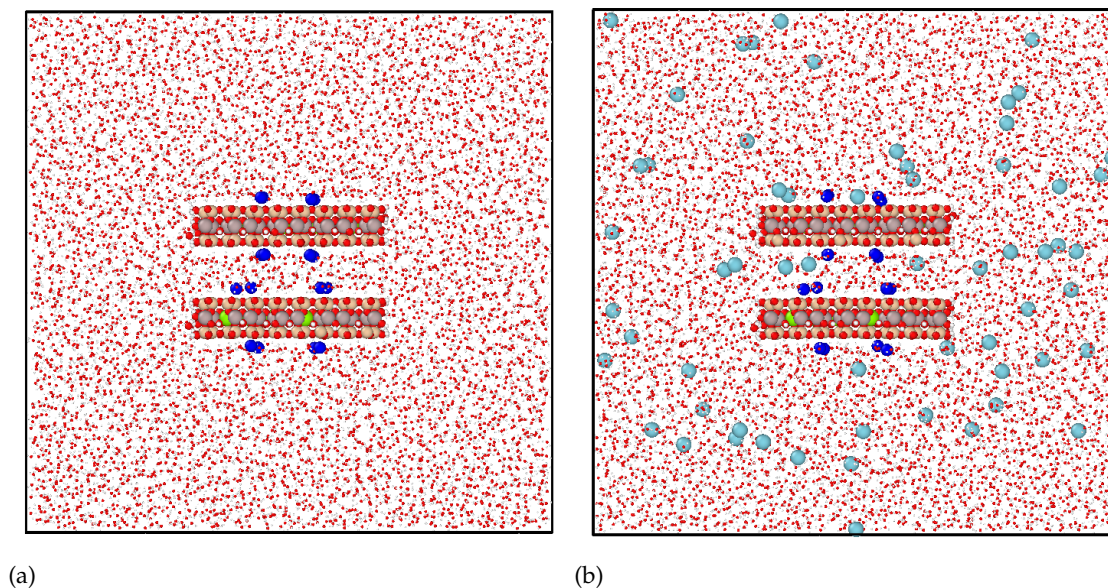


FIGURE 4.2: Simulation box representing smectite clay mineral (Na-montmorillonite) submerged in water (a) pure water and (b) 0.5 mol/L gas solution (gas molecules are represented in light blue) viewed in the x-direction. The y- and z- directions of the simulation box are approximately 10 nm.

To investigate the effect of d-spacing on the swelling pressure of Na-montmorillonite, a periodic simulation box was constructed, with dimensions of $2.09 \text{ nm} \times 10 \text{ nm} \times 10 \text{ nm}$, containing a small Na-montmorillonite particle with an initial d-spacing of 1.2 nm. The d-spacing was systematically varied from 1.2 nm to 3.0 nm in increments of 0.1 nm to generate individual systems of variable initial d-spacing. The simulation box was filled with approximately 6000 water molecules, randomly distributed throughout the space. The system was subjected to an energy minimization step, followed by a 1 ns equilibration in the NPT ensemble at a pressure of 1 bar and temperature of 300 K, with all dimensions of both clay layers fixed. The velocity rescaling thermostat [9] and Berendsen barostat [8] were employed to regulate the temperature and pressure, respectively. A 50 ns production simulation was then conducted in the NVT ensemble to calculate the equilibrium spacing between the parallel clay particles.

In this simulation, the lower clay particle was fixed in all dimensions, while the upper particle was fixed only in the x and y directions. A total of 64 springs with force constants ranging from 1 to 12 kJ/mol/nm^2 (in steps of 1 kJ/mol/nm^2) were fixed to the upper tetrahedral plate of the top layer. The force constant was kept constant for all springs in each individual simulation. The Lennard-Jones and short-range Coulomb potentials were used to calculate the short-range interactions with a cutoff of 0.9 nm, while the long-range electrostatic interactions were calculated using the smooth particle-mesh Ewald (PME) method [13]. A time step of 1.0 fs was used and data were collected every 5 ps.

For each combination of force constant and initial d-spacing, individual simulations were performed with pure water and dissolved gas solutions of CO_2 , CH_4 , H_2 , Ar, and He. A gas concentration of 0.5 mol/L was achieved by randomly distributing the gas molecules in the

system of pure water (as shown in Figure 4.2b). To ensure that the system was properly equilibrated, solvent and solute exchanges were monitored and it could be demonstrated that the average lifetime of the molecules in the interlayer is less than 50 nm, and as such molecules of water and gases effectively do exchange during equilibration and production. Simulation runs were also investigated at the smallest interlayer distances.

4.3 Results and discussion

4.3.1 Swelling pressure of Na-montmorillonite in pure water

First molecular dynamics simulations of Na-montmorillonite swelling in pure water were performed to validate the simulation setup. Figure 4.3 shows the results of the swelling pressure calculations as a function of the initial dry density of the clay and compares them with the previous theoretical studies as well as experimental measurements [3, 22, 23, 46]. We would like to emphasize that our simulations cover a broad range of dry densities up to 2.0 g/cm^3 , well beyond the one typically studied in the past by molecular simulations.

The graph clearly demonstrates the exponential relationship between swelling pressure and the dry density of clay. Swelling pressure ranging from approximately 0.1 MPa at a dry density of 0.8 g/cm^3 to approximately 35 MPa at a dry density of 1.65 g/cm^3 was observed in this study. These results agree well with previous results obtained with the same modeling approach and the simulation conditions, such as Akinwunmi et al. [3] and Sun et al. [46]. Although a difference of around 5 MPa was noted, it can be explained by the variation in layer charge associated with Na-montmorillonite. In this study, the layer charge of montmorillonite is $-1.0 e$ per unit cell, whereas Akinwunmi et al. [3] and Sun et al. [46] employed a layer charge of $-0.5 e$ per unit cell. It has been previously demonstrated by Sun et al. [45] that smectites with a higher layer charge exhibit lower swelling pressures compared to those with a lower layer charge. Moreover, the results obtained in this study are in good agreement (from 0.8 g/cm^3 to 1.6 g/cm^3) with experimental swelling studies conducted on smectite clay by Karnland et al. [22, 23].

Interestingly, the simulation at higher dry densities, e.g. above 1.65 g/cm^3 , results in a broad range of swelling pressures varying from nearly 3 to 20 MPa, with an average value of 11 MPa. The obtained average swelling pressure is thus lower than the peak value of 35 MPa observed for 1.65 g/cm^3 . At first glance, the predicted decrease in swelling pressure at high compaction seems to contradict the experimentally observed exponential trend. However, careful structural analysis of the interlayer water density reveals that the system set up at 2.0 g/cm^3 corresponds to a d-spacing of 1.27 nm, which is typical for monolayer water density distribution. In such a structural configuration, the interlayer cations are primarily coordinated by basal oxygen sites (e.g. inner sphere complexes) and are only partially solvated by water molecules. This principal change in the solvation structure of the interlayer cations, e.g. the transition from fully hydrated outer-sphere complexes to the partially hydrated inner-sphere cations is clearly seen in Figure S1-S8. This structural change in the interlayer is the main reason for the

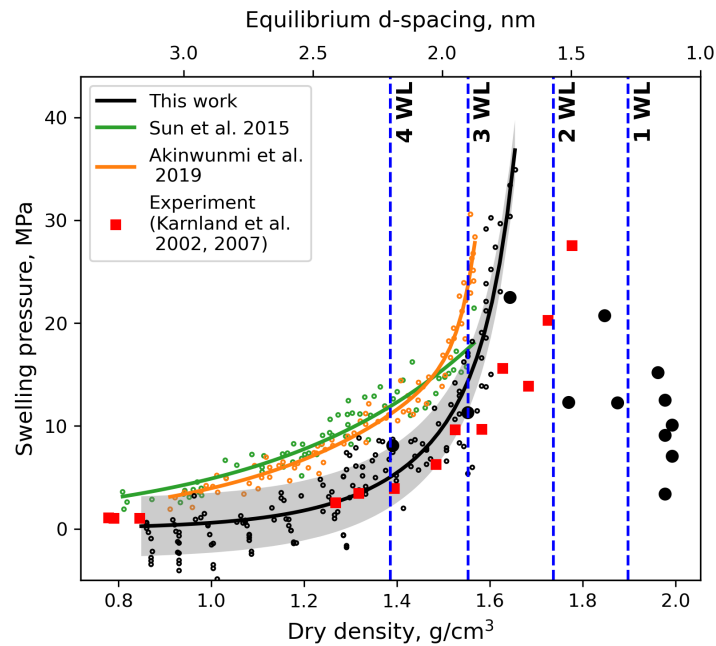


FIGURE 4.3: Swelling pressure of Na-montmorillonite in pure water as a function of clay dry density from molecular dynamics simulations [3, 46] and experimental study [22, 23]. The solid black circles represent the simulation of pure water at high density.

apparent reduction of swelling pressure. The mono- and bi-layer state of the interlayer water are stable structural configurations corresponding to a local minimum of the free energy of montmorillonite. The large variability in the simulation runs at 2.0 g/cm^3 is likely related to different structural arrangements of sodium ions in the interlayer. Kosakowski et al. [25] have shown that in a low hydration state, the interlayer cations are located either on the top of octahedral sites or in the hexagonal cavities of the basal plane. These conformations result in slightly different interlayer spacing, water content, and eventually the swelling pressure.

The discrepancy observed between the experimental behavior of highly compacted macroscopic samples and the modeling results at small d-spacing can be attributed to the macroscopic microstructure of clay, namely specifically the arrangement of clay stacks, as well as the presence of disorder. The setup in molecular dynamic simulations primarily considers the interaction between perfectly aligned clay platelets, whereas the measured experimental samples consist of semi-aligned and partially disordered mineral grains represented by aligned TOT stacks. The main factor contributing to the experimentally measured swelling pressure under such conditions is the interaction of poorly aligned platelets at grain boundaries. Figure 4.4 shows a model-based representation of macroscopic clay particle arrangement used in the simulation of clay microstructure. The MD simulations reflect the interaction between the perfectly aligned clay platelets. The natural samples consist of mineral grains represented by aligned TOT stacks similar to the one used in the MD simulations. The contribution of the TOT stacks with mono- and bi-layer water to swelling pressure is small. The main contribution to the experimentally measured swelling pressure is coming under such a condition due to osmotic interaction in larger inter-particle pores and at grain boundaries.

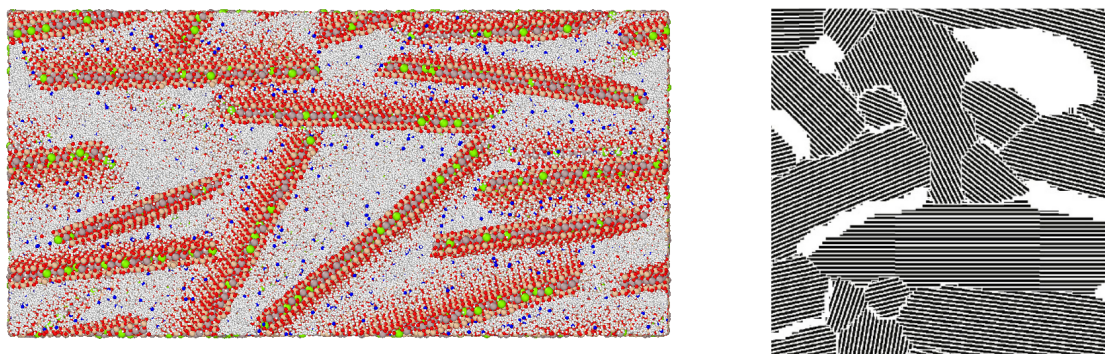


FIGURE 4.4: The structure of clay from a macroscopic perspective, highlighting poorly aligned platelets at the boundaries between grains. The left image displays an atomistic view, while the right shows a pore-scale view. Reproduced with permission [17, 49].

4.3.2 Swelling pressure of Na-montmorillonite in the presence of dissolved gases

The swelling pressure of Na-montmorillonite in the presence of gas molecules is shown in Figure 4.5. The system was set up by randomly inserting CO_2 , Ar, H_2 , He, and CH_4 molecules with the aim of achieving a concentration of 0.5 mol/L for each gas in the pure water phase. The concentration of gaseous molecules used in this study exceeds the experimental solubility limit under ambient conditions but is close to the in situ conditions in the underground repository at 12 MPa. This concentration was chosen due to a balance between computational efficiency and statistical uncertainty. Previous MD simulations of gas diffusion in a similar clay system have demonstrated that the diffusion coefficient of dissolved gases at a concentration of 0.5 mol/L are well in agreement with data reported for a system with lower concentration corresponding to the solubility at 0.1 MPa [34].

The swelling behavior of clay minerals, including Na-montmorillonite, is controlled by the chemical potential and osmotic pressure difference between the bulk-like and the interlayer solution [29, 48]. The chemical potential is a fundamental quantity that characterizes the thermodynamic state of the system and depends on a number of variables such as temperature, pressure, and concentration of the chemical composition of the system [44]. The chemical potential solvent is particularly sensitive to the concentration of solutes. At least in dilute electrolytes, it increases with an increase in the ionic concentration [4]. This dependence drives water from domains with higher chemical potential to compartments with lower chemical potential. In pure water, the osmotic pressure gradient between the interlayer (high osmotic pressure) and the surrounding solution (low osmotic pressure), triggers water influx into the interlayer and eventually causes the dispersion of clay particles in the absence of confinement. The extent of swelling is influenced by several factors, including the charge, size, and hydration energy of cations as well as other parameters related to the chemical composition of clay minerals and their structure [44, 48]. The presence of ions in the solution reduces the chemical potential of water and, consequently, reduces the swelling pressure of clay minerals [31]. Due to the hydrophobic nature of the interaction between non-polar gas molecules and water, the activity

coefficient of water in the presence of gases can become greater than one [36]. This behavior can be attributed to a decrease in solvent entropy. Therefore, a comprehensive understanding of the intricate interplay between the various factors that influence the swelling behavior of clay minerals is critical for predicting and controlling their behavior in diverse applications.

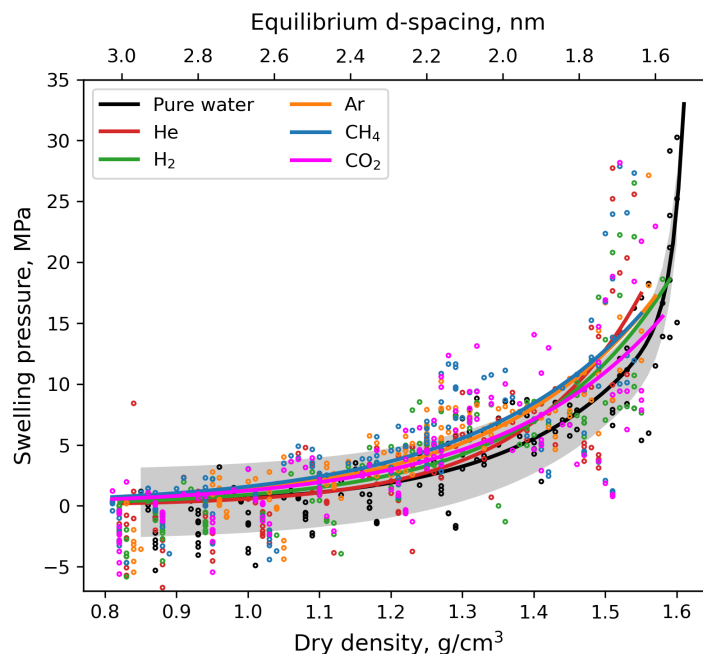


FIGURE 4.5: Swelling pressure of Na-montmorillonite in dissolved gas solution as a function of clay dry density from molecular dynamics simulations. The gray area shows the error margin for simulations with pure water. This consists of 720 individual simulations of different d-spacing, force constant, and gas species combinations.

The simulation results shown in Figure (4.5), indicate a slight increase in the swelling pressure of Na-montmorillonite up to about 3 MPa in comparison to its swelling in pure water. Analysis of the trajectory of gas particles indicates that gas molecules increase in concentration within the interlayer from large to low d-spacings (see Figure 4.6 leading to an increase in osmotic potential and a higher swelling pressure in the interlayer. The observed effect of the addition of gas molecules on swelling is contrary to the behavior of electrolyte solution [3, 15, 18, 46], which typically leads to a reduction of swelling pressure. The observed integral effect is related to several factors, including the partitioning of gas molecules between the bulk solution and interlayer space, hydrophobic interactions of non-polar gases, and the increase in the gas solubility in water with increasing pressure. These factors collectively contribute to a positive deviation of the non-ideality of water mixing in the presence of dissolved gas molecules.

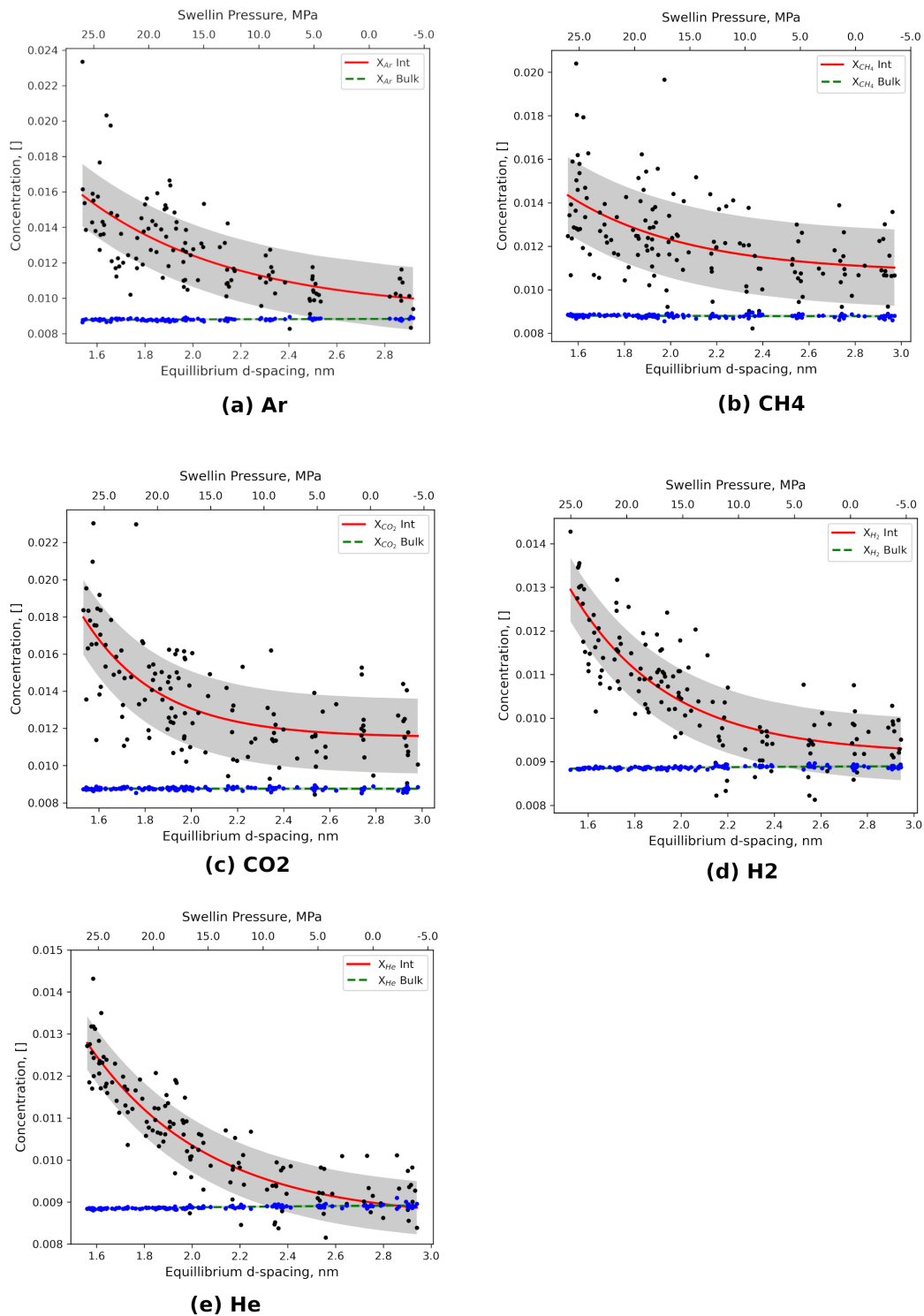


FIGURE 4.6: Mole fraction of gas in the interlayer as a function of equilibrium interlayer spacing.

Figure 4.6 shows the mole fraction of gas in the interlayer as a function of interlayer spacing and also the swelling pressure. At low dry density (large d-spacing) the composition of the fluid in the external reservoir and the interlayer are nearly the same, indicating that "large interlayer" and bulk domains are thermodynamically identical at such conditions. As d-spacing decreases

(higher dry density and swelling pressure in the interlayer), the gas solubility in the interlayer increases resulting in a stronger affinity of gas molecules towards the interlayer. Consequently, the observed increase in the swelling pressure of Na-montmorillonite in the presence of gas molecules should be attributed to the chemical potential gradient leading to the partitioning of gas molecules in the interlayer with decreasing d-spacing.

The results shown in Figure 4.5 indicate that polyatomic larger gas molecules (Ar, CO₂, and CH₄), exhibit a slightly elevated swelling pressure of approximately 2 MPa relative to smaller gas molecules (He, and H₂) at high dry densities (> 1.0 g/cm³). At very low dry densities (<1.0 g/cm³), however, the aforementioned trend is less significant where all swelling behavior converges to the behavior of pure water. To explore further the correlation between gas species and swelling behavior, we express the fluid composition in the interlayer as a function of molecular size (see Figure 4.7), indicated by the position of the first maxima of the gas-water (Oxygen of water) radial distribution function (r_{max}). Subsequently, we conducted a comparison of the swelling pressures within the dry density range of 0.9 - 1.5 g/cm³. The observed trends are likely to be explained by the pressure dependence of gas solubility and the stronger effect of the larger polyatomic molecules.

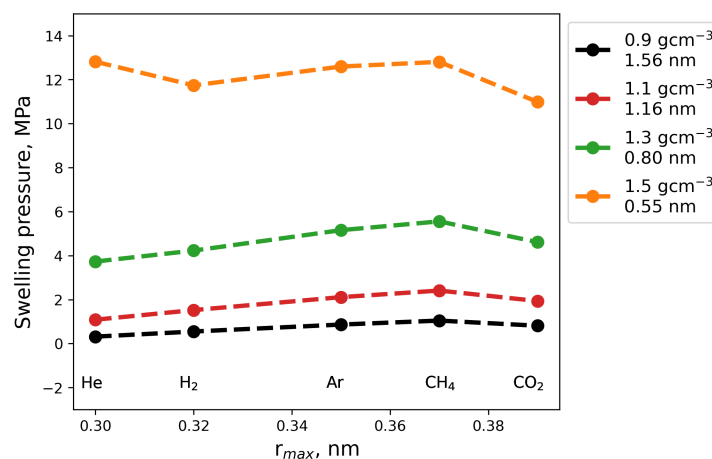


FIGURE 4.7: Comparison of swelling pressure of Na-montmorillonite for dry densities: 0.9 - 1.5 g/cm³. Lines are shown to guide the eye. The values below the density values in the legend indicate the interlayer pore size.

4.4 Conclusions

Classical molecular dynamics simulations were used in this study to examine the impact of dissolved gas molecules on the swelling pressure of smectite clay. The simulations employed the spring model and analyzed the swelling pressures of Na-montmorillonite with various gas species (Ar, He, H₂, CO₂, and CH₄) in a systematic manner. For validation and comparison with gas-containing systems, simulations were also performed for Na-montmorillonite in pure water. The results revealed that the presence of gas molecules increased the swelling pressure of Na-montmorillonite by approximately 3 MPa. This can be explained by the increase of the gas solubility with the swelling pressure. The swelling pressure behavior varied based on the

dry density of the clay and the type of gas species present. Small monoatomic gases exhibited lower swelling pressures than polyatomic gases at high dry densities, but this behavior was less significant at low dry densities, where all swelling behavior converged to the behavior of pure water. The concentration and size of gas molecules in the interlayer were identified as critical factors influencing the osmotic pressure difference that affects swelling. These findings provide insight into the intricate interactions between gas molecules and clay minerals, their impact on swelling pressure, and their potential utilization in designing and optimizing effective barriers for deep geological disposal of nuclear waste. Additional studies are needed to examine the influence of gas concentration on swelling pressure. Recent research [5] suggests that methane solubility increases under confinement, indicating the need for further investigation in this area.

Supporting Information

The supporting information (Appendix) contains the plots of the density distribution of water and gases in the interlayer of smectites as well as their radial distribution functions.

Acknowledgement

The research reported in this paper was supported by EURAD GAS FUTURE and DONUT Work Packages, Laboratory for Waste Management at the Paul Scherrer Institute, NAGRA, and the University of Bern Geological Institute. Molecular dynamics simulations were carried out using resources from the Paul Scherrer Institute (MERLIN 6), the University of Bern (UBELIX), and the Swiss National Super Computing Centre (Piz Daint). The authors acknowledge the co-funding from Horizon 2020 EURAD project Grant ID 847593.

4.5 Appendix

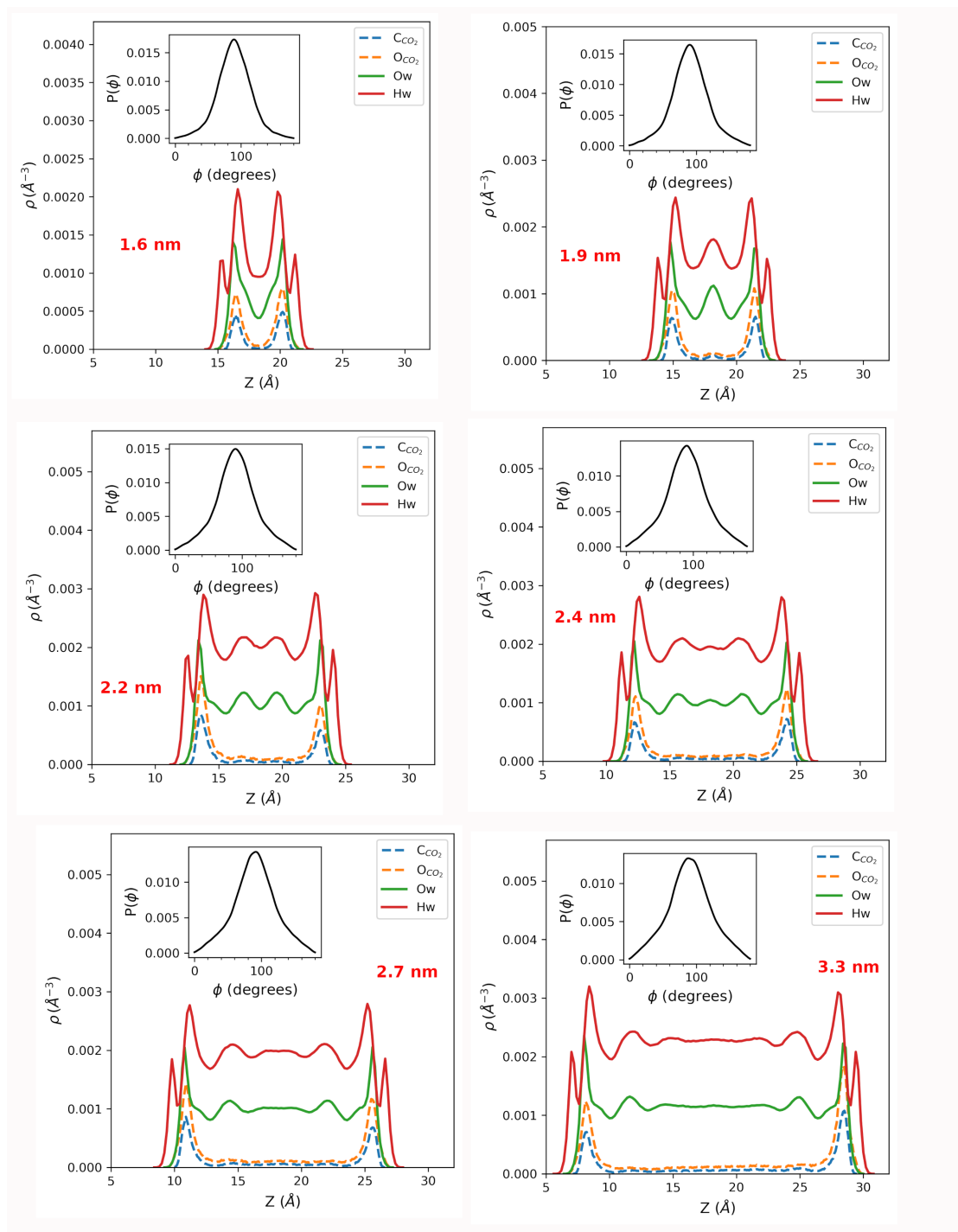


FIGURE 4.8: Density profiles of water and for CO₂ molecules in the interlayer ranging from d-spacing of 1.6 to 3.3 nm [34]

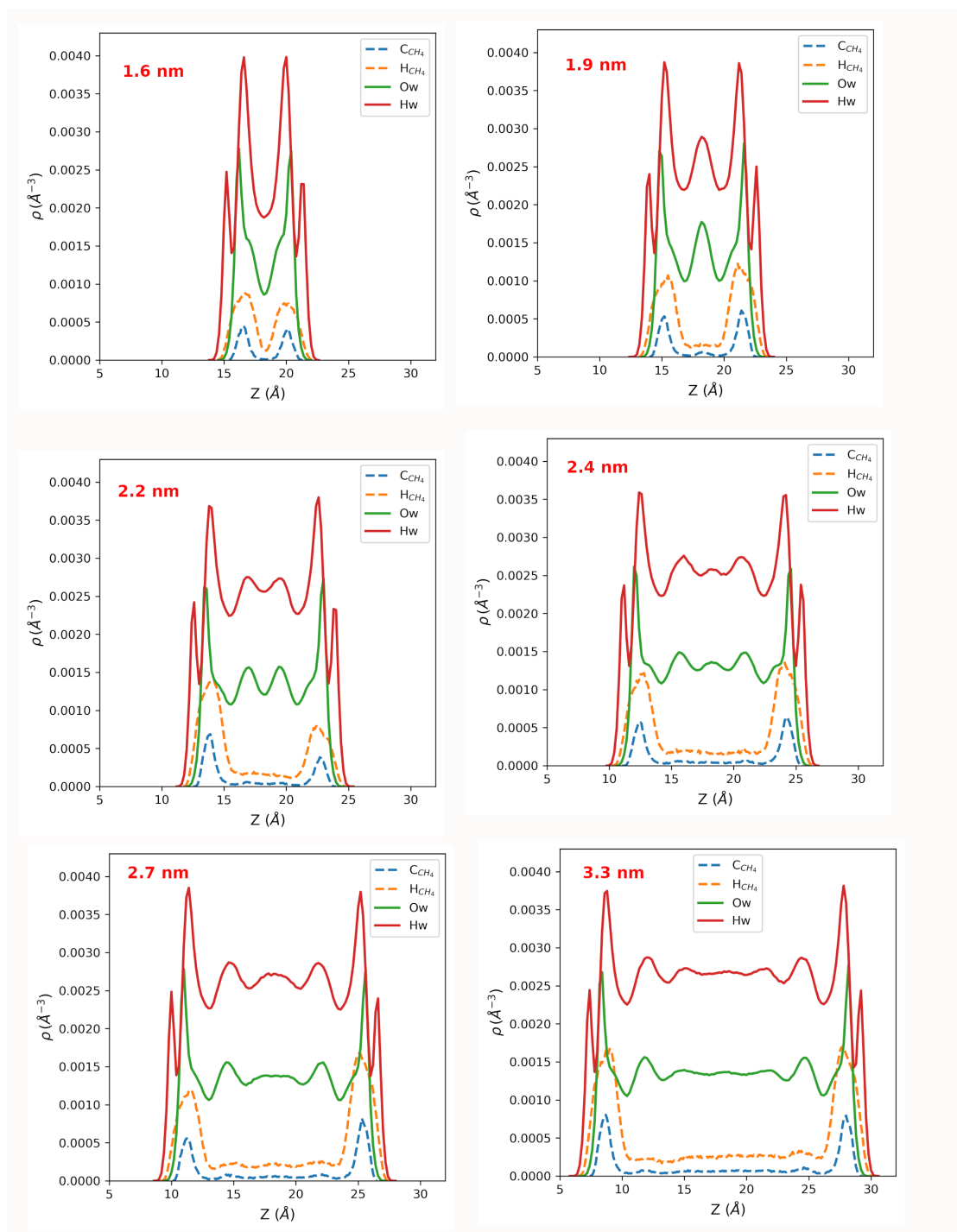


FIGURE 4.9: Density profiles of water and for CH_4 molecules in the interlayer ranging from d-spacing of 1.6 to 3.3 nm [34]

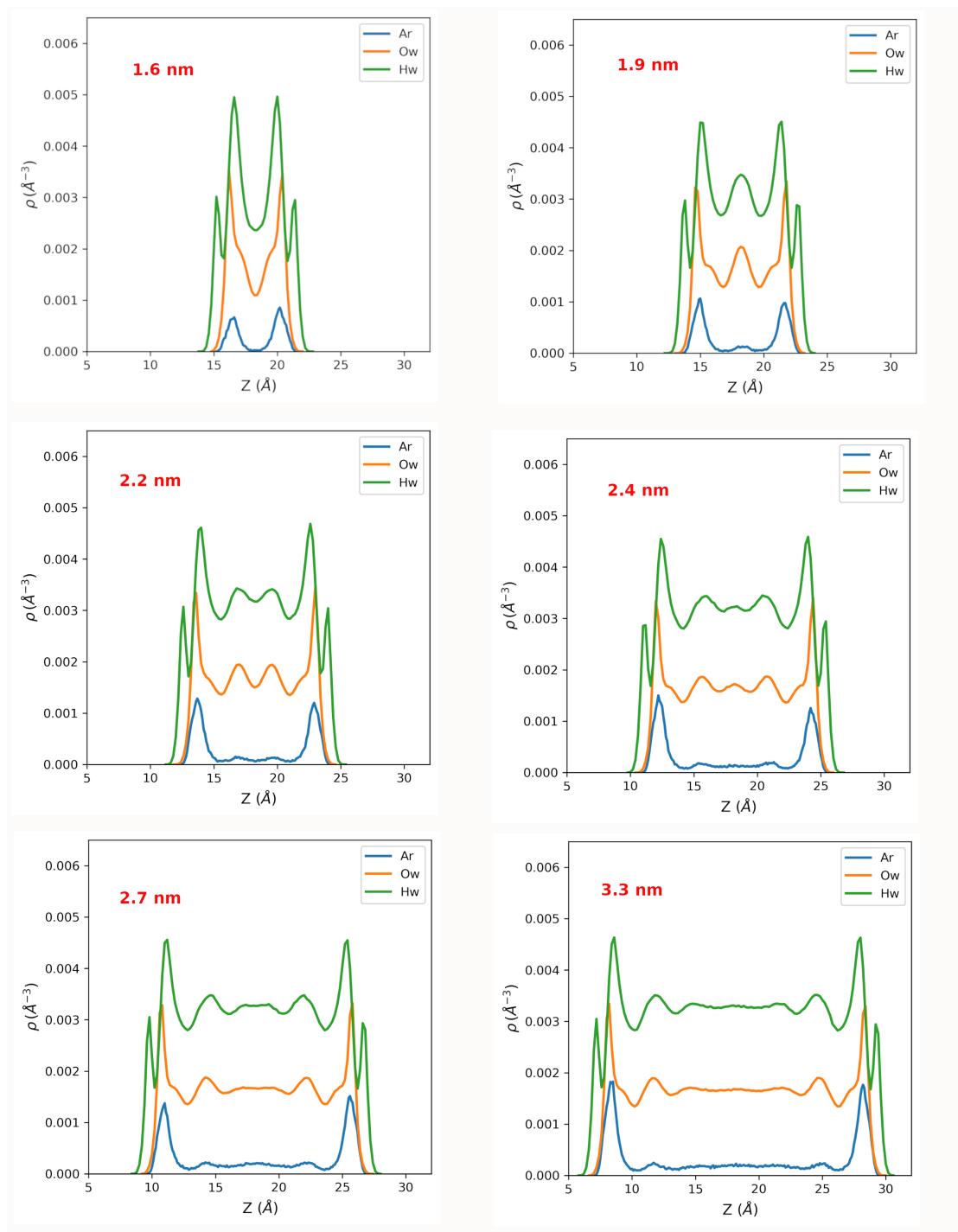


FIGURE 4.10: Density profiles of water and for Ar molecules in the interlayer ranging from d-spacing of 1.6 to 3.3 nm [34]

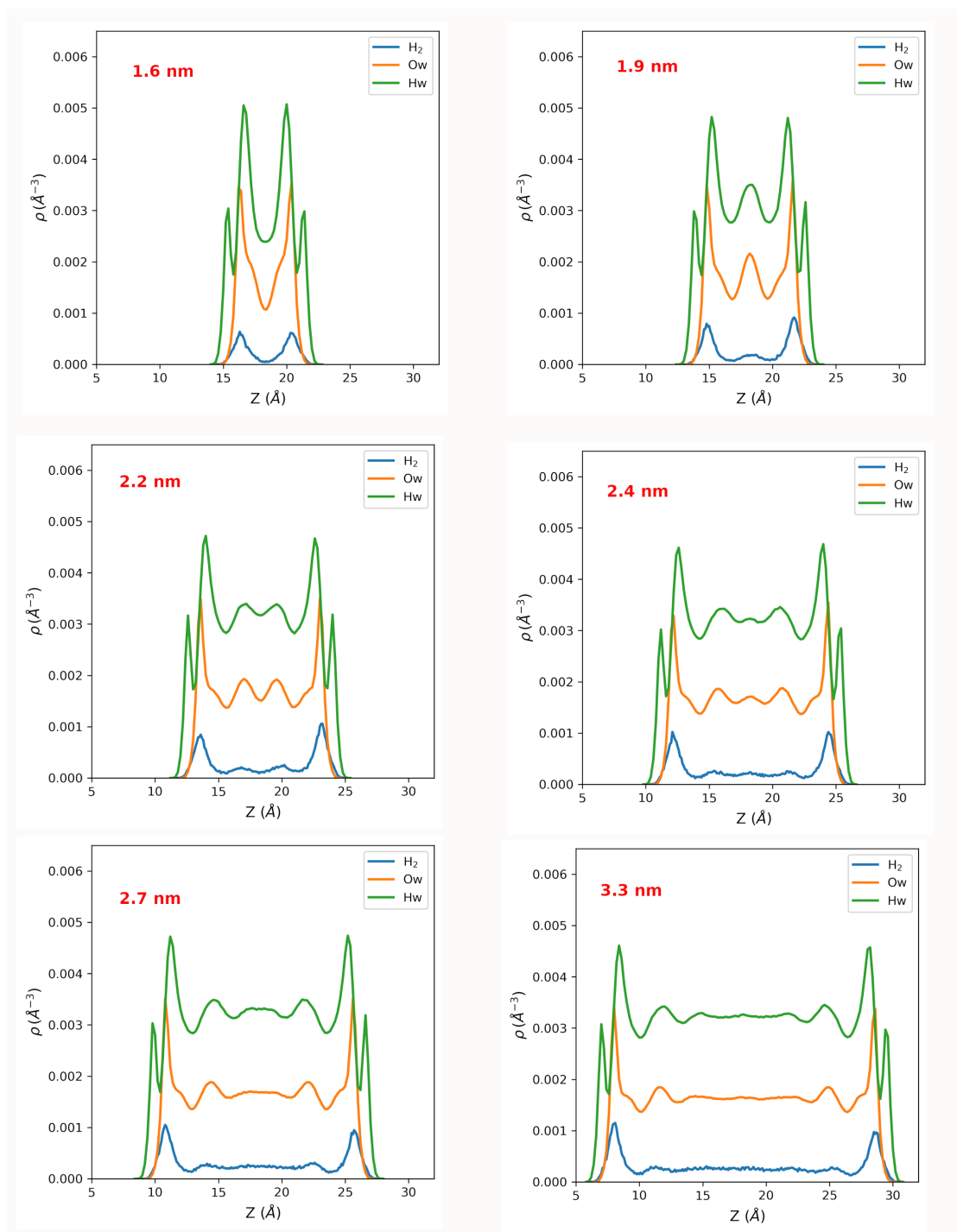


FIGURE 4.11: Density profiles of water and for H_2 molecules in the interlayer ranging from d-spacing of 1.6 to 3.3 nm [34]

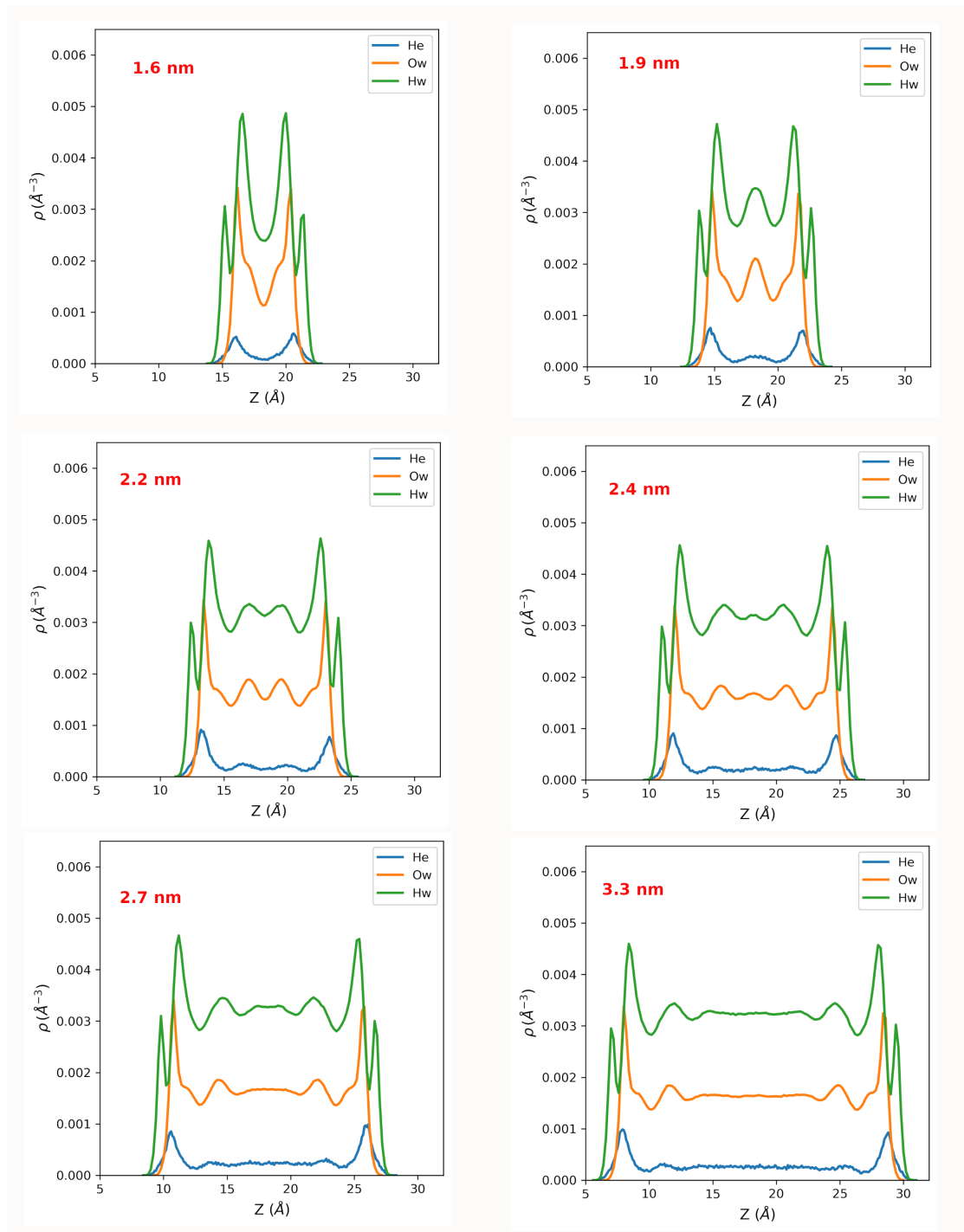


FIGURE 4.12: Density profiles of water and for He molecules in the interlayer ranging from d-spacing of 1.6 to 3.3 nm [34]

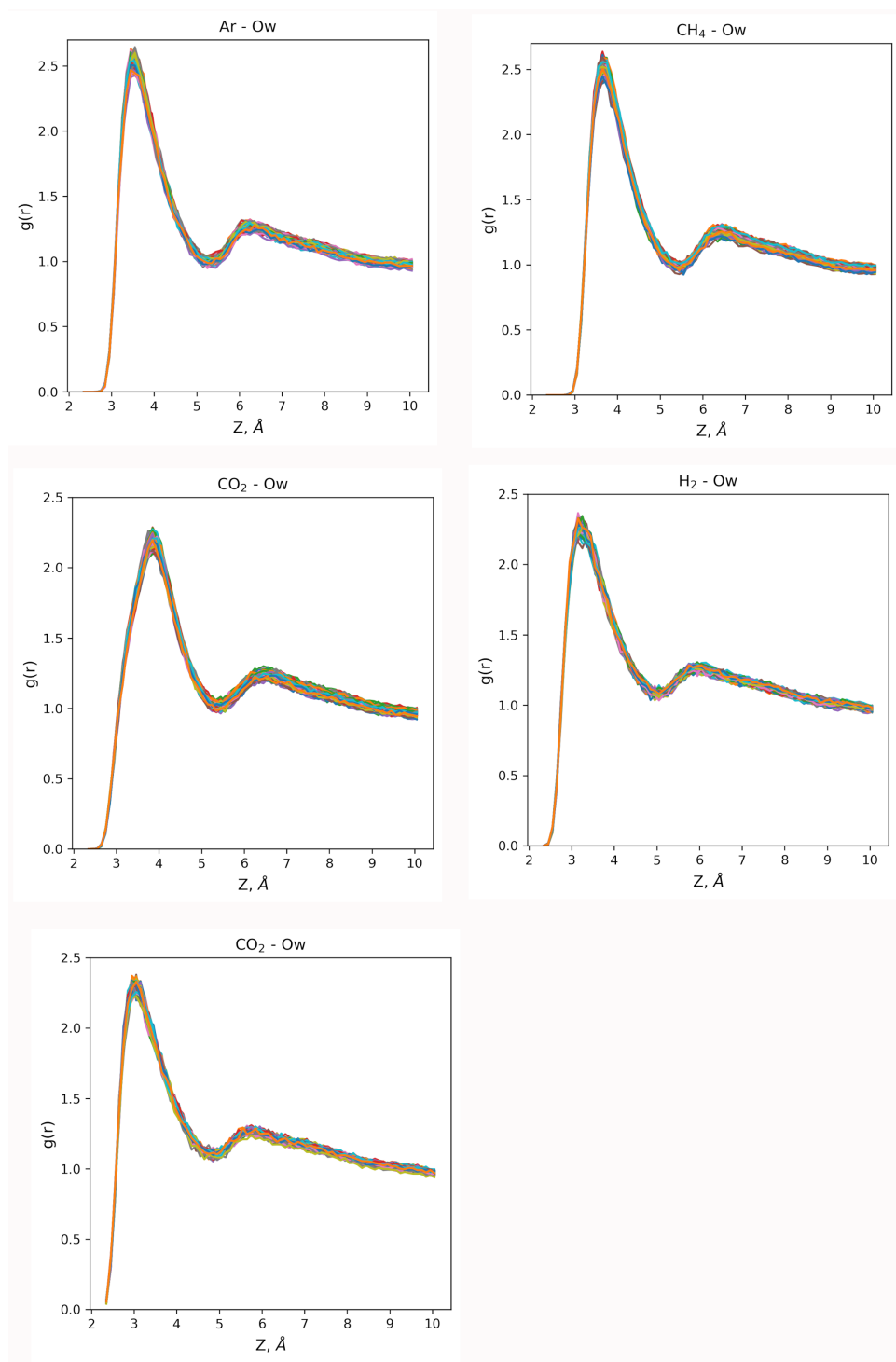


FIGURE 4.13: Radial distribution function of gas molecules and oxygen of water molecule for all d-spacings and force constants

4.6 References

- [1] Akinwunmi, B., Hirvi, J. T., Kasa, S., and Pakkanen, T. A. (2020a). Swelling pressure of na-and ca-montmorillonites in saline environments: A molecular dynamics study. *Chemical Physics*, 528:110511.
- [2] Akinwunmi, B., Kporha, F. E., Hirvi, J. T., Kasa, S., and Pakkanen, T. A. (2020b). Atomistic simulations of the swelling behaviour of na-montmorillonite in mixed nacl and cacl₂ solutions. *Chemical Physics*, 533:110712.
- [3] Akinwunmi, B., Sun, L., Hirvi, J. T., Kasa, S., and Pakkanen, T. A. (2019). Influence of temperature on the swelling pressure of bentonite clay. *Chemical Physics*, 516:177–181.
- [4] Baierlein, R. (2001). The elusive chemical potential. *American Journal of Physics*, 69(4):423–434.
- [5] Benazzouz, B. K., Ho, K. H., Nguyen, P. T., Hoang, H., and Galliero, G. (2022). Diffusive transport of gases in saturated nanopores: Caprock leakage from a molecular simulation perspective. *Journal of Natural Gas Science and Engineering*, 98:104383.
- [6] Bérend, I., Cases, J.-M., François, M., Uriot, J.-P., Michot, L., Masion, A., and Thomas, F. (1995). Mechanism of adsorption and desorption of water vapor by homoionic montmorillonites: 2. the li⁺ na⁺, k⁺, rb⁺ and cs⁺-exchanged forms. *Clays and Clay Minerals*, 43(3):324–336.
- [7] Berendsen, H., Grigera, J., and Straatsma, T. (1987). The missing term in effective pair potentials. *Journal of Physical Chemistry*, 91(24):6269–6271.
- [8] Berendsen, H. J., Postma, J. v., Van Gunsteren, W. F., DiNola, A., and Haak, J. R. (1984). Molecular dynamics with coupling to an external bath. *The Journal of chemical physics*, 81(8):3684–3690.
- [9] Bussi, G., Donadio, D., and Parrinello, M. (2007). Canonical sampling through velocity rescaling. *The Journal of chemical physics*, 126(1):014101.
- [10] Churakov, S. V. (2013). Mobility of na and cs on montmorillonite surface under partially saturated conditions. *Environmental science & technology*, 47(17):9816–9823.
- [11] Churakov, S. V., Hummel, W., and Fernandes, M. M. (2020). Fundamental research on radiochemistry of geological nuclear waste disposal. *Chimia*, 74(12):1000–1000.
- [12] Cygan, R. T., Greathouse, J. A., Heinz, H., and Kalinichev, A. G. (2009). Molecular models and simulations of layered materials. *Journal of Materials Chemistry*, 19(17):2470–2481.
- [13] Darden, T., York, D., and Pedersen, L. (1993). Particle mesh ewald: An nlog(n) method for ewald sums in large systems. *The Journal of chemical physics*, 98(12):10089–10092.
- [14] Delage, P., Cui, Y.-J., and Tang, A. M. (2010). Clays in radioactive waste disposal. *Journal of Rock Mechanics and Geotechnical Engineering*, 2(2):111–123.

- [15] Fayoyiwa, A. D., Sun, L., Hirvi, J. T., Kasa, S., and Pakkanen, T. A. (2019). Effect of iron (iii) on the swelling pressure of dioctahedral smectites: A molecular dynamics study. *Chemical Physics Letters*, 736:136818.
- [16] Fu, M., Zhang, Z., and Low, P. (1990). Changes in the properties of a montmorillonite-water system during the adsorption and desorption of water: hysteresis. *Clays and Clay Minerals*, 38:485–492.
- [17] Gimmi, T. and Churakov, S. V. (2019). Water retention and diffusion in unsaturated clays: Connecting atomistic and pore scale simulations. *Applied Clay Science*, 175:169–183.
- [18] Herbert, H.-J., Kasbohm, J., Sprenger, H., Fernández, A. M., and Reichelt, C. (2008). Swelling pressures of mx-80 bentonite in solutions of different ionic strength. *Physics and Chemistry of the Earth, Parts a/b/c*, 33:S327–S342.
- [19] Hess, B., Kutzner, C., Van Der Spoel, D., and Lindahl, E. (2008). Gromacs 4: algorithms for highly efficient, load-balanced, and scalable molecular simulation. *Journal of chemical theory and computation*, 4(3):435–447.
- [20] Higgo, J. (1987). Clay as a barrier to radionuclide migration. *Progress in Nuclear Energy*, 19(2):173–207.
- [21] Hsiao, Y.-W. and Hedstr oom, M. (2017). Swelling pressure in systems with na-montmorillonite and neutral surfaces: a molecular dynamics study. *The Journal of Physical Chemistry C*, 121(47):26414–26423.
- [22] Karnland, O. and Muurinen, A. (2002). Bentonite swelling pressure in nacl solutions-experimentally determined data and model calculations.
- [23] Karnland, O., Olsson, S., Nilsson, U., and Sellin, P. (2007). Experimentally determined swelling pressures and geochemical interactions of compacted wyoming bentonite with highly alkaline solutions. *Physics and Chemistry of the Earth, Parts A/B/C*, 32(1-7):275–286.
- [24] Komine, H. and Ogata, N. (1996). Prediction for swelling characteristics of compacted bentonite. *Canadian geotechnical journal*, 33(1):11–22.
- [25] Kosakowski, G., Churakov, S. V., and Thoenen, T. (2008). Diffusion of na and cs in montmorillonite. *Clays and Clay Minerals*, 56(2):190–206.
- [26] Laird, D. A. (1999). Layer charge influences on the hydration of expandable 2: 1 phyllosilicates. *Clays and Clay Minerals*, 47:630–636.
- [27] Laloui, L., Ferrari, A., and Bosch Llufrui, J. A. (2020). Bentonite clay barriers in nuclear waste repositories. In *E3S Web of Conferences*, volume 205. EDP SCIENCES.
- [28] Malikova, N., Marry, V., Dufrêche, J.-F., and Turq, P. (2004). Na/cs montmorillonite: temperature activation of diffusion by simulation. *Current opinion in colloid & interface science*, 9(1-2):124–127.

- [29] Meleshyn, A. and Bunnenberg, C. (2005). The gap between crystalline and osmotic swelling of na-montmorillonite: A monte carlo study. *The Journal of chemical physics*, 122(3):034705.
- [30] Meunier, A., Velde, B., and Griffault, L. (1998). The reactivity of bentonites: a review. an application to clay barrier stability for nuclear waste storage. *Clay Minerals*, 33(2):187–196.
- [31] Mooney, R., Keenan, A., and Wood, L. (1952). Adsorption of water vapor by montmorillonite. ii. effect of exchangeable ions and lattice swelling as measured by x-ray diffraction. *Journal of the American Chemical Society*, 74(6):1371–1374.
- [32] Norrish, K. (1954). The swelling of montmorillonite. *Discussions of the Faraday society*, 18:120–134.
- [33] Ortiz, L., Volckaert, G., and Mallants, D. (2002). Gas generation and migration in boom clay, a potential host rock formation for nuclear waste storage. *Engineering geology*, 64(2-3):287–296.
- [34] Owusu, J. P., Karalis, K., Prasianakis, N. I., and Churakov, S. V. (2022). Mobility of dissolved gases in smectites under saturated conditions: Effects of pore size, gas types, temperature, and surface interaction. *The Journal of Physical Chemistry C*, 126(40):17441–17455.
- [35] Parfitt, R., Giltrap, D., and Whitton, J. (1995). Contribution of organic matter and clay minerals to the cation exchange capacity of soils. *Communications in soil science and plant analysis*, 26(9-10):1343–1355.
- [36] Prausnitz, J. M., Lichtenthaler, R. N., and De Azevedo, E. G. (1998). *Molecular thermodynamics of fluid-phase equilibria*. Pearson Education.
- [37] Pusch, R. (1992). Use of bentonite for isolation of radioactive waste products. *Clay minerals*, 27(3):353–361.
- [38] Pusch, R. and Yong, R. N. (2006). *Microstructure of smectite clays and engineering performance*. CRC Press.
- [39] Rodwell, W., Harris, A., Horseman, S., Lalieux, P., Müller, W., Ortiz Amaya, L., and Pruess, K. (1999). Gas migration and two-phase flow through engineered and geological barriers for a deep repository for radioactive waste. *EUR(Luxembourg)*.
- [40] Salles, F., Beurroies, I., Bildstein, O., Jullien, M., Raynal, J., Denoyel, R., and Van Damme, H. (2008). A calorimetric study of mesoscopic swelling and hydration sequence in solid na-montmorillonite. *Applied Clay Science*, 39(3-4):186–201.
- [41] Schanz, T. and Al-Badran, Y. (2014). Swelling pressure characteristics of compacted chinese gaomiaozhi bentonite gmz01. *Soils and Foundations*, 54(4):748–759.
- [42] Segad, M., Jonsson, B., Åkesson, T., and Cabane, B. (2010). Ca/na montmorillonite: structure, forces and swelling properties. *Langmuir*, 26(8):5782–5790.

- [43] Small, J. S., Nykyri, M., Vikman, M., Itävaara, M., and Heikinheimo, L. (2017). The biogeochemistry of gas generation from low-level nuclear waste: Modelling after 18 years study under in situ conditions. *Applied Geochemistry*, 84:360–372.
- [44] Smith, D. E., Wang, Y., Chaturvedi, A., and Whitley, H. D. (2006). Molecular simulations of the pressure, temperature, and chemical potential dependencies of clay swelling. *The Journal of Physical Chemistry B*, 110(40):20046–20054.
- [45] Sun, L., Ling, C. Y., Lavikainen, L. P., Hirvi, J. T., Kasa, S., and Pakkanen, T. A. (2016). Influence of layer charge and charge location on the swelling pressure of dioctahedral smectites. *Chemical Physics*, 473:40–45.
- [46] Sun, L., Tanskanen, J. T., Hirvi, J. T., Kasa, S., Schatz, T., and Pakkanen, T. A. (2015). Molecular dynamics study of montmorillonite crystalline swelling: Roles of interlayer cation species and water content. *Chemical Physics*, 455:23–31.
- [47] Teich-McGoldrick, S. L., Greathouse, J. A., Jove-Colon, C. F., and Cygan, R. T. (2015). Swelling properties of montmorillonite and beidellite clay minerals from molecular simulation: comparison of temperature, interlayer cation, and charge location effects. *The Journal of Physical Chemistry C*, 119(36):20880–20891.
- [48] Tournassat, C., Bourg, I. C., Holmboe, M., Sposito, G., and Steefel, C. I. (2016). Molecular dynamics simulations of anion exclusion in clay interlayer nanopores. *Clays and Clay Minerals*, 64(4):374–388.
- [49] Underwood, T. R. and Bourg, I. C. (2020). Large-scale molecular dynamics simulation of the dehydration of a suspension of smectite clay nanoparticles. *The Journal of Physical Chemistry C*, 124(6):3702–3714.
- [50] Xu, T., Senger, R., and Finsterle, S. (2008). Corrosion-induced gas generation in a nuclear waste repository: Reactive geochemistry and multiphase flow effects. *Applied Geochemistry*, 23(12):3423–3433.
- [51] Ye, W.-M., Zheng, Z., Chen, B., Chen, Y.-G., Cui, Y.-J., and Wang, J. (2014). Effects of pH and temperature on the swelling pressure and hydraulic conductivity of compacted gmz01 bentonite. *Applied Clay Science*, 101:192–198.
- [52] Yong, R., Taylor, L. O., and Warkentin, B. P. (1962). Swelling pressures of sodium montmorillonite at depressed temperatures. *Clays and Clay Minerals*, 11:268–281.
- [53] Yu, L. and Weetjens, E. (2009). Summary of gas generation and migration. *Current State-of-the-Art. SCK-CEN ER-106. SCK+ CEN, Mol, Belgium*.

Chapter 5: From Molecular Insights to Macroscopic Behavior: Up-scaling Diffusion in Smectites via Heterogeneous Pore-Scale Modeling

(manuscript in preparation)

From Molecular Insights to Macroscopic Behavior: Up-scaling Diffusion in Smectites via Heterogeneous Pore-Scale Modeling [†]

Jerry P. Owusu,^{*,‡,¶} Athanasios Mocos,[¶] Konstantinos Karalis,[‡] Nikolaos I. Prasianakis,[‡] and Sergey V. Churakov^{*,‡,¶}

[‡]*Laboratory for Waste Management, Paul Scherrer Institute, 5232 Villigen-PSI, Switzerland*

[¶]*University of Bern, Institute of Geological Sciences, 3012 Bern, Switzerland*

Abstract

The very low hydraulic conductivity of smectite-rich clay rocks makes them suitable host-rock for the construction of nuclear waste repositories and gas storage. The dominant mechanism governing solute and fluid transport in these clays is diffusion. Conventional approaches to solute transport describe clays as continuum media, oversimplifying the complex structure of pore space at the micro to nanometer scales. To address the effect of molecular scale interaction between solutes and mineral surfaces as well as the complexity of the pore space on the mobility of solutes in clays we conducted a comprehensive study of water diffusion combining the large-scale molecular dynamics simulations with pore-scale random walk simulations (RW) and lattice Boltzmann modeling (LB). Initially, we obtained local diffusion coefficients of water in smectite clays through molecular dynamics simulations, considering pore size and the effects relevant to the proximity to clay surfaces. These local diffusion coefficients were then assigned to the pore-scale smectite clay model, where RW and LB simulations were performed to determine the effective diffusion coefficient. To validate our approach, we compared the results of the pore scale simulations with large-scale MD simulations performed for the same structural model. Our findings demonstrate the significance of considering local diffusivities within the representative elementary volume (REV) to obtain a comprehensive understanding of transport mechanisms in porous materials, particularly across chemically reactive surfaces like clay minerals.

5.1 Introduction

Clay-based materials possess distinct physical and chemical properties that render them highly significant in various geological and environmental systems. Recently, these properties have acquired attention in the field of energy and waste storage due to their low permeability and high solute retention capacities, which effectively restrain the passage of fluids and chemical substances through their structure [2, 4, 36, 63]. Numerous studies have dedicated considerable attention to the examination of smectite clays as a prospective constituent in the deep geological disposal of High-Level Radioactive Waste (HLW) for the purpose of effectively sequestering the hazardous materials from the surrounding environment [17, 32, 35, 43]. In subsurface environments, smectite clays like Na-montmorillonite exhibit nearly negligible hydraulic conductivity [4], resulting in molecular diffusion becoming the primary mechanism for fluid and solute transport.

Macroscopic diffusion phenomena are commonly described by Fick's diffusion law [19]. Fick's second law mathematically predicts the impact of diffusion on concentration changes over time and can be expressed as:

$$\epsilon \frac{\partial C_i}{\partial t} = -\nabla \cdot J_i + R_i = \nabla \cdot (\epsilon D_p^{REV} \nabla C_i) + R_i \quad (5.1)$$

where, J_i represents the diffusion flux of species i , D_p^{REV} denotes the pore diffusion coefficient of species i in the Representative Elementary Volume (REV), C_i corresponds to the concentration of the i 's species, ϵ represents the porosity and R_i accounts for source and sink effects arising from the precipitation/dissolution of solid phases and sorption/desorption on mineral surfaces.

Considering the macroscopic properties of materials, the complex porous structure of clay media is often simplified by treating it as a continuum, where the properties of the media within a Representative Elementary Volume (REV) are averaged [3]. The REV represents the smallest volume from which a representative measurement can be obtained for the entire medium. At smaller sampled volumes, variations in material properties exist, while at larger volumes, properties remain constant. Continuum scale modeling divides domains into smaller volumes, with the assumption that the smallest volume represents a volume equal to or larger than a REV. This approach smears out phenomena occurring at scales below the REV. Molecular dynamics (MD) is a powerful method to study the diffusive transport of chemical species ranging from nm to sub μm scale [1, 12, 20, 21, 49, 58, 59, 65]. Such information from the sub-REV scale is necessary to understand molecular mechanisms responsible for the macroscopic diffusion pathways in porous media, its relation to the local geometry of pore space, and the details of the fluid surface interaction [14].

Advancements in molecular dynamics simulations have proven effective in studying the properties of clay materials [52, 53, 56]. With improved computational resources and parallelized algorithms, realistic atomistic models of clay mineral systems can be simulated on a large scale [52, 53]. However, conducting such simulations still requires substantial computational resources and incurs high costs.

Pore-scale modeling is an intermediate simulation scale that bridges the atomistic scale and the continuum scale. Various pore-scale methodologies such as random walk (RW) [14, 24, 29–31], lattice Boltzmann (LB) [26, 34], finite volume (FVM) [9, 46], smoothed particle hydrodynamics (SPH) [54, 67] and pore network modeling (PNM) [42, 60] have proven effective in examining complex characteristics, including the pore structure of porous materials at a reduced computational cost compared to large-scale MD simulations. The study of diffusive transport in porous clay materials has witnessed significant attention, particularly through the use of stochastic particle-based simulations. Notably, techniques such as random walk (RW) [14, 24, 29–31] and lattice Boltzmann (LB) [26, 34, 45] methods have emerged as prominent methods in this field.

The diffusion of chemical species within clays can be effectively studied using random walk (RW) simulations. In a random walk method, mass and/or energy carriers (random walker

particles) move stochastically with random displacement and directions defined by an algorithm-dependent probability distribution function. Specific reflection conditions are implemented if particles encounter impermeable boundaries. This stochastic process is characteristic of various phenomena, including the Brownian motion of small particles due to thermal motion or the spreading of an atom in a fluid. By applying appropriate statistical treatment, the random walk model can reproduce Fick's equation, which describes diffusion.

Labolle et al. [29] utilized random walk simulations to examine the properties of subsurface porous materials, considering their spatial variability and the resulting changes in transport coefficients. Churakov et al. [14] adopted a similar approach to explore the impact of mineralogical heterogeneities and anion exclusion on larger-scale diffusion coefficients in a model clay structure that resembled typical clay materials. Furthermore, Gimmi et al. [24] employed random walk simulations to replicate significant observations from experiments conducted on Opalinus and Callovo Oxfordian claystone. Their study focused on investigating water retention properties and solute transport in clay under unsaturated conditions [24].

The kinetic theory of gases explains that gases consist of particles that interact according to classical mechanics. However, due to the large number of particles involved, a statistical approach is needed. The Boltzmann distribution function, based on random collisions between gas particles, describes the probability distribution of particle velocities in gas at equilibrium. The Maxwell-Boltzmann distribution function quantifies the probability of finding a particle with a specific velocity. Lattice Boltzmann models simplify Boltzmann's concept by discretizing time and space, allowing the simulation of fluid behavior with fewer parameters. This method has been shown to be an accurate solver for the weakly compressible Navier-Stokes equation [48, 55]. The lattice Boltzmann modeling approach provides a versatile framework for simulating a wide range of dynamic phenomena. These include unsteady flows, phase separation, evaporation, condensation, cavitation, solute and heat transport, buoyancy, and surface interactions [7, 10, 11, 18, 23, 25, 33, 39, 44, 45, 47, 51, 57, 62, 64, 66]. Moreover, this method proves effective in achieving persistent metastable states [50].

Yang et al. [61] used lattice Boltzmann modeling to examine the diffusive transport of ions in porous microstructures of clays, focusing specifically on anion exclusion. They successfully provided direct evidence of flux variations resulting from an external temperature gradient applied to saturated clay. Genty et al. [22] also employed a Two-relaxation-time (TRT) lattice Boltzmann model to determine the effective diffusion coefficient of a non-reactive tracer within a micro-fracture of argillite. The study conducted unveiled a quasi-linear correlation between the effective diffusion coefficient at saturation within the range of 0.8 to 1. Furthermore, they observed a power law relationship at saturations ranging from 0.2 to 0.8. The lattice Boltzmann method offers an approach for coupling with other multi-physical models, enabling enhanced comprehension of transport phenomena within porous materials [27, 37]. For instance, O'Brien et al. [37] successfully combined the lattice Boltzmann model with a reactive transport model to investigate heterogeneous reactive transport of chemical species in a porous media. This coupling facilitated the incorporation of feedback between flow dynamics and chemical alterations. The validity of their model was confirmed through passive and reactive flow-cell

experiments conducted at a laboratory scale.

In this study, we present an upscaling methodology that bridges the molecular and pore scales, enabling a comprehensive analysis of the relationship between clay arrangement and the transport of chemical species. Specifically, we propose a heterogeneous pore-scale simulation method to investigate water diffusion in compacted porous smectite clay structures. Our approach utilizes a bottom-up strategy, leveraging molecular dynamics to extract essential information. The compacted smectite clay structure was developed by Underwood et al. [56], by a step-wise dehydration process in a large-scale molecular dynamics simulation, allowing the clay particles to self-align and form structures resembling those observed in natural clays. In our heterogeneous pore-scale model, we assign local diffusion coefficients derived from deterministic molecular dynamics simulations within a smectite nanopore. This assignment correlates diffusion with the proximity of the pore space to the clay surface and the size of the bounding clay interlayer, capturing microscopic porosity and local transport. By doing so, we establish a connection between the molecular interactions occurring within individual pores and the overall behavior observed at larger scales. To validate our modified approach, we compare the results of the pore-scale simulations with a large-scale molecular dynamics (MD) simulation performed on the same compacted smectite clay structure. Through this comparison, we calculate crucial transport parameters, such as the effective diffusion coefficient and the geometric factor, which provide valuable insights into fluid and chemical species transport on a continuum scale over the long term. Furthermore, we establish a correlation between clay structural arrangement and the effective diffusion coefficient.

5.2 Methods

5.2.1 Molecular dynamics simulation

The simulation setup is based on a set of clay model structures established by Underwood et al. [56]. In that study, 30 hexagonal clay particles with random orientation solvated in $24 \times 24 \times 40 \text{ nm}^3$ were compacted in a series of molecular dynamics simulations. To simulate the compaction of clay, a gradual dehydration process was employed. This involved the progressive removal of water molecules and equilibration of the system under constant pressure and temperature [56]. By conducting the dehydration process in a step-wise manner, the clay particles were able to align themselves and form structures that resemble those observed during the dehydration of natural clay samples [56].

Several structures with different degrees of compaction were used for the simulation of diffusive transport. One highly compacted clay structure (Figure 5.1). was employed in this study for a direct benchmarking of the diffusion coefficient obtained by molecular dynamics simulations and a multi-scale modeling approach based on LB and RW simulations. The structure consisted of 30 particles arranged within a simulation cell measuring $24 \times 24 \times 7 \text{ nm}^3$, with a dry density of 1.67 g/cm^3 and a porosity of 0.45. The individual clay particle used was a Na-montmorillonite, characterized by the stoichiometry $\text{Na}_{0.8}[\text{Al}_{3.2}\text{Mg}_{0.8}]\text{Si}_8\text{O}_{20}(\text{OH})_4$. Isomorphous substitutions of Mg^{2+} with Al^{3+} in the octahedral sheets were randomly distributed

while maintaining the constraint of no adjacent substitutions. To achieve charge neutrality, the resulting negative structural charge was counterbalanced through adsorbed Na ions.

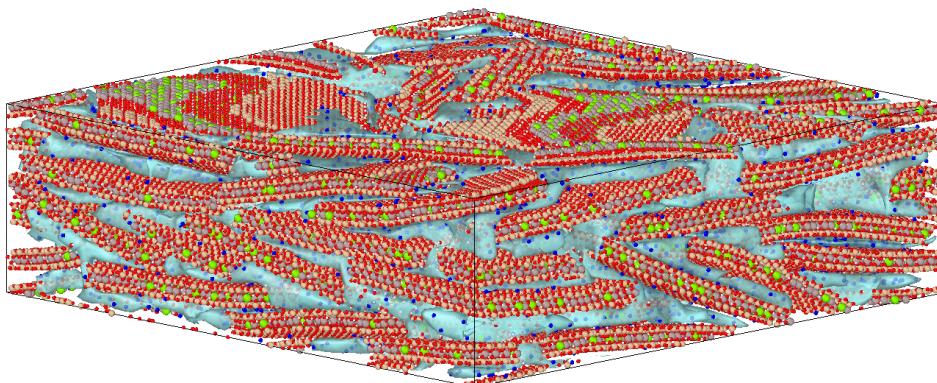


FIGURE 5.1: Snapshot of compacted smectite clay structure solvated with water. The system shows stacking features and correlations representative of the clay matrix. In the visualization, water molecules are depicted in cyan, while the clay platelets are represented by different colors: oxygen in red, silicon in light brown, aluminium in grey, magnesium in green, hydrogen in white, and sodium in blue. Reproduced with permission [56].

Classical molecular dynamics simulations were conducted using the GROMACS software package to investigate the behavior of the system. The interatomic interactions within the clay atoms were modeled using the CLAYFF force field [15], while the SPC/E model [5] was employed to describe the water molecules. To prepare the system for production runs, an energy minimization step was performed, followed by a 1 ns equilibration period in the NVT ensemble at a temperature of 300 K. Periodic boundary conditions were applied to mimic an infinite system. Subsequently, a 72 ns long production run was carried out in the NVT ensemble to calculate the diffusion coefficient of water in the composite clay model. The temperature of the system was regulated using the velocity rescaling thermostat [8].

For the calculation of short-range interactions, the Lennard-Jones potential and short-range Coulomb potential were employed, with a cutoff distance set at 1.2 nm. Long-range electrostatic interactions were evaluated using the particle-mesh Ewald (PME) method [16]. In order to maintain the stability of bonds involving hydrogen atoms in both clay and water, the LINCS algorithm was utilized as a restraint. Additionally, the SHAKE algorithm was applied to constrain the geometry of each water molecule during the simulation.

The diffusion coefficients D_{MD} were derived from the slope of a plot of the mean square displacement using the Einstein relation:

$$D_{MD} = \frac{1}{2nt} \langle |r(t_0) - r(t + t_0)|^2 \rangle \quad (5.2)$$

where $r(t_0)$ is the position of the molecule of interest at time zero; $r(t + t_0)$ is the position of the particle after t-time interval and n is the dimension of the diffusion process considered.

To account for factors influencing diffusion through the porous medium, such as fluid-surface

interaction and geometric effects, the geometric factor (G) was calculated (assuming the accessible porosity to be equal to the total porosity) using the following relationship:

$$D_e = \theta_a \frac{D_0}{G} \quad (5.3)$$

where, D_e represents the effective diffusion coefficient, D_0 is the bulk diffusion coefficient, G represents the geometric factor and θ_a is the accessible porosity.

5.2.2 Pore structure setup for the pore-scale simulations

The clay geometry, which comprised platelets composed of atoms, was converted into a 3D numerical grid representing clay solids and pores. The grid had a resolution of 0.1 nm in all dimensions (Figure 5.1). The extent of the solid was adjusted to ensure that the total mass of water in the system is equivalent to that of the molecular dynamics (MD) setup. As a result, the masses of water in the pore-scale setup and MD setup for the highly compacted clay were 125.43 g/kg_{clay} and 110.7 g/kg_{clay}, respectively. The impermeable regions (solids) were assigned a diffusion coefficient of zero, thereby restricting particle mobility solely to the open pore space of the sample.

Water structure and mobility at the clay water interface are affected by the interaction with the clay surface. Studies on water distribution within a smectite slit pore have revealed distinct structural arrangements near the clay surface, transitioning to behavior similar to the bulk at distances greater than 1.0 nm from the surface [13, 38]. In pores smaller than 1.0 nm, the water behavior differs from that at the surface of larger pores, as there is no bulk-like region, and water molecules are entirely confined by clay surfaces.

Three upscaling approaches with increasing levels of complexity were employed to evaluate the water diffusivity for the entire sample. In the first approach, a constant diffusion coefficient, equivalent to the bulk diffusion coefficient of water, was assigned to the entire pore space domain. The second approach involved determining local diffusion coefficients for each pore voxel based on its proximity to the clay surface. These coefficients were obtained from independent molecular dynamics simulations of water in a smectite slit pore with a size of 4.7 nm. The density distribution profile of water within the slit pore shows well defined layer-like structure within 1.0 nm of interface Figure 5.2. The diffusion coefficients in each layer were determined from MD simulation in our previous study [38]. These data were assigned to the voxels depending on their closest distance to the surface (see Table 5.1). Note that the interlayer and the big pores were treated in the same way in the first two approaches. In the third approach, the system complexity was increased considering the interlayer as an additional pore type. Pore voxels located in between clay platelets 0.1 - 0.9 nm apart were indexed as interlayers. The specific values obtained are reported in Table 5.1. To visualize the diffusion coefficients within the pore space and demonstrate the three different approaches, Figure 5.3 shows the setup of the pore-scale system for the highly compacted smectite clay and the corresponding distribution. Additional information regarding the color bars in Figure 5.3 can be found in Table 5.1, where

each number from 0 to 7 represents the local diffusion coefficient associated with a particular system.

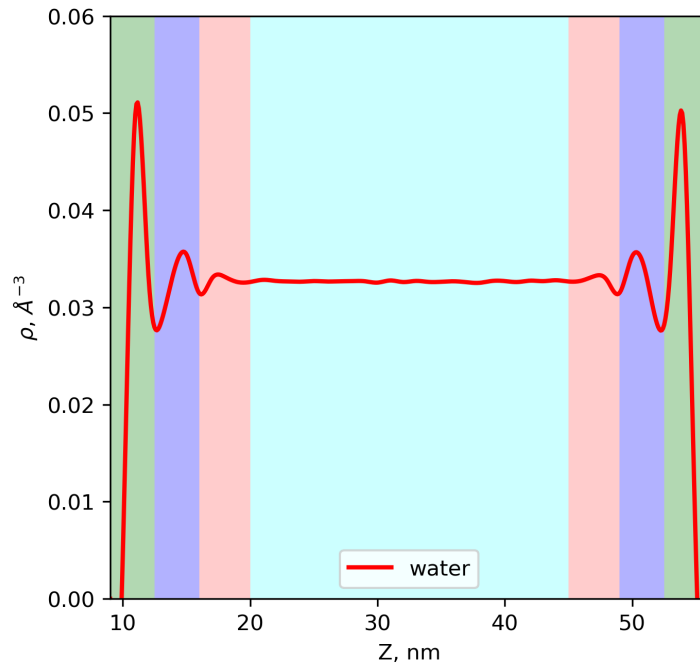


FIGURE 5.2: Density distribution of water in a 4.7 nm smectite slit pore. The shaded regions represent the different structuring of water within the pore. Green, blue, pink, and cyan shades are used to denote surface 1, surface 2, surface 3, and bulk respectively. These regions are of sizes 0.35, 0.35, 0.40, and 2.5 nm respectively.

TABLE 5.1: Distribution of Local diffusion coefficients

	Solid	Interlayers			External pores			
		1W	2W	3W	surface 1	surface 2	surface 3	bulk
D (nm ² /ns)	0.0	0.15	1.23	1.58	1.80	1.91	2.03	2.30
Color bar ^a								
A1	0							1
A2	0				1	2	3	4
A3	0	1	2	3	4	5	6	7

^a Description of color bars in each approach as shown in Figure 5.3

The highly compacted clay structure of 1.67 g/cm³ presented in Figure 5.3 was used as a benchmark to compare random walk, lattice Boltzmann and molecular dynamics simulations. To investigate the influence of microstructural arrangement on transport, a set of five smectite clay structures with different porosity levels were used to perform pore-scale simulations. The initial structures were developed by Underwood et al. [56]. Figure 5.4 shows the porous clay structures, demonstrating the distribution of local diffusion coefficients using approach A3 across various porosity levels.

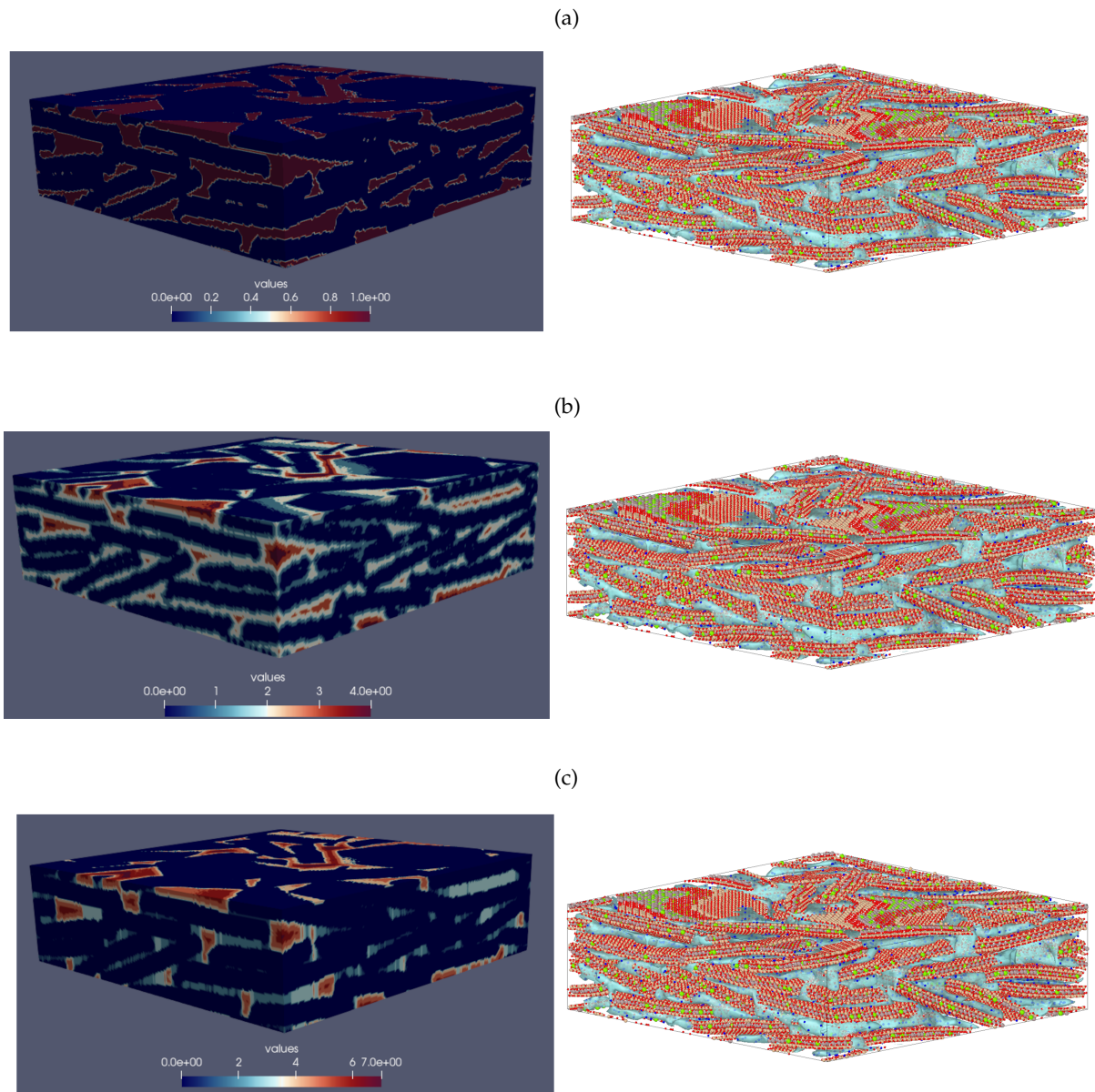


FIGURE 5.3: A snapshot of the random walk system configuration illustrating the distribution of diffusion coefficients within the pore space. The corresponding equivalent MD system configuration is on the right. The three systems can be defined as follows: (a) A1: This system is populated with a constant diffusion coefficient throughout the entire pore space. (b) A2: In this system, diffusion coefficients vary locally within the pore space based on proximity to the clay surface. (c) A3: Similar to A2, this system incorporates local diffusion coefficients dependent on proximity to the clay surface. Additionally, it considers pore spaces within 1-3 water layers. The color bar is described in Table 5.1.

5.2.3 Random walk simulation

To simulate pore-scale diffusion in the porous clay structure, a random walk algorithm, as described by Churakov et al. [14], was utilized. This algorithm offers the advantage of accurately incorporating heterogeneous local diffusion coefficients. The governing equation fundamental

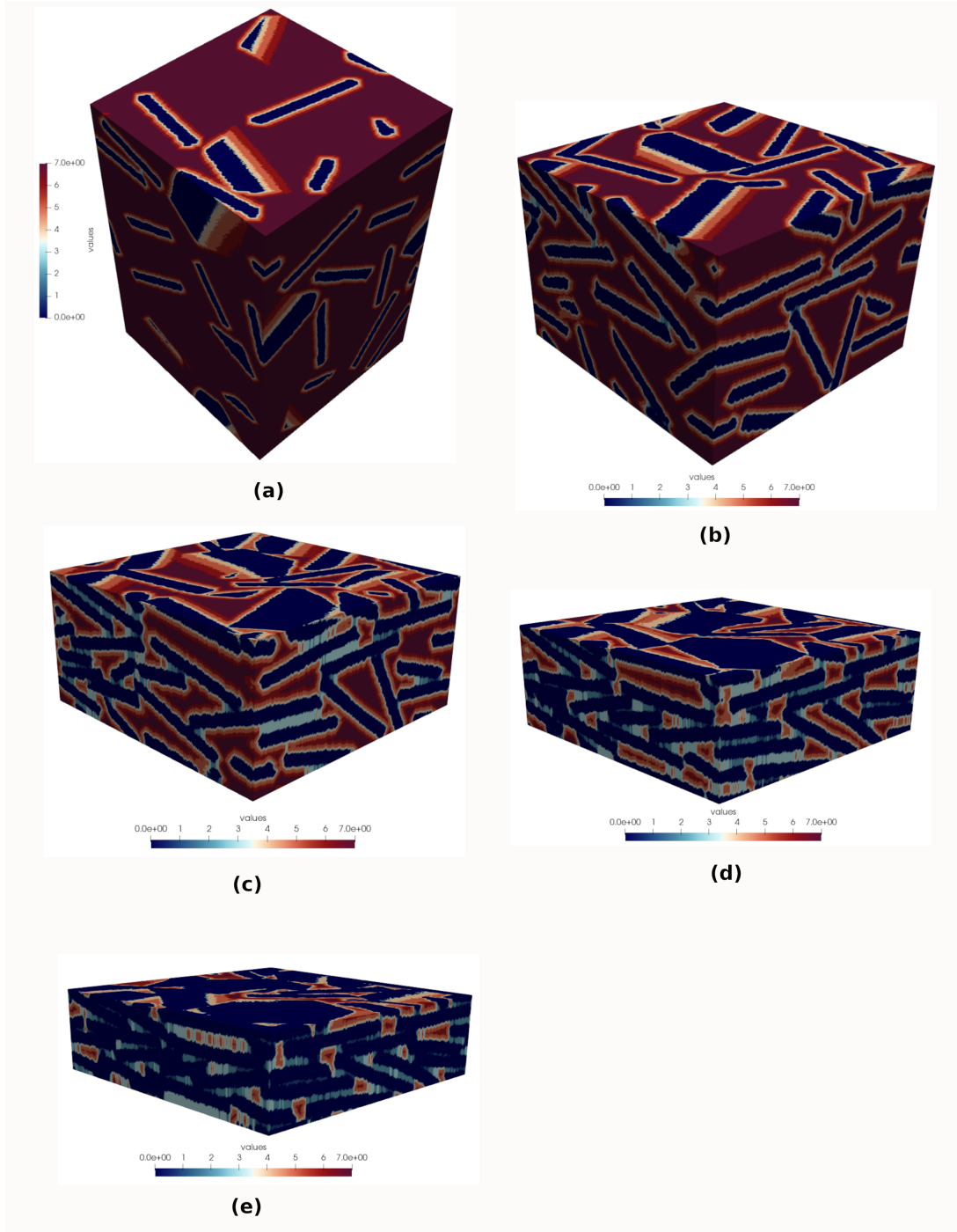


FIGURE 5.4: A snapshot showing the distribution of diffusion coefficients within the pore space for various pore structures. The pore structures (a) to (e) correspond to different configurations: (a) $\rho_{dry} = 0.33 \text{ g/cm}^3$, $\theta = 0.89$; (b) $\rho_{dry} = 0.67 \text{ g/cm}^3$, $\theta = 0.78$; (c) $\rho_{dry} = 1.00 \text{ g/cm}^3$, $\theta = 0.67$; (d) $\rho_{dry} = 1.32 \text{ g/cm}^3$, $\theta = 0.56$; (e) $\rho_{dry} = 1.67 \text{ g/cm}^3$, $\theta = 0.45$.

to this algorithm was applied:

$$\delta x = Z \sqrt{2D(x(t))\Delta t} \quad (5.4)$$

$$x_k(t + \Delta t) = x(t) + Z \sqrt{2D(x(t) + \delta x)\Delta t} \quad (5.5)$$

where, δx represents the predictor step, Z denotes a random number generated from a Gaussian distribution, $D(x(t))$ corresponds to the diffusion coefficient of a particle located at the position $x(t)$. Additionally, $D(x(t) + \delta x)$ represents the diffusion coefficient obtained at position $x(t) + \delta x$ and x_k denotes the position of a particle after a time increment of $t + \Delta t$.

In this algorithm, the random number (R) is employed to generate the predictor step (δx). Subsequently, the diffusion coefficient ($D(x(t) + \delta x)$) at the position $x(t) + \delta x$ is determined. This diffusion coefficient is then utilized in the corrector step to displace the particle to the position $x_k(t + \Delta t)$, using the same random number (R). This algorithm and the computer implementations have been verified through comparisons with analytical solutions [14, 31].

3D random walk (RW) simulations of sample scale diffusion were conducted with a periodic boundary condition implemented in all directions. Within each simulation run, 2×10^4 particles were uniformly distributed within the pore space. The choice of this particle number was based on a convergence test performed by Churakov et al. [14] in RW simulations. The time step used in the simulations was determined according to the equation:

$$\Delta t = 10^{-3} \frac{\Delta x^2}{D_{\max}} \quad (5.6)$$

The small time step (eq 5.6) allows particles to accurately capture the local diffusion properties as they move through the sample, ensuring that regions with low diffusion coefficients are not neglected. Furthermore, this time step minimizes errors associated with reflections at impermeable boundaries [14].

The diffusion coefficients D_{RW} were derived from the slope of a plot of the mean square displacement using the Einstein relation:

$$D_{RW} = \frac{1}{2nt} \langle |r(t) - r(0)|^2 \rangle \quad (5.7)$$

5.2.4 Lattice Boltzmann modeling

In this work, lattice Boltzmann simulations were conducted using the passive scalar advection and diffusion model described by Prasianakis et al. [40]. At the macroscopic level, the model involves a fluid medium represented by discrete kinetic equations for populations denoted as $f_i(x, t)$, aiming to accurately reproduce the Navier-Stokes equations. Furthermore, the model incorporates multiple sets of passive scalar coupled populations, enabling the simulation of solute diffusion.

The Boltzmann equation using the Bhatnagar-Gross-Krook collision approximation reads:

$$\frac{\partial f_i}{\partial t} + c_i \cdot \nabla f_i + F \cdot \nabla_{c_i} f_i = -\frac{f_i - f_i^{eq}}{\tau} \quad (5.8)$$

where, the single-particle distribution function in the phase space (x, c_i, t) is represented by $f(x, c_i, t)$, while the corresponding equilibrium distribution function is denoted as $f^{eq}(x, c_i)$. Here, x refers to the position vector, c_i represents the microscopic velocity, $F(x, t)$ is a body

force, and τ is the relaxation time. The relaxation parameter is related to the local diffusion coefficient:

$$D = \frac{\tau}{3} \quad (5.9)$$

For the 2D simulations, the guided equilibrium D2Q9 lattice model was selected as the basis model [41], for which the discrete velocities of the populations f_i are:

$$cx = \{0, 1, 0, -1, 0, 1, -1, -1, 1\} \quad (5.10)$$

$$cy = \{0, 0, 1, 0, -1, 1, 1, -1, -1\} \quad (5.11)$$

The corresponding population-moments to the density of the solution ρ , the velocity u_a and the momentum j_a in the x,y direction is given as:

$$\rho = \sum_{i=0}^8 f_i \quad (5.12)$$

and

$$u_a = \frac{1}{\rho} \sum_{i=0}^8 f_i c_{ia} \quad (5.13)$$

and

$$j_a = \sum_{i=0}^8 f_i c_{ia} \quad (5.14)$$

The guided equilibrium populations f^{eq} for the fluid density is given as:

$$f_i^{eq} = \rho \prod_{a=x,y} \frac{2c_{ia}^2 - 1}{2c_{ia}^2} (c_{ia}^2 - 1 + c_{ia}u_a + u_a^2) \quad (5.15)$$

To model the diffusion of solutes, a second equilibrium population of solute concentration is necessary. This is given as:

$$g_i^{eq} = C_i \prod_{a=x,y} \frac{2c_{ia}^2 - 1}{2c_{ia}^2} (c_{ia}^2 - 1 + c_{ia}u_a + u_a^2) \quad (5.16)$$

where C_i is the concentration of solute and u_a is the macroscopic velocity obtained from the basis model (eqn 5.13). The relevant population moment that corresponds to the concentration is:

$$C_i = \sum_{i=0}^8 f_i \quad (5.17)$$

The lattice Boltzmann (LB) simulation employed periodic boundary conditions at the top and bottom of the computational domain. On the left and right boundaries, a differential concentration (in lattice units) was applied, creating a diffusive gradient across the domain from left to right (along the direction parallel to the clay layering (Figure 5.3)). The mass flux was locally measured at a cross-section in the middle of the computational domain, perpendicular to the flux direction. The simulation was run until a steady state was reached, which allowed

to measure the effective diffusivity along the direction parallel to the clay layering. A similar approach was adopted for the top and bottom boundaries, with a differential concentration, while periodic boundaries were used on the left and right boundaries. This setup enabled the examination of diffusion in both parallel and perpendicular directions to the clay layering.

5.3 Results and discussion

5.3.1 Validation of pore-scale simulation methodology

To validate our different upscaling approaches, we compared the results of the large-scale molecular dynamics (MD) simulation with the random walk (RW) simulations. Both MD and RW simulations were conducted for a total simulation time of 72 ns, and the mean square displacement (MSD) was calculated using the particle trajectories throughout the entire simulation period.

Figures 5.5a and 5.5b compare the mean square displacement (MSD) plots obtained from MD simulations and RW simulations (A1 and A2 approaches). In A1, a constant bulk water diffusion coefficient of $2.3 \text{ nm}^2/\text{ns}$ was uniformly applied throughout the entire pore domain. However, in A2, local diffusion coefficients were assigned to different regions of the pore space based on their proximity to the clay surface. The results reveal a noticeable difference between the MD simulations and A1/A2 simulations, with A1 and A2 exhibiting a considerably steeper slope. This difference suggests that the particle mobility in A1 and A2 is significantly higher than in the MD simulations, indicating that A1 and A2 fail to accurately capture molecular-scale dynamics. Merely incorporating local diffusion coefficients based on surface behavior is inadequate to fully replicate the particle dynamics observed in the MD simulations within the RW simulations. One possible explanation is that in larger pores, the impact of surface diffusion on overall pore diffusion diminishes, and the dominant factor becomes the bulk diffusion behavior of water. This idea finds support in the significant bulk behavior observed in larger pores, as evident from the density distributions of water in a slit pore at various pore sizes [38].

Figure 5.5c presents a comparison of the mean square displacement plots between the MD simulation and the RW approach A3 simulation. In A3, we extended the A2 approach by taking into account the behavior occurring within 1 - 3 water layers, which corresponds to the typical size of a clay interlayer. Within this interlayer, the bulk behavior diminishes or may not exist, leading to potentially different mobility compared to the surface. The results demonstrate that the mean square displacement curves of the MD and A3 simulations are nearly parallel, indicating that the retention of particles at the clay surface and within clay interlayers is accurately captured.

Generally, it is widely observed that particle displacement along the layering of clay particles (x- and y-direction) is faster compared to displacement perpendicular to the layering (z-direction), as shown in Figure 5.5c. The mean square displacement (MSD) curves exhibit an initial ballistic regime, extending up to 20 ns in the RW simulation and up to 10 ns in the MD

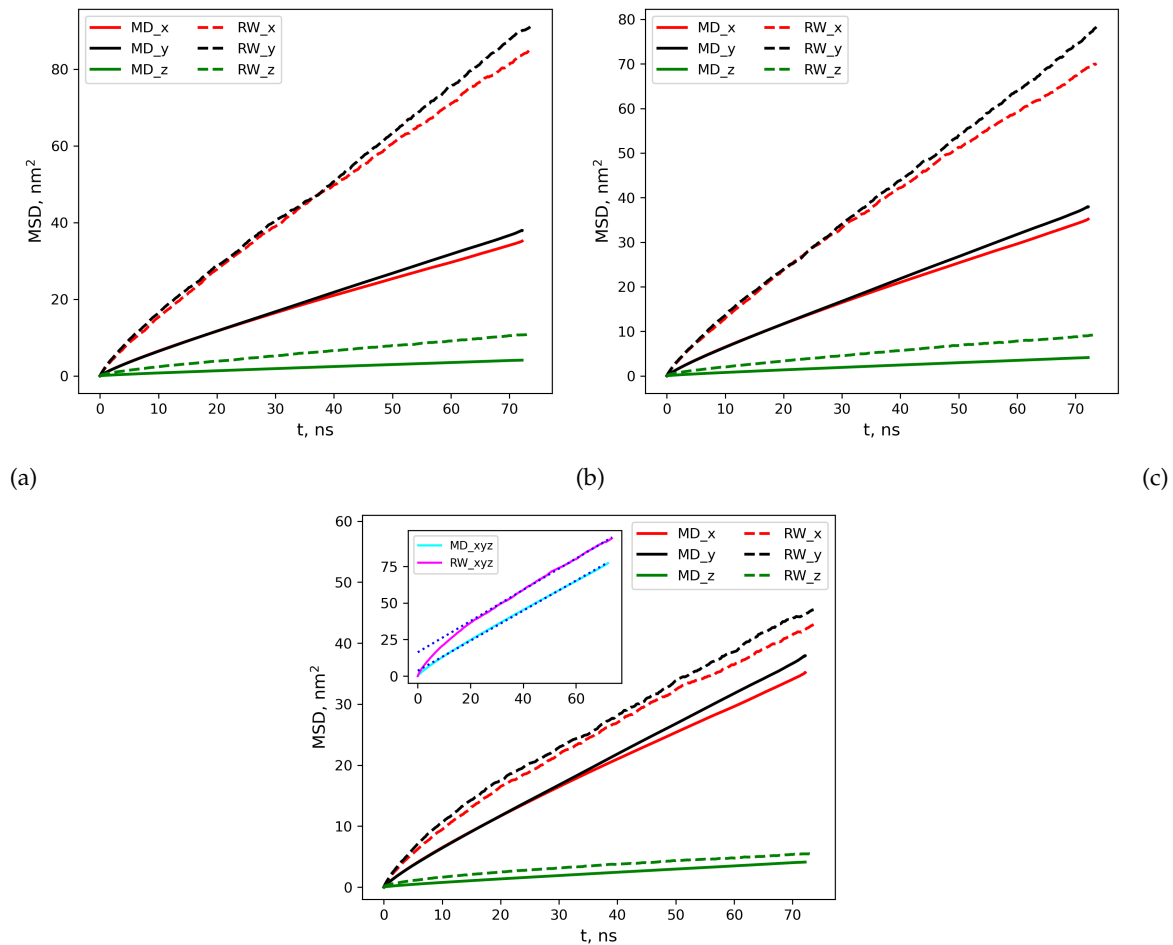


FIGURE 5.5: Comparison of the mean square displacement obtained in large-scale MD and RW simulations from approach (a) A1 (b) A2 (c) A3

simulation. These differences in the short-time behavior of the MSD curves are due to the differences in the short-range interaction between MD and RW particles. This short time dynamics however is irrelevant to the macroscopic diffusion.

Comparison of 2D lattice Boltzmann and 2D RW simulation

A 2-dimensional representation of the clay pore structure was obtained by extracting a slice from the 3D geometry shown in Figure 5.3a. Minor adjustments were made to improve connectivity in the 2D plane, with minor interventions. The resulting 2D geometry used for the lattice Boltzmann (LB) simulation is shown in Figure 5.6.

The upscaling approach A1 and A2 were implemented in the lattice Boltzmann (LB) simulation. The 2D configuration of the lattice Boltzmann simulation, illustrating the distribution of local diffusion coefficients (nm^2/ps) within the pore space based on proximity to the clay surface, is shown in Figure 5.7.

The 2D lattice Boltzmann modeling involves measuring a species concentration transport rate at a steady state under the given concentration gradient. This rate is then compared to the diffusion coefficient of the species in bulk water, resulting in the determination of the effective

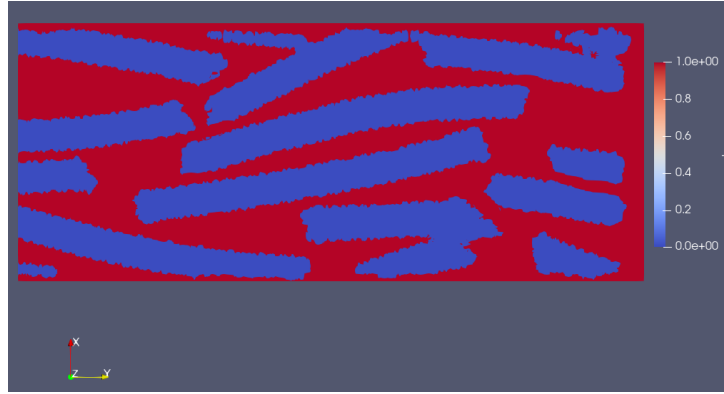


FIGURE 5.6: Configuration of the 2D clay structure for lattice Boltzmann modeling. Clay particles and pore space are represented by red and blue regions, respectively.

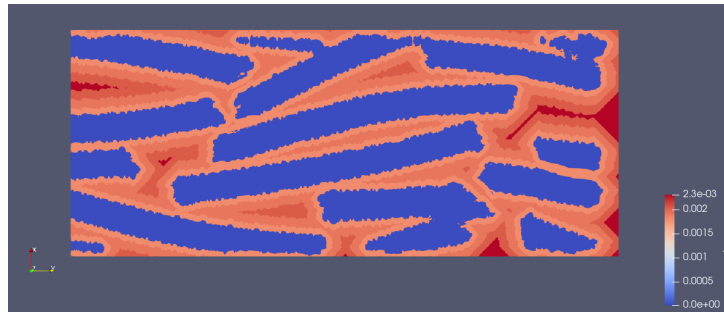


FIGURE 5.7: Snapshot of the lattice Boltzmann system configuration showcasing the spatial distribution of diffusion coefficients (nm^2/ps) within the pore space based on proximity to the clay surface.

diffusion coefficient (D_e). To further compare the lattice Boltzmann modeling with random walk simulation, a random walk simulation was conducted using the same 2D clay structure as the lattice Boltzmann model. Table 5.2 presents the D_e values obtained from both the lattice Boltzmann (LB) and random walk (RW) simulations.

TABLE 5.2: Effective diffusion coefficients derived from 2D LB and RW simulations

	diffusion coefficients [$10^{-10}, m^2s^{-1}$]	
	$D_{e\parallel}$	$D_{e\perp}$
LB-2D-A1	3.13	0.84
LB-2D-A2	2.27	0.63
RW-2D-A1	3.44	0.79
RW-2D-A2	2.75	0.59

The results demonstrate a good agreement between the random walk (RW) simulation and the lattice Boltzmann (LB) modeling with a deviation factor of about 1.1. As we proceed, our future work aims to extend the LB modeling approach to encompass a three-dimensional (3D) model, thereby enhancing the accuracy and applicability of our findings. The actual wall time for the simulations in a 1 CPU core is 8.2×10^1 seconds for the RW simulation and 4.3×10^5 seconds for the LB simulation. It is worth noting that the RW simulation offers a computational

advantage compared to the LB and MD simulations, however, the advantage of LB is that it can be extended to simulate ions transport.

5.3.2 Diffusion of water in highly compacted smectite clay

The effective diffusion coefficient for water in the model clay sample was determined using equations 5.2 and 5.7 for the large-scale MD and RW simulations, respectively. The calculation excluded the ballistic regime and focused on the linear part of the slope to determine the effective diffusion coefficient. The obtained effective diffusion coefficients for the MD and RW simulations are presented in Table 5.3.

TABLE 5.3: Effective diffusion coefficients derived from large-scale MD and RW simulations for clay sample with density 1.67 g/cm^3

	diffusion coefficients [$10^{-10}, m^2s^{-1}$]			
	$D_{e\parallel}$	$D_{e\perp}$	G_{\parallel} [-]	G_{\perp}
MD	2.33	0.26	9.87	88.46
RW-A1	5.66	0.64	4.06	35.82
RW-A2	4.61	0.52	4.99	43.98
RW-A3	2.20	0.24	10.45	97.45

The effective diffusion coefficient values reveal that A1 and A2 simulations overestimate the diffusion coefficient compared to the MD simulation by factors of approximately 2.45 and 1.99, respectively. In contrast, A3 shows a close agreement with the large-scale MD simulation, differing by only 4%. These results highlight the significance of incorporating both surface diffusion and interlayer diffusion behavior in pore-scale random walk simulations to accurately determine the effective diffusion coefficient and validate the proposed model, RW-MD for estimation of the sample-scale diffusion coefficients. It is also worth mentioning that computational resources necessary for the estimation of water diffusion in MD are almost 10^5 orders of magnitude larger than the ones needed for the combined MD-RW approach. Furthermore, the RW-MD approach can rely on existing MD data for clay minerals conducted in the past.

5.3.3 Dependence of diffusion on porosity

The random walk simulation was performed for a prolonged period of 5×10^6 ns on the porous clay structures (Figure 5.4) in order to study the influence of microstructural alterations on diffusion. The relationship between porosity and relative effective diffusion coefficients is shown in Figure 5.8. The results demonstrate that the effective diffusion coefficient increases with increasing porosity. This increase is attributed to the decreased tortuosity experienced by fluid particles in highly porous clay structures.

Furthermore, it was observed that the effective diffusion perpendicular to the clay layering eventually converges to the value of the effective diffusion coefficient parallel to the clay layering at high porosity. This convergence can be attributed to the almost uniform tortuosity observed in all directions at higher porosity levels, as the tightly packed structural arrangement becomes less compact and ordered. The difference between the structural arrangements

at 90% porosity (Figure 5.4a) and 45% porosity (Figure 5.4e) clearly illustrates this distinction. Additionally, in Figure 5.8, the experimental data of the effective diffusion coefficient in Na-montmorillonite [6] and Na-bentonite [28] is shown. The effective diffusion coefficient obtained from pore-scale modeling demonstrates a fairly good agreement with the experimental values.

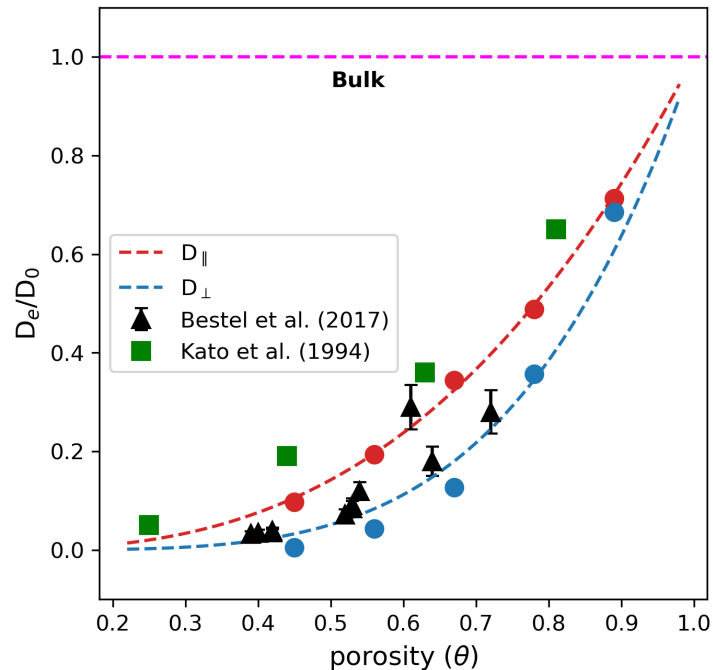


FIGURE 5.8: Relative effective diffusion coefficients of water as a function of clay porosity. Red and blue markers represent values obtained from this study for diffusion parallel and perpendicular to clay layering respectively. Black and green markers represent experimental data obtained for Na-montmorillonite [4] and Na-bentonite [28] respectively.

5.4 Conclusions

In this study, we have presented computationally efficient and comprehensive pore-scale modeling to accurately determine the effective diffusion coefficient of water in compacted porous Na-montmorillonite combining atomistic simulations and pore-scale modeling based on the random walk and/or lattice Boltzmann. Our approach involved multiple steps, including the generation of a compacted clay structure using molecular dynamics simulations [56], derivation of local diffusion coefficients based on pore space proximity to clay surfaces and interlayer size, 3D large-scale molecular dynamics simulation to determine the effective diffusion coefficient of water, conversion of the MD structure to a numerical grid, and subsequent 3D random walk simulations.

Our modeling reveals that both surface diffusion and interlayer mobility need to be explicitly considered to obtain an accurate estimation of diffusion coefficients in pore-scale modeling.

Furthermore, the effective diffusion coefficients obtained from the refined random walk simulation and the large-scale MD simulation exhibit good agreement with experimental data.

Furthermore, we conducted a comparative analysis between the random walk simulation and lattice Boltzmann modeling, employing the up-scaling principles, and discovered a good agreement between the two approaches. Notably, the random walk simulation exhibits a notable advantage in terms of computational resource utilization when compared to lattice Boltzmann modeling and molecular dynamics simulations. However, it is worth mentioning that the lattice Boltzmann method possesses the added advantage of being adaptable for simulating ion transport, a task that would prove more challenging using the current random walk method.

The obtained effective diffusion coefficients can now be used as input parameters for continuum diffusion equations. The proposed up-scaling approach proves to be robust, versatile, and capable of unraveling the complex relationship between the structural and diffusion properties of porous media. In future studies, we aim to extend our simulations to larger samples and consider partial saturation to further enhance our understanding of these systems.

Acknowledgement

The research reported in this paper was supported by EURAD GAS FUTURE and DONUT Work Packages, Laboratory for Waste Management at the Paul Scherrer Institute, NAGRA, and the University of Bern Geological Institute. Molecular dynamics simulations were carried out using resources from the Paul Scherrer Institute (MERLIN 6), the University of Bern (UBELIX), and the Swiss National Super Computing Centre (Piz Daint). The authors acknowledge the co-funding from Horizon 2020 EURAD project Grant ID 847593.

5.5 References

- [1] Apostolopoulou, M., Santos, M. S., Hamza, M., Bui, T., Economou, I. G., Stamatakis, M., and Striolo, A. (2019). Quantifying pore width effects on diffusivity via a novel 3d stochastic approach with input from atomistic molecular dynamics simulations. *Journal of chemical theory and computation*, 15(12):6907–6922.
- [2] Avisar, D., Primor, O., Gozlan, I., and Mamane, H. (2010). Sorption of sulfonamides and tetracyclines to montmorillonite clay. *Water, Air, & Soil Pollution*, 209:439–450.
- [3] Bear, J. and Bachmat, Y. (2012). *Introduction to modeling of transport phenomena in porous media*, volume 4. Springer Science & Business Media.
- [4] Benson, C. H. and Trast, J. M. (1995). Hydraulic conductivity of thirteen compacted clays. *Clays and clay minerals*, 43:669–681.
- [5] Berendsen, H., Grigera, J., and Straatsma, T. (1987). The missing term in effective pair potentials. *Journal of Physical Chemistry*, 91(24):6269–6271.
- [6] Bestel, M., Glaus, M. A., Frick, S., Gimmi, T., Juranyi, F., Van Loon, L. R., and Diamond, L. W. (2018). Combined tracer through-diffusion of hto and 22na through namontmorillonite with different bulk dry densities. *Applied geochemistry*, 93:158–166.
- [7] Boek, E. S. and Venturoli, M. (2010). Lattice-boltzmann studies of fluid flow in porous media with realistic rock geometries. *Computers & Mathematics with Applications*, 59(7):2305–2314.
- [8] Bussi, G., Donadio, D., and Parrinello, M. (2007). Canonical sampling through velocity rescaling. *The Journal of chemical physics*, 126(1):014101.
- [9] Catalano, E., Chareyre, B., and Barthélemy, E. (2014). Pore-scale modeling of fluid-particles interaction and emerging poromechanical effects. *International Journal for Numerical and Analytical Methods in Geomechanics*, 38(1):51–71.
- [10] Chen, S., Tölke, J., and Krafczyk, M. (2009). Simulation of buoyancy-driven flows in a vertical cylinder using a simple lattice boltzmann model. *Physical Review E*, 79(1):016704.
- [11] Chen, X.-P., Zhong, C.-W., and Yuan, X.-L. (2011). Lattice boltzmann simulation of cavitating bubble growth with large density ratio. *Computers & Mathematics with Applications*, 61(12):3577–3584.
- [12] Churakov, S. V. (2013a). Mobility of na and cs on montmorillonite surface under partially saturated conditions. *Environmental science & technology*, 47(17):9816–9823.
- [13] Churakov, S. V. (2013b). Mobility of na and cs on montmorillonite surface under partially saturated conditions. *Environmental science & technology*, 47(17):9816–9823.
- [14] Churakov, S. V. and Gimmi, T. (2011). Up-scaling of molecular diffusion coefficients in clays: A two-step approach. *The Journal of Physical Chemistry C*, 115(14):6703–6714.

- [15] Cygan, R. T., Greathouse, J. A., Heinz, H., and Kalinichev, A. G. (2009). Molecular models and simulations of layered materials. *Journal of Materials Chemistry*, 19(17):2470–2481.
- [16] Darden, T., York, D., and Pedersen, L. (1993). Particle mesh ewald: An $n \log(n)$ method for ewald sums in large systems. *The Journal of chemical physics*, 98(12):10089–10092.
- [17] Delage, P., Cui, Y.-J., and Tang, A. M. (2010). Clays in radioactive waste disposal. *Journal of Rock Mechanics and Geotechnical Engineering*, 2(2):111–123.
- [18] Ezzatneshan, E. (2017). Study of surface wettability effect on cavitation inception by implementation of the lattice boltzmann method. *Physics of Fluids*, 29(11):113304.
- [19] Fick, A. (1855). Poggendorff's flannel. *Physik*, 94(59):297.
- [20] Frentrup, H., Avendaño, C., Horsch, M., Salih, A., and Müller, E. A. (2012). Transport diffusivities of fluids in nanopores by non-equilibrium molecular dynamics simulation. *Molecular Simulation*, 38(7):540–553.
- [21] Gadikota, G., Dazas, B., Rother, G., Cheshire, M. C., and Bourg, I. C. (2017). Hydrophobic solvation of gases (co₂, ch₄, h₂, noble gases) in clay interlayer nanopores. *The Journal of Physical Chemistry C*, 121(47):26539–26550.
- [22] Genty, A., Gueddani, S., and Dymitrowska, M. (2017). Computation of saturation dependence of effective diffusion coefficient in unsaturated argillite micro-fracture by lattice boltzmann method. *Transport in Porous Media*, 117(1):149–168.
- [23] Genty, A. and Pot, V. (2013). Numerical simulation of 3d liquid–gas distribution in porous media by a two-phase trt lattice boltzmann method. *Transport in porous media*, 96:271–294.
- [24] Gimmi, T. and Churakov, S. V. (2019). Water retention and diffusion in unsaturated clays: Connecting atomistic and pore scale simulations. *Applied Clay Science*, 175:169–183.
- [25] He, X. and Luo, L.-S. (1997). Lattice boltzmann model for the incompressible navier–stokes equation. *Journal of statistical Physics*, 88:927–944.
- [26] Kang, J., Prasianakis, N. I., and Mantzaras, J. (2013). Lattice boltzmann model for thermal binary-mixture gas flows. *Physical Review E*, 87(5):053304.
- [27] Kang, Q., Lichtner, P. C., and Zhang, D. (2006). Lattice boltzmann pore-scale model for multicomponent reactive transport in porous media. *Journal of Geophysical Research: Solid Earth*, 111(B5).
- [28] Kato, H., Muroi, M., Yamada, N., Ishida, H., and Sato, H. (1994). Estimation of effective diffusivity in compacted ben tonite. *MRS Online Proceedings Library (OPL)*, 353:277.
- [29] LaBolle, E. M., Fogg, G. E., and Tompson, A. F. (1996). Random-walk simulation of transport in heterogeneous porous media: Local mass-conservation problem and implementation methods. *Water Resources Research*, 32(3):583–593.

- [30] LaBolle, E. M., Quastel, J., and Fogg, G. E. (1998). Diffusion theory for transport in porous media: Transition-probability densities of diffusion processes corresponding to advection-dispersion equations. *Water Resources Research*, 34(7):1685–1693.
- [31] LaBolle, E. M., Quastel, J., Fogg, G. E., and Gravner, J. (2000). Diffusion processes in composite porous media and their numerical integration by random walks: Generalized stochastic differential equations with discontinuous coefficients. *Water Resources Research*, 36(3):651–662.
- [32] Laloui, L., Ferrari, A., and Bosch Llufrui, J. A. (2020). Bentonite clay barriers in nuclear waste repositories. In *E3S Web of Conferences*, volume 205. EDP SCIENCES.
- [33] Li, Q., Luo, K., Kang, Q., and Chen, Q. (2014). Contact angles in the pseudopotential lattice boltzmann modeling of wetting. *Physical Review E*, 90(5):053301.
- [34] Maier, M.-L., Patel, R. A., Prasianakis, N. I., Churakov, S. V., Nirschl, H., and Krause, M. J. (2021). Coupling of multiscale lattice boltzmann discrete-element method for reactive particle fluid flows. *Physical Review E*, 103(3):033306.
- [35] Meunier, A., Velde, B., and Griffault, L. (1998). The reactivity of bentonites: a review. an application to clay barrier stability for nuclear waste storage. *Clay Minerals*, 33(2):187–196.
- [36] Ng, E.-P. and Mintova, S. (2008). Nanoporous materials with enhanced hydrophilicity and high water sorption capacity. *Microporous and Mesoporous Materials*, 114(1-3):1–26.
- [37] O’Brien, G., Bean, C., and McDermott, F. (2002). A comparison of published experimental data with a coupled lattice boltzmann-analytic advection–diffusion method for reactive transport in porous media. *Journal of Hydrology*, 268(1-4):143–157.
- [38] Owusu, J. P., Karalis, K., Prasianakis, N. I., and Churakov, S. V. (2022). Mobility of dissolved gases in smectites under saturated conditions: Effects of pore size, gas types, temperature, and surface interaction. *The Journal of Physical Chemistry C*, 126(40):17441–17455.
- [39] Peng, Y., Zhou, J., and Burrows, R. (2011). Modelling solute transport in shallow water with the lattice boltzmann method. *Computers & fluids*, 50(1):181–188.
- [40] Prasianakis, N., Curti, E., Kosakowski, G., Poonosamy, J., and Churakov, S. (2017). Deciphering pore-level precipitation mechanisms. *Scientific reports*, 7(1):13765.
- [41] Prasianakis, N., Karlin, I., Mantzaras, J., and Boulouchos, K. (2009). Lattice boltzmann method with restored galilean invariance. *Physical Review E*, 79(6):066702.
- [42] Prat, M. (2002). Recent advances in pore-scale models for drying of porous media. *Chemical engineering journal*, 86(1-2):153–164.
- [43] Pusch, R. and Yong, R. N. (2006). *Microstructure of smectite clays and engineering performance*. CRC Press.

- [44] Qin, F., Del Carro, L., Moqaddam, A. M., Kang, Q., Brunschwiler, T., Derome, D., and Carmeliet, J. (2019). Study of non-isothermal liquid evaporation in synthetic micro-pore structures with hybrid lattice boltzmann model. *Journal of Fluid Mechanics*, 866:33–60.
- [45] Rosén, T., Eller, J., Kang, J., Prasianakis, N. I., Mantzaras, J., and Büchi, F. N. (2012). Saturation dependent effective transport properties of pefc gas diffusion layers. *Journal of The Electrochemical Society*, 159(9):F536.
- [46] Scheibe, T. D., Perkins, W. A., Richmond, M. C., McKinley, M. I., Romero-Gomez, P. D., Oostrom, M., Wietsma, T. W., Serkowski, J. A., and Zachara, J. M. (2015). Pore-scale and multiscale numerical simulation of flow and transport in a laboratory-scale column. *Water Resources Research*, 51(2):1023–1035.
- [47] Spaid, M. A. and Phelan Jr, F. R. (1997). Lattice boltzmann methods for modeling microscale flow in fibrous porous media. *Physics of fluids*, 9(9):2468–2474.
- [48] Succi, S. (2001). *The lattice Boltzmann equation: for fluid dynamics and beyond*. Oxford university press.
- [49] Sui, H., Yao, J., and Zhang, L. (2015). Molecular simulation of shale gas adsorption and diffusion in clay nanopores. *Computation*, 3(4):687–700.
- [50] Sukop, M. (2006). Dt thorne, jr. lattice boltzmann modeling lattice boltzmann modeling.
- [51] Sukop, M. C. and Or, D. (2004). Lattice boltzmann method for modeling liquid-vapor interface configurations in porous media. *Water Resources Research*, 40(1).
- [52] Suter, J. L., Anderson, R. L., Greenwell, H. C., and Coveney, P. V. (2009). Recent advances in large-scale atomistic and coarse-grained molecular dynamics simulation of clay minerals. *Journal of Materials Chemistry*, 19(17):2482–2493.
- [53] Suter, J. L., Coveney, P. V., Greenwell, H. C., and Thyveetil, M.-A. (2007). Large-scale molecular dynamics study of montmorillonite clay: emergence of undulatory fluctuations and determination of material properties. *The Journal of Physical Chemistry C*, 111(23):8248–8259.
- [54] Tartakovsky, A. M. and Meakin, P. (2006). Pore scale modeling of immiscible and miscible fluid flows using smoothed particle hydrodynamics. *Advances in Water Resources*, 29(10):1464–1478.
- [55] Timm, K., Kusumaatmaja, H., Kuzmin, A., Shardt, O., Silva, G., and Vigen, E. (2016). The lattice boltzmann method: principles and practice. *Cham, Switzerland: Springer International Publishing AG*.
- [56] Underwood, T. R. and Bourg, I. C. (2020). Large-scale molecular dynamics simulation of the dehydration of a suspension of smectite clay nanoparticles. *The Journal of Physical Chemistry C*, 124(6):3702–3714.

- [57] Walsh, S. D. and Saar, M. O. (2010). Macroscale lattice-boltzmann methods for low peclet number solute and heat transport in heterogeneous porous media. *Water Resources Research*, 46(7).
- [58] Wang, S., Feng, Q., Zha, M., Javadpour, F., and Hu, Q. (2018). Supercritical methane diffusion in shale nanopores: effects of pressure, mineral types, and moisture content. *Energy & fuels*, 32(1):169–180.
- [59] Wang, S., Javadpour, F., and Feng, Q. (2016). Molecular dynamics simulations of oil transport through inorganic nanopores in shale. *Fuel*, 171:74–86.
- [60] Yang, Y., Wang, K., Zhang, L., Sun, H., Zhang, K., and Ma, J. (2019). Pore-scale simulation of shale oil flow based on pore network model. *Fuel*, 251:683–692.
- [61] Yang, Y. and Wang, M. (2018). Pore-scale study of thermal effects on ion diffusion in clay with inhomogeneous surface charge. *Journal of colloid and interface science*, 514:443–451.
- [62] Yin, H., Felicelli, S., and Wang, L. (2011). Simulation of a dendritic microstructure with the lattice boltzmann and cellular automaton methods. *Acta Materialia*, 59(8):3124–3136.
- [63] Yu, L., Rogiers, B., Gedeon, M., Marivoet, J., De Craen, M., and Mallants, D. (2013). A critical review of laboratory and in-situ hydraulic conductivity measurements for the boom clay in belgium. *Applied Clay Science*, 75:1–12.
- [64] Zhang, J. (2011). Lattice boltzmann method for microfluidics: models and applications. *Microfluidics and Nanofluidics*, 10:1–28.
- [65] Zhao, Y., Luo, M., Liu, L., Wu, J., Chen, M., and Zhang, L. (2022). Molecular dynamics simulations of shale gas transport in rough nanopores. *Journal of Petroleum Science and Engineering*, 217:110884.
- [66] Zhou, Y., Zhang, R., Staroselsky, I., and Chen, H. (2004). Numerical simulation of laminar and turbulent buoyancy-driven flows using a lattice boltzmann based algorithm. *International journal of heat and mass transfer*, 47(22):4869–4879.
- [67] Zhu, Y. and Fox, P. J. (2002). Simulation of pore-scale dispersion in periodic porous media using smoothed particle hydrodynamics. *Journal of Computational Physics*, 182(2):622–645.

Chapter 6: Conclusions and Outlook

6.1 Conclusions

This thesis investigates the transport mechanisms of gas in porous clay materials and explores the relationships between the structural properties of the clay minerals and the mobility of small gaseous molecules. Specifically, it focuses on smectite-rich clay rocks, which are considered suitable host rocks for deep geological repositories of nuclear waste. A thorough comprehension of gas transport behavior and related processes within these repositories is essential to ensure the safe and reliable design of waste storage systems.

Conventionally, experimental studies are conducted to investigate the behavior of fluids in porous media, with the goal of obtaining their transport parameters. These parameters are crucial for assessing the suitability of host rocks and designing effective barrier materials. However, laboratory and field experiments may not fully capture the long-term evolution of transport processes and the changes in thermo-hydro-mechanical-chemical conditions specific to the subsurface environment. Consequently, numerical and computer simulations have emerged as invaluable tools for investigating transport mechanisms and examining system behavior beyond the limitations of experimental methodologies. Moreover, numerical and computer simulations offer a unique opportunity to comprehend experimental results, explore scales and processes that are not detectable through experiments alone, and enhance our understanding of the underlying transport mechanisms. In this study, molecular dynamics simulations have been employed to observe fluid behavior at the nanoscale, and a methodology has been developed to upscale the results to a pore scale using pore-scale simulations. By integrating these simulation techniques, a more comprehensive understanding of gas transport in porous clay materials can be achieved.

We have conducted a comprehensive investigation of gas diffusion behavior at the nanoscale using molecular dynamics simulations. Our main objective was to gain insights into the mobility of gases within clay nanopores and interlayer spaces. Gas mobility is influenced by several factors, including pore size, degree of saturation, pressure, temperature, and the specific interaction between the gas molecule and mineral surfaces. To this aim, the mobility of gases (Ar, He, H₂, CH₄, and CO₂) was investigated in fully saturated and partially saturated slit pores of smectite particles using classical molecular dynamics simulations. In the fully saturated system, gas molecules were dissolved into the water and the pore size was varied at a constant molar ratio of gas to water. By analyzing simulation results, a general relationship between the mobility of gases and their fundamental molecular properties was established. Our findings revealed that the diffusion of gases is significantly influenced by three key factors: the mineralogy of the confinement (specifically, the type of clay), the size of the clay nanopore, and the hydrodynamic radius of the gas molecule (which indicates the gas type). Based on these results, we derived an equation that effectively connects these parameters. This equation will be invaluable for macro-scale numerical modeling and laboratory experiments. The repository is expected to undergo a temporal desaturation process that will require a significant amount of time for the system to re-saturate. Gas mobility in this case will be in partial saturation. Consequently, a two-phase model was setup containing a hydrated surface of smectite particles

and gas-filled porosity. By varying the water film thickness, different degrees of saturation in the system were emulated. In such a setup the gas migration takes place both in the gas-rich and liquid-rich phases. At the partially saturated conditions, the advective transport in the gas phase can be a dominant transport mechanism. Accordingly, both gas diffusion and gas dynamics were investigated under partial saturation. The simulation results suggest that the gas-diffusive behavior in this system exhibits a transition regime characterized by a combination of molecular diffusion and Knudsen diffusion. As a result, Fick's law, which is commonly used to describe diffusion processes, is not suitable in this case. Our findings highlighted that gas diffusion is influenced by multiple factors, including the thickness of the water films, the mean-free path of the gas molecules, and the average available pore width. A Bosanquet-type approximation was successfully applied to establish a relation between these parameters and the diffusion coefficient. When a pressure gradient is applied, gas under partial saturation begins to flow as a free phase, and the transport of the gas phase is controlled by the dynamic viscosity of the gas. This emphasizes the significance of the second approach, which focuses on gas dynamics under partial saturation. To investigate the viscosity of gases confined between water films in a clay nanopore, classical non-equilibrium molecular dynamics simulations were conducted. Similar to diffusivity, the viscosity evolution as a function of pore size exhibits a transition regime, being controlled by the thickness of the water films, the mean-free path of gas molecules, and the average available pore width. In the same way, the relationships between these parameters and viscosity could be approximated by the Bosanquet-type approximation.

While studying the gas transport mechanism through clay barriers and how the conditions within the clay influence this transport, it is essential to acknowledge the mutual effects at play. It is equally important to understand how the clay barrier itself is affected by gas generation and transport. One significant aspect of this interaction is the swelling behavior of clay. By investigating the swelling behavior, one can gain insights into the potential changes in clay structure, permeability, and other properties, which in turn affect gas transport and barrier integrity. The effect of dissolved gases on the swelling pressure in smectites was investigated by classical molecular dynamics simulations in the osmotic ensemble. The results of the simulations suggest that the presence of gas molecules had a notable impact on the swelling pressure of Na-montmorillonite, resulting in an increase of approximately 3 MPa. This increase in swelling pressure can be attributed to the increased solubility of the gas molecules as the swelling pressure rises. As the pressure within the clay increases, more gas molecules dissolve into the system, leading to an enhanced swelling pressure.

Molecular dynamics simulations provide insight into fluid behavior at the nanoscale to microscale. However, when it comes to designing clay barriers, the actual parameters used are based on macroscopic observations. In order to bridge the gap between molecular and continuum behavior, an intermediate scale (pore scale) simulation was implemented. This simulation incorporates the molecular interactions between the fluid and mineral surfaces, thus connecting them to the larger continuum behavior. Large-scale molecular dynamics simulations can achieve this as well, but they require significant computational resources. In this study, two pore-scale simulation approaches; random walk (RW) and lattice Boltzmann (LB) simulations

were benchmarked. These simulations enabled us to calculate the effective diffusion coefficient of water in a compacted porous smectite clay sample. The results were then compared with large-scale molecular dynamics simulations performed on the same clay sample. A very good agreement between the 3D RW simulation and the large-scale MD simulations, as well as between 2D lattice Boltzmann modeling and 2D random walk simulations was observed. This work highlights also the consistency and transferability of results between the different computational methods. Overall, the results demonstrated a close agreement with experimental work conducted on Na-montmorillonite and Na-bentonite, and a relationship between the effective diffusion coefficient and the microstructural changes was established.

Although molecular dynamics allows for the exploration of numerous molecular properties, this study simplified certain steps. Specifically, we focused on a basic Na-montmorillonite clay with Mg substituting for Al in the octahedral sheet. However, it's important to note that in natural montmorillonite, Al can also replace Si in the tetrahedral sheet. This substitution leads to variations in the clay's surface charge and surface charge distributions. Previous studies have demonstrated that the specific distribution of these substitutions affects the hydrated montmorillonite's structural and dynamic properties, including the mobility of aqueous species, swelling behavior, and interlayer structure (Liu et al., 2008; Ngouana et al., 2014; Kosakowski et al., 2008; Sun et al., 2015). Therefore, the transport parameters and swelling pressure calculations obtained in this study are limited to our simplified clay model and may not precisely capture the behavior of other clay structures. Nonetheless, they provide a valuable initial approximation.

The concentration of gas plays a significant role in determining the diffusion coefficient, making gas solubility an essential parameter to consider [1, 3, 5]. Moreover, studies have revealed that confinement enhances gas solubility, particularly in the case of methane [1]. Typically, at ambient conditions, gases exhibit low solubility, resulting in an insufficient number of molecules for accurate molecular dynamics simulations. In our study, we employed a gas concentration of 0.5 mol/L, which exceeds the typical gas solubility limit observed in bulk water under ambient conditions. Despite this higher solubility limit, our model successfully replicated experimental results for self-diffusion coefficients. To accurately quantify gas diffusion under varying conditions, a recommended approach involves conducting a Grand Canonical Molecular Dynamics simulation to accurately estimate gas solubility. Subsequently, diffusion computations can be performed.

The assumptions made in partial saturation simulations, such as considering planar thin films of water adsorbed to slit clay nanopores, may oversimplify the gas phase transport process. Clay nanopores, however, exhibit diverse morphologies including spherical or cylindrical shapes, which can deviate from perfect planarity [2, 4]. These variations in pore size and geometry can significantly influence pore saturation. Furthermore, gas transport may not occur as a continuous phase along the thin water film, but rather as gas bubbles enveloped by water, leading to curvature in the water layer. Thus, to accurately describe the behavior of gas in actual clay materials, it is crucial to consider the influence of pore morphology on gas diffusion and the diffusion of gas bubbles through the water.

The molecular dynamics simulation accurately predicted the swelling pressure of smectite clay based on its dry density. However, when the clay dry density was very high, there was a discrepancy compared to experimental results obtained from macroscale smectite samples. This difference arises because the molecular dynamics simulations mainly consider the interaction between perfectly aligned clay platelets, whereas the experimental samples are composed of partially aligned and disordered mineral grains represented by aligned TOT stacks. The contribution of TOT stacks with mono- and bi-layer water to the swelling pressure is minimal. The primary factor influencing the experimentally measured swelling pressure under these conditions is the osmotic interaction occurring in larger inter-particle pores and at the grain boundaries. Therefore, when dealing with high densities, a more robust methodology such as pore-scale swelling pressure calculations is necessary to accurately quantify swelling pressures.

Pore-scale simulations of water diffusion in porous clay smectite structures successfully provided insights into the diffusion process. It should be acknowledged, however, that this study solely considered a saturated system, neglecting the possibility of partial saturation where some pores are fully filled, while others may be dry or partially filled. In the case of partial saturation, the transport of water or gas species becomes more complex. In order to provide a more comprehensive understanding of the transport phenomena within the clay structures, specific transport processes due to the saturation of the pore must be described. The 2D lattice Boltzmann model was successfully applied and compared to the 2D random walk simulation. It was however challenging, from the side of the computational resources to apply a full 3D lattice Boltzmann simulation of a finely resolved complex structure of clay's tortuous characteristics. Consequently, there is a need for an enhanced lattice Boltzmann simulation in a 3D environment to accurately assess the applicability and limitations of the lattice Boltzmann method.

6.2 Outlook

The large-scale smectite clay structure investigated in this work by RW and LB simulations considered clay particles to be rigid. This means that any variations in the chemical composition of the fluid or changes in swelling pressure are not accounted for in the microstructure. Consequently, such a model would not be able to capture the effects related to alterations in pore size distribution or particle orientation resulting from phenomena such as swelling, shrinkage, precipitation, and dissolution.

A flexible representation of clay particles and accounting for the mechanical coupling between them would be an important step toward the development of the clay microstructure models. This approach will enable to account for the influence of mechanical load and pore water thermo-chemistry factors, such as ionic strength, temperature-controlled swelling, and capillary forces on the evolution of clay microstructure, including changes in pore size distribution and clay particle arrangement. This will lead to a breakthrough in accurately describing the pore structure and its response to changes in thermal-hydraulic-mechanical-chemical (THMC) conditions.

Another critical aspect to explore is the time-dependent evolution of clay microstructure during the de- and re-saturation processes. By studying the hysteresis in water uptake and the accompanying changes in microstructure, one can gain insights into the cracking mechanisms that occur during desaturation. Additionally, investigating the potential self-sealing mechanism of macroscopic cracks caused by local clay particle dispersion and swelling into the macroscopic pore space holds promise for understanding the sealing efficiency of clay barriers.

Another significant aspect for future studies could involve exploring reactive transport scenarios that incorporate precipitation and dissolution reactions within the simulation framework, coupled with sensitivity analyses. This approach will enable predicting the effect of pore changes as a result of the chemical reaction on the clay surface on the mobility of the gas transport and design appropriate mitigation strategies.

In summary, future research endeavors should focus on the development of a molecular/pore-scale model to capture clay microstructure evolution and the evaluation of gaseous molecule transport within clay systems. By integrating these advancements into our simulations, we can enhance our understanding of the intricate interplay between physical, chemical, and mechanical factors influencing clay behavior. This, in turn, will enable more accurate predictions and improved reliability of clay-based geological barriers in various applications.

6.3 References

- [1] Benazzouz, B. K., Ho, K. H., Nguyen, P. T., Hoang, H., and Galliero, G. (2022). Diffusive transport of gases in saturated nanopores: Caprock leakage from a molecular simulation perspective. *Journal of Natural Gas Science and Engineering*, 98:104383.
- [2] Guo, C., Wei, M., and Liu, H. (2015). Modeling of gas production from shale reservoirs considering multiple transport mechanisms. *PloS one*, 10(12):e0143649.
- [3] Jähne, B., Heinz, G., and Dietrich, W. (1987). Measurement of the diffusion coefficients of sparingly soluble gases in water. *Journal of Geophysical Research: Oceans*, 92(C10):10767–10776.
- [4] Strangfeld, C. (2021). Quantification of the knudsen effect on the effective gas diffusion coefficient in partially saturated pore distributions. *Advanced Engineering Materials*, 23(10):2100106.
- [5] Wise, D. L. and Houghton, G. (1966). The diffusion coefficients of ten slightly soluble gases in water at 10–60 c. *Chemical Engineering Science*, 21(11):999–1010.

Curriculum vitae

Jerry Peprah Owusu

Nelkenweg 1, 5417 Untersiggenthal (Switzerland)
jerrycalves@gmail.com
(+41) 0787288539

Summary

Passionate research scientist and experienced geological engineer, adept in overseeing scientific research and engineering projects and offering innovative solutions. Ambitious in contributing to innovative strategy and exploitation of new technology.

Education

University of Bern

PhD Earth Sciences

Oct 2019 – August 2023

Dissertation: Numerical simulations of gas transport in clay materials

ETH Zurich

MSc ETH Earth Sciences

Sept 2017 – Aug 2019

Thesis: Observation of cracking in damage controlled tensile fracturing

Kwame Nkrumah University of Science and Technology

BSc Geological Engineering

Sept 2012– June 2016

Thesis: The use of geophysical seismic survey in geotechnical site investigation

Experience

Paul Scherrer Institute

Doctoral Research Candidate

Nov 2019 – Current

- Developed mechanistic understanding of fluid and solute transport in porous materials using molecular dynamics simulations
- Reviewed and developed in-house numerical modeling codes in high-performance computing for fluid and solute transport
- Derived an up-scaling method for fluid and solute transport in porous media using pore-scale modeling methods

Swiss Competence Center for Energy-Supply of Electricity

Student Assistant

Dec 2018 – Jun 2019

- Identifying key geological features and potential hazards in the Bedretto Tunnel, using advanced mapping techniques and geological knowledge
- Delivered critical insights into rock behavior and stability through an innovative hydraulic measurement system design that exceeded project requirements and expectations

Kinross Gold Corporation, Chirano Gold Mines

Exploration Geologist/Geotechnical Engineer

Sept 2016 – Aug 2017

- Enabled a 5-year expansion of the mine by providing geological expertise in the planning of a new underground mine
- Provided geotechnical guidance for mine operations that limited and managed wall failure
- Designed exploration and geotechnical drilling programme and supervised over 10 staff for drilling and exploration activities
- Interpreted the behaviour of hydrothermal fluid deposits using XRF experiments on drill core and solved a puzzle about changes in ore grade
- Collected geochemical data and analyzed it in terms of resource economics and modeling which maximized mine production and profits

CSIR Building and Roads Research Institute

Geotechnical Engineering Intern

May 2015 – Sept 2015

- Provided ground engineering expertise in the safe design of embankments, road pavements, excavations, and foundations
- Determined the suitability of excavated earth as subsoil or substructure for road construction by geotechnical experiments and analysis
- Derived stabilization mechanisms for problematic and expansive soils from geotechnical laboratory experiments
- Investigated the stability of the subsurface of a site as a foundation for a massive church building

Technical Skills

- **Programming:** C++, Python, Matlab, Bash scripting
- **Software:** Linux OS, Windows OS, AutoCAD, ArcGIS, LAMMPS, CP2K, Comsol, OpenGeoSys, OpenFOAM, Plaxis 3D, Surpac, Ansys, MapInfo, Slide, Slope/w, FLAC, LAMMPS, CP2K, GROMACS, Dips, Flotran, PHREEQC, GEMS, Leapfrog Geo

Core competencies

Computational fluid dynamics, Molecular dynamics simulations, Reactive transport modeling, Finite element and Finite difference analysis, Geotechnical site investigation, Fracture mechanics, Geochemical modeling, Hydrogeology, Data analytics, Machine learning, Mineral exploration, Mine geology, Geological field and laboratory experimentation

Publications

Owusu, J. P.; Karalis, K.; Prasianakis, N. I.; Churakov, S. V. Mobility of Dissolved Gases in Smectites under Saturated Conditions: Effects of Pore Size, Gas Types, Temperature, and Surface Interaction. *The Journal of Physical Chemistry C* 2022, 126, 17441–17455.

Owusu, J. P.; Karalis, K.; Prasianakis, N. I.; Churakov, S. V. Diffusion and Gas Flow Dynamics in Partially Saturated Smectites. *The Journal of Physical Chemistry C* 2023 – Under Review

Owusu, J. P.; Karalis, K.; Prasianakis, N. I.; Churakov, S. V. Swelling Pressure of Na-Montmorillonite in the presence of gas from molecular dynamics study. *The Journal of Physical Chemistry C* 2023 – Under Review

References

Head of Laboratory

Professor Dr. Sergey V. Churakov

Paul Scherrer Institute

sergey.churakov@psi.ch

+41 56 310 4113

University of Bern

Institute of Geological Sciences

sergey.churakov@geo.unibe.ch

+41 31 631 8710

Line Manager

Dr. Nikolaos I. Prasianakis

Paul Scherrer Institute

nikolaos.prasianakis@psi.ch

+41 56 310 2415

Declaration of Originality

Declaration of consent

on the basis of Article 18 of the PromR Phil.-nat. 19

Name/First Name: Owusu Jerry Peprah

Registration Number: 17-940-487

Study program:

Bachelor

Master

Dissertation

Title of the thesis: Numerical simulations of gas transport in argillaceous rocks:
A molecular dynamics simulation and pore-scale Lattice
Boltzmann modeling study

Supervisor: Professor Dr. Sergey V. Churakov

I declare herewith that this thesis is my own work and that I have not used any sources other than those stated. I have indicated the adoption of quotations as well as thoughts taken from other authors as such in the thesis. I am aware that the Senate pursuant to Article 36 paragraph 1 litera r of the University Act of September 5th, 1996 and Article 69 of the University Statute of June 7th, 2011 is authorized to revoke the doctoral degree awarded on the basis of this thesis.

For the purposes of evaluation and verification of compliance with the declaration of originality and the regulations governing plagiarism, I hereby grant the University of Bern the right to process my personal data and to perform the acts of use this requires, in particular, to reproduce the written thesis and to store it permanently in a database, and to use said database, or to make said database available, to enable comparison with theses submitted by others.

Untersiggenthal, 17.06.2023

Place/Date

Signature

